# Ab initio theory of electronic excitations at surfaces

**Dissertation**

**zur Erlangung des Grades**

**Doktor der Naturwissenschaften (Dr. rer. nat.)**

**von**

**Matthias Timmer**

**aus Dorsten**


**vorgelegt der und genehmigt von der**
**Fakultät für Physik der**
**Universität Duisburg-Essen**
**Tag der mündlichen Prüfung: 29. Juni 2010**

*Ich versichere, dass ich die vorliegende Arbeit selbstständig*
*und nur unter Zuhilfenahme der angegebenen Hilfsmittel angefertigt habe.*

Duisburg, 20.04.2010

**Erstgutachter: Prof. Dr. Peter Kratzer**
**Zweitgutachter: Prof. Dr. Dietrich Wolf**
**Drittgutachter: Prof. Dr. Axel Groß**

# Contents

# List of Figures

The following publications are derived from this thesis:

Published:

- M. Timmer and P. Kratzer, "Electron-hole spectra created by adsorption on metals from density-functional theory", Phys. Rev. B **79**, 165407 (2009)

- M. Timmer and P. Kratzer, "Theoretical investigation of the influence of isotope mass on chemicurrents during adsorption of H on K(110)", Surf. Sci. **604**, 1452 (2010).

In preparation:

- U. Hagemann, M. Timmer, D. Krix, P. Kratzer, and H. Nienhaus, "Electronic excitations in Magnesium epitaxy: Theory and Experiment", in preparation (2010).

# Chapter 1

# Introduction

During the last years there has been constant progress in the area of non-adiabatic effects, especially at surfaces. Experimentally there has been progress, e.g., in the area of energy dissipation mechanisms as investigated in the Sonderforschungsbereich (SFB, collaborative research center) 616, "Energy Dissipation at Surfaces", of the Deutsche Forschungsgemeinschaft (DFG, German research foundation), see the SFB's website http://www.sfb616.uni-due.de/index.htm. Here a wide range of effects have been observed, connected to the area of excitation and decay. Examples include the excitation and decay of vibrational damping of adsorbate vibrations on metals, measured by SFG spectroscopy [1], measurements of ballistic electrons moving through adsorbates on metal surfaces [2] and especially electronic excitations in metals [3], based upon previous work on that subject [4]. The experimental results propose a measurable electronic excitation during many processes involving a metal surface, including epitaxy. Theoretical results support these measurements [5, 6]. The vibrational decay on non-metal surfaces has also been investigated [7, 8].
The physical reason behind excitation of electrons and holes is that a metal offers a continuum of electronic states, so that arbitrary small excitation energies are possible, and hence the adiabatic limit for scattering or adsorption of particles is ill-defined [9]. Dissipation of some part of the particle's energy to the metal surface via electronic excitation has been known for a long time, and is the physical cause for exo-electron emission [10, 11] and the so-called chemicurrents (see below). Moreover, for the sticking of atoms or molecules to a surface, it is necessary that at least some part of the adsorption energy is dissipated into the substrate. While the role of the *nuclear* excitation processes (e.g., phonons) is comparatively well understood, the role of *electronic* excitation processes in the energy dissipation during adsorption and other dynamical processes at surfaces is elusive. The ubiquity of (albeit small) non-adiabatic contributions to chemical reactions at metal surfaces underlines the practical importance of understanding the process of electronic dissipation [12]. So far, most calculations addressing gas-surface interactions assume that an adiabatic regime would exist, by treating the interaction dynamics on a Born-Oppenheimer potential energy surface. While this assumption may often yield plausible results, it is strictly speaking not justified for metals, since some electronic excitations must always occur, as discussed above. On the basis of calculations for dissociative adsorption of hydrogen molecules, it has been argued recently that the energy dissipated to the electronic system is rather small [13], even on a metal, and thus has little effect e.g. on the energy dependence of the sticking coefficient [14]. These results seem to suggest that some (probably the larger) part of the adsorption energy of the sticking particles is dissipated to excitations of the lattice. Note, however, that in a comment on Ref. [13] the applied method [15] is criticized, providing good arguments. Anyway, the authors of Ref. [13] claim that their main conclusion, the small influence of electronic excitations, still holds. Other theoretical results (for the impact of a keV silver atom on a silver surface) claim that after some 100 fs, about 60 % of the kinetic energy is transferred to electronic excitations, localized near the impact point [16]. These excitations decay into lattice vibrations on the timescale of ps. Further experimental clarification of this point is desirable, but it is possible to conclude that electronic excitations play an important role in at least some systems, and may even be essential to understand the dynamics. One approach to investigate the importance of electronic excitations is the observation of vibrational decay, where one finds generally that the decay is the stronger the more metallic a system is, i.e. decay lasts longer

on an insulator than on a semiconductor than on a metal [17, 18, 19]. Since the main difference between these kinds of system is the possibility of electronic excitations, this result again shows the importance of electronic excitations on metal surfaces. Vibrational decay of NO on gold has recently been investigated theoretically, and it was shown that conversion of vibrational energy into electronic energy is efficient [20, 21]. However, this approach has not yet been applied to chemicurrents, see below.

The measurement of chemicurrents offers a possibility to quantify the amount of electronic excitation that takes place during chemisorption. In these experiments, the gas-phase particles are adsorbed on a metal film, fabricated either by previous deposition on a semiconductor substrate or a thin insulating barrier layer, forming a Schottky diode [11] or a metal-insulator-metal (MIM) device [3], respectively.

While particles are being adsorbed, an electric current is detected, originating from carriers that have been excited sufficiently strongly to overcome the in-built potential barrier of the detection device. Typical barrier heights are of the order 0.4 – 1 eV. In the investigated systems of the present work they are around 0.5 eV. The physics of the underlying processes is similar to the emission of exo-electrons, only differing in the fact that the lower internal barrier, e.g. in a Schottky diode, allows for detection of a larger fraction of the excited carriers as compared to emission into the vacuum. The latter process is possible solely for electrons whose energy exceeds the work function of the metal, typically several eV. Therefore in the chemicurrent setup it is possible to detect electronic excitations with an energy much lower than the work function. The size of the measured chemicurrents is dependent on the chemical nature of the adsorbing species, and to a lesser extent also on the metal surface [4].

It is possible to investigate the chemicurrent detected for different isotopes during adsorption on metal surfaces, each starting with the same kinetic energy. The strong observed isotope effect (so far only data for hydrogen versus deuterium adsorption on silver are available, differing by about a factor three to four [22]) clearly shows that the origin of the measured chemicurrents is related to *dynamical* electronic excitations. *Static* energy transfer gave approximately the same results for all isotopes, since all isotopes have the same adsorption energy, and a static process would dissipate the same percentage of this energy into the metal. The size of the isotope effect is, so far, the most sensitive test for a theoretical description of chemicurrents, as it reflects the small high-energy tail of the spectrum of electronic excitations. Therefore all theoretical investigations of chemicurrents should describe this effect well.

Because of the importance of the dynamics, it is necessary to include it in the theoretical description of these processes.

Previously, there have been several approaches in use to calculate chemicurrents: In recent work, the dynamics of the full electronic system of a slab model of the surface has been calculated from time-dependent density functional theory (TDDFT) [6] for the system H/Al(111). In this approach, the time-evolution of the electronic wavefunctions of an adsorbate-substrate system is calculated. The resulting non-adiabatic occupation of the Kohn-Sham states, and the total energy of the system, is compared to their adiabatic occupation, and the energy of the adiabatic state. This defines the electronic excitation and, by comparing the total energies, dissipation into the electronic system. The approach is conceptually very appealing, but computationally cumbersome. Moreover, it requires high numerical accuracy, as the excitation energy of the electronic system, a small number, needs to be calculated by comparing huge numbers, the total internal energies in the ground state and the excited state. Additionally the numerical size of this ansatz still enforces convergence parameters for the calculation, which are off a good treatment of the system, ranging from a too small basis set for the wave functions to a coarse resolution of the Brillouin zone. In these calculations the adsorbate keeps sticking to the surface, and is oscillating in the chemisorption well, until the chemisorption energy is transferred into the substrate. Results show a large difference in the excitation of different spin channels, for both electrons and holes, labeled spin effect, after the first half round trip in the chemisorption well, i.e. when it has first approached the surface. The spin effect disappears after the first full round trip, i.e. when the particle is scattered back a few Å into the vacuum. This spin effect is resulting from the DFT spin transition, which is the loss of the spin polarization of the adsorbing hydrogen atom when it approaches the surface. The spin effect may be an artifact of DFT calculations; a conclusion which is supported by as yet unpublished results of Monte-Carlo simulations of the ground state [23]. The numerical reason behind this artifact may be found in the correlation error of DFT when

using present-day XC-functionals [24]. Moreover, recent as yet unpublished results for hydrogen adsorption on silicon have proven that the aforementioned definition of dissipated energy is ill-defined, since some of the changes in the electronic structure at the surface are reversible, but are counted as dissipated energy after one half round trip of the particle in the chemisorption well [25].
In a different approach, the energy dissipated to the electronic system has been calculated from the theory of electronic friction [26, 5], that was originally developed in the context of adsorbate vibrational damping. However, this theory does not yield directly the spectra of the excited carriers. Instead, it is assumed that the excitation is made up from a superposition of individual electron-hole (e-h) pairs of small excitation energies. These energies are assumed to be limited to a narrow energy region around the Fermi energy of the metal, allowing for a calculation of the excitation probability solely based on the properties of electronic states right at the Fermi level. For higher excitation energies, the probability is calculated by referring to the additional assumption of independent multiple electron-hole pair excitations that can be described by a Poissonian process [27]. This is the so-called forced oscillator model (FOM). Thus, the assumptions made do not allow one to take into account the electronic single-particle properties of the metal under study further away from the Fermi energy. Additionally there appear conceptual problems when a divergence of the friction coefficient is observed, which must be artificially patched [27], and a suspiciously broad energy range around the Fermi energy is included in the calculation of the friction coefficient, which is defined as excitation close to the Fermi energy [26]. Note that in the present work it is demonstrated that the FOM is not justified.
Another theory has been worked out that allows the calculation of chemicurrents by solving the dynamics of an appropriate model system, described by a Newns-Anderson (NA) Hamiltonian [28, 29, 30, 31]. This scheme is computationally lighter than the full TDDFT dynamics, and allows the discussion of interesting trends over a variety of model systems [29]. Material-specific physics can be described by matching model parameters to values calculated from DFT [30]; however, no detailed account of the metallic band structure for the excitation of chemicurrents is attempted in this theory. Furthermore the results are stronlgy dependent on model parameters, which must be fitted, and the problem of the spin transition in DFT calculations (on the adsorbate's way back from the surface) is not accounted for (though present).
Finally, yet another model has been worked out recently. This is the time-dependent tight binding approach, which is still unpublished [32]. It is conceptually similar to the NA model approach: A single level atom interacts with a simple cubic lattice. The model includes a time-dependence in the adsorbate energy level and an adsorbate-surface hopping term. This method allows comparison between a perturbative and non-perturbative tight-binding approach. However, the parametrization for real systems is not straightforward.
In order to develop a reliable theory of electronic excitation, which can be applied to real systems, it is desirable to investigate several points:

1. Is it possible to obtain a theory, which is computationally appealing, but still gives results compatible with experimental data?
2. What is the range of validity for such a theory?
3. How can one treat the spin transition and charge transfer in adsorption, and what is their role?
4. Is it possible to take effects into account, which rely on properties of excited states?
5. How can the theory be reformulated to widen its range of validity?
6. Do present-day theories describe the physical properties of electronic excitations correctly?

The present work will try to give some insight into these topics. It is organized as follows:
In chapter 2, an introduction is given into the relevant aspects of DFT calculations, necessary for this work. Some physical concepts behind the treatment of electronic excitations used in this work are presented. The chapter includes some basic theories for electronic excitations, which have been implemented in a self-written code. A time-dependent perturbation theory for electronic excitations, suitable for post-processing in many

DFT codes, the most important part of this work, is developed. The electronic friction / forced oscillator model, which is used nowadays by experimentalists to explain their data, is recapitulated. Chapter 3 gives possible extensions of the theory, and discusses briefly on the problems of these extensions. Also the developed perturbative approach is investigated in more detail. In chapter 4 results are shown for the calculation of electronic excitations during adsorption of hydrogen isotopes on the Al(111) surface. The effects of several extensions proposed in chapter 3 are investigated. This chapter contains comparisons with available data from other theoretical approaches, and shows which of the extensions and approaches work, and which are not compatible with experimental data. It is shown that a simple perturbative approach gives reasonable results, with the possible exception of spin effects. It is also shown that the total dissipated energy, which is dominated by the central peak of the spectra, is probably not well-described by the perturbative approach, but the tails of the spectra are. Moving on to other systems, chapter 5 deals with electronic excitations in the system H/K(110). In this chapter the effects of the narrow metal band of potassium are investigated, demonstrating that narrow bands influence excitation spectra in a way that should be observable in experiments. Also the isotope effect and corresponding mass-scaling is investigated thoroughly in this chapter. It is concluded that the forced oscillator model is not justified, and the number of electrons detectable in experiments is larger than expected from the forced oscillator model for heavy isotopes. Electronic excitations in metal epitaxy are investigated in chapter 6 for the system Mg/Mg(0001). Although Mg is a rather heavy atom, and thus moving slowly when adsorbing, electronic excitations play a more important role than was believed by many researchers up to now, and they can be observed in metal epitaxy. However, for detectable chemicurrents in metal epitaxy surface defects play an important role. This is shown in this chapter, and their role is investigated. Theoretical calculations also show that chemicurrent observation in metal epitaxy may be possible. Finally chapter 7 gives insight into the application of the perturbative approach on the system $Cl_2$/K(110), where charge transfer effects are important. One trajectory of the $Cl_2$ molecule is calculated within the framework of molecular dynamics (MD), and several important conclusions may be drawn from this calculation. One of the main results is that the surface dynamics should be taken into account for theoretical investigations of this system, since it is very involved. However, it is also shown that the system is outside the range of validity of the perturbative approach, and different approaches must be taken to describe this system correctly. The large chemisorption energy of the $Cl_2$ molecule on the potassium surface plays a dominating role here. Some remarks can be made about the ionization of the molecule, which breaks up during the adsorption process. It is proposed that the general form of the spectra resembles a Lorentzian more than an exponential in the energy range around the Schottky energy (0.5 eV). A discussion of the results and an outlook concludes this work in chapter 8.

# Chapter 2

# Fundamental Considerations

In this work the tool of Density Functional Theory (DFT), and a perturbation theory based on the results of these DFT calculations, is used to describe electronic excitations. While it is not the purpose of this work to give a full overview of DFT or introduction into it, a short description of its principal ideas, some approximations done, and its limitations will be useful to understand the results in this thesis. A lot of work on DFT has already been published. As an introduction the author proposes the excellent book of Richard Martin [33], which contains numerous references to the literature.
In this chapter, first the theoretical foundations and some principal results from DFT are described. This part rests partially on the thesis by F. Charry [34], and in section 2.1 this work is quoted heavily. Details are presented where necessary to understand theoretical considerations for electronic excitations. The Born-Oppenheimer approximation is explained in section 2.2.1, and provides the prerequisites for the calculation of electronic excitations in this work. The explanation is taken from Ref. [33]. This section also contains remarks on the trajectory approximation used throughout this work. Remarks on electron-hole pair excitations are found in section 2.2.2, especially in connection with an adsorbate approaching a surface, and detection devices are explained in section 2.2.3. The theoretical methods to describe electron-hole pair excitations in adsorption are explained in section 2.3, and it is explained, how the methods work in combination with DFT. The terms 'adiabatic' and 'nonadiabatic' are explained within the framework of electronic excitations in section 2.4. In section 2.5 the electronic friction model for electronic excitations is explained, including its extension to the forced oscillator model.

## 2.1 Density Functional Theory Framework

The main goal of an *ab initio* computational method, given the exact composition and structure of a system, is to calculate its properties as accurately as possible by solving the (many-body) electronic Schrödinger equation. These methods do not make use of empirical information or free (fit) parameters. However, to find the quantum ground state of a condensed system is a correlated many-body problem, which at present can only be solved approximately. In practice, even the correct solution of the correlated spin states of an $N$-electron system would require at least $2^N$ bytes of hard disk space, i.e. $10^{51}$ GB for a 200 electron problem, which is currently far beyond any realistic size.
DFT, among the *ab initio* methods, is now one of the most widely used approaches to the many-electron problem. It is, in principle, an exact theory for interacting electrons, but in practice it is an approximate methodology in terms of single electron equations.

### 2.1.1 The Hohenberg-Kohn Theorems

P. Hohenberg and W. Kohn formulated the basis of DFT in 1964 [35]. They established that any property of a system of many interacting particles, in an external potential $V_{\mathrm{ext}}(\mathbf{r})$, for condensed matter usually the ionic Coulomb potential of the atomic nuclei, can be seen as a functional of the density of particles in its ground state

$n_0(\mathbf{r})$. In this way, given this functional of $n_0(\mathbf{r})$, it is possible, in principle, to get all the information of the system. To put it into a nutshell, every observable $\hat{O}$ can be determined by just knowing the ground density of a system:

$$\left\langle \Psi[n_0] \left| \hat{O} \right| \Psi[n_0] \right\rangle = O[n_0], \tag{2.1}$$

where the $|\Phi[n_0]\rangle$ denote the many-particle wavefunction of the system, as functionals of the ground state density. The most important statement of the theorem is that the observable is a functional of the *density*, and not necessarily of the many-body wavefunction, which dramatically reduces the dimension of the problem.
Strictly speaking, DFT is based on only two theorems:

- For any system of interacting particles in an external potential $V_{\text{ext}}(\mathbf{r})$, the potential $V_{\text{ext}}(\mathbf{r})$ is determined uniquely, except for a constant, by the ground state density $n_0(\mathbf{r})$.
- For any particular $V_{\text{ext}}(\mathbf{r})$, the exact ground state energy of the system is the global minimum value of the energy functional $E[n]$; and the density $n(\mathbf{r})$ that minimizes the functional is the exact ground state density $n_0(\mathbf{r})$.

These can be expressed in this alternative form: the density of the particles in the ground state uniquely determines the external potential $V_{\text{ext}}(\mathbf{r})$ acting on them, and vice-versa.
In this way, the total energy of the ground state of a system of $N$ interacting electrons in an external potential can be obtained from the minimization of the Hohenberg-Kohn electronic total energy functional $E_{HK}[n]$,

$$E_{V_{\text{ext}}}[n] = \mathcal{F}_{HK}[n] + \int d\mathbf{r} V_{\text{ext}}(\mathbf{r}) n(\mathbf{r}), \tag{2.2}$$

where the functional $\mathcal{F}_{HK}[n]$ is the sum of a kinetic term and the interaction term between electrons,

$$\mathcal{F}_{HK}[n] = T[n] + W[n]. \tag{2.3}$$

These expressions are basically the expectation value of the many-body wavefunction rewritten in a functional manner, and the minimization of the energy can be done following Ritz' principle. For a system made of atoms, which contain electrons and nuclei, the external potential felt by the electrons contains the electron-nuclei interaction, and an additional, classical term $E_{II}$ describing the interaction between nuclei must be added to the total energy in equation (2.2). This term is a constant with respect to the energy of the electronic system, and so it is unproblematic.
In this formulation, the problem of evaluating the functional $\mathcal{F}_{HK}[n]$ prevails, for which an explicit form is not known. Obtaining this form is equivalent to solving the original many-body problem; something which is only possible for systems with very few particles, very far from real and interesting systems like molecules, crystals or surfaces. So up to now all these results are only principle ones without much practical use, because the mathematical proof is only a proof of existence, not a (fully) contructive one. The fact that transformed DFT in a primary practical tool for electronic calculations, was the proposal of the Kohn-Sham ansatz in 1965 [36].

### 2.1.2 The Kohn-Sham Ansatz

In this ansatz, Kohn and Sham [36] assume that the exact ground state density of the original interacting system is equal to that of a fictitious non-interacting system. Then the ground state density of $N$ electrons can be rewritten in the form

$$n_0(\mathbf{r}) = \sum_{j=1}^{N} \sum_{\mathbf{k}\epsilon BZ} \left|\psi_{j,\mathbf{k}}(\mathbf{r})\right|^2, \tag{2.4}$$

where $\psi_{j,\mathbf{k}}$ are the occupied ground state wave functions of each independent electron (including the spin). The sum over $\mathbf{k}$ denotes the integration over the Brillouin zone (BZ), executed as a sum in practice. A weight factor has been included in the wavefunctions. These are eigenstates of the equation

$$(H_{KS,\mathbf{k}} - \varepsilon_{j,\mathbf{k}})\psi_{j,\mathbf{k}} = 0, \tag{2.5}$$

where $H_{KS}$ ist the one-particle Hamiltonian, which reads:

$$H_{KS} = -\frac{\nabla^2}{2} + \hat{V}_{\text{eff}}. \tag{2.6}$$

Atomic Hartree units are used throughout this chapter. $\hat{V}_{\text{eff}}$ is now an operator describing the effective potential in which one electron is embedded. In order to get the correct form of this effective potential one has first to describe the functional form of the energy taken by Kohn and Sham in their approach. At first, they took into account the classical Coulomb potential created by the electronic distribution. This is known as the Hartree potential, having the form

$$V_H = \int d\mathbf{r}' \frac{n(\mathbf{r}')}{|\mathbf{r} - \mathbf{r}'|}. \tag{2.7}$$

From here, the Hartree energy functional is defined as the self-interaction energy of the density $n(\mathbf{r})$ treated as a classical charge density

$$E_H[n] = \frac{1}{2}\int d\mathbf{r} V_H(\mathbf{r}) n(\mathbf{r}) = \frac{1}{2}\int d\mathbf{r} d\mathbf{r}' \frac{n(\mathbf{r}) n(\mathbf{r}'))}{|\mathbf{r} - \mathbf{r}'|} \tag{2.8}$$

The ground state energy functional in the Kohn-Sham formalism has the form

$$E_{KS} = T_S[n] + \int d\mathbf{r} V_{\text{ext}}(\mathbf{r}) n(\mathbf{r}) + E_H[n] + E_{XC}[n]. \tag{2.9}$$

The term $T_S[n]$ is the kinetic energy of this fictitious system of non-interacting electrons with the same density as the interacting one. In this way the complexity coming from electron interactions have been displaced into a new term: the exchange-correlation (XC) functional $E_{XC}$. Note that the total energy contains an additional term due to the ion-ion interactions.

In order to understand the meaning of $E_{XC}$, equations (2.9) and (2.2) must be compared. This leads to the expression

$$E_{XC}[n] = \langle T \rangle - T_S[n] + \langle \hat{V}_{\text{Coulomb}} \rangle - E_H[n]. \tag{2.10}$$

In this expression one can see that $E_{KS}$ is, in fact, the difference of the kinetic and the interaction energies between the true interacting many body system and the fictitious independent particle system with the electron-electron in $\hat{V}_{\text{Coulomb}}$ interaction replaced by the Hartree energy [33]. In other words, one recovers here what was lost assuming an independent particle framework. The definition *exchange-correlation*, in this manner, is not fully appropriate, because $E_{XC}$ contains, in addition to the exchange and correlation energies, a correction to the fictitious kinetic energy. In the above interpretation of $E_{XC}$, an exact analytical form of this functional is still unknown.

In essence, the Kohn-Sham approach transforms the problem of $N$ interacting electrons into the simpler problem of solving $N$ independent Schrödinger equations for $N$ non-interacting electrons moving in an effective potential. The effective potential is usually assumed to be local, and takes the form:

$$\begin{aligned} V_{\text{eff}}(\mathbf{r}) &= V_{\text{ext}}(\mathbf{r}) + \frac{\delta E_H}{\delta n(\mathbf{r})} + \frac{\delta E_{XC}}{\delta n(\mathbf{r})} \\ &= V_{\text{ext}}(\mathbf{r}) + V_H(\mathbf{r}) + V_{XC}(\mathbf{r}). \end{aligned} \tag{2.11}$$

Therefore, the many body effects are described by the exchange-correlation potential $V_{XC}$, related with the XC energy functional (2.10). If the exact form of $E_{XC}$ is known, the exact ground state energy and density of the interaction system could (probably) be found by solving the Kohn-Sham equations in a self-consistent way. A small amendment must be made: There exists no rigorous proof of this ansatz [33].

It is important to note that the one-particle Kohn-Sham wave functions $\psi_{j,\mathbf{k}}$ have nothing to do with the true many-body ground state wave function $\Psi_0$ of the interacting system, except that both define the same ground state density $n_0(\mathbf{r})$. This warning is also valid for the eigenvalues in Eq. (2.5), which can not, strictly speaking,

be considered as electronic energy levels. Only the highest occupied eigenvalue of the Kohn-Sham equation in a finite system has a physical meaning, namely the ionization energy of the atom. This eigenvalue dominates the long-range tail of the density, which must agree with the true density by definition [33]. In spite of this, and the known deficiencies in the description of gap energies (in semiconductors and insulators), it has been customary to adopt the interpretation that the Kohn-Sham eigenvalues closely resemble the physical energy levels, and the Kohn-Sham wavefunctions closely resemble the many-body wavefunction. More accurate methods, such as the GW approximation [37], are much more expensive than plain DFT, and often more restricted. Note, however, although this statement is still correct in principle, newer results have shown that the eigenvalues are indeed close to the experimental values, if the used XC functionals fulfill some exact conditions on the exact functional, see Ref. [38] and references therein.
Thus, with the help of the Kohn-Sham ansatz, DFT becomes a practical methodology. However, now the problem of the exact form of $E_{XC}$ prevails. Approximate expressions to this functional have been proposed in order to be able to solve the $N$ non-interacting Kohn-Sham equations.
The exchange-correlation energy gives the smallest contribution to the total energy. Since the kinetic and the Hartree energy are already explicitly taken into account in the Kohn-Sham equation, the exchange-correlation potential can often be assumed to be local with a good approximation.
There are two standard approximations for the $E_{XC}[n]$ functional, the Local Density Approximation (LDA) and the Generalized Gradient Approximation (GGA). While LDA is expected to work very well for systems with an electronic density close to a homogeneous gas (due to its definition), it is not justified for inhomogeneous cases. Nonetheless, LDA often works quite well even in such systems. However, this work deals with effects at surfaces. Here the system is inhomogeneous by construction. In order to avoid possible failures of LDA, it is better to not use it in these systems.
In order to overcome this deficiency of LDA, GGA has been proposed. Recognizing the failure of the LDA expression to describe the dependence of the energy density on spatial variations of the particle density, GGA [39] includes the dependence of the gradient (and further derivatives) of the density. In this way, the total exchange-correlation energy is now expressed in a generalized form as

$$E_{XC}^{GGA}[n(\mathbf{r})] = \int d\mathbf{r} n(\mathbf{r}) \epsilon_{XC}^{GGA}(n(\mathbf{r}), \nabla n(\mathbf{r}), ...), \tag{2.12}$$

where $\epsilon_{XC}$ is the exchange correlation energy density of a nonuniform electron gas. The gradient expansion is called generalized because a simple gradient expansion violates sum rules, especially for the so-called correlation hole. This hole describes the interaction of an electron with its surrounding, positively charged environment. It must of course be equal to one positive electronic charge, because one electron will vacate its surroundings to an amount equal to one electronic charge.
There are several parametrizations of the GGA. Among them, the parametrization of GGA proposed by Perdew, Burke and Ernzerhoff [39], from first principles calculations, is probably the most used one, and the best for the present work. So this parametrization is sticked to throughout this work.
It is also possible to take exchange perfectly correct into account, e.g. by the EXX exchange potential, where an exchange part similar to the Hartree-Fock exchange is introduced [40]. This removes the spurious self-interaction of the density with itself in Eq. (2.8). In practice the correlation part must then be taken from anywhere else, and the calculations require a lot of additional time.

### 2.1.3 PWSCF Implementation

The solution of the Kohn-Sham equations for systems of many atoms, in a numerical way, is the goal of practical DFT formulations. The good results provided by these formulations have made them increasingly used by the scientific community. At the same time, the number of codes developed to perform these calculations, and their capabilities and efficiency, has increased dramatically, making them available for an increasingly wider community of DFT practitioners.

All DFT calculations done in this work have been carried out using the *PWSCF* code (Plane Wave Self-Consistent Field), and its various post-processing tools [41], including a self-written one, see section 3.2. There are several advantages of this code with respect to other codes, especially that it is free under the GNU licence, and that the source code is open. Because a lot of post-processing tools had to be implemented by the author, an open source code, with the possibility to have an interface with existing parts of the code, was an absolute necessity.
A detailed description of the code is not given here, neither are its implementation or capabilities explained in detail. A lot of information can be found on the *PWSCF* website[1] and in the user guide[2]. In Ref. [41] a more general overview is found, describing aspects of the code.
Some features are commonly used in the calculations within this work. These are described in the next part.

### 2.1.4 Pseudopotentials

An atom's electrons can be divided into two groups, core and valence electrons. Core electrons reside in the deeper shells and are strongly bound to the nuclei. As a consequence, the core electrons are not strongly affected by the chemical environment in which the atom is embedded; they usually do not participate in the chemical bonding and seldom in electronic excitations. A certain amount of judgement remains for the scientist: The distribution among "valence" and "core" is not unique or well-defined. Instead, it depends on the system one wants to investigate, how many electrons have to be taken into the valence; usually as few as possible are wished for. From the numerical point of view, the core electrons represent a very high computational cost, especially when using a plane wave basis (cf. section 2.1.7). Besides increasing the number of orbitals to be computed, orthogonality between the valence and core wave functions is required. Thus, core electrons impose the presence of nodes in the valence and core wave functions. To be able to describe these nodes, the basis set must be larger, and the calculations are more expensive from a computational point of view. For instance, in plane wave calculations, a huge number of plane waves would be required to describe the nodes near the core.
To reduce the computational cost the pseudopotential approximation was proposed. In this approximation, the strong nuclear potential and the core electrons are replaced by an effective ionic potential (pseudopotential) action on the valence electrons.
Once these pseudopotentials have been generated, an important condition they must fulfill is their transferability. A pseudopotential should be suitable, not only to describe the single electronic configuration it was constructed for, but also similar configurations. This means that the total energies gained from pseudopotential calculations have to differ by only a small amount from the energies gained by all-electron calculations, on diverse electronic configurations differing from the starting one.
Some general characteristics define the pseudopotentials used within this work: (a) The pseudopotentials used are norm-conserving, in which the norm of the pseudowave function is the same as the one of the true wave functions [42, 43]. (b) The use of cutoff radii: These radii define the region beyond which the pseudo-charge density as well as the pseudo valence orbitals are equal to the all-electron ones. (c) The use of core-corrections [44]: These corrections account, at least partially, for the nonlinearity in the exchange and correlation potential in the charge density. Its use is strongly recommended when there is a large overlap between valence and core charge, e.g. in the transition metals. With this correction the true core charge is replaced by a fictitious and smoother charge, which is added to the valence charge. (d) They are fully separable: they are formed by a local part, common for all angular momenta, and a non-local part, which depends on each angular momentum following the method proposed by Kleinman and Bylander [45].
A general overview over pseudopotential methods has been given by Pickett [46].
A sketch of the effect of the introduction of a pseudopotential can be seen in Fig. 2.1, taken from Ref. [47]: The exact wavefunction, which has several nodes, is substituted by a pseudo wavefunction, which has no nodes, thereby reducing computational effort to calculate it. The potential is also substituted by a pseudopotential, which takes into account the collective effect of the inner-shell electrons on the outer-shell wavefunctions.

[1] http://www.quantum-espresso.org/wiki/index.php/Bibliography
[2] http://www.quantum-espresso.org/wiki/index.php/User_Guide

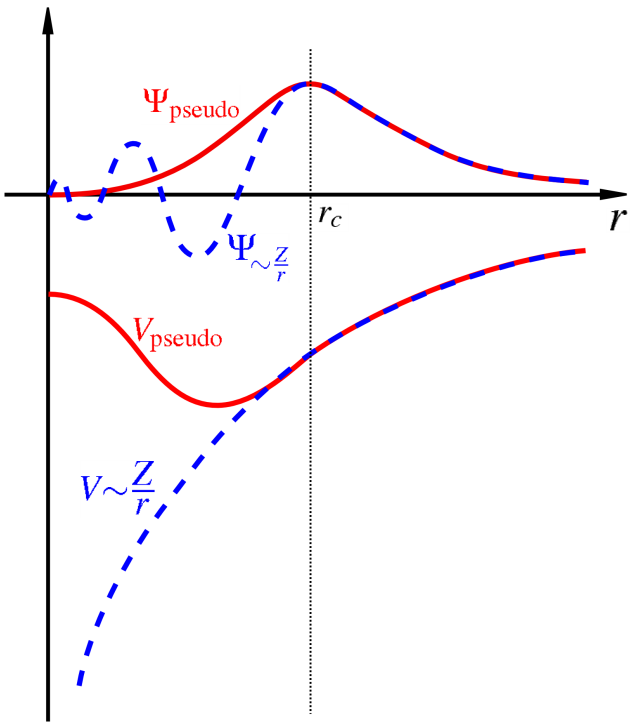


Figure 2.1: Comparison of a wave function in the (Coulomb) potential of the nucleus, i.e. $\Psi$ in the potential $V$ (both blue), and a pseudowave function in the corresponding pseudopotential, i.e. $\Psi_{\text{pseudo}}$ in the potential $V_{\text{pseudo}}$ (both red). The all-electron and the pseudo-wavefunction and the potentials are equal above some cutoff radius $r_c$. For radii smaller than the cutoff radius the number of nodes of the pseudo-wavefunction is significantly reduced, namely to zero.

Only beyond a certain cutoff radius $r_c$ is the pseudo wavefunction equal to the all-electron wavefunction.

### 2.1.5 Sampling of the Brillouin Zone

The first Brillouin zone (BZ) is the Wigner-Seitz cell of the reciprocal lattice, which is defined by the planes that are the perpendicular bisectors of the vectors from the origin to the reciprocal lattice points. Evaluation of many quantities, such as energy and density, requires integration over the BZ. Accurate integration is done with a discrete set of points in the BZ, which are called the k-points. The required density of the points to achieve numerically converged results is specific to the problem, and must be tested for a system under consideration. A quantity $I$ is then calculated by

$$I = \frac{1}{N_k} \sum_{\mathbf{k}} f(\mathbf{k}), \tag{2.13}$$

where $f(\mathbf{k})$ is the value of a function $f$ at the k-point $\mathbf{k}$, and $N_k$ is the total number of k-points.
Throughout this work the general method proposed by Monkhorst and Pack [48] is used because it leads to a uniform set of points determined by a simple formula valid for any crystal, where the k-points are given by

$$\mathbf{k}_{n_1,n_2,n_3} \equiv \sum_{i=1}^{3} \frac{2n_i - N_i - 1}{2N_i} \mathbf{G}_i. \tag{2.14}$$

Here $\mathbf{G}_i$ are the primitive vectors of the reciprocal lattice. By simply increasing the total number of points $N_i$ in a specific direction, a denser sampling of the BZ is achieved. It is possible to reduce the number of k-points which must be calculated by using the symmetry operations of the crystal under investigation. Two k-points,

which are equivalent by symmetry, yield the same value $f(\mathbf{k})$ to the summation (2.13). This can be used to define the irreducible wedge of the BZ (IBZ), where only k-points are found, which are not equivalent by symmetry to another k-point. Only these k-points must be calculated. A weight factor $w(\mathbf{k})$ is then assigned to each k-point in the IBZ, which counts the number of points it is symmetric to, normalized by the total number of points. Eq. (2.13) is then equivalent to

$$I = \sum_{\mathbf{k}}^{\mathrm{IBZ}} w(\mathbf{k}) f(\mathbf{k}). \tag{2.15}$$

Since the computational effort is proportional to the number of k-points calculated in DFT, this considerably reduces computation times in symmetric systems.

### 2.1.6 Broadening Schemes

In order to calculate properties of metals, one must integrate a function over the BZ which is discontinuous due to the partial filling of the energy bands. This is the case in metals near the Fermi surface for those bands that cross the Fermi energy when the Fermi factor varies rapidly. In principle a dense k-point grid can be chosen when the integrand varies rapidly. However, this requires a huge computational effort.
In particular it is the goal to evaluate the integral

$$I = \int_{BZ} d\mathbf{k}\, S(E(\mathbf{k}) - \varepsilon_{\mathrm{F}}) f(\mathbf{k}) = \int_{-\infty}^{\infty} d\varepsilon\, S(\varepsilon - \varepsilon_{\mathrm{F}}) \int_{BZ} d\mathbf{k}\, f(\mathbf{k}) \delta(\varepsilon - E(\mathbf{k})). \tag{2.16}$$

Here, $\varepsilon_{\mathrm{F}}$ is the Fermi energy, and $E(\mathbf{k})$ represents an energy band as function of the wave vector. The function to be integrated, $f$, is multiplied by the step function $S(x) = 1 - \theta(x)$. For instance, in the case $f \equiv 1$, the integral $I$ is the total charge within the Fermi surface.
In the case of a function given on a discrete grid, the integration over the Brillouin zone is replaced by a summation, following Eq. (2.15).
It is then possible to replace the step function $S(\varepsilon - \varepsilon_{\mathrm{F}})$, which is the Fermi-Dirac distribution at a temperature $T = 0$, by a smooth function. The function, which must be integrated, is then continuous. This smoothing can be done following different broadening schemes. Throughout this work, two schemes are used. The first is the Fermi-Dirac scheme, where $S(x)$ is replaced by a Fermi-Dirac function of finite temperature. The second is the Methfessel-Paxton scheme (of first order) [49], where

$$S(x) = 1 - \mathrm{erf}(x) - \frac{1}{4\sqrt{\pi}} H_1(x) e^{-x^2}, \tag{2.17}$$

where $\mathrm{erf}(x)$ is the error function, and $H_1(x)$ is the first Hermite polynomial. When replacing $S(x)$ by a smooth function, thereby replacing a step function, a numerical expression for the $\delta$-function should be obtained by $\delta(x) = -\frac{d}{dx} S(x)$. This is done throughout this work.
In the present work usually a Fermi-Dirac broadening scheme with a small temperature ($\sim 0.01$ eV) is used, and the numerical definiton of the $\delta$-function is the negative derivative of the Fermi-Dirac function.

### 2.1.7 Basis Sets

In order to solve the one-electron KS problem numerically, the wave functions $\psi_{j,\mathbf{k}}$ are represented by a linear combination of basis set functions:

$$\psi_{j,\mathbf{k}} = \sum_{u=1}^{p} c_{j,\mathbf{k},u} \phi_{u,\mathbf{k}}(\mathbf{r}). \tag{2.18}$$

There is a broad variety of functions that can be chosen as basis set, e.g. planes waves, augmented plane waves, muffin-tin orbitals, gaussians, Slater-type orbitals, numerical radial atomic-like orbitals, etc. *PWSCF* uses plane

waves.
A general plane wave at k-point $\mathbf{k}$ has the form

$$\phi_{u,\mathbf{k}}(\mathbf{r}) = \frac{1}{\sqrt{V}} e^{i(\mathbf{k}+\mathbf{G}_u)\mathbf{r}}. \tag{2.19}$$

In principle there exists an infinite number of plane waves; however, in practice only a finite amount can be dealt with. The number of plane waves, i.e. the size of the basis set, is defined through the cutoff energy

$$E_{\text{cut}} = \max_{\mathbf{G}} \frac{(\mathbf{k}+\mathbf{G})^2}{2}. \tag{2.20}$$

This energy has to be chosen sufficiently high that additional plane waves have only very small coefficients, so that changes of the physical properties due to an enhanced cutoff are tolerable. The absolute value of the cutoff depends on the accuracy desired, and of course on the investigated system.

### 2.1.8 Description of the Spin

According to the Hohenberg-Kohn theorem, only the density is needed to describe a system properly. However, this statement is only correct if the exact exchange-correlation potential was known. While the density is in principle sufficient to describe all physical properties of a system, in practice it is often necesary to impose an artificial breaking of the symmetry, introducing spin densities $n^{\uparrow}(\mathbf{r})$ and $n^{\downarrow}(\mathbf{r})$, for the spin up and spin down case, respectively, with the total density $n(\mathbf{r}) = n^{\uparrow}(\mathbf{r}) + n^{\downarrow}(\mathbf{r})$. This breaking of the symmetry introduces an additional degree of freedom, the spin polarization $\zeta(\mathbf{r}) = n^{\uparrow}(\mathbf{r}) - n^{\downarrow}(\mathbf{r}))$. Introducing an additional degree of freedom generally reduces the total energy of a system, if the symmetry belonging to the degree of freedom is broken in the system. For instance the total energy of a spin-polarized free electron gas is described better using spin-polarized DFT in comparison with exact results using the spin polarization degree of freedom, than without using it [33]. The ground state energy is described correctly only in the case that one uses the spin polarization degree of freedom. In some cases, e.g. in the case that a hydrogen atom is calculated far away from a surface, this separation of the spins is necessary to describe the ground-state energy correctly. In DFT calculations, without introducing the spin degree of freedom, a spinless hydrogen far away from the surface possesses a potential energy which is too large in comparison with experiments an exact results. An illustrative graphic on this effect on the ground state energy can be found in Ref. [6] and Fig. 4.23. Additionally, using spin polarization it is possible to describe magnetic effects an an easy way.
Introducing the spin polarization, it is necessary to treat both spin subsystems separately, and combining them in the density. In that case the exchange-correlation potential $V_{XC}$, which can be separated into an exchange part $V_X$ and a correlation part $V_C$ using $V_{XC} = V_X + V_C$, can also be separated for the spin subsystems,

$$\begin{aligned} V_X\left(n(\mathbf{r})\right) &\longrightarrow V_X\left(n^{\uparrow}(\mathbf{r}), n(\mathbf{r})\right) + V_X\left(n^{\downarrow}(\mathbf{r}), n(\mathbf{r})\right) \\ V_C\left(n(\mathbf{r})\right) &\longrightarrow V_C\left(n^{\uparrow}(\mathbf{r}), n^{\downarrow}(\mathbf{r})\right). \end{aligned} \tag{2.21}$$

In DFT calculations the spin polarization $\xi = \int d\mathbf{r}\zeta(\mathbf{r})$ for the H atom should be one, if it is far away from the surface.
However, note that the introduction of the spin degree of freedom introduces the so-called static correlation error in DFT, see Ref. [24] for details. This error arises since present-day XC-functionals are not able to treat correlated electronic states properly. For instance, the ground state energy of a free hydrogen atom should be the same for all wavefunctions of the form $|\psi\rangle = c_{\uparrow}|\uparrow\rangle + c_{\downarrow}|\downarrow\rangle$, with $|c_{\uparrow}|^2 + |c_{\downarrow}|^2 = 1$. However, this is not the case in DFT calculations.

## 2.2 Physical Concepts

### 2.2.1 Born-Oppenheimer Approximation

In order to solve the electronic structure problem, in principle the many-body Schrödinger equation must be solved,

$$\hat{H}\Psi_s(\{\mathbf{r},\mathbf{R}\}) = \left(\hat{T}_N + \hat{T}_e + \hat{U}\right)\Psi_s(\{\mathbf{r},\mathbf{R}\}) = E_s\Psi_s(\{\mathbf{r},\mathbf{R}\}). \tag{2.22}$$

Here $s$ labels the states for the coupled system of electrons with coordinates $\{\mathbf{r}\}$ and nuclei with coordinates $\{\mathbf{R}\}$. One now introduces the eigenvalues $E_i(\{\mathbf{R}\})$ and corresponding wavefunctions $\Psi_i(\{\mathbf{r}\}:\{\mathbf{R}\})$ for the electrons, which depend on the nuclear positions as parameters, through

$$\left[\hat{T}_e + \hat{U}\right]\Psi_i(\{\mathbf{r}\}:\{\mathbf{R}\}) = \hat{H}_e\Psi_i(\{\mathbf{r}\}:\{\mathbf{R}\}) = E_i(\{\mathbf{R}\}). \tag{2.23}$$

These wavefunctions define a complete set of states for the electrons at each $\{\mathbf{R}\}$. The full solution of (2.22) can be written in terms of

$$\Psi_s(\{\mathbf{r},\mathbf{R}\}) = \sum_i \chi_{si}(\{\mathbf{R}\})\Psi_i(\{\mathbf{r}\}:\{\mathbf{R}\}), \tag{2.24}$$

where $\chi_{si}(\{\mathbf{R}\})$ are the coefficients depending on the nuclear coordinates. Inserting (2.24) into (2.22), multiplying with $\Psi_i(\{\mathbf{r}\}:\{\mathbf{R}\})$ from the left, and integrating over the electronic coordinates, one gets

$$\left[T_N + E_i(\{\mathbf{R}\}) - E_s\right]\chi_{si}(\{\mathbf{R}\}) = -\sum_{i'} C_{ii'}\chi_{si'}(\{\mathbf{R}\}), \tag{2.25}$$

where $T_N = -1/2\left(\sum_J \nabla_J^2/M_J\right)$, with $M_J$ denoting the nuclear masses, and the matrix elements $C_{ii'}$ contain derivatives of $\Psi_i(\{\mathbf{r}\}:\{\mathbf{R}\})$ with respect to the nuclear coordinates,

$$C_{ii'} = \sum_J \frac{1}{M_J}\langle\Psi_i(\{\mathbf{r}\}:\{\mathbf{R}\})|\nabla_J|\Psi_{i'}(\{\mathbf{r}\}:\{\mathbf{R}\})\rangle\nabla_J + \sum_J \frac{1}{2M_J}\langle\Psi_i(\{\mathbf{r}\}:\{\mathbf{R}\})|\nabla_J^2|\Psi_{i'}(\{\mathbf{r}\}:\{\mathbf{R}\})\rangle. \tag{2.26}$$

The Born-Oppenheimer (BO) approximation is to ignore the off-diagonal $C_{ii'}$. This has the consequence that the electrons remain in a given state as the nuclei move. Thus, in the BO approximation, the nuclear motion is decribed by a purely nuclear equation for each electronic state.
This approximation is justified if the off-diagonal terms are negligible. One can express the first term of Eq. (2.26) by

$$\begin{aligned}\langle\Psi_i(\{\mathbf{r}\}:\{\mathbf{R}\})|\nabla_J|\Psi_{i'}(\{\mathbf{r}\}:\{\mathbf{R}\})\rangle &= \frac{\langle\Psi_i(\{\mathbf{r}\}:\{\mathbf{R}\})|\left[\nabla_J,\hat{H}_e\right]|\Psi_{i'}(\{\mathbf{r}\}:\{\mathbf{R}\})\rangle}{E_{i'}(\{\mathbf{R}\}) - E_i(\{\mathbf{R}\})} \\ &= \frac{\langle\Psi_i(\{\mathbf{r}\}:\{\mathbf{R}\})|\frac{dU}{d\mathbf{R}_J}|\Psi_{i'}(\{\mathbf{r}\}:\{\mathbf{R}\})\rangle}{E_{i'}(\{\mathbf{R}\}) - E_i(\{\mathbf{R}\})}.\end{aligned} \tag{2.27}$$

The second term may be approximated by the square of this term. This means that the Born-Oppenheimer approximation is justified, if the potential energy surfaces $E_{i'}(\{\mathbf{R}\})$ and $E_i(\{\mathbf{R}\})$ are well separated. Thus in metals the BO approximation in not justified.
If one is only interested in the electronic degree of freedom, Eq. (2.23) is solved in a first step. Afterwards, the additional operator $\hat{T}_N$ in Eq. (2.22) is treated perturbatively. This is justified, if the kinetic energy of the electrons is much larger than the kinetic energy of the nuclei, and thus if the electron mass $m_e \ll M_J$, which is indeed the case for static calculations (assuming similar momenta for electrons and nuclei). However, if one of the nuclei moves fast, the BO approximation is not justified. Such a perturbative treatment is done in section 2.3.1. For the energy spectrum of excited electrons one gets an expression similar to the square of Eq. (2.27). Throughout this work, electronic excitations are calculated using DFT. Standard DFT only treats the adiabatic

ground state of an investigated system. This means that the BO approximation is used for the calculations in a first step, fixing the nuclear positions and then calculating the Kohn-Sham wavefunctions. Afterwards (2.25) is expanded to linear order in the displacement of the nuclei, thereby allowing electronic excitations to occur due to the movement of the nuclei, see Ref. [33] and section 2.3.1 for details.

#### Trajectory Approximation

Having separated the electronic and nuclear degrees of freedom, the nuclear coordinate of the adsorbing atom can be described separately. In principle this must be done quantum-mechanically.
However, since the ionic movement is rather slow on the electronic scale, one can take a different approach and describe the trajectory classically. Thus the resulting trajectory must be understood as the quantum-mechanical expectation value. Electronic excitations only influence the trajectory through the expectation value of the dissipated energy into the electronic system.
A further approximation is to describe the many adsorption processes in experiments by a single effective trajectory. Such an approximation works quite well if the trajectories leading to different electronic excitations closely resemble each other [50]. If they differ qualitatively, this approximation does not work, and more refined approaches must be employed.
While it is not possible to describe a single adsorbate approaching a surface using this approximation, it should be appropriate to describe events that are caused by averaging over the trajectories of a large number of adsorbing atoms. This is the case for present-day chemicurrent experiments.
However, energy dissipated into the electronic system is transferred away from the adsorbing atom, and thus necessarily its trajectory is changed. For a high-energy electron-hole pair (larger than the Schottky barrier in experiments, see section 2.2.3) to become excited, this energy has to be available as kinetic energy $E_{\mathrm{kin}}$, (or, in principle, potential energy) at the specific point of the trajectory where the e-h pair becomes excited. This point is somewhere within in the chemisorption well in the investigated cases, where some of the initial potential energy has been converted into kinetic energy. Also must the excitation matrix elements be non-negligible. Thus the adsorbate must first move into a position close to the bottom of the chemisorption potential. In systems where the kinetics are not overly involved, such as in the case of atomic hydrogen adsorption with a reasonably low kinetic energy (approximately $E_{\mathrm{kin}} \leq 1$ eV), excitation of electron-hole pairs should only effect the particle's velocity, but not the trajectory itself. Since the trajectories of the adsorbing atoms are usually calculated for a half round trip in the chemisorption well, the influence of high-energy electronic excitations on the trajectory should be rather small, and so a major effect on the calculated spectra is not expected in such systems. The energy regime of the spectra close to the Schottky energy dominates the behavior of the chemicurrent. In this energy range, the effects of electronic excitations onto the trajectory are only of quantitative, not qualitative interest. So the 'effective trajectory' approximation for the calculation of chemicurrents seems justified, and it has been employed by various groups up to now [26, 6, 51].
In this work the 'effective trajectory' approximation is used for simplicity, and in order to be able to compare to these previous approaches. However, different approaches may be thought of, e.g. those of Refs. [50, 52, 21].

### 2.2.2 Electron-Hole Pairs

At zero temperature the electronic states of a system are filled up to the Fermi level $\varepsilon_{\mathrm{F}}$. Injecting (e.g., thermal) energy into the electronic system, excited electrons are created above the Fermi level. In a metallic system this can happen with infinitesimal small energy, since the Fermi level is located within the conduction band. The excitation of the electron leaves an empty state below the Fermi level, which is described as a hole. Thus excitation of an electron never appears alone, but electron-hole pairs are always created; however, these are not necessarily bound. The energy distribution for electrons and holes is not necessarily equal, even after thermalization, since the density of states may be different for electrons and holes. For temperatures larger than zero these considerations always hold.
During adsorption, an atom or molecule, generally an adparticle, adsorbing onto a substrate loses energy, the

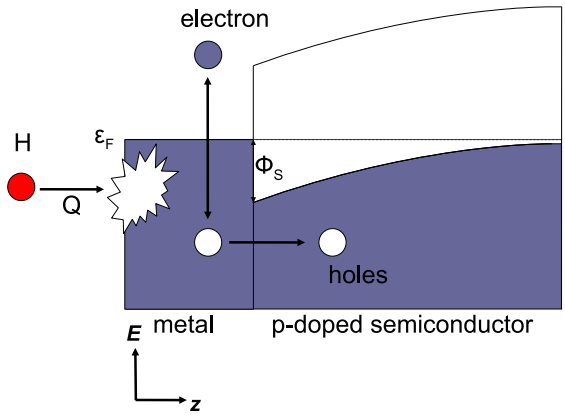


Figure 2.2: Sketch of a hole-detecting Schottky diode. An adsorbate, a hydrogen atom, H, approaches a metal surface, moving along its reaction coordinate Q. It excites e-h pairs during this approach. If excited sufficiently deep below the Fermi energy $\varepsilon_F$, the hole can pass through the metal film, and then pass the Schottky barrier $\Phi_s$ into the p-doped semiconductor. The metal film has a thickness of the order of 100 nm.

chemisorption (or adsorption) energy, i.e. the difference in energy for the adsorbed particle vs. the free particle far away from the surface. This energy has to be transferred into the substrate or lost in another suitable way, e.g. chemiluminescence. Energy transfer into the substrate system can happen via excitation of phonons and electron-hole pairs. Energy dissipation by excitation of phonons is possible, and leads to heating of the system, but is not of major interest in this thesis: Here electronic excitations are the major focus, i.e. the energy transfer into the electronic system of the substrate.
A common way to describe the energy transfer into the electronic system is by electronic friction [53, 27], where a classical friction force is assumed to act on the adparticle, which is proportional to its velocity. This is an effective description of the many-electron scattering of the substrate electrons with the electrons of the adparticle. The energy lost by the adparticle through this channel is transferred into the electronic system of the substrate. Expanding the electronic friction approach to the forced oscillator model, one can calculate the spectra of electrons and holes. In the FOM it is assumed that the number of electron-hole pairs excited by a single adparticle follows a Poissonian distribution, which is founded on the view that multiple low-energy electron-hole pairs are excited [27]. Note that this is another reason for a possible non-equal distribution of electrons and holes.
The electronic friction approach is described more thoroughly in section 2.5.

### 2.2.3 Schottky Diodes and Chemicurrents

In the past ten years a new way to measure the quantity of electrons or holes created in an adsorption process has been developed, namely the detection of chemicurrents during adsorption in Schottky diodes [54, 4, 55, 11]. The Schottky diodes in these experiments consist of a thin metal film on a (usually p-)doped semiconductor. This design leads to the formation of a Schottky barrier on the interface, as illustrated in Fig. 2.2. A low-energy atomic or molecular beam, with a kinetic energy of $\sim$ 10 meV, is then directed on the Schottky diode, which leads to adsorption of these atoms or molecules, and thereby to excitation of electron-hole pairs in the metal. Since only high-energy electrons or holes, depending on the doping, can pass the barrier into the semiconductor, a current can be measured between metal and semiconductor. This is a direct evidence for the creation of electrons or holes. Because the Schottky barrier is much lower than the vacuum barrier, the chemicurrent setup using a Schottky diode is much more sensitive for the detection of electrons than exoemission measurements, and the only well-defined way the author knows of to detect holes in such experiments.

## 2.3 Theoretical Methods

In this section, the theoretical approach to described electron-hole pair excitation, which is a basic of this work, is presented. The methods presented here have already been published about 40 years ago. Some room for extensions is therefore available. Some of the extensions are presented here and in chapter 3, and difficulties for the implementation of the methods in DFT codes are commented upon in section 3.6.

### 2.3.1 Müller-Hartmann Approach

The Müller-Hartmann (MHRT) approach, presented in this section, provides a prerequisite for the perturbative approach developed in section 3.1. This perturbative approach provides a generalization of the MHRT approach, in the way that the electron-hole pair excitation here can be split up into an electronic and hole part. Some further extensions of this approach are proposed in chapter 3, it is explained how it is implemented in a DFT postprocessing code, and the difficulties of the extensions are commented upon in section 3.6.
The MHRT approach describes the excitation of electron-hole pairs in a Fermi gas by a localized time-dependent perturbation. It has been proposed by Müller-Hartmann *et al.* in Ref. [56]. The following section is essentially taken from this paper.
The authors determine the time evolution of an initial state $|\psi(t_0)\rangle$, which will be understood later as the (temperature-dependent) ground state of a substrate, i.e. an unperturbed substrate slab in DFT calculations. This initial state is the ground state of the unperturbed Hamiltonian $H_0 = T_0 + V_0$, where $T_0$ is the unperturbed kinetic energy, and $V_0$ the unperturbed and time-independent potential of the substrate. The time-dependent Hamiltonian is then given by

$$\begin{aligned} H_F(t) &= \sum_{k,\sigma} \varepsilon_{k,\sigma} \psi^\dagger_{k,\sigma} \psi_{k,\sigma} + \frac{\mathbf{p}^2}{2M} + \sum_{k,k',\sigma} V_{kk'\sigma}(t) \psi^\dagger_{k,\sigma} \psi_{k',\sigma} e^{i(\mathbf{k}-\mathbf{k}')\mathbf{Q}} \\ &= T_0 + V_0 + \frac{\mathbf{p}^2}{2M} + V(t) \\ &= H_0 + \frac{\mathbf{p}^2}{2M} + V(t). \end{aligned} \tag{2.28}$$

Here $\varepsilon_{k,\sigma}$ is the spin-($\sigma$-)dependent quasiparticle energy, while $V_{kk'\sigma}(t)$ is the time-dependent single-particle potential of an external perturbation of the substrate. In the present case this is an adsorbing particle, although the theory is applicable to other kinds of perturbations as well. This particle moves along its classical trajectory, defined by the reaction coordinate $\mathbf{Q}(t)$. The particle possesses a kinetic energy $\frac{\mathbf{p}^2}{2M}$, where $M$ is the mass of the particle. The use of the Hamiltonian (2.28) for a charge perturbation in an electron gas requires some justification. First, it is assumed that the screening of the charge due to Coulomb interactions occurs instantly. Since the response of the electron gas to charge fluctuations has a time scale of the plasmon frequency $\omega_p$, the results will not describe properly the immediate response to potentials, which vary on that time scale. Second, it is assumed that there are no long-time transient effects ($t \gg \omega_p^{-1}$) associated with the screening and that all transient effects arise from the response of the quasiparticles to the screened time-dependent potential. This is probably reasonable, because the low-energy electron-hole pair excitations responsible for the long-time transient effects are not prominently involved in the screening. Therefore it is assumed that the quasiparticles are noninteracting. This means that the excitation frequency of interest, $\nu$, should fulfill the condition $\nu \gg (2\pi\tau)^{-1}$, where $\tau$ is the duration of the impact (in scattering) or of half a round trip (in adsorption), i.e. there will be errors for small frequencies. The author has slightly generalized the formulation of Müller-Hartmann, in the sense that the description now includes the electron spin. Nonetheless a spin-flip excitation is not considered, so it is assumed that the excitation of electron-hole pairs always occurs in the same spin channel. This is probably a good description, which will include the major part of the excitations.
It is now assumed that the perturbation is zero in the past ($t < 0$), and constant, possibly zero, at some point in the future ($t > \tau$). This means that the adsorbate starts far away from the surface, and is either adsorbed or scattered back from the surface again.

The approaching adsorbate will create a number of electron-hole pairs. The energy spectrum of these excitations with respect to the eigenstates of the Hamiltonian $H_0$ is given by

$$S_\tau(\omega) = \frac{1}{2\pi}\int_{-\infty}^{\infty} dt e^{i\omega t}\langle\psi(\tau)\left|e^{-iH_0 t}\right|\psi(\tau)\rangle >, \tag{2.29}$$

which is accessible if the states $|\psi(t)\rangle$ are known. This is, however, the case here, since

$$|\psi(t)\rangle = U(t,t_0)\,|\psi(t_0)\rangle. \tag{2.30}$$

It is not easy to calculate the excitation spectrum exactly. It is, however, possible to bosonize the electron-hole pairs. This means that the particle-hole operators $\psi$ are replaced with boson-creation and boson-annhilation operators $b^\dagger$ and $b$, i.e.

$$\psi^\dagger_{k_>}\psi_{k'_<} \text{ by } b^\dagger_j, \tag{2.31}$$

where the subscripts $k_>$ and $k'_<$ mean that $k$ is outside the Fermi sphere and $k'$ is inside. This operator applied to the ground state creates a hole $k'$ and a particle $k$ while imparting a momentum $\mathbf{k}'-\mathbf{k}$ to the potential source. (Note, however, that the impartion of a momentum is not possible in a periodic system, as is the case in the *PWSCF* code, which uses plane waves and the Bloch theorem.) The operators $b^\dagger_j$ are assumed to be bosons in the usual sense. The energy of one such electron-hole pair is thus $\varepsilon_j = \varepsilon_{k_>} - \varepsilon_{k'_<}$. The time-dependent potential can then be written as

$$V(t) = \sum_j \left[V_j(t)b^\dagger_j e^{i(\mathbf{k}-\mathbf{k}')\mathbf{Q}} + V^*_j(t)b_j e^{-i(\mathbf{k}-\mathbf{k}')\mathbf{Q}}\right], \tag{2.32}$$

where $V_j(t) = V_{kk'}(t)$ and $V^*_j(t) = V_{k'k}(t)$. The part of the potential which creates and destroys only electrons or only holes, proportional to $\psi^\dagger_{k_>}\psi_{k'_>}$ and $\psi^\dagger_{k_<}\psi_{k'_<}$, respectively, is omitted. Clearly, this gives nothing when it acts on the ground state, except for an energy shift, which can be lumped into $H_0$. The complete boson approximation to the Hamiltonian (2.28), i.e. without the omitted part, is then

$$H = \sum_j \varepsilon_j b^\dagger_j b_j + \sum_j \left[V_j(t)b^\dagger_j e^{i\mathbf{q}_j\mathbf{Q}} + V^*_j(t)b_j e^{-i\mathbf{q}_j\mathbf{Q}}\right] + \frac{\mathbf{p}^2}{2M}, \tag{2.33}$$

where $\mathbf{q}_j$ is the net momentum of the particle $j$, i.e. $\mathbf{q}_j = (\mathbf{k}-\mathbf{k}')$.
It is now possible to solve Eq. (2.29) using Hamiltonian (2.33). This has been done, and the result is

$$P(\omega) = \int dt\, e^{i\omega t}\exp\left[-\sum_{ij}\left|\frac{\lambda_{ij}(\tau)}{\varepsilon_j-\varepsilon_i}\right|^2\left(1-e^{-i(\varepsilon_j-\varepsilon_i)t}\right)\right], \tag{2.34}$$

where the matrix elements

$$\begin{aligned}\lambda_{ij}(\tau) &= \int_0^\tau dt'\left\langle\varepsilon_j\left|\frac{dV}{dt'}\right|\varepsilon_i\right\rangle\exp(i(\varepsilon_j-\varepsilon_i)t') \\ &= \int dQ\left\langle\varepsilon_j\left|\frac{dV(Q)}{dQ}\right|\varepsilon_i\right\rangle\frac{dQ}{dt'}(Q)\exp(i(\varepsilon_j-\varepsilon_i)t'(Q))\end{aligned} \tag{2.35}$$

were introduced. The eigenstates $|\varepsilon_{i,j}\rangle$ are eigenstates of the Fermionic Hamiltonian. The velocity of the adsorbate $dQ/dt$ at position $Q$ of the trajectory has been introduced, and for sake of simplicity the notation now restricts itself to a one-dimensional trajectory, although generalisation to multiple dimensions is straightforward. During calculation of the spectrum (2.34) a partial integration was used, which explains the time derivative of the potential in (2.35), and the energy difference in the denominator of the exponential in (2.34). The time derivative is helpful in order to combine this theory with DFT methods, which are described in section 2.3.3.

The spectrum of the electron-hole pairs (2.34) has a large part at zero, where there is no excitation at all. One has to keep that in mind when normalizing it. It is then useful to write the excitation spectrum as

$$P(\omega) = p_0\,\delta(\omega) + P_{\mathrm{ex}}(\omega), \tag{2.36}$$

where $p_0$ describes the non-excited electron-hole pairs, and $P_{\mathrm{ex}}(\omega)$ is the excited part we are interested in. $P(\omega)$ is defined as the spectrum after a half or full round trip of the adsorbate in the chemisorption well.
Extending the theory to finite electronic temperature by introducing Fermi occupation functions $f(\varepsilon)$, one has to consider the possibility of transitions where the metal electrons loose energy by going from occupied states above $\varepsilon_{\mathrm{F}}$ to unoccupied states below $\varepsilon_{\mathrm{F}}$. Thus, it is necessary to define $P_{\mathrm{ex}}(\omega) = 0$ for $\omega < 0$. Following Ref. [57], Eq. (2.34) needs to be generalized to

$$P(\omega) = \theta(\omega) \int dt\, e^{i\omega t} \exp\left[ -\sum_{ij} \left| \frac{\lambda_{ij}(\tau)}{\varepsilon_j - \varepsilon_i} \right|^2 (f(\varepsilon_i) - f(\varepsilon_j)) \left(1 - e^{-i(\varepsilon_j - \varepsilon_i)t}\right) \right] \theta(\varepsilon_j - \varepsilon_i), \tag{2.37}$$

where $f$ is the Fermi-Dirac occupation function. The total energy loss is the expectation value $E_{\mathrm{diss}} = \int d\omega\, \omega\, P_{\mathrm{ex}}(\omega)$.
Eq. (2.37) can be expanded into a Taylor series around the perturbation $|\lambda_{ij}|^2$. In first order one gains

$$\begin{aligned} P(\omega) &= \theta(\omega) \left[ \left( 1 - \sum_{ij} \left| \frac{\lambda_{ij}(\tau)}{\varepsilon_j - \varepsilon_i} \right|^2 (f(\varepsilon_j) - f(\varepsilon_i)\theta(\varepsilon_j - \varepsilon_i)) \right) \delta(\omega) \right. \\ &\quad \left. + \sum_{ij} \left| \frac{\lambda_{ij}(\tau)}{\varepsilon_j - \varepsilon_i} \right|^2 (f(\varepsilon_i) - f(\varepsilon_j)\theta(\varepsilon_j - \varepsilon_i))\, \delta(\omega - (\varepsilon_j - \varepsilon_i)) \right]. \end{aligned} \tag{2.38}$$

Comparing (2.36) and (2.38), in first order one finds

$$P_{\mathrm{ex}}(\omega) = \sum_{ij} \left| \frac{\lambda_{ij}(\tau)}{\varepsilon_j - \varepsilon_i} \right|^2 (f(\varepsilon_i) - f(\varepsilon_j)\theta(\varepsilon_j - \varepsilon_i))\, \delta(\omega - (\varepsilon_j - \varepsilon_i)). \tag{2.39}$$

### 2.3.2 Gunnarsson-Schönhammer Approach

In several papers Gunnarsson and Schönhammer have developed a theory to calculate the energy spectrum of electron-hole pair excitation when an adsorbate approaches a surface [58, 59, 60, 61]. Their theory is an evolution of the MHRT approach [56]. While the general formalism stays essentially the same as before, Gunnarsson and Schönhammer base their theory on the time-dependent adiabatic wavefunctions. The only formal difference is that the matrix elements (2.35) are exchanged by the Gunnarsson-Schönhammer matrix elements

$$\lambda_{ij}(t) = \int_0^\tau dt' \left\langle \varepsilon_j^t \left| \frac{dV}{dt'} \right| \varepsilon_i^t \right\rangle \exp(i(\varepsilon_j - \varepsilon_i)t'). \tag{2.40}$$

Here they introduced the time-dependent adiabatic wavefunctions of the substrate, $\left|\varepsilon_j^t\right\rangle$. This method is named BA I in their work. One obvious point is that the energy differences $\varepsilon_j - \varepsilon_i$ are not time-dependent, although their corresponding eigenstates are time-dependent. Gunnarsson and Schönhammer argue that the energy difference does not change if one treats a semi-infinite substrate. This is not possible in DFT calculations. However one can take a large slab and assume that the change of energy differences between two Kohn-Sham states in DFT calculations is sufficiently small, when the adsorbate approaches the surface.
A second extension (BA II) is the treatment of multiple small-energy excitations, where only eigenstates in a small region around the Fermi energy are taken into account. This is combined with the new matrix elements

(2.40) of BA I. However, all three theories (MHRT, BA I, BA II) are complementary, and correct in certain limiting cases: While BA I and BA II should be correct for slowly moving perturbations of arbitrary strength, and BA I additionally for rapidly moving adsorbates, MHRT is justified over a wider region for rapidly moving adsorbates. An illustrative graphic can be found in Ref. [61].

### 2.3.3 Application to DFT Methods

In this section the approach necessary to convert the theoretical considerations in section 2.3.1 into a practical approach using DFT methods is presented. For simplicity, the notation assumes a one-dimensional motion along a reaction coordinate $Q(t)$, but generalisation to multiple dimensions is straightforward. Typically the particle makes many oscillations in the adsorption well before it has dissipated the chemisorption energy into the substrate. In the following, just the first round trip of the trajectory in the adsorption potential in the time interval between 0 and $\tau$ is considered. For conceptual clarity, it is assumed that a trajectory unaffected by energy dissipation can be used. This assumption is a good first approximation in many cases of practical interest, but it can be lifted without much difficulty if required. For a full description of adsorption, one should decompose the oscillating trajectory into many round trips, and use a somewhat different energy and corresponding starting point for each segment of the trajectory. But if one starts with a low kinetic energy, the energy loss during the first round trip can already be sufficient for the particle to become trapped.
According to the Runge-Gross theorem [62], time-dependent density functional theory (TDDFT) establishes a mapping of the electronic many-particle problem onto an effective single-particle Hamiltonian of the form

$$H^\sigma(t) = -\frac{1}{2}\nabla^2 + V^\sigma_{\text{eff}}[n](\mathbf{r}, \mathbf{r}', t). \tag{2.41}$$

The effective potential $V_{\text{eff}}[n](\mathbf{r}, \mathbf{r}', t)$ is generally non-local and a functional of the density $n$, and consists of

$$V^\sigma_{\text{eff}}[n](\mathbf{r}, \mathbf{r}', t) = V_H[n](\mathbf{r}, t) + V^\sigma_{XC}[n](\mathbf{r}, \mathbf{r}', t) + V_{\text{ion}}(\mathbf{r}, t). \tag{2.42}$$

$V_{\text{ion}}$ depends on time implicitly through the particle's position $Q(t)$. The charge density needs to be calculated self-consistently from the solution of the time-dependent Kohn-Sham equations. Hence the Hartree and exchange-correlation potentials, $V_H$ and $V_{XC}$, are time-dependent, too. While TDDFT is in principle exact, suitable approximations to arrive at a computationally simpler scheme are sought. With this motivation, it is assumed that the true effective potential $V_{\text{eff}}(t)$ in the time-dependent Kohn-Sham equations can be approximated by the effective potential $V_{\text{eff}}(Q)$ of a time-independent problem, namely, the electronic ground state for a system with the particle located at $Q(t)$. This is similar to the considerations in section 2.3.1. In view of the density of excited electrons and holes being small compared to the overall charge density, this approximation appears plausible. However, there are cases where deviations from the instantaneous ground state are strong, in particular those system where exoemission has been observed. From the theory point of view, a class of system can be envisaged where the adsorbate, in some points of its trajectory, must be described (at least in an approximative sense) by quantum numbers (such as charge state, spin, etc.) that differ from those of the instantaneous ground state. For these systems, one may anticipate that one may need to go beyond the perturbative approach outlined here. This point is investigated further in chapter 7, and it is found that this is indeed the case.
The change of the effective potential due to the scattering of an incident particle constitutes a localized time-dependent perturbation. The chemicurrent consists of propagating charge carriers that are detected (in principle) far away from the particle's impact point. These carriers are described by the eigenstates $|\varepsilon_i\rangle$ of the Hamiltonian $H_0 := H(Q_0)$. Depending on the physics one wants to study, one would chose different definitions of $H(Q_0)$: In order to describe vibrational damping, $Q_0$ should be taken as the adsorption height. In the case of interest here, $Q_0 \to -\infty$ is taken, i.e., $H_0$ describes the (semi-infinite) metal with the particle far away from the surface. This defines a decomposition of the Hamiltonian into an unperturbed part $H_0$ and a perturbation

$$V(Q) = V_{\text{eff}}(Q) - V_{\text{eff}}(-\infty) \tag{2.43}$$

that depends on time implicitly through $Q(t)$. While $V(Q)$ is generally *not* small, its perturbative treatment relies on the fact that $V(Q(t))$ varies rapidly and is different from zero only within a short time interval. Here, the author is interested in electron-hole pair excitations above some threshold energy $\varepsilon_{\mathrm{S}} \gtrsim 0.5$ eV due to the high-frequency components of the perturbation. For the validity of the perturbative treatment, it is required that the response of the electronic system on the time scale set by $\varepsilon_{\mathrm{S}}^{-1}$ is sufficiently weak, according to the considerations in section 2.3.1.
Applying first-order time-dependent perturbation theory, the transition amplitude for an excitation of an electron from an occupied state $i$ into an unoccupied state $j$ is given by

$$p_{ij}(t) = \langle \varepsilon_j \left| V(Q(t)) \right| \varepsilon_i \rangle \exp(i(\varepsilon_j - \varepsilon_i)t), \tag{2.44}$$

and the excitation spectrum is obtained from

$$P_{\mathrm{ex}}(\omega) = \sum_{ij} \left| \int_0^\tau dt\, p_{ij}(t) \right|^2 \delta\left(\omega - (\varepsilon_j - \varepsilon_i)\right) . \tag{2.45}$$

For a full round trip of the (dissipationless) trajectory, $V$ vanishes both in the initial and final (again unperturbed) state, and one may integrate by parts to obtain an expression for the spectrum of electron-hole pairs,

$$P_{\mathrm{ex}}(\omega) = \sum_{ij} \left| \frac{\lambda_{ij}}{\varepsilon_j - \varepsilon_i} \right|^2 \delta\left(\omega - (\varepsilon_j - \varepsilon_i)\right) \tag{2.46}$$

with

$$\lambda_{ij} = \int_0^\tau dt \left\langle \varepsilon_j \left| \frac{dV}{dt} \right| \varepsilon_i \right\rangle \exp(i(\varepsilon_j - \varepsilon_i)t). \tag{2.47}$$

One can now compare (2.47) with (2.35). The conclusion is that the perturbation potential $V(t)$ from section 2.3.1 has been mapped onto the difference in effective potentials (2.43). Comparison of (2.39) with (2.45) shows the analogy.
To summarize the section, a general theory was presented, the MHRT approach to excitation of electron-hole pairs, and it was described how one can handle it within the framework of DFT.

## 2.4 Adiabatic vs. Nonadiabatic

Within this work the terms 'adiabatic' and 'nonadiabatic' play an important role. Generally spoken, adiabatic means a slow transition of a system from one state to another, while nonadiabatic means a comparatively fast transition. The terms 'fast' and 'slow' are defined by comparison of the transition time $t_{\mathrm{trans}}$ to the time the system needs to relax into its current ground state $t_{\mathrm{relax}}$. For a slow transition, $t_{\mathrm{trans}} \gg t_{\mathrm{relax}}$ holds.
While electronic excitations are a nonadiabatic effect, it is not necessary to treat the whole system nonadiabatically. If, on a grand scale, $t_{\mathrm{trans}} \approx t_{\mathrm{relax}}$, a nonadiabatic effect may be calculated from the adiabatic ground state by perturbation theory. This is indeed the case here.
Within this work, all geometry calculations are done for the adiabatic ground state, i.e. the nuclear positions are prescribed, and the electronic ground state is then calculated within DFT, without further constraints. Excitations or the time $t_{\mathrm{relax}}$ are not taken into account for these calculations. In order to be able to describe nonadiabatic effects, a perturbative approach is then undertaken, with the adiabatic (ground-state) system working as the unperturbed case. The perturbative description allows to avoid difficult calculations for the fully nonadiabatic system, i.e. the non-ground state system. The result from this perturbative approach may then be used to calculate the nonadiabatic behavior of the system, when it is not in its ground state. Two major points are discussed: (1) electronic excitations in general, and (2) The spin relaxation at the spin transition point.
Electronic excitations are handled within the framework of section 2.3.3.
A possible nonadiabatic treatment of the spin relaxation is described in section 3.3. Within section 3.3, a perturbative approach to calculate the effective potential is developed. This calculation starts from the adiabatic

calculations. The occupation factors of the adiabatic states are then changed nonadiabatically, and the effective potential is re-calculated from these nonadiabatic occupation factors.
So, while this work describes principally nonadiabatic effects, not compatible with the BO approximation (section 2.2.1), the DFT calculations on which the results rest are adiabatic. In a first step the system is treated as being in the adiabatic (ground) state, and afterwards perturbation theory gives information about the nonadiabatic (non-ground state) case.

## 2.5 Electronic Friction and the Forced Oscillator Model

In Refs. [27, 63] a forced-oscillator model was invoked to describe the spectra, thus extending the electronic friction approach [27] for this purpose. Since this model is used nowadays by experimentalists to make predictions on the magnitude of chemicurrent they expect to measure, the most important results of the FOM are summarized here.
The theory of electronic friction starts from an expression for the imaginary part of dynamic self-energy $\Lambda(Q,\omega)$,

$$\begin{aligned} \mathrm{Im}\Lambda(Q,\omega) &= -\frac{2\pi}{m}\sum_{i,j}\left|\left\langle \varepsilon_j \left| \frac{dV(Q)}{dQ} \right| \varepsilon_i \right\rangle\right|^2 \\ &\quad \times (f(\varepsilon_i) - f(\varepsilon_j))\,\delta(\omega - (\varepsilon_j - \varepsilon_i)), \end{aligned} \tag{2.48}$$

cf. Ref. [57]. A friction coefficient $\eta(Q)$ can be defined for any point $Q(t)$ along the trajectory by considering the limit $\lim_{\omega\to 0} m\Lambda(Q,\omega)/\omega$ and replacing the states $|\varepsilon_i\rangle$ and $\langle\varepsilon_j|$ by the states at the Fermi energy.
Taking into account the proper normalization of these states on the energy shell one can show that this limit exists, i.e., the friction coefficient is mathematically well-defined. The friction coefficient can then be used to calculate the classical friction force on the moving adsorbate using

$$F_{el} = -\eta\dot{Q}, \tag{2.49}$$

where $\dot{Q}$ denotes the velocity of the adsorbate along its reaction coordinate. Following the arguments above, the friction coefficient is defined as

$$\eta = \pi\sum_{\sigma}\sum_{\mathbf{k}}\sum_{i,j}\left|\left\langle \psi_{\mathbf{k},j,\sigma} \left| \frac{dV^{\sigma}_{\mathrm{eff}}}{dQ} \right| \psi_{\mathbf{k},i,\sigma} \right\rangle\right|^2 w_{\mathbf{k}}\delta(\varepsilon_{\mathrm{F}} - \varepsilon_{\mathbf{k},i,\sigma})\delta(\varepsilon_{\mathrm{F}} - \varepsilon_{\mathbf{k},j,\sigma}). \tag{2.50}$$

Here, $\sigma$ denotes the summation over spin, $\mathbf{k}$ denotes summation over $\mathbf{k}$-points with weight $w_{\mathbf{k}}$, $i,j$ denote summation over electronic states and $\varepsilon_{\mathrm{F}}$ is the Fermi energy. A more detailed description of this concept is described in Ref. [26] and references therein.
This simple definition usually only works if one does *not* use the adiabatic potential, because if there is a spin transition (cf. section 3.3), then the potential has a $\sqrt{Q}$-like behavior at the transition point. This leads to a $Q^{-1}$-divergence at this point for the friction coefficient (2.50), resulting in the conclusion that it is not well-defined.
Energy dissipation within the electronic friction model is described by the friction coefficient $\eta(Q)$. The dissipated energy into the electronic system $E_{\mathrm{diss}}$ is then measured by the integral

$$E_{\mathrm{diss}} = \int dQ\,\eta(Q)\frac{dQ}{dt}. \tag{2.51}$$

Neglecting the small initial kinetic energy, the velocity $dQ/dt$ reached by the adsorbate stems from acceleration in the chemisorption potentials, and hence scales like $m^{-1/2}$. Therefore it follows that the dissipated energy

$$E_{\mathrm{diss}} \sim \frac{1}{\sqrt{m}}. \tag{2.52}$$

Within the FOM, the electron (hole) spectra $P_e(\varepsilon)$ ($P_h(\varepsilon)$) are obtained by making additional assumptions on the excitation mechanism. One of the assumptions is that the excitation energy is made up from a large number of small electron-hole pairs following a Poissonian distribution. Another assumption is that electrons and holes are distributed evenly around the Fermi energy, which means $P_e = P_h$. For further details, see Ref. [27]. This leads to the expression

$$P_e(\varepsilon) = \frac{1}{\hbar}\int_{\varepsilon}^{\infty} d\epsilon\, \frac{1}{\epsilon}\sum_{\sigma}\frac{1}{\pi\epsilon}\left|\int_{-\infty}^{\infty} dt\, \eta_{\sigma}^{1/2}(Q)\frac{dQ}{dt}e^{-i\epsilon t/\hbar}\right|^2, \tag{2.53}$$

where $\sigma$ denotes a spin dependence of the friction coefficient. Inserting the mass-scaling of the adsorbate's velocity into this equation, the spectra obey a scaling relation,

$$P_{e/h}(\varepsilon, m) = \sqrt{m}\tilde{P}_e(\sqrt{m}\varepsilon). \tag{2.54}$$

Numerical work on H/Al has been analyzed in terms of Eq. (2.54) in Ref. [63]. The authors claim that the high-energy tail of the spectra can be described as an exponential of the form

$$P_e^{\mathrm{fit}}(\varepsilon, m) = A(m)\exp(-|\varepsilon|/k_B T_{\mathrm{eff}}(m)), \tag{2.55}$$

where, according to (2.54), for the effective temperature $T_{\mathrm{eff}}$ one finds $T_{\mathrm{eff}}(m) \sim (m/m_{\mathrm{H}})^{-1/2}$. $A(m)$ is a mass-dependent constant.
The number of electrons (or holes) $N_{e/h}^{\varepsilon_{\mathrm{S}}}$ above the Schottky barrier $\varepsilon_{\mathrm{S}}$ is defined by

$$N_e^{\varepsilon_{\mathrm{S}}}(m) = \int_{\varepsilon_{\mathrm{S}}}^{\infty} d\epsilon P_e(\epsilon, m) \tag{2.56}$$

Assuming that the pre-factor $A(m)$ is weakly mass-dependent, one can show that the number of particles above the Schottky barrier follows the relation

$$\ln\left(N_e^{\varepsilon_{\mathrm{S}}}\right) \sim \mathrm{const} - \left(\frac{m}{m_{\mathrm{H}}}\right)^{1/2}. \tag{2.57}$$

# Chapter 3

# Extension of the Theoretical Approaches

Having described the basic theories for electronic excitations used within this work in 2.3, and given an explanation how they can be applied within a DFT approach, in this chapter extensions to these approaches are described. The developed perturbative approach is also investigated in more detail.
In section 3.1 first-order time-dependent perturbation theory is used to calculate the excitation spectra of electrons and holes separately. The method is compared to the theory of electronic friction, section 2.5. Part of this work has been published [64]. Since the basic theories do not respect energy conservation, it is enforced on the theory in section 3.1.3. In section 3.1.4 some analytical results are considered.
Using these fundamental considerations, it is possible to implement the perturbative approach in a working DFT code. This is described in section 3.2, and is the standard procedure developed in and used throughout this work, if not mentioned otherwise.
In previous theoretical works the spin transition during adsorption of hydrogen atoms on a metal surface led to an unphysical divergency [27]. The spin of the adsorbate vanishes at a certain distance above the surface. This point is investigated in section 3.3. In this section a method to calculate a nonadiabatic spin transition behavior within the framework of a constrained DFT is proposed as well. However it turns out that the application to a test system yields wrong results for the isotope effect (section 4.3.2). Multi-dimensional trajectories are dealt with in section 3.4. The dimensions are condensed into a one-dimensional coordinate, the arc length $Q$. The problem of the change of the Kohn-Sham eigenenergies during adsorption, which is important when dealing with the Gunnarsson-Schönhammer approach of section 2.3.2, is addressed in section 3.5.
The extensions proposed in sections 3.3 and 3.5, as a supplement of section 2.3.2, face severe difficulties, and it turns out that these extensions lead to unphysical results. The problems experienced are commented upon in section 3.6, along with a comment on the required computation time and hard disk space for the calculations.

## 3.1 Perturbative Approach and Electron and Hole Spectra

In this section a first-order time-dependent perturbation theory is described, which allows to calculate the excitation spectra of electrons and holes. The method is compared to the theory of electronic friction. Energy conservation is enforced, and analytical results for the theory are considered.

### 3.1.1 Fundamental Considerations

Considering the excitation spectrum (2.37), and its practical implementation into a DFT approach using (2.47), it is found that this result, while non-perturbative, does not give information about the spectra of electrons and holes without their counterpart. Additionally, the derivation of (2.37) is quite elaborate, cf. Ref. [56]. It is possible to remedy these deficiencies under certain circumstances, using only first-order time-dependent perturbation theory.
It is assumed that the excitations are sufficiently weak, so that the spectrum in Eq. (2.34) can be approximated

by expanding the exponential and taking into account only the first non-zero and non-$\delta(\omega)$ order. Taking into account Eq. (2.36) and temperature effects one then gets (2.39)

$$P_{\mathrm{ex}}(\omega) = \sum_{ij} \left| \frac{\lambda_{ij}}{\varepsilon_j - \varepsilon_i} \right|^2 (f(\varepsilon_i) - f(\varepsilon_j))\, \delta\left(\omega - (\varepsilon_j - \varepsilon_i)\right) \theta(\omega)\theta(\varepsilon_j - \varepsilon_i). \tag{3.1}$$

Interpreting defect electrons below the Fermi energy $\varepsilon_F$ as holes, first-order perturbation theory then gives explicit expressions for the electron and hole spectra

$$\begin{aligned} P_{\mathrm{ex,el}}(\omega) &= \sum_{ij} \left| \frac{\lambda_{ij}}{\varepsilon_j - \varepsilon_i} \right|^2 (f(\varepsilon_i) - f(\varepsilon_j)) \\ &\quad \times \delta\left(\omega - (\varepsilon_j - \varepsilon_F)\right) \theta(\omega)\theta(\varepsilon_j - \varepsilon_i) \\ P_{\mathrm{ex,ho}}(\omega) &= \sum_{ij} \left| \frac{\lambda_{ij}}{\varepsilon_j - \varepsilon_i} \right|^2 (f(\varepsilon_i) - f(\varepsilon_j)) \\ &\quad \times \delta\left(\omega - (\varepsilon_i - \varepsilon_F)\right) \theta(-\omega)\theta(\varepsilon_j - \varepsilon_i). \end{aligned} \tag{3.2}$$

These spectra can be calculated spin-dependent, which is straightforward. The total energy loss of the trajectory is defined by

$$\Delta E = \int_0^\infty d\omega\, \omega\, P_{\mathrm{ex}}(\omega). \tag{3.3}$$

Within this work, the spectra for a half round trip in the adsorption well rather than a full one are discussed, in order to compare to previous results in the literature. Also for a dissipationless trajectory, asssuming vertical adsorption onto the surface, the ways 'in' and 'out' are equivalent by time inversion symmetry, and within the presented approach the spectrum of the half round trip is equal to one half of the spectrum for the full round trip. Also, it is noted that time-reversal symmetry implies $\lambda_{ij} = 0$ as $|\varepsilon_i - \varepsilon_j| \to 0$. Note this implies that the limit of $P_{\mathrm{ex}}(\omega)$ for $\omega \to 0$ can be shown to exist, see section 3.1.2. The present theory is applicable under the following conditions: the energy loss $\Delta E$ during one round trip must be a small fraction of the total energy of the adsorbing particle, measured from the bottom of the adsorption well, to justify the 'unperturbed trajectory' approximation. Moreover, the particle is required to move sufficiently rapidly to justify the use of static (rather than adiabatic) electronic wavefunctions in evaluating the matrix elements. This means that the excitation frequency of interest, $\nu = |\varepsilon_j - \varepsilon_i|$, should fulfill the condition $\nu \gg (2\pi\tau)^{-1}$, which was remarked upon in section 2.3.1. The latter condition is fulfilled for electronic excitations detected by a Schottky diode ($h\nu > 0.5$ eV, i.e. $\varepsilon_{\mathrm{S}} = 0.5$ eV) even for light particles such as thermal hydrogen atoms, where $\tau \sim 20$ fs.
Hence, the present theory seems to be more appropriate for the high-energy part of the excitation spectrum, detectable as chemicurrents, than the forced oscillator formalism of section 2.5. However, the low-energy part of the spectrum dominates the dissipated energy. Thus the perturbative approach is probably not able to describe the energy dissipation correctly, where instead the adiabatic electronic wavefunctions should be considered for evaluation of the matrix elements.
The present, extended theory has some technical advantage concerning the so-called spin transition: In most practical implementations of DFT, the electronic correlation effects between the electrons close to the adsorbing particle, e.g. hydrogen, and the metal electrons are described in an approximate way by solutions that break spin symmetry, by assigning a spin moment to the free hydrogen atom, cf. section 2.1. During adsorption, spin symmetry is restored. In such ground-state DFT calculations, the spin transition has a formal analogy to a first-order phase transition, and thus leads to a $\sqrt{Q}$-type dependence of the effective potential near the transition point on the reaction path. In the theory of electronic friction, this singularity results in a divergence of $\Lambda(Q, \omega)$, rendering the theory inapplicable [27].
In the present theory, the $\lambda_{ij}$, and hence $P_{\mathrm{ex}}(\omega)$, remain well-defined, since the integrand in Eq. (3.10) diverges at most like $Q^{-1/2}$, and hence remains integrable. Phrased in other words, the abrupt change of the spin polarization in a ground-state DFT calculation and the quasi-static limit are incompatible. The present

theory circumvents this difficulty. However, it is mentioned that in a time-dependent treatment of spin, both in TDDFT [6] or in the mean-field approximation to the Newns-Anderson model [29], the spin polarization changes smoothly, and this difficulty doesn't arise anyway.
A final note shall be made on the Gunnarsson-Schönhammer approach: In Eq. (3.2) the matrix elements $\lambda_{ij}$ appear. In principle it is possible to either take the MHRT matrix elements (2.35) or the Gunnarsson-Schönhammer (GS) matrix elements (2.40). Using either of these can lead to quite different results, which is demonstrated in chapter 4. Throughout this work it is specifically mentioned, when the GS matrix elements are used, hereby defining the term "GS-like perturbation theory".

### 3.1.2 Comparison to the Theory of Electronic Friction

The theory presented here has some similarities with, but also important differences to the theory of electronic friction worked out earlier [57], section 2.5. To see this, one assumes the separability of the matrix elements appearing in Eq. (2.35) (see Ref. [27] for a discussion of this point), and takes the quasi-static limit. This limit implies that the excitation frequencies of interest are sufficiently small, such that the states $|\varepsilon_i\rangle$ and $\langle\varepsilon_j|$ are essentially indistinguishable from states at the Fermi surface, $|\varepsilon_\mathrm{F}\rangle$. The resulting theory is formally identical to the theory of electronic friction, with the important difference that the friction approach uses wavefunctions changing adiabatically with the position of the adsorbate, while the present perturbative approach uses wavefunctions of the bare substrate to calculate the matrix elements. The reader is reminded that the theory of electronic friction starts from Eq. (2.48). This definition is somewhat analogous (although not equivalent) to the definitions in Eqs. (2.47) and (2.37). Whereas the present definition of $P_\mathrm{ex}$ uses the squared modulus of a time integral, the definition of Im $\Lambda$ (2.48) starts from the square moduli of matrix elements. This way, the friction coefficient can be defined for any point $Q(t)$ along the trajectory.
Also note that the friction coefficient (2.50) has a $Q^{-1}$-divergence at the adiabatic spin transition point, leading to the problem that it is not well-defined. Therefore it appeared unwise to include the effect of electronic friction on the trajectories within the present work.
A similar reasoning employing the quasi-static limit can be used to establish that the total energy loss, Eq. (3.3), is a well-defined quantity also in the perturbative approach, both for a full and a half round trip. The limit of $P_\mathrm{ex}(\omega)$ for $\omega \to 0$ can be shown to exist, as the expression can be decomposed into the two factors, $|\lambda_{ij}|^2/|\varepsilon_j - \varepsilon_i|$ and $(f(\varepsilon_j) - f(\varepsilon_i))/|\varepsilon_j - \varepsilon_i|$, which both have a finite limit for $|\varepsilon_i - \varepsilon_j| \to 0$. For the first factor, the proof is analogous to the derivation of the finiteness of $\eta$ in electronic friction theory. The second factor is finite for any non-zero electronic temperature $T$. Considering the total energy loss, one may even calculate the limit $T \to 0$. The combined limiting process $\omega \to 0; T \to 0$ for the integrand $\omega P_\mathrm{ex}(\omega)$ remains well-defined for any fixed ratio $\omega/(k_\mathrm{B}T)$.
In extension over electronic friction, the perturbative approach allows to address the excitations of a single electron-hole pair at *any finite* energy, even further away from the Fermi level. Compared to adsorbate vibrational damping, chemisorption is accompanied by stronger variations of the effective electronic potential, and hence components of higher frequency, also much higher than the vibrational frequency in the adsorption well, may become excited non-resonantly.

### 3.1.3 Energy Conservation

In the DFT calculations of the potential energy surface (PES), the adsorbing atom has a finite energy available for electronic excitations. Simply using (2.39) with (2.35) to calculate the probability for excitation of electron-hole pairs of a certain energy does not take into account this finite energy, and indeed one finds that excitations with an energy larger than the available (chemisorption) energy may be predicted by the equations in this case. In order to take into account energy conservation, (2.35) must be extended to include the maximum energy available for electron-hole pair excitations, $E_\mathrm{max}$. One obtains

$$\lambda_{ij}(\tau) \;=\; \int_0^\tau dt' \left\langle \varepsilon_j \left| \frac{dV}{dQ} \right| \varepsilon_i \right\rangle \frac{dQ}{dt'} \exp(i(\varepsilon_j - \varepsilon_i)t') \theta\left(E_\mathrm{max} - (\varepsilon_j - \varepsilon_i)\right). \tag{3.4}$$

This implementation of energy conservation leads to changes of the calculated spectra when the e-h pair excitation energy approaches $E_{\max}$, but not for e-h pairs whose excitation energies are much lower than $E_{\max}$. In chapter 5 it is found that the e-h pair spectrum differs notably in an energy range of about 0.2 eV close to $E_{\max} = 1.1$ eV.

### 3.1.4 Analytical Considerations

#### General Form of the Spectra

Justified by later results, the author tentatively proposes that the general form of the spectrum might be similar for all adsorbates. This proposition needs justification in form of a simple model. Indeed, starting from simple model assumptions, a general form of the electron-hole pair spectrum can be found. The model is developed here for energies larger than the Schottky barrier, i.e. for the tails of the spectra.
However, note that conclusions drawn from this model remain rather general. While it serves the purpose to provide some general ideas on the form of the spectra and the mass-scaling of chemicurrents, it is not meant as a conclusive treatment of the form of the spectra.
In a first step the matrix elements

$$M_{ij}(Q) = \langle i \left| V_{\text{eff}}(Q) \right| j \rangle \tag{3.5}$$

are considered, where the states $|i\rangle$ and $|j\rangle$ are unperturbed states of the clean slab, and $V_{\text{eff}}(Q)$ is the effective potential at reaction coordinate $Q$. The initial assumption is that these matrix elements decay as $\exp(-\kappa Q)$ outside the slab, which is reasonable, since the wavefunctions do. The time-dependence of the velocity $v_{\text{ad}}(t)$ of the adsorbing particle does not influence the form of the spectra decisively in the relevant energy range around 0.5 eV (the Schottky energy). However, a low velocity leads to a Lorentzian form of the spectra in this energy range, in contrast to the approximately exponential form observed for high velocities. Thus, since the time-dependence of the velocity is not dominating the form of the spectra, the velocity shall be regarded as a constant, given by the particle's energy, i.e. $v_{\text{ad}}(t) \equiv (2E_{\max}/m)^{1/2}$.

It is possible to introduce an energy dependence of the matrix elements, which could be, according to Fig. 4.15, roughly exponential, i.e. proportional to $\exp(-\alpha\omega)$. Here, $\omega$ is the excitation energy. (However a Lorentzian dependence may also be thought of.) The time dependence is converted to a spatial dependence via $Q = v_{\text{ad}}t$. The matrix elements (3.12) are then given by the integral

$$\lambda(\omega) = f(\omega) \int_0^\infty dQ \left( \frac{d}{dQ} e^{-\alpha\omega} e^{-\kappa Q} \right) \exp\left( i \frac{\omega Q}{\hbar} \sqrt{\frac{m}{2E_{\max}}} \right) \theta\left[ E_{\max} - \omega \right]. \tag{3.6}$$

A further energy dependence of the matrix elements was hidden into an additional function $f(\omega)$. By straightforward integration and taking the absolute square of the result, one gets the squared absolute values of the matrix elements (3.12), which are given by

$$\left|\lambda\right|^2(\omega) = \left|f(\omega)\right|^2 \frac{\left|\kappa\right|^2 e^{-2\alpha\omega}}{\left|\kappa\right|^2 + \frac{m\omega^2}{2\hbar^2 E_{\max}}} \theta\left[ E_{\max} - \omega \right]. \tag{3.7}$$

Summation over all matrix elements should give a curve of a similar form. By introducing the energy denominator of the spectra (3.2) the matrix elements would diverge for small energies. However, it is already known that the full expression is well-defined, even in the low-energy limit. Thus the energy denominator of the spectra (3.2) can be incorporated into the function $f(\omega)$, which is then weakly energy-dependent.
Following these arguments also the full spectra (3.2) follow Eq. (3.7), with $f(\omega) \equiv \text{const}$. Inserting reasonable values of the order of 1/Å for the decay constant $\kappa$, 1/eV for the energy decay $\alpha$, the particle's mass $m$, and the calculated energy $E_{\max}$, the form of the model curve is found to be comparable with the form of the high-energy tails of the calculated spectra in subsequent chapters.
The spectra then consist of two factors, $\left|\kappa\right|^2 / \left( \left|\kappa\right|^2 + \frac{m\omega^2}{2\hbar^2 E_{\max}} \right)$ and $e^{-2\alpha\omega}$. Depending on the exact choice of $\alpha$ and $\kappa$, either factor may dominate the spectra, and thus it is possible to fit Eq. (3.7) to a wide range of curves,

ranging from Lorentzian to exponential.
The model may be refined to include, e.g., a weak energy dependence of $\kappa$, a further energy dependence of the matrix elements, or a better approximation for the particle's velocity. However, whether a Lorentzian is observable in the spectra, is strongly dependent on the particle's mass. This model was designed to be approximately correct for large energies, and as such is correct above a certain mass-dependent minimum energy. For particles of the hydrogen mass, this minimum energy is much larger than the Schottky energy. Thus, only for particles of masses considerably larger than the hydrogen mass may a Lorentzian decay be observed. Compared to assumed spectra following the Boltzmann distribution, this model leads to stronger excitations for particles of large mass, and therefore to larger chemicurrents than expected from a simple Boltzmann-like exponential extrapolation of currents. Such larger chemicurrents are observed within the experiments [65, 66]; however, the spectra are not directly accessible there. At present this model can give a qualitative, but not a quantitative description of the spectra, since it is not straightforward to specify $f(\omega)$, or how to exactly treat the low-energy limit. Also, beginning at about 0.2 eV below $E_{\max}$, the spectra decay much more rapidly than descibed by the model. This is caused by a rapid reduction of the density of states available for excitations close to $E_{\max}$. For instance, an excited electron, which possesses an energy close to $E_{\max}$, requires an excited hole very close to the Fermi energy. Possible processes are thus restricted by the accessible Hilbert space.
Therefore this model is not investigated further within this work, but it may serve as a starting point for future investigations. Note that the matrix elements (3.5) are strongly dependent on the states $|i\rangle$ and $|j\rangle$ coupled by the potential, cf. Fig. 4.15. Thus it is difficult to evaluate the matrix elements (2.35) analytically. However, two regimes can be considered: For large energy differences $(\varepsilon_j - \varepsilon_i) \to \infty$, the rapid oscillation of the exponential leads to $\lambda_{ij} \to 0$. For small energy differences $(\varepsilon_j - \varepsilon_i) \to 0$, the oscillation of the exponential is negligible, and thus $\lambda_{ij}$ is independent of the particle's velocity. This may explain the rather similar form of the spectra close to the Fermi energy found in later chapters.

### Mass-Dependence of the Spectra

In this work, the total number of excited charge carriers $N_{e/h}^{\varepsilon_S}(m)$ above the Schottky barrier $\varepsilon_S$, whose value is always taken from experiment, was evaluated numerically following (2.56).
Following results for the FOM (2.57), the number of charge carriers can be tentatively fitted to a generalized form of Eq. (2.57),

$$\ln(N_{e/h}^{\varepsilon_S}(m)) \sim \text{const} - \left(\frac{m}{m_H}\right)^{\gamma}, \tag{3.8}$$

treating $\gamma$ as parameter.
Model calculations for H/Cu [51] found a cross-over from $\gamma = 1/4$ for slow velocities of the impinging H atom (up to approximately 1 Å/fs) to $\gamma = 1/2$ for higher velocities. Following Ref. [51], there are two scaling regimes, one where the integrand in (3.12) makes *many* oscillations on the time scale $\tau$ of the particle impact, and another one where the integrand does *not* undergo a full oscillation. It is noted that the cross-over in the scaling exponent $\gamma$ in Ref. [51] coincides with the transition from 'many oscillations' to 'no oscillation'. For a quantitative analysis, one has to consider $(\varepsilon_j - \varepsilon_i) \gtrsim \varepsilon_S$ in Eq. (3.12), since only excitations above the Schottky barrier $\varepsilon_S$ are detectable. For slow velocities $< 1$ Å/fs, many oscillations occur when $(\varepsilon_j - \varepsilon_i)\tau \gtrsim \varepsilon_S\tau \gg 1$. In the opposite limit, $(\varepsilon_j - \varepsilon_i)\tau \ll 1$, i.e. at high velocities, scaling with $(m/m_H)^{1/2}$ is recovered. Adsorption of thermal atoms or molecules must be considered as 'slow' for this purpose. This point is investigated in chapter 5, where the author concludes that using the FOM to calculate excitation spectra for electrons and holes is inappropriate for these small velocities. Thus electronic excitations are more important for massive particles than deduced from the FOM.

## 3.2 Perturbative Approach: Implementation to DFT

The standard method to calculate electronic excitations throughout this work is described in the following section. The code was developed based on *PWSCF* versions 3.2 initially, but has been improved, and is now based on version 4.0.5 [41], see section 3.2.1.
Using the perturbative approach of section 3.1, the standard method works as follows:
In a first step, an adsorbing particle is calculated at several discrete positions along an adsorption trajectory above a surface using DFT. This position is described by a single reaction coordinate $Q$, which measures the atom's distance from the surface. Generally, the movement of a single particle is investigated, and the others are kept rigid. However, this restriction can be lifted by means of section 3.4. This has been done in chapter 7. In this case, $Q$ measures the arc length of the movement of all particles.
In a second step, the matrix elements

$$M_{ij}^{\mathrm{old}}(Q) = \left\langle \varepsilon_j \left| \frac{\Delta V(Q)}{\Delta Q} \right| \varepsilon_i \right\rangle \tag{3.9}$$

are calculated, which requires knowledge of the effective potential at every position. For evaluating $\lambda_{ij}$ (2.47), the integrand is evaluated at discrete timesteps, and the expression

$$\lambda_{ij} = \int_0^\tau dt \left\langle \varepsilon_j \left| \frac{\Delta V(Q)}{\Delta Q} \right| \varepsilon_i \right\rangle \frac{dQ}{dt} \exp(i(\varepsilon_j - \varepsilon_i)t). \tag{3.10}$$

is used. It requires knowledge of the particle's velocity along the trajectory, which is calculated in a third step, using the forces on the adsorbing particle gained from the DFT calculations. The forces are interpolated using a third-order spline. Discrete time steps are used to calculate the particles's velocity. The matrix elements (3.10) are then calculated by interpolating (3.9) between different positions of the particle along its trajectory, and evaluating these at the discrete timesteps used for calculation of the adsorbing particle's velocity.
This method to calculate the matrix elements (3.10) is rather flexible, and allows to apply perturbative corrections on the effective potential $V(Q)$. Thus it is used in chapter 4, since the extensions of section 3.3 and the Gunnarsson-Schönhammer-like perturbation approach mentioned in section 3.1 are tested there. However, this method of calculation is cumbersome, since one has to first read all local potentials from all geometries, calculate the derivative of the local potential, and then calculate the matrix elements at each geometry, see section 3.2.1 for an improvement.
In order to plot the calculated spectra, it is necessary to replace the $\delta$-functions in Eqs. (2.37) and (3.2) by a function of finite width. In practice, the $\delta$-functions are replaced by the negative derivative of the Fermi-Dirac function, $\delta(\varepsilon) = -\partial f(\varepsilon)/\partial\varepsilon$, as described in section 2.1.6. The same electronic temperature $T$ as in the DFT calculations is used for the broadening. Matrix elements with a very small energy ($|\varepsilon_i - \varepsilon_j| \lessapprox$0.0136 eV (1 mRy)) have to be handled with care. Although the limit $|\varepsilon_i - \varepsilon_j| \to 0$ is mathematically well-defined, the numerical results are not reliable due to rounding errors. In the plots, and also in the calculations, this energy region is therefore omitted. Also, there is always a $\delta$-function at zero energy. Evaluation of (2.37) or taking into account the $\delta$-function of (2.36) makes it necessary to treat small energies with extreme care.
The total energy loss is not affected by this omission, since the contribution of such small-energy transitions to $\Delta E$ is negligible. (For a full round trip, $P_{\mathrm{ex}}(0) = 0$).
Taking into account these considerations, evaluation of the excitation spectra (3.2) is then straightforward at discrete energies.
It is noted that the approach presented here can be extended beyond first-order perturbation theory (see section 2.3.1). In this case, the electron-hole spectrum (but not the separate spectra for electrons and holes) can be calculated analytically. The method is applicable to weak and swift perturbations [56]. Note that evaluation of Eq. (2.37) is numerically demanding, since a $\delta$-peak is found at zero energy. This peak is found as an underlying constant in the integrand on the right hand side of this equation. (A constant is the Fourier transform of the $\delta$-function.) This constant must be subtracted in order to get rid of numerical oscillations caused by the Fourier transform of this constant. This can be done by expansion of Eq. (2.37) to the order sufficient for the

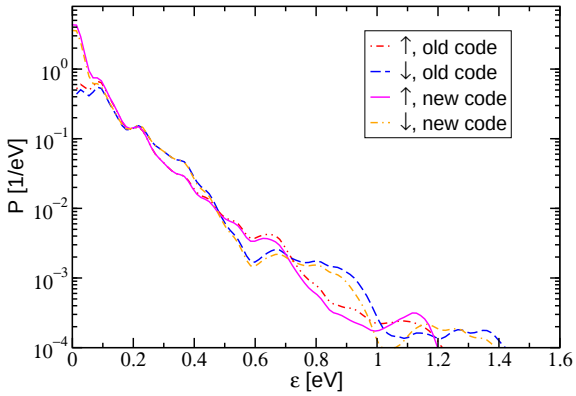


Figure 3.1: Comparison of the electron-hole pair excitation probabilities in first order perturbation theory for the adsorption of H/Al(111) for the two code versions, cf. section 4.2. Both curves are essentially on-top each other, with only minor deviations. The only notable exceptions are values close to zero energy. It turns out that these values have only little effect on the total dissipated energy and on the particle yield for experiments with Schottky barriers of around 0.5 eV. The 'old code' curve data is taken from Fig. 4.7.

oscillations to vanish, similar to what is done in Eq. (2.38). A simpler approach is taking the mean average of the numerical result over the energy interval defined by an oscillation frequency, which turns out to be sufficient in the investigated cases.
For the systems under study, it is always tested, whether a perturbative approach is sufficient, or not, by comparing results for the electron-hole pair spectrum gaines by the perturbative approach of first order and the MHRT approach, which takes into account all orders.

### 3.2.1 Improvement of the Code

While conceptually clear, the method to calculate the matrix elements (3.10) described above used up to this point has proven itself cumbersome. The main reason for this is that one has to read in the effective potential for all geometries, interpolate and take its derivative then, and afterwards combine it with the wavefunctions. While it is possible to investigate certain possible extension of the theory, see, e.g., sections 4.3.2 and 4.3.1, it is shown that they do not give correct results for the isotope effect. Therefore they are abandoned.
If one uses only the unperturbed adiabatic wavefunctions and occupations, it is much more feasible to calculate the matrix elements (3.5) first. Only after evaluation of these matrix elements for all geometries is the differential of $M_{ij}$ with respect to $Q$ calculated numerically, using a third-order spline interpolation, and

$$\frac{\Delta}{\Delta Q}\left\langle \varepsilon_j \left| V(Q) \right| \varepsilon_i \right\rangle = \left\langle \varepsilon_j \left| \frac{\Delta V(Q)}{\Delta Q} \right| \varepsilon_i \right\rangle . \tag{3.11}$$

As an advantage, $M_{ij}(Q)$ can be calculated both for local and non-local potentials by the algorithms implemented in *PWSCF*, while the calculation method mentioned above is cumbersome in case of non-local potentials. The matrix elements $\lambda_{ij}$ can then be calculated using the derivative of the matrix elements $M_{ij}$ with respect to the reaction coordinate,

$$\lambda_{ij} = \int_0^\tau dt \left( \frac{d}{dQ} M_{ij}(Q(t)) \right) \frac{dQ}{dt} \exp(i(\varepsilon_i - \varepsilon_j)t)\theta\left[E_{\max} - (\varepsilon_i - \varepsilon_j)\right] . \tag{3.12}$$

Here, $\tau$ is the interaction time of the adsorbing particle with the surface. In principle, $\tau = \infty$ holds for the adsorption process, since this kind of interaction only happens when the particle is close to the surface and moves. However, in the present calculations the trajectory starts at time 0, and ends at time $\tau$. Within this work, $\tau$ is the time the particle needs for a half round trip in the chemisorption well. $E_{\max}$ is the maximum energy

available to excite electron-hole pairs; i.e. $E_{\max}$ is the particle's energy here.
This method accelerates the code by a factor 3. The code rests on *PWSCF* V 4.0.5, while in chapter 4 code version 3.2 was used, with the exception of section 4.3.1. Since interfaces have changed, the code had to be re-programmed from scratch.
Test calculations give the same results as in chapter 4, with the notable exception of excitations around zero energy (for e-h pairs) or the Fermi energy (for e and h spectra alone), where the new code version proved to be much more stable numerically. The excitation probabilities of electron-hole pairs for the improved and the old code versions are compared in Fig. 3.1.
Evaluating the data gives only small deviations from the data of chapter 4, where the old code version is used, within the order of 5 % for absolute values, which were to be expected due to numerical inaccuracies. Deviations for relative values, e.g. the ratio of detected holes above the Schottky barrier for different isotopes, are much smaller. One also gets a better match of the form of the curves with results from TDDFT [6] close to zero energy. Excitation probabilities close to zero or the Fermi energy are regarded as being dominated by numerical inaccuracies in chapter 4.
The author concludes that the improved code version has better numerical behavior for small excitation energies, i.e. values close to zero or the Fermi energy. Since these values are not experimentally observable up to now, this can only be proven by comparing to the form of theoretical curves from other methods [27, 30]. The comparison supports this conclusion, since the new form is more similar.

## 3.3 Nonadiabatic Description of the Spin Dynamics

Certain systems within DFT are investigated within the framework of spin-polarized density functional theory, i.e. the spin-up and spin-down densities, $n^{\uparrow}$ and $n^{\downarrow}$, are considered as independent degrees of freedom. An example is the system H/Al(111) [27, 28, 6]. In this system, the ground state energy for the adsorbate far away from the surface is wrong, if a degree of freedom in addition to the charge density $n(\mathbf{r}) = n^{\uparrow}(\mathbf{r}) + n^{\downarrow}(\mathbf{r})$, the local spin polarization $\zeta(\mathbf{r}) = n^{\uparrow}(\mathbf{r}) - n^{\downarrow}(\mathbf{r})$, is not introduced, cf. section 2.1.8. This is due to deficiencies of the XC functional [38]. Calculating the projected density of states, using suitably defined atomic orbitals, it is possible to define an atomic spin polarization $\xi^{at} = N_{at}^{\uparrow} - N_{at}^{\downarrow}$, where $N_{at}^{\sigma} = \int d\mathbf{r}\, n_{at}^{\sigma}(\mathbf{r})$, with $n_{at}^{\sigma}(\mathbf{r})$ the local spin density of an atom.
The atomic spin polarization of an approaching adsorbate atom may disappear at a certain point in the adiabatic case, called the the adiabatic spin transition point. In the example H/Al(111) this happens about 2.5 Å above the surface [6]. The physical reason behind this phenomenom is the scattering of the substrate electrons with the adsorbate electron. This leads to the fact that the spin of the adsorbate is not a good quantum number close to the surface, while it is a good quantum number far away from the surface. The correct description of an H atom in front of a surface includes a superposition of spin up and spin down states. Present-day DFT calculations do not describe such a superposition properly [38].
The transition between a spin polarized and unpolarized case in DFT calculations is known to be problematic: In previous theoretical works, this has lead to an unphysical behavior of the electronic friction coefficient [27]. The reason behind this is a root-like singularity of the derivative of the effective potential at the adiabatic spin transition point. The atomic spin polarization is shown in Fig. 3.2, where the adiabatic occupation of the spin up and spin down states during adsorption of H on-top an Al(111) surface in DFT calculations vs. its distance $Q$ from this surface is presented. A square-root behavior of the occupations is observed, which corresponds to the behavior of the potential at the position of the adsorbate. The figure was calculated following results of chapter 4.
Physically, the scattering of the substrate and adsorbate electrons takes some time. Only after this time the spin disappears. This is an inherent nonadiabatic property of the moving adsorbate atom, whose ground state is spin-polarized in DFT calculations [28]. This point is investigated later.
A fundamental question at this point is the physical meaning of this behavior. A criticism, which should be taken seriously, is that an atomic beam approaching a surface in chemicurrent experiments is not spin-polarized (cf. [54, 4, 11]), but unpolarized. On the other hand, DFT calculations using LSDA or GGSDA (GGA including

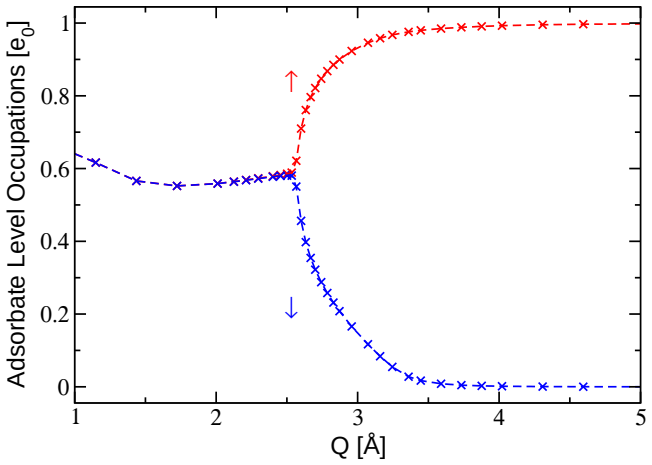


Figure 3.2: Adiabatic occupation of the spin up and spin down states of an H atom vs. its distance $Q$ from an Al(111) surface. H is positioned on the on-top position of this surface. Far away from the surface there is an atomic spin polarization of approximately 1 electron, which will eventually become 0 after the adiabatic spin transition point at about 2.5 Å, after which it vanishes. A $\sqrt{Q}$-dependence of the atomic spin polarization can be observed. This leads to a $Q^{-1/2}$-behavior of the derivative of the effective potential.

spin) give the result that it is spin-polarized, keeping in mind that this is probably unphysical. Physically, far away from the surface the spin of the H electron is a good quantum number. This is not the case when H is adsorbed at the surface, since then the electron is in the Fermi sea of the substrate. Consequently, there must be a transition between these two regimes, where the one-particle picture of an electron localized at the H atom and the many-particle picture of electrons in the Fermi sea collide. The correct description for the H atom far away from the surface is a superposition of states. However, such a superposition is not possible in present-day DFT calculations [38].

Anyway, if the hydrogen atom is scattered back from the surface, the spin is a good quantum number again. If the electronic spin of the H atom is measured while it moves towards the surface, and again after reflection, both measurements are independent, if the hydrogen is slow enough. The two measurements are uncorrelated. This is the reason why the mean-field approximation to the time-dependent Newns-Anderson model of Refs. [28, 29] does not give an atomic spin polarization at all after a scattering event. On the other hand, if in a theoretical calculation the total spin of the system is fixed, so that a constraint is introduced in the calculations, the hydrogen electron is in the majority spin channel far away from the surface even after scattering every time [6]. Remembering the correct many-body picture of the system, it is straightforward to see that a correct description must include an energetically degenerate superposition of states, which is not possible within the framework of GGSDA.

Therefore, the spin majority channel after the scattering event must be chosen by the investigator in order to be able to calculate the correct chemisorption energy. It is calculationally preferable to use the same direction which was used before the scattering took place.

The additional degree of freedom introduced in spin-polarized DFT, when applied to infinite systems, allows to study the ground state of a system with a defined overall spin polarization $\xi$. Formally, this is done by adding a term to the total-energy expression

$$E(\xi) = \min \left[ E\{n(\vec{r}), \zeta(\vec{r})\} + H \left( \int_V \zeta(\vec{r}) d^3r - \xi \right) \right]. \tag{3.13}$$

It has been noticed long ago [67], that the Lagrange multiplier $H$ has the physical interpretation of (one component of) a magnetic field, applied along the quantization axis introduced through the definition of $n^{\uparrow}$ and $n^{\downarrow}$. Electronic excitations in a dynamical system must in principle be treated in time-dependent density functional theory. In its spin-polarized version, this implies that both the spin polarization $\xi(t)$ and the constraint $H(t)$

should be chosen time-dependent.
Since time-dependent density functional theory is computationally very involved, a simpler, approximative point of view is proposed here: For most electronic degrees of freedom of the investigated systems, the dynamics are very close to being adiabatic. These can be treated, to an excellent approximation, by minimizing the total energy at every instant in time, possibly subject to constraints provided by the dynamics of a few, truly non-adiabatic degrees of freedom. In the framework of constrained density-functional theory [68, 69], a formalism has been devised how constraints can be handled in a very general manner.
For the systems investigated here, the spin polarization of a single approaching atom, $\xi_{ads}$, is considered as a constraint (the only one) that should be treated in this way. Formally, this quantity is defined using a projection operator

$$\xi_{ads}(Q) = \sum_i \left[ \left| \langle a | \varepsilon^{\uparrow}_{i,Q} \rangle \right|^2 f(\varepsilon^{\uparrow}_{\mathrm{F},Q} - \varepsilon^{\uparrow}_{i,Q}) - \left| \langle a | \varepsilon^{\downarrow}_{i,Q} \rangle \right|^2 f(\varepsilon^{\downarrow}_{\mathrm{F},Q} - \varepsilon^{\downarrow}_{i,Q}) \right] \tag{3.14}$$

with $|a\rangle$ being a (suitably defined) adsorbate atomic orbital, and a term is added to the total energy. Note that the Fermi energies $\varepsilon^{\uparrow}_{\mathrm{F},Q}$ for the spin up and $\varepsilon^{\downarrow}_{\mathrm{F},Q}$ for the spin down case are only equal if the adiabatic ground state is calculated. In DFT calculations constraining the spin polarization these two Fermi energies are generally not equal. The equation of motion for the time-dependent constraint can now be defined by

$$\frac{d}{dt}\xi_{ads}(t) = \frac{1}{\hbar}\left(\mathbf{H}(t) \times \xi_{ads}(t)\right). \tag{3.15}$$

The (set of) Lagrange multipliers $\mathbf{H}(t)$ is interpreted as a 'local' magnetic field that affects only the energy of the orbital $|a\rangle$.
One needs to impose the time-dependent constraint on the overall system in order to ensure consistency between the numerous nearly-adiabatic degrees of freedom and the local spin polarization. In practice, this is achieved by performing a fixed-spin-moment calculation for the *total* system, i.e. using Eq. 2.5, and subsequently projecting the spin densities onto the local orbital $|a\rangle$. Only if the adsorbate spin polarization, evolving in time according to Eq. 3.15, differs from the spontaneous spin polarization in the adiabatic ground state $\xi^{\mathrm{adiabatic}}_{ads}$, defined by Eq. 3.14 in the adiabatic case, a non-zero value of the Lagrangian $\mathbf{H}(t)$ is required to enforce the *excess non-adiabatic spin polarization* on the system. This allows one to establish a relation between the quantities $\xi_{ads}(t)$ and $H(t)$,

$$H(Q(t)) = \chi^{-1}(Q)\left(\xi_{ads}(Q(t)) - \xi^{\mathrm{adiabatic}}_{ads}(Q(t))\right), \tag{3.16}$$

where only the relevant directions of the magnetic field and spin polarization are taken into account. The (possibly non-linear) magnetic susceptibility occurring in Eq. 3.16 is principally accessible through spin-constrained DFT calculations:

$$H = \frac{1}{2\mu_B}(\varepsilon^{\uparrow}_{\mathrm{F}} - \varepsilon^{\downarrow}_{\mathrm{F}}). \tag{3.17}$$

The theory described here has a well-defined limit for small incident energies of the adsorbate. For slowly moving particles, the time-dependent occupation converges towards the adiabatic ground-state occupation. In the adiabatic case the slope of the occupation number, and thus the effective potential, diverges and develops a $Q^{-1/2}$ singularity. However, the integral defining the transition rates, Eq. 2.47, remains well-defined, as the singularity is integrable. In this respect, the theory presented here is superior to the simpler theory of electronic friction, where a divergence of the friction coefficient $\eta(Q)$ is unavoidable at a transition between different spin states [26].
For implementing this into a DFT code it is useful to rewrite the aforementioned considerations in a more practical way: It is necessary to provide a method to describe the current local spin polarization $n^{\uparrow} - n^{\downarrow}$ of the approaching adsorbate. In principle this can be done in the following way:
Assumed is a two niveau system, which has the density operator

$$\rho = \begin{pmatrix} \rho^{\uparrow\uparrow} & \rho^{\uparrow\downarrow} \\ \rho^{\downarrow\uparrow} & \rho^{\downarrow\downarrow} \end{pmatrix}. \tag{3.18}$$

The coupling between these two levels will be done through a magnetic field, using the matrix

$$\mathbf{H}(t) = \mu_B \begin{pmatrix} 0 & H(t) \\ H(t) & 0 \end{pmatrix}. \tag{3.19}$$

This magnetic field is the driving force behind the spin transition. It is principally accessible in DFT calculations (3.16). The equation of motion is

$$i\hbar \frac{d}{dt}\rho = [\mathbf{H}(t), \rho] = \mu_B H(t) \begin{pmatrix} \rho^{\downarrow\uparrow} - \rho^{\uparrow\downarrow} & \rho^{\downarrow\downarrow} - \rho^{\uparrow\uparrow} \\ -(\rho^{\downarrow\downarrow} - \rho^{\uparrow\uparrow}) & -(\rho^{\downarrow\uparrow} - \rho^{\uparrow\downarrow}) \end{pmatrix}. \tag{3.20}$$

It is now possible to introduce the variables $a = \rho^{\downarrow\downarrow} - \rho^{\uparrow\uparrow}$ and $b = \rho^{\downarrow\uparrow} - \rho^{\uparrow\downarrow}$, and get the equation of motion

$$\frac{d}{dt}\begin{pmatrix} a \\ b \end{pmatrix} = \frac{2i}{\hbar}\mu_B H(t) \begin{pmatrix} b \\ a \end{pmatrix}. \tag{3.21}$$

Note that in the system H/Al(111) $\rho^{\uparrow\uparrow}(t)+\rho^{\downarrow\downarrow}(t) \equiv 1$, because the sum over the occupations of both levels must be one, and $\rho^{\downarrow\uparrow}(t) = -\rho^{\uparrow\downarrow}(t)$ for symmetry reasons. The normalization simplifies the calculations. Including the initial condition $\rho^{\uparrow\uparrow}(t=0) = 1$, while $\rho^{\downarrow\downarrow}(0) = \rho^{\downarrow\uparrow}(0) = \rho^{\uparrow\downarrow}(0) = 0$, the solution of (3.21) is

$$\begin{aligned} \rho^{\uparrow\uparrow}(t) &= \cos^2\left(\frac{\mu_B}{\hbar}\int_0^t dt' H(t')\right) \\ \rho^{\downarrow\downarrow}(t) &= \sin^2\left(\frac{\mu_B}{\hbar}\int_0^t dt' H(t')\right) \\ \rho^{\uparrow\downarrow}(t) = -\rho^{\downarrow\uparrow}(t) &= \frac{i}{2}\sin\left(\frac{2\mu_B}{\hbar}\int_0^t dt' H(t')\right) \end{aligned} \tag{3.22}$$

for the movement of the adsorbate towards the surface. This equation only enforces a change in the occupation of the two levels until $\rho^{\uparrow\uparrow}(t) = \rho^{\downarrow\downarrow}(t)$, which happens at a certain time $t = t_c$. From this point on $H(t) = 0 (t > t_c)$ (3.16).
The implementation of this equation is best done using the derivatives

$$\begin{aligned} \frac{d}{dt}\rho^{\uparrow\uparrow}(t) &= -\frac{\mu_B}{\hbar}H(t)\sqrt{1-\left(\rho^{\uparrow\uparrow}(t) - \rho^{\downarrow\downarrow}(t)\right)^2} \\ \frac{d}{dt}\rho^{\downarrow\downarrow}(t) &= \frac{\mu_B}{\hbar}H(t)\sqrt{1-\left(\rho^{\uparrow\uparrow}(t) - \rho^{\downarrow\downarrow}(t)\right)^2}. \end{aligned} \tag{3.23}$$

So the derivatives of $\rho^{\uparrow\uparrow}(t)$ and $\rho^{\downarrow\downarrow}(t)$ are only dependent on the values of these two parameters themselves. This equation allows to treat the spin transition in a nonadiabatic way, which in turn results in a differentiable effective potential. However, such a nonadiabatic treatment still contains a transition from the polarized case to the unpolarized one, which is thus labeled spin transition anyways. That has the consequence that a smooth spin transition is still observable; however, the unphysical divergence is absent.

### 3.3.1 Implementation to DFT

The theoretical considerations up to this point have been general ones. In order to use them in a practical DFT calculation, it is necessary to implement them in the code.
The calculated adsorbate spin polarization must be localized at the adsorbate. In order to achieve this, the projector $|a\rangle$ is defined, and also a nonadiabatic occupation of the wavefunctions

$$f^{\sigma}_{\mathrm{nonad}}(\varepsilon_{i,k}) = f^{\sigma}\left(\varepsilon_{\mathrm{F}} - \varepsilon_{i,k,\sigma}\right)\left(1 - |\langle a,\sigma|\, i,k,\sigma\rangle|^2\right) + |\langle a,\sigma|\, i,k,\sigma\rangle|^2 f^{\sigma}\left(\varepsilon^{\mathrm{eff}}_{\mathrm{F},\sigma} - \varepsilon_{i,k,\sigma}\right). \tag{3.24}$$

Here, the parameter $\varepsilon_{\mathrm{F},\sigma}^{\mathrm{eff}}$ was introduced, which plays the role of a "nonadiabatic effective Fermi energy", but has no physical meaning. This scheme works best if the DFT implementation is orbital based, since in that case the wavefunctions are localized around the atomic cores, which is not the case in other (e.g., plane-wave) implementations.
The $Q$-dependent number of electrons at the adsorbate is defined by

$$\begin{aligned} N_{ad}(Q) &= \sum_i \left[ \left| \langle a | \varepsilon_{i,Q}^{\uparrow} \rangle \right|^2 f(\varepsilon_{\mathrm{F},Q} - \varepsilon_{i,Q}^{\uparrow}) + \left| \langle a | \varepsilon_{i,Q}^{\downarrow} \rangle \right|^2 f(\varepsilon_{\mathrm{F},Q} - \varepsilon_{i,Q}^{\downarrow}) \right] \\ &= N_{ad}^{\uparrow}(Q) + N_{ad}^{\downarrow}(Q). \end{aligned} \tag{3.25}$$

In section 3.3 $N_{ad}(Q) \equiv 1$, which is a constraint lifted here. This number must not change when the atomic spin polarization is changed.
In the perturbative approach presented here the adiabatic wavefunctions are taken for the calculations, but the states are reoccuppied using (3.24). The reoccupation allows to calculate the nonadiabatic effective potential. Ideally a self-consistency scheme should be adopted at this point. However, such a scheme depends on the projectors on the atomic orbitals, and is very cumbersome, while little gain is expected from such a scheme, cf. also section 4.3. Thus it was not implemented into the code.
Implementation of (3.23) into DFT codes must rest on (modified) predictor-corrector algorithms. In general a finite number of geometries located at positions $Q_i$ along the reaction path are used to provide information about the adsorption process. With $N_{ad}^{\uparrow}$ analogous to $\rho^{\uparrow\uparrow}$ and $N_{ad}^{\downarrow}$ analogous to $\rho^{\downarrow\downarrow}$ it follows, that

$$\begin{aligned} N_{ad}^{\uparrow}(Q_i) &= N_{ad}^{\uparrow}(Q_{i+1}) \frac{N_{ad}(Q_i)}{N_{ad}(Q_{i+1})} - \frac{\mu_B}{\hbar} H(Q_{i+1}) \sqrt{(N_{ad}(Q_{i+1}))^2 - \left( N_{ad}^{\uparrow}(Q_{i+1}) - N_{ad}^{\downarrow}(Q_{i+1}) \right)^2} \\ &\quad \frac{1}{2}(Q_i - Q_{i+1}) \left( \frac{1}{v(Q_i)} + \frac{1}{v(Q_{i+1})} \right). \end{aligned} \tag{3.26}$$

Here the velocity of the adsorbate above the surface $v(Q)$ was introduced. The last line is the Newton-Cotes expression of the time difference $t_i - t_{i+1}$.
Using (3.26), the effects of a nonadiabatic reoccuption of adiabatic orbitals on the adsorption process can be studied. This is done in section 4.3.2. However, it is found that the reoccupation scheme is not able to predict the experimental isotope effect correctly.

## 3.4 Multi-Dimensional Trajectories

The arguments up to now have mostly concentrated on one-dimensional trajectories along a reaction coordinate. In a physical system, at least 3 coordinates exist along which an adsorbate atom may move. Considering an adsorbing molecule, the potential energy surface on which the adsorbate moves becomes high-dimensional, especially in the case that the dynamics of the substrate is taken into account. In practice such a description by a multi-dimensional trajectory is not very efficient. Instead, one wants to describe the movement along a single coordinate, the reaction coordinate [70, 71].
In order to be able to describe this, the arc length is defined,

$$\begin{aligned} Q(t) &= \int_0^t dt\, \dot{\mathbf{x}}(t) \\ &= \int_0^t dt\, \sqrt{\dot{x}^2 + \dot{y}^2 + \dot{z}^2}(t) \\ &\approx \sum_{q=1}^{N_Q} \sqrt{(\Delta x_q)^2 + (\Delta y_q)^2 + (\Delta z_q)^2}, \end{aligned} \tag{3.27}$$

where $x$, $y$, $z$ are the coordinates of a single adsorbate atom, and the calculation of the arc length is done via summation over $N_Q$ discrete steps. If $N_{ad}$ adsorbate atoms exist, e.g. in an $N_{ad}$-atomic adsorbing molecule, the arc length is defined via

$$Q = \sum_{q=1}^{N_Q} \sqrt{\sum_{n=1}^{N_{ad}} ((\Delta x_{q,n})^2 + (\Delta y_{q,n})^2 + (\Delta z_{q,n})^2)}. \tag{3.28}$$

Assuming that the adsorbate is a diatomic molecule, the coordinate $\mathbf{x}_{i+1,j}$ (j=1,2) can be expressed via

$$\mathbf{x}_{i+1,j} = \mathbf{x}_{i,j} + \mathbf{v}_{i,j}t + \frac{t^2}{2m}\mathbf{F}_{i,j}, \tag{3.29}$$

where $\mathbf{v} = \dot{\mathbf{x}}$ is the velocity of one atom, $\mathbf{F}$ the force acting on it, and $t$ is the time needed for the atom to travel between the two positions. Note that $t$ is assumed to be infinitesimally small for the derivation of the following equations. It follows:

$$\begin{aligned} \dot{Q}(t) &= \sqrt{\left(\mathbf{v}_1 + \frac{\mathbf{F}_1}{m_1}t\right)^2 + \left(\mathbf{v}_2 + \frac{\mathbf{F}_2}{m_2}t\right)^2} \\ &\approx \sqrt{\mathbf{v}_1^2 + \mathbf{v}_2^2} + \left(\frac{\mathbf{v}_1\mathbf{F}_1}{m_1} + \frac{\mathbf{v}_2\mathbf{F}_2}{m_2}\right)\frac{t}{\sqrt{\mathbf{v}_1^2 + \mathbf{v}_2^2}} \\ &\approx \sqrt{\mathbf{v}_1^2 + \mathbf{v}_2^2} + \left(\frac{(\Delta\mathbf{x}_1)\mathbf{F}_1}{m_1} + \frac{(\Delta\mathbf{x}_2)\mathbf{F}_2}{m_2}\right)\frac{t}{\sqrt{(\Delta\mathbf{x}_1)^2 + (\Delta\mathbf{x}_2)^2}}. \end{aligned} \tag{3.30}$$

Here, the discrete representation of the velocity, $\mathbf{v} = \Delta\mathbf{x}/\Delta t$ has been used. The total acceleration $a_{\mathrm{tot}}$ acting on the adsorbate system *along its reaction coordinate* appears,

$$a_{\mathrm{tot}} = \left(\frac{(\Delta\mathbf{x}_1)\mathbf{F}_1}{m_1} + \frac{(\Delta\mathbf{x}_2)\mathbf{F}_2}{m_2}\right)\frac{1}{\sqrt{(\Delta\mathbf{x}_1)^2 + (\Delta\mathbf{x}_2)^2}}. \tag{3.31}$$

This allows one to treat any multi-dimensional trajectory using a 1-D reaction coordinate, if the reaction path is known, and if two consecutive geometries along the reaction path are close enough.
The generalization of this definition to more than two adsorbing atoms is straightforward.
In chapter 7 this scheme is employed to calculate electronic excitations during adsorption of a $Cl_2$ molecule on a potassium surface.

## 3.5 Change of the Kohn-Sham Eigenenergies

In section 2.3.2 an approximate solution was described, where instead of the unperturbed eigenstates of a system the adiabatic eigenstates are used. In this approach, the eigenenergies of the system depend on the value of the reaction coordinate.
Gunnarsson and Schönhammer, in developing the approach, use the property that the differences between Kohn-Sham eigenenergies, with one energy below the Fermi level, and one above, are independent of time, when a semi-infinite substrate is considered [60]. Since they only treat electron-hole pairs, it is entirely possible to neglect the change in the Kohn-Sham eigenenergies. The only important consideration is to identify the energies belonging to the substrate. This can be done using a PDOS calculation when the adsorbate is sufficiently far away from the surface.
For numerical calculations (using *PWSCF*) the differences between the Kohn-Sham eigenenergies vary, because it is impossible to deal with such a semi-infinite substrate within DFT when calculating adsorption. One reasonable method to deal with this problem is to take only the energy differences of the unperturbed slab as the physically meaningful energy differences, since in a semi-infinite system these unperturbed energy differences

should not change.
This, on the other hand, leads to the problem that one can not decide which wavefunctions at a given time step evolved from which wavefunctions at the step before. In principle this problem can be solved in the following way:
First, one needs a calculation of the (unperturbed) substrate slab without adsorbate. Additionally one needs a number of equilibrium geometries, where the adsorbate positions do not differ too much, i.e. a maximum of $10^{-10} - 10^{-12}$m, depending on the exact position of the adatom. It is then possible to calculate the overlap between wavefunctions of the unperturbed slab, and the wavefunctions of a minimally perturbed slab, with the adatom far away from the surface. This should give a distinct mapping of the substrate wavefunctions onto the wavefunctions of the whole system. In this way one may define the substrate wavefunctions for the minimally perturbed slab. In a next step it is possible to calculate the overlap between the mapped substrate wavefunctions of one geometry with the wavefunctions of the next geometry, and so on, and so get a continuous mapping of the substrate wavefunctions onto the wavefunctions of the complete system for all positions of the adsorbate.
However, this method leads to several problems discussed in section 3.6.3.

## 3.6 Problems of the Theoretical Approaches

### 3.6.1 Spin Transition and the Plane-Wave Approach

In section 3.3 a method to calculate the spin localized at the adatom was presented. Results are shown in section 4.3.2. By comparing the spin polarization of the adsorbate with results from TDDFT [6], it is justified to claim that the method is able to predict the nonadiabatic spin polarization, at least for the way towards the surface.
In numerical calculations, minor problems may arise when calculating the magnetic field $H$. Due to the comparatively large distances between subsequent adsorbate positions for different geometries, which are no infinitesimally small, the magnetic field changes between subsequent geometries. These changes must be taken into account, which may be done by using modified predictor-corrector methods.
Nonetheless a major problem remains unsolved: The spin must be localized at the adsorbate. In a plane wave approach projectors onto the Kohn-Sham wavefunctions must be defined in order to be able to calculate a localized spin. These projectors are not uniquely defined. Assuming a somewhat atomic orbital around the adsorbate, it happens that a "substrate" wavefunction has not decayed sufficiently at a spatial position, where this atomic adsorbate orbital is notably different from zero. So the projector identifies a part of the "substrate" wavefunction as an atomic orbital. Thus any reoccupation of the atomic adsorbate orbital includes a reoccupation of the "substrate' wavefunctions. Since the substrate wavefunctions are not localized, such as the atomic adsorbate orbital, this reoccupation changes electronic occupations *across the whole substrate slab*, and so it changes the effective potential across the whole slab. This results in excitations far away from the adsorbate, without any physical reason. In section 3.3 it is shown that a background signal appears in the spectra when using the reoccupation scheme, which is interpreted as being caused by this effect. Comparing to experimental values and spin-constrained calculations in section 4.3.3 it seems that this feature is an artifact of the reoccupation.
However, it is formally not necessary to include reoccupation: The effective potential possesses a $Q^{-1/2}$-singularity, but the matrix elements $\lambda_{ij}$ are defined as an integral over the potential. The singularity is integrable, and a reoccupation is not necessary to get well-defined results.
A possible method to overcome this problem is the use of a code which makes use of orbital-based wavefunctions. In such a code the reoccupation is well-defined, and should not lead to the aforementioned problems. Such a reoccupation scheme has been successfully applied before in an orbital-based code [69].
Another possible explanation of the background signal is that self-consistency was not included in 3.3, and these self-consistency errors might be the reason why the background signal appears. Thus, it might be necessary to include self-consistency. In a plane wave code this requires the definition of projectors, reoccupation, an SCF cycle, and possibly a re-definition of projectors (if orthogonality of projectors is enforced), until self-consistency is reached. Such a self-consistent method would be very cumbersome in a plane wave code, und

an orbital-based code would still be a better choice. Additionally, such a method is not implemented in the *PWSCF* code.
In order to investigate, whether self-consistency problems can solely explain the appearance of such background signals, a spin-constrained calculation is done in section 4.3.3, where self-consistency was guaranteed. It is shown that the appearance of a background signal is mainly due to delocalization of the spin across the whole slab, and not due to self-consistency errors. Therefore it was not seen to be worth the effort to implement a self-consistent reoccupation scheme in the *PWSCF* code.

### 3.6.2 Gunnarsson-Schönhammer and the Mapping of States

A similar problem occurs when using the Gunnarsson-Schönhammer perturbation theory of section 2.3.2. In this section adiabatic eigenstates of the different geometries are used, which define transition matrix elements. These transition matrix elements are integrated over time, defining the matrix elements $\lambda_{ij}$ (2.40).
In order to be able to define such a time integral, one must define which adiabatic wavefunction at a certain position (or time) evolved from which adiabatic wavefunction, i.e. there must be a unique mapping of the wavefunctions at one position onto the wavefunction on another position. However, such a unique mapping is not well-defined, see below. A possible approach is to define the evolved wavefunction as the wavefunction with the largest overlap to a previous one. The mapping can be done as described in section 3.5.
This definition requires the assumption that a unique mapping of states between different geometries exists. This is not guaranteed. Instead, when an adsorbate approaches a surface, the substrate and adsorbate states will form new compound states. Such a compound state may contain non-negligible parts of the adsorbate-derived wavefunctions.
In section 4.3.1 it is shown that this leads to results not compatible with experiment, probably since the picture of evolving wavefunctions is principally flawed: Compound states always appear where the system changes, i.e. close to the position of the adsorbate. The GS approach was tested anyway. However, it should not be a surprise that the spectra have significant differences to spectra from TDDFT and model calculations, and the experimental isotope effect can not be reproduced.
The author notes that the use of an orbital-based code might lead to better results, since composition of states may be less frequent, and substrate-derived and adsorbate-derived states may be better defined. Also a method which circumvents the unique mapping may produce better results.

### 3.6.3 Gunnarsson-Schönhammer and the Eigenenergies

In the theory of Gunnarsson and Schönhammer [58, 59, 60, 61] one important point is that the differences of the eigenenergies of the substrate do not vary. In DFT calculations, where there is no semi-infinite substrate (in the direction of the surface normal), this is not the case.
One reasonable approach to take into account the fundamental result that the difference between eigenenergies does not change is to take the eigenenergies of the unperturbed substrate slab, see section 3.5, but other methods may also be considered.
It was been mentioned in section 3.6.2, that this requires the assumption that a unique mapping of states between different geometries exists, which is not guaranteed: Some compound states contain non-negligible parts of the adsorbate wavefunctions, leading to a shift in the energy differences. In a semi-infinite system this can not happen, because the states will be spread out across a semi-infinite crystal, and so a small perturbation on the surface does not result in a large effect on the eigenenergies.
A solvable problem occurs when defining electron and hole spectra by Eq. (3.2). Here one additionally needs the difference between the Fermi energy and one eigenenergy. This energy difference is nothing Gunnarsson and Schönhammer write about, since they only treat electron-hole pairs. Nonetheless, if the eigenenergies change, their differences remain constant, and the occupation numbers of the electronic states stay the same. Thus, all energies must change by the same amount, including the Fermi energy.
One may also choose other geometries as reference, from which to take the energy differences. Test calculations performed by the author have shown that there is only a small effect of the choice of the reference geometry,

which provides the energy differences, on the excitation spectra within the GS-like perturbation theory.

### 3.6.4 File Size and Calculation Time

The calculation as a whole is resting on the calculations of several (typically a few ten) geometries. It is possible to parallelize these calculations, but the wavefunction files have to be saved in practice, in order to be able to access the effective potential (including projectors).
It is useful to calculate the geometries separately beforehand, and not on-the-fly. The first reason to do this is the duration of the calculations as a whole: By calculating beforehand, one can calculate the geometries parallel to each other, leading to a drastically reduced time until they all are converged. The second reason is stability: If one relaxation does not work as expected, the whole calculation would either crash, or code development would be extremely difficult in order to catch these problems. A separate calculation catches this problem by default. Finally, if one first calculates the derivative of the potential, and then the matrix elements $\lambda_{ij}$, one needs all geometries in order to calculate the derivative.
The geometries necessarily have a huge vacuum region, where the vacuum gap is at least twice the distance of the adsorbate to the surface at the outermost position of the adsorbate in the calculations. This leads to large wavefunction files of a few GB in size, which must be stored locally. At least around 40 geometries are needed, where the position of the adsorbate changes slightly. The total file size for the calculations of chapter 4 was about 200 GB, but this can be exceeded, e.g. if more geometries are used.
If one decides to use, e.g. larger cutoff energies, more k-points, more layers in the slab or a larger supercell, file size and the calculation time also increases. However, the spectra seem to be weakly dependent on these parameters, if they are chosen within a reasonable range for the bulk system (cf., e.g., Fig. 4.6).
Regarding calculation time the post-processing code which calculates the excitation spectra can be parallelized, although this was not done. Serial calculation using the post-processing code employed in chapter 4 took about six days. However, in section 3.2.1 an improvement of the code is described, which reduces the calculation time to about two days for the same case.

# Chapter 4

# Results: H on Al(111)

In this chapter the excitation of electrons and holes in the system H/Al(111) is investigated. The plane-wave code PWSCF [41] (version 3.2) and a self-written post-processing tool (section 3.2) is used for the calculations. It is assumed that the hydrogen atom is approaching an aluminium surface perpendicularly. Because of the experimental setup used in chemicurrent experiments one can safely assume that the adatom has no horizontal velocity component. The on-top position of the substrate was chosen for adsorption, since this geometry was used in previous theoretical works [6].
In section 4.1, the numerical convergence parameters, and the way they were chosen, are described. The approach is essentially the same as described in depth in section 5.1 for potassium. Section 4.2 continues with results from the perturbation theory presented in section 3.1. One essential goal of this chapter is to establish the validity of the perturbative approach by comparing to previous TDDFT [6] calculations for the same system, and the experimental results for the similar system H/Ag [72, 22]. Moreover the system H/Al is used as a benchmark to test the validity of the various alternative theories introduced in chapters 2 and 3, which is done in section 4.3. Section 4.3.1 gives a short look on results from the GS-like perturbation theory explained in section 2.3.2. It is demonstrated that the perturbative approach gives good agreement with experimental works, but the results of the GS-like perturbation theory can not explain the experimental isotope effect, and do not agree with previous theoretical works regarding the decay of the spectra. It is proposed that the main reason for this is the mapping of states. A DFT code using atomic orbitals as basis functions might give better results, see section 3.6.2. However, the dissipated energy is closer to results from TDDFT and model calculations, and thus the GS-like approach probably gives better results for the low-energy part of the spectra.
The other essential goal of this chapter is to investigate the spin transition. Spin dynamics can essentially be treated in two ways, either by allowing a spin dynamics, or by explicitly forbidding the dynamics. Thus spin dynamics is investigated considering two cases (I, II), with two sub-cases (a, b) each. Case I is to take into account spin dynamics. Case Ia is adiabatic spin dynamics, investigated in section 4.2. This is the standard procedure, following the Born-Oppenheimer PES. Case Ib, nonadiabatic reoccupation of the wavefunctions following section 3.3, is investigated in section 4.3.2. It is shown that results from case Ia are comparable to the experimental isotope effect, but case Ib, the reoccupation, is not compatible to this effect. In order to investigate this further, case II explicitly avoids spin dynamics in the sense that the total spin is constrained. In case IIa it is tested whether self-consistency problems can explain the found discrepancies of case Ib, and thus a self-consistent scheme, constraining the total spin polarization of the system to the initial value of one, is investigated in section 4.3.3. Also the results of this section are not compatible with experiments, and it is proven that missing self-consistency alone can not explain the huge discrepancies of section 4.3.2 between theory and experiment. In case IIb an approach not using the spin-density approximation is investigated in section 4.3.4, thereby constraining the total spin to zero. It is demonstrated that the spin plays a minor role for the dissipated energy when adiabatic spin dynamics (spin case Ia) is considered, and a larger energy disspation appears when the spin polarization of the adsorbate changes close to the surface. Discussion (section 4.4) and conclusions (section 4.5) close this chapter.
Large parts of this chapter have already been published [64].

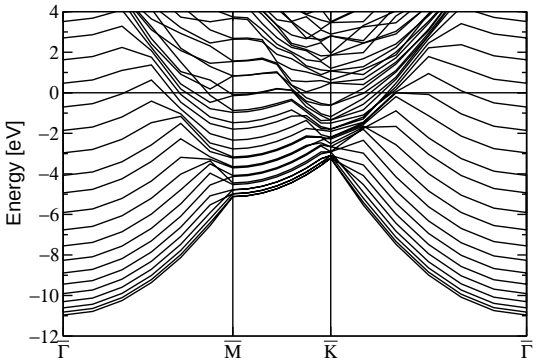


Figure 4.1: Kohn-Sham band structure of an Al(111) slab consisting of 12 layers in a $(1 \times 1)$ unit cell calculated within PBE-GGA. A Monkhorst-Pack **k**-point mesh of $16 \times 16 \times 1$ points has been used to calculate the charge density and the self-consistent potential. The Fermi energy is set to 0. Qualitative and quantitative agreement with the literature with respect to the lowest states below the Fermi energy is achieved [73].

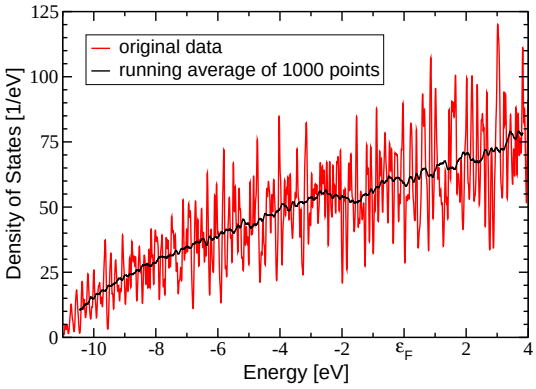


Figure 4.2: Density of states of a clean Al slab of 12 layers. The Fermi energy $\varepsilon_{\mathrm{F}}$ is set to zero. The oscillating part is directly taken from the data of the DOS calculation, but a running average of 1000 points is additionally shown in the graph, in order to show the general trend. The H atomic orbital has an energy of -6.49 eV in DFT calculations. The Al work function is 4.09 eV in the calculations, compared to 4.28 eV experimentally.

The restriction of the $\theta$-function (3.4) is lifted throughout this chapter for sake of simplicity, and comparison with previous theoretical approaches. Anyway, this does not influence the conclusions drawn from this chapter.

## 4.1 Convergence Parameters

For the investigation of the system H/Al(111), numerical parameters were determined in a first step. The parameters in question are the k-point set, the cutoff energy for the plane-wave expansion, the size of the unit cell, the number of layers in the slab and the broadening of the Fermi-Dirac occupation function. The aluminium lattice constant must be calculated using the same energy cutoff.
Norm-conserving pseudopotentials utilizing a PBE GGA exchange-correlation functional were employed, and an initial spin up polarization of the hydrogen atom far away from the surface was assumed. The spin polarization is necessary within DFT calculations to get the correct potential energy surface (PES) for the adsorbing H atom. The choice between up or down is arbitrary, but necessary. The spin was treated within a generalized gradient spin density approximation (GGSDA). The pseudopotential for aluminium was taken from the *PWSCF*-Website, and the pseudopotential for hydrogen was self-constructed and excessively tested, cf. section 4.A. Both pseudopotentials are norm-conserving. The calculations can not be expected to give full quantitative agreement when comparing to TDDFT calculations [6], because the energy cutoff in the present work was more

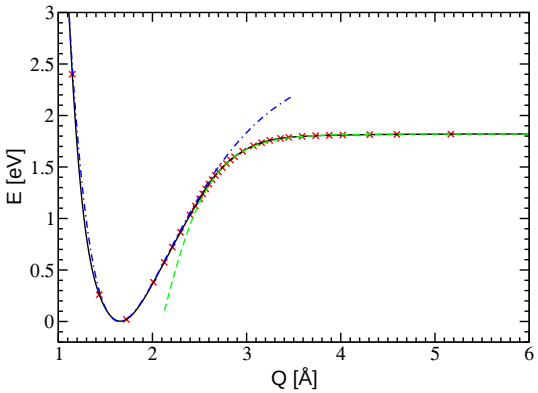


Figure 4.3: Chemisorption potential of a H atom above the on-top position of an Al(111) surface using GGSDA. The spin polarization in the ground-state DFT calculations vanishes at about 2.6 Å. The dashed lines are two Morse potentials fitted to either branch of the PES.

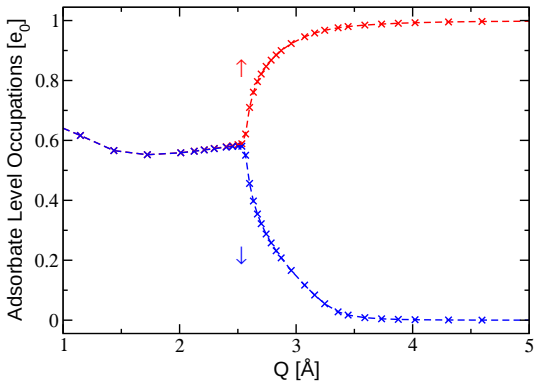


Figure 4.4: Ground-state occupation of the spin-up and spin-down orbital of an approaching H atom vs. its distance from an Al(111) surface using GGSDA. Far away from the surface, the electronic charge at the H atom, corresponding to one electron, is fully spin-polarized. Both spin-up and spin-down orbitals become equally populated after the spin transition point. The spin polarisation shows a $\sqrt{Q}$-behavior close to the transition point.

than twice the cutoff used in the TDDFT case, and in the TDDFT case only a single k-point was used. Thus the numerical parameters in the present work are much better than in the TDDFT case.
The size of the unit cell was adopted from TDDFT calculations [6]. The main reason for this was to avoid possible differences due to different unit cells. A $2\sqrt{3} \times 2\sqrt{3}$ unit cell was chosen. The vacuum region was chosen sufficiently large, keeping in mind that the adsorbate starts at a high altitude above the surface. Since the adsorbate's position furthest away from the surface was 7.2 Å above, and the slab itself is 25.8 Å high, a unit cell size of 51.7 Å in z-direction was found to be sufficient. Test calculations were made which proved this. Note that such a large vacuum region is indeed required: Using a smaller vacuum region results in a small effect on the forces on the H atom, although this effect is not observable in the total energy (cf. Fig. 4.3).
To fix the k-point set, an arbitrarily large cutoff was taken, and the equilibrium lattice constant was calculated in a unit cell containing only 1 atom. When scaling down the required k-point-set to the larger unit cell it was found that a k-point set of $4 \times 4 \times 1$ is sufficient, with the single k-point in the direction of the surface normal. For the cutoff energy a value of 286 eV (21 Rydberg (Ry)) was found to be sufficient for aluminium. This value is also found using calculations of the lattice constant. The result was verified by relaxing the substrate layers as described below.
However, this cutoff is not sufficient for the hydrogen atom. The cutoff chosen is better than what was possible in TDDFT calculations, though. The pseudopotential for the hydrogen was self-constructed, so that the

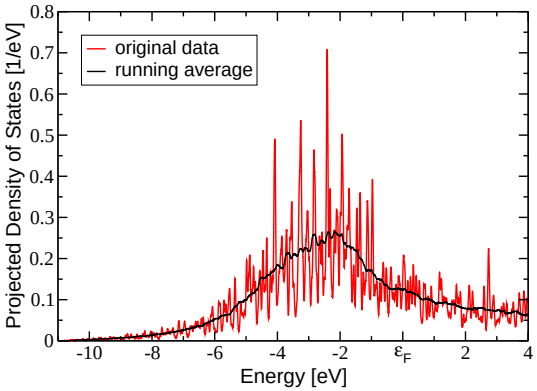


Figure 4.5: Projected density of states of an H atom adsorbing on-top a clean Al(111) surface at the equilibrium geometry. The Fermi energy $\varepsilon_{\mathrm{F}}$ is set to zero. The oscillating part is directly taken from the data of the PDOS calculation, but a running average of 1000 points is additionally shown in the graph, in order to show the general trend.

best possible compromise between accuracy of the results and RAM and hard drive memory requirements of the calculations was achieved. The calculated adsorption energy using a cutoff of 544 eV (40 Ry) is 1.86 eV, and using a cutoff of 286 eV (21 Ry) it is 1.83 eV, so there is a difference of only 0.03 eV. This difference is tolerable, and so the cutoff energy is sufficient. TDDFT calculations did not even reach this cutoff if a reasonable calculation time is a necessity, but the results from static calculations compare well to the numbers fo the present work (1.90 vs. 1.87 eV for 40 and 20 Ry cutoff, respectively) [6].
A broadening of 0.0136 eV (1 mRy) using a simple Fermi-Dirac occupation function was used, which corresponds roughly to the experimental temperatures [74].
Using the aformentioned parameters a lattice constant of 4.061 Å was calculated, while the experimental value is 4.050 Å.
The number of layers necessary for a converged result was calculated by investigating the layer relaxation. The criterion chosen was the relaxation of the upper layers with respect to their interlayer distance. The number of layers necessary so that the interlayer distances are converged is regarded as sufficient, to be sure that the forces are converged. It is found that 12 layers are needed for that cause. This is also the number of layers used in TDDFT calculations. This is another reason to choose 12 layers.
The above results were verified by comparing the relaxation of the substrate layers to experimental values, while keeping the lowest 3 layers fixed. An outward relaxation of about 1.1 % for the outermost layer was found, and an inward relaxation of -0.3 %, which corresponds to the experimental values, cf. Ref. [73] and references therein. It is found, however, that the 7 layers used for relaxation in Ref. [73] are not at all sufficient for the relaxation in order to achieve convergence. The calculated values of the present work seem to be perfectly within the error bars of other calculations [75].
Fig. 4.1 shows the calculated band structure of an Al(111) slab of 12 layers with a $(1 \times 1)$ unit cell. Comparison with the literature [73] shows good agreement. The lowest state at the $\overline{\Gamma}$-point of the present work is about 11 eV below the Fermi energy, at the $\overline{M}$-point it is about 5 eV below, and at the $\overline{K}$-point it is about 3 eV. Holes in the band structure are not observable, though, which is due to the fact that the states in the present calculation are not close enough with respect to energy. Also Fig. 4.1 does not show a projected bandstructure, in contrast to the literature graph.
The density of states (DOS) of this slab is shown in Fig. 4.2, where the numerical parameters set before are used. The DOS is generally root-like in appearance, which is typical for metals.
Fig. 4.3 shows the chemisorption potential of hydrogen above the on-top site of Al(111). The ground-state potential energy surface (PES) consists of two branches, fitted locally with Morse potentials of the form

$$V_{\mathrm{Morse}} = D\left(e^{-2\alpha(Q-Q_{\mathrm{eq}})} - e^{-\alpha(Q-Q_{\mathrm{eq}})}\right) + c, \tag{4.1}$$

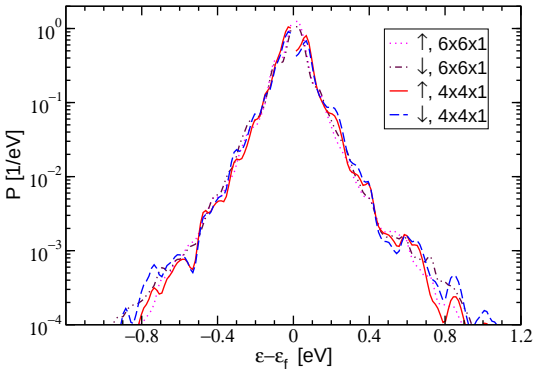


Figure 4.6: Spin-resolved excitation spectra of electrons (positive energies) and holes (negative energies) for an impinging H atom with an initial kinetic energy of 60 meV on the on-top position of an Al(111) surface after one half round trip in the chemisorption well. The plot shows the differences for different k-point sets. A difference between the two spin channels can not be observed. The dashed lines correspond to a k-point set of $4 \times 4 \times 1$ for the wavefunctions, and the straight lines to $6 \times 6 \times 1$. There are only minor differences in the spectra, i.e. the larger k-point set leads to a smoother curve. Although differences between electrons and holes appear to be small, the yield of detected particles is different, see Tab. 4.2. Values close to the Fermi energy ($|\varepsilon - \varepsilon_F| < 0.0136$ eV) are not plotted because of numerical inaccuracies in this energy range.

that intersect at a distance of about 2.6 Å above the surface. For larger distances, the DFT ground state is spin-polarized, while the electronic system is non-polarized when the H atom comes closer. As observable in Fig. 4.4, the electronic spin polarization at the H atom vanishes below this point. Fig. 4.4 shows the result of a population analysis for the atomic (1s) orbital of the H atom using the Löwdin approach implemented in *PWSCF*. The DFT ground-state wavefunctions of either spin for each position along the trajectory were projected onto the H (1s) orbital. Below the spin transition point at about 2.6 Å both the spin-up and the spin-down orbitals show a population of about 0.6 electrons. Further away from the surface, the H atom is spin-polarized, i.e., the spin-up orbital gets fully populated while the spin-down orbital gets depleted. Right above the transition point the spin polarization shows a sharp, square-root-like increase. The projected density of states (PDOS) onto the atomic H (1s) orbital is shown in Fig. 4.5, with the H atom at the equilibrium geometry. One observes that the atomic (1s) orbital is broadened close to the surface, due to the interaction with the bulk material, and that it has shifted. Both the spin up and spin down PDOS are the same. In the supercell, even for the adsorbate's position furthest from the surface an influence of the bulk metal is observed: The occupied H spin majority (up) (1s) orbital is roughly 3 eV below the Fermi energy, while the Al work function is 4.09 eV in the calculations. Thus the H (1s) spin majority orbital is 7.1 eV below the vacuum barrier in the supercell, compared to 6.5 eV in the purely atomic case. The H (1s) spin minority orbital is more than 4.5 eV above the Fermi energy. The experimental Al work function is 4.38 eV.

## 4.2 Results from Perturbation Theory (Spin Case Ia)

The classical trajectory is calculated for vertical impact of the H-atom onto the on-top site of Al(111) from Newton's equations for an initial kinetic energy of 60 meV, and starts 3.16 Å above the surface. Thereby, the small effect of electronic friction on the trajectory is neglected. The total time needed for one half round trip is 20 fs. In order to calculate the isotope effect, i.e. the number of electrons or holes detected above the Schottky barrier for isotopes of different mass, the mass of the approaching adsorbate in the kinetic equations is changed. The numerical evaluation of Eq. (2.35) proceeds as follows, cf. also section 3.2: The derivative $dV/dQ$ is calculated numerically, using the first derivative of a third-order spline interpolation. The potential used is the effective potential from the ground-state DFT calculations. The matrix elements in Eq. (2.35) are computed in two steps: First a summation is performed in real space to calculate $dV/dQ|\varepsilon_i\rangle$. Then a Fast Fourier Transform

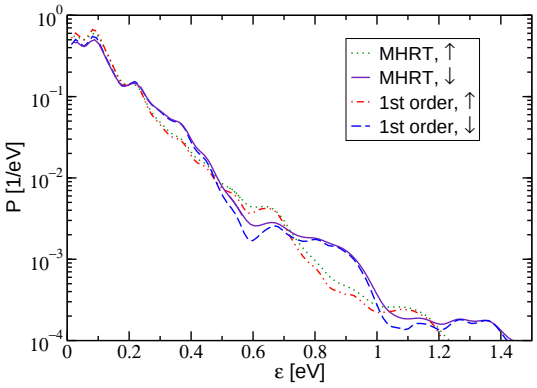


Figure 4.7: Spin-resolved excitation spectrum of electron-hole pairs for an impinging H atom with an initial kinetic energy of 60 meV on the on-top position of an Al(111) surface after one half round trip in the chemisorption well. The curves calculated in first-order perturbation theory are in good agreement with those obtained by a resummation of the perturbation expansion following Müller-Hartmann *et al.* (MHRT). Obviously there is no difference between the two spin channels. Values close to zero energy ($\varepsilon < 0.0136$ eV) are not plotted (and omitted in the calculations) because of numerical inaccuracies in this energy range.

| Isotope | Perturbation theory | | TDDFT [63] | |
|---|---|---|---|---|
| | $T^e_{\text{eff}}$ [K] | $T^h_{\text{eff}}$ [K] | $T^e_{\text{eff}}$ [K] | $T^h_{\text{eff}}$ [K] |
| D | $1100\frac{-300}{+400}$ | $1000\frac{-200}{+300}$ | | |
| H | $1400\frac{-300}{+700}$ | $1300\frac{-300}{+700}$ | $900\frac{-100}{+100}$ | $1100\frac{-100}{+100}$ |
| $\text{H}_{\text{Exp}}$ | | 1680 [72, 22] | | |
| $\text{H}_{0.1m_H}$ | $3000\frac{-500}{+1400}$ | $2600\frac{-500}{+1400}$ | $2700\frac{-200}{+200}$ | $2300\frac{-200}{+200}$ |
| $\text{H}_{0.01m_H}$ | $8900\frac{-3800}{+300}$ | $7300\frac{-2900}{+200}$ | $9300\frac{-200}{+200}$ | $7800\frac{-2200}{+200}$ |

Table 4.1: Slope parameter $T_{\text{eff}}$ of the electron ($T^e_{\text{eff}}$) and hole ($T^h_{\text{eff}}$) spectra for different isotope masses. The middle column contains the fits to our data, and the right column contains fits to data from TDDFT calculations [63]. The value $\text{H}_{\text{Exp}}$ is the experimental value for H adsorption on Ag. The error bars for the fits are quite large. The reason is that the fits can be made over a wide energy area, starting and ending on different points, and thus are rather arbitrary in a certain range.

to wave-vector space is made, and the result is multiplied by $\langle\varepsilon_j|$. The wavefunctions are those of the initial state at $Q(-\infty)$, but omitting adsorbate wavefunctions. Likewise, the energies in the exponential function of Eq. (2.35) are the Kohn-Sham energies of the initial state. The time integration is then done using a spline interpolation of the matrix elements. For the technical implementation the state indices $i$ and $j$ incorporate band index, **k**-point and spin. Only transitions within the same **k**-point and spin channel are considered. However, the restriction regarding the **k**-points can be lifted [26]. A weight factor for the summation over **k**-points also must be introduced.

The main results of the theory presented here are the spectra of the electrons and holes excited by a hydrogen atom impinging with thermal kinetic energy. From the part of the spectra exceeding the Schottky barrier, the predicted yield of the measured chemicurrent is directly derived. In order to study the isotope effect systematically, not only calculations for H and D are carried out, but also for fictitious atoms of mass $0.1m_H$ and $0.01m_H$. The spectra are shown for a half round trip in the adsorption potential (until the particle has reached the turning point on the repulsive branch of the PES), to be able to compare with earlier results [30]. It is noted that in the experiments the particles perform many round trips before they have dissipated the chemisorption energy and come to rest. Hence the average number of electron-hole pairs per incident hydrogen atom in an actual experiment can be significantly higher than the values displayed in the figures.

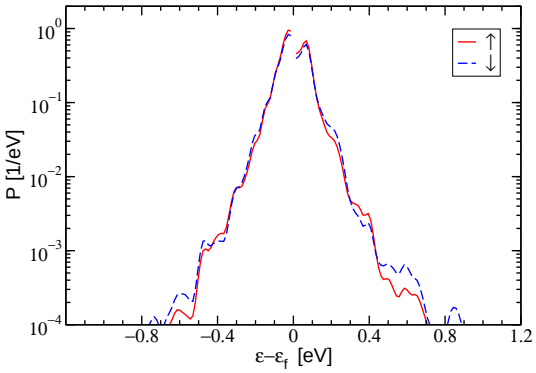


Figure 4.8: Spin-resolved excitation spectra of electrons and holes for D with an initial kinetic energy of 60 meV impinging on-top Al(111) after one half round trip in the chemisorption well. The spectrum is qualitatively similar to the spectrum for H, shown in Fig. 4.6, but the decay is much faster. Due to this stronger decay, isotopes with a larger mass than deuterium can only be calculated if numerical noise is extremely low, which will otherwise superimpose data in the tail of the spectra. This makes it much easier to investigate smaller masses when investigating different isotopes.

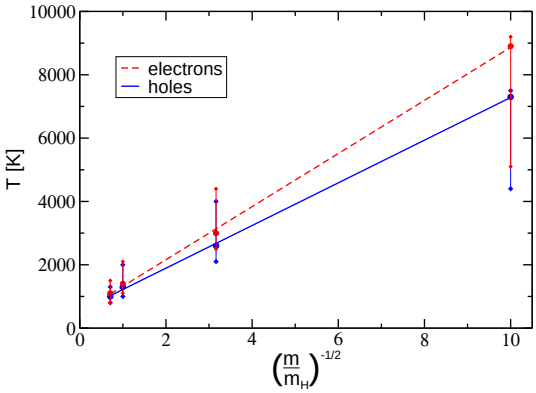


Figure 4.9: Slope parameter $T_{\text{eff}}$ of the electron (red, upper curve) and hole (blue, lower curve) excitation spectra plotted versus the mass-scaling parameter $(m/m_H)^{-1/2}$. $m$ denotes the mass of the adsorbing atom. The lines are linear fits to the data. A linear dependence between the slope parameter $T$ and the mass scaling parameter is suggested, although the slope parameter can be varied in an interval of about 30 %. The plotted values correspond to the fits in Fig. 4.10. The graphic is a representation of table 4.1.

Fig. 4.6 shows the spectra of electrons (positive energies) and holes (negative energies) for a half round trip of an H atom. It is noticed that the spectra of electrons and holes are quite similar, which is a difference to other methods used before. Moreover, differences in the spectra of spin-up electrons (same spin polarization as the impinging H atom) and spin-down electrons (opposite spin polarization as the impinging H atom) are only marginal when plotted on a logarithmic scale. The same holds for the holes of either spin.
The full and dashed lines in Fig. 4.6 indicate the results of convergence tests. While a metal has a continuous spectrum of excitations, the slab used in the DFT calculations has a large but finite number of states, due to the finite thickness and the number of **k**-points used to sample the Brillouin zone. For convergence tests, this sampling was increased from a $4 \times 4 \times 1$ **k**-point mesh to a $6 \times 6 \times 1$ mesh. (This refers to the Kohn-Sham wavefunctions $|\varepsilon_i\rangle$ used to calculate the matrix elements in Eq. (2.35); the potential is assumed to be converged already for the smaller **k**-point set.) Fig. 4.6 shows that the spectra are almost identical, albeit the $6 \times 6 \times 1$ calculations gives somewhat smoother curves. The energy loss $\Delta E$ is 23 meV for the smaller **k**-point set and 20 meV for the larger one. This difference of 15 % is about the same as one can get using different interpolation schemes for the matrix elements. Consequently the error appears to be tolerable, and for the following

| Isotope | Electrons | Holes |
|---|---|---|
| D | 0.000246 | 0.000175 |
| H | 0.000781 | 0.000561 |
| $N/N_D$ | 3.17 | 3.21 |
| $N/N_{D,\text{Experiment}}$ | | $3.7 \pm 0.7$ [72, 22] |
| $H_{0.1m_H}$ | 0.021502 | 0.014713 |
| $N/N_H$ | 27.53 | 26.23 |
| $H_{0.01m_H}$ | 0.088775 | 0.064376 |
| $N/N_H$ | 113.67 | 114.75 |

Table 4.2: Average number of electrons and holes created per impinging H isotope with an initial kinetic energy of 60 meV above the Schottky barrier, per half round trip.

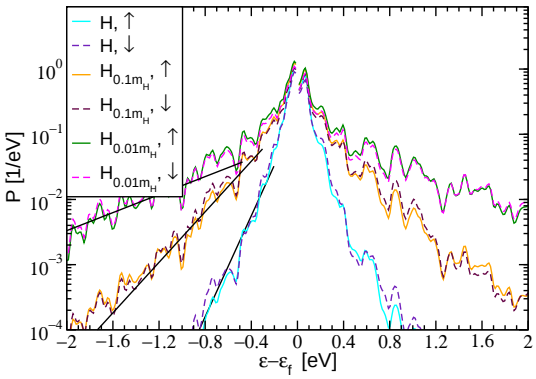


Figure 4.10: Spin-resolved excitation spectra of electrons and holes for different impinging isotopes of H with an initial kinetic energy of 60 meV after one half round trip in the chemisorption well. Spectra for three isotopes (H, $H_{0.1m_H}$ and $H_{0.01m_H}$) are shown, where lower masses give spectra with a larger amplitude. Decaying exponentials with $A\exp(-\varepsilon/k_BT_{\text{eff}})$ are fitted to the hole part of the spectra. There is some freedom in choosing the energy window for the fit, and hence the slopes are associated with large error bars. The lines shown in the plot correspond to $T_{\text{eff}}$= 1300 K, 2600 K, and 7300 K, respectively.

calculations, the smaller set was used.

Note that the energy loss is just a small fraction, about 1%, of the chemisorption energy, see Fig. 4.3. Hence, the use of an elastic trajectory in calculation of the matrix elements appears to be justified.

Fig. 4.7 shows the spectrum of the electron-hole pairs. Here the results of first-order perturbation theory, Eq. (2.37), are compared to the treatment by Müller-Hartmann and co-workers [56] that sums up all orders in the perturbation expansion. It is found that the two approaches yield very similar spectra when plotted on a logarithmic scale. This demonstrates that first-order perturbation theory is sufficient for the high-lying excitations with small excitation probability, which are of interest to the calculation of chemicurrents. Another remark is of interest here: If only the combined electron-hole spectrum were known, one would be tempted to assume that electrons and holes are distributed symmetrically around the Fermi energy. Comparing to Fig. 4.6, it is found that this assumption is reasonable in the present case (but not for the stronger excitations by fictitious H isotopes lighter than H, see below).

Next, the isotope effect is investigated. The electron and hole spectra for deuterium are shown in Fig. 4.8. They are qualitatively similar to those of H, but the excitation probability decays more strongly with increasing excitation energy of the charge carriers. Following the reasoning in Ref. [63] it is generally not a good idea to use the physical masses when one wants to calculate spectra in the TDDFT approach employed in that reference, because at some point one will have large superimposed numerical noise. Also the calculations last unreasonably long for larger adsorbate masses. Regarding numerical parameters for evaluation of the matrix elements,

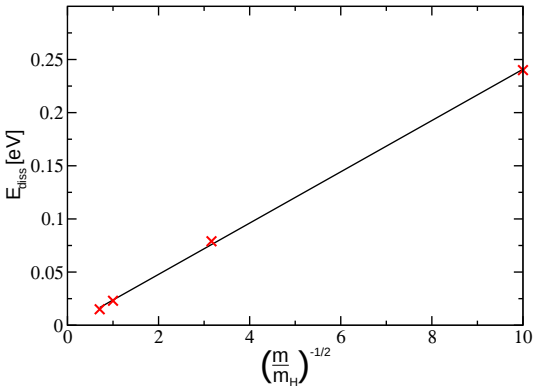


Figure 4.11: Total energy loss vs. the mass scaling parameter $1/\sqrt{m/m_H}$. $m$ denotes the mass of the adsorbing atom. The line is a linear fit to the data. The fitted linear dependence between these two quantities is compatible with the data.

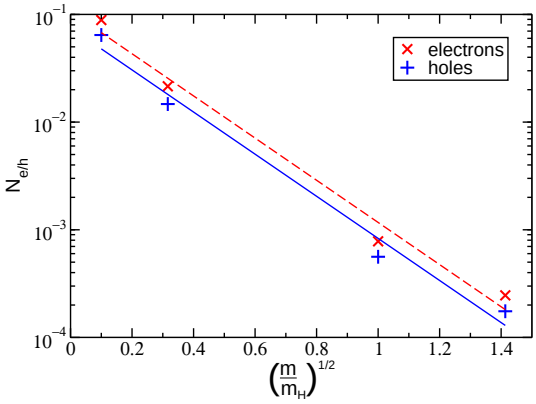


Figure 4.12: Yield of the electron (red, upper curve) and hole (blue, lower curve) excitation spectra plotted versus the mass-scaling parameter $\sqrt{m/m_H}$. $m$ denotes the mass of the adsorbing atom. The lines are linear fits to the data.

this has been tested for a reasonable parameter range in the present work. It occurs that in the present work, this problem is not predominant. For instance, the calculation for deuterium can still be done. However, using smaller masses, it is possible to get a larger energy dissipation, and the effects of interest are thus enlarged. So inspired by Ref. [63], fictitious isotopes of smaller mass, $0.1m_H$ and $0.01m_H$ are also used, in order to get stronger excitations that facilitate the analysis. These isotopes are labelled $\mathrm{H}_{0.1m_H}$ and $\mathrm{H}_{0.01m_H}$, respectively. The spectra are collected in Fig. 4.10.

Similar to previous work [63], an 'effective temperature' $T_{\mathrm{eff}}$ is fit to the high-energy tails of the spectra, using the two-parameter fit (2.55). For the hole spectra, the fitted regions are shown in Fig. 4.10. The temperatures obtained from the fit are given in table 4.1. A graphical representation is shown in Fig. 4.9. The quite large error bars were estimated by varying the fitting window and are of the order of 30 %. They indicate that the distributions are not truly exponential. A similar uncertainty of the fitted temperatures was also noticed in previous works [63, 30]. Nonetheless, the fitted slope parameter $T_{\mathrm{eff}}$ shows a linear dependence on $(m/m_H)^{-1/2}$, which is demonstrated by Fig. 4.9, similar to the FOM (2.57). It is noted that the temperatures fitted for the excited electrons are systematically higher than for the holes. This is particularly obvious for the $\mathrm{H}_{0.1m_H}$ and $\mathrm{H}_{0.01m_H}$, but also holds for H and D, despite the nearly symmetric appearance of the spectra in Fig. 4.6. Within the error bars, the temperatures obtained from perturbation theory are in reasonable agreement both with experiment and with the TDDFT calculations.

Although the effective temperatures are helpful for identifying trends, an analysis of the isotope effect on this

basis is not conclusive due to the large error bars. It is safer to study the isotope effect in the total energy loss, and in the integrated probability of excited carriers above the Schottky barrier. Fig. 4.11 shows the linear relationship between the total energy loss and the mass scaling parameter $(m/m_H)^{-1/2}$.
This can be rationalized in view of electronic friction theory. In this theory, the friction coefficient depends only on the electronic properties of the system, and hence would be the same for all isotopes of the same chemical element. The frictional force is thus proportional to the velocity of the impinging particle, see (2.52). By plotting the energy loss as a function of $(m/m_H)^{-1/2}$, one would therefore expect all data points to fall on a straight line. This also holds in the present, more elaborate theory. The integrated probabilities $N_e$ and $N_h$ of excited carriers above the Schottky barrier are shown in table 4.2, where a barrier height of 0.48 eV has been assumed, typical of experimental Schottky barriers for Ag on Si [22, 76]. Although a higher number of excitations per atom is expected due to oscillations of the adsorbing atoms in the potential well, a number of holes in the order of $10^{-4}$ per impinging atom is calculated, which compares very well with the literature [72, 22]. In FOM, the excitation probabilities are assumed to be Poissonian distributions [27]. All moments of such a distribution are solely determined by its first moment. It follows that all excitation spectra (of different isotopes) for a given chemical species impinging on a given substrate are described by a one-parameter family of curves. Then, a single parameter, e.g. the energy loss $\Delta E$, is sufficient to characterize the spectra completely. Here, it is tested if such a simple description of the spectra also applies to the results of our theory. The scaling properties of $\Delta E$ have already been established above. If one supposes a proportional dependence of the effective temperatures $T_{\text{eff}}$ of the high-energy tail on the total energy loss $\Delta E$, one would expect that (2.57) holds. This would mean that a logarithmic plot of $N_e$ or $N_h$ shows a linear dependence on $(m/m_H)^{1/2}$. Fig. 4.12 demonstrates that this is a good approximation for isotope masses between those of D and $\mathrm{H}_{0.01m_H}$, i.e., it is fair to approximate the energy spectra by a single-parameter family of curves. However, note that a linear dependence on $(m/m_H)^{1/4}$ gives a better fit, cf. Fig. 4.26. The ratio of the integrated probabilities $N_{e/h}$ for H and D atoms is about 3.2. (3.17 if calculated for the excited electrons, 3.21 for the holes, see table 4.2). Experimentally, the hole excitation probabilities are more accessible, since Schottky barriers on p-type silicon can be fabricated with a high quality of the metal-semiconductor interface. The experimental ratio of the yields for H and D for Ag/Si Schottky diodes is $3.7 \pm 0.7$ [72, 22], which agrees well with the results of the perturbative approach of the present work.

## 4.3 Validity of Alternative Theories

In this section the validity of alternative theories is investigated. It is found that the best description of the high-energy tail of the spectra is the perturbative approach presented above.
The section starts with an investigation of the Gunnarsson-Schönhammer approach of section 2.3.2 in section 4.3.1. At first, a short technical discussion is necessary, where a numerical problem (arbitrary phase) is solved. Then results are presented. It is shown that the high-energy tail of the spectra is not described well by this approach. However, the dissipated energy is closer to the results of TDDFT and model calculations [6, 30]. Note that the section uses spin case Ia, as in section 4.2.
Afterwards the different spin cases are investigated: In section 4.3.2 the spin dynamics following section 3.3, spin case Ib, is investigated. While the dissipated energy is larger, the tail of the spectra is described worse than in case Ia. Constraining the spin to its initial value of one, in section 4.3.3 spin case IIa is investigated. It is proven that self-consistency problems alone can not explain the discrepancies of section 4.3.2, since the tail of the spectra are still not described well. In section 4.3.4 the spinless case, IIb, is investigated. It is shown that the dissipated energy is only marginally influenced by the adiabatic spin dynamics of case Ia, when using the perturbative approach.

### 4.3.1 Gunnarsson-Schönhammer-like Perturbation Theory (Spin Case Ia)

Section 2.3.2 describes a theory which makes use of the adiabatic wavefunctions, instead of the unperturbed ones. It has been adapted to DFT calculations in section 3.5, so that it can be implemented in numerical

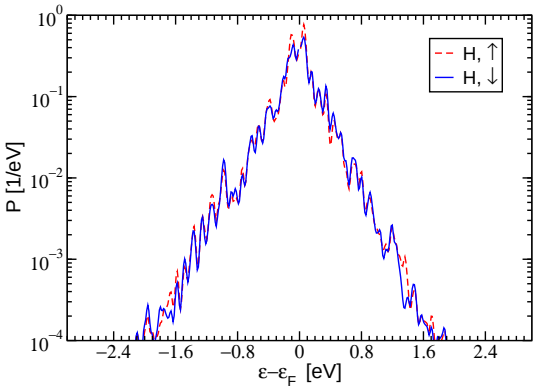


Figure 4.13: Spin-resolved excitation spectrum of electrons and holes for an impinging H atom with an initial kinetic energy of 60 meV on the on-top position of an Al(111) surface after one half round trip in the chemisorption well. The Kohn-Sham states have been phase-corrected following Eq. (4.2). The spectrum is calculated using the Gunnarsson-Schönhammer-like perturbative approach from section 2.3.2. Excitations with energies too small to be numerically certain ($\varepsilon - \varepsilon_{\mathrm{F}} < 0.0136$ eV) have been left out of the calculations.

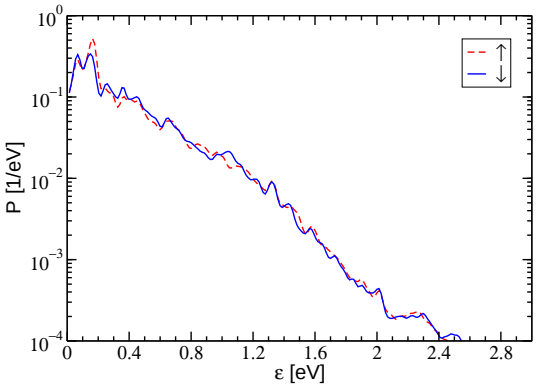


Figure 4.14: Spin-resolved excitation spectrum of the electron-hole pairs for an impinging H atom with an initial kinetic energy of 60 meV on the on-top position of an Al(111) surface after one half round trip in the chemisorption well. The Kohn-Sham states have been phase-corrected following Eq. (4.2). The spectrum is calculated using the Gunnarsson-Schönhammer-like perturbative approach from section 2.3.2. Excitations with energies too small to be numerically certain ($\varepsilon - \varepsilon_{\mathrm{F}} < 0.0136$ eV) have been left out of the calculations.

calculations. The reader is reminded that technical difficulties appear, which are discussed in sections 3.6.2 and 3.6.3. The two major problems are the mapping of the wavefunctions, and the change of the eigenenergies.
In this section, the statement is proven that severe difficulties exist for the Gunnarsson-Schönhammer-like (GS-like) perturbation theory, and it is shown that the results can not explain experimental observations for the high-energy tail of the spectra. However, the low-energy regime may be described better by the GS-like theory. One problem of the mapping is the phase of the Kohn-Sham wavefunctions. At every k-point, every single Kohn-Sham wavefunction has an arbitrary phase. Mapping one onto another, at a different geometry, leads to an arbitrary phase in the calculations of the matrix elements (2.40). Calculation of the temporal integral (2.40) without taking this phase into account is an approximation, which assumes that the influence of this phase on the matrix elements is small. Such an assumption may be correct for purely computational reasons. However, one may take this phase into account, by multiplying the wavefunction at one geometry with a phase correction

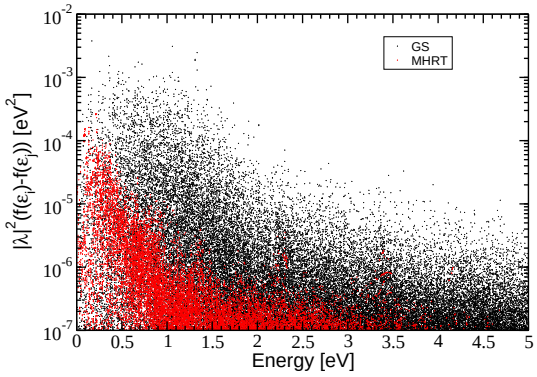


Figure 4.15: Comparison of the squared absolute values of the matrix elements (2.35), times the occupation function $f(\varepsilon_i) - f(\varepsilon_j)$, for the 1st order perturbation theory of section 4.2, labeled MHRT, and the GS-like theory of section 4.3.1. The matrix elements in the MHRT-like case decay much stronger with energy than those in the GS-like case.

factor, which leads to

$$\left|\varepsilon_{i,Q}^{\text{phase-corrected}}\right\rangle = \frac{\left\langle \varepsilon_{i,Q}^{\text{uncorrected}} \middle| \varepsilon_{i,Q-1}^{\text{phase-corrected}} \right\rangle}{\left| \left\langle \varepsilon_{i,Q}^{\text{uncorrected}} \middle| \varepsilon_{i,Q-1}^{\text{phase-corrected}} \right\rangle \right|} \left|\varepsilon_{i,Q}^{\text{uncorrected}}\right\rangle, \tag{4.2}$$

where $Q$ denotes the geometries.
For numerical implementation, a new code version was used, which rests on *PWSCF* V 4.0.5, while the non-phase-corrected GS rests on *PWSCF* V 3.2. Since the interfaces have changed, the code had to be re-programmed from scratch.
For the purpose to show the difficulties and the contradictions to the experiment, Figs. 4.14 and 4.13 show the calculated spectra of electron-hole pairs and of electrons and holes alone using the GS-like perturbation theory. These figures should be compared to Figs. 4.6 and 4.7. The spectra decay much slower with respect to energy, and a difference between spin channels is also not observable. The absence of spin features is in accordance with the results for the perturbative approach of second order in the time-dependent tight binding model [32]. A comparison to literature results, Ref. [30] and references therein, allows to make an important observation: While the calculated spectra within the GS-like perturbation theory decay with an effective temperature of 3000 K for electrons and 2600 K for holes, the literature values are 1380 K (1500 K) for electrons and 1760 K (1600 K) for holes in the Newns-Anderson model and TDDFT approaches, respectively. Thus the effective temperatures are about a factor of two too large in the GS-like perturbative approach. Also the holes are decaying slower in the GS-like perturbation theory, in contract to the literature results, where the electrons are decaying slower.
However, the energy loss during one half round trip for the H atom is 0.072 eV, comparing fairly well to theoretical values from Newns-Anderson model (0.166 eV) and TDDFT calculations (0.104 eV) [6, 30], and thereby being much closer to the TDDFT results than the dissipated energy obtained by the perturbative approach of section 4.2. The low-energy regime of the spectra dominates the dissipated energy. Thus the GS-like approach probably describes the low-energy part of the spectra better.
It is not possible to explain the experimental isotope effect using the calculated spectra in the GS-like perturbation theory: A direct evaluation of the measured currents from the spectra, as done in section 4.2, yields a ratio of detectable particles between hydrogen and deuterium which is 2.3 for holes and 2.6 for electrons. This is beyond the experimental error bars, where a ratio of $3.7 \pm 0.7$ was measured [72, 22].
The difference in the spectra can be traced back to the size of the matrix elements (2.35), times the occupation function $f(\varepsilon_i) - f(\varepsilon_j)$, cf. Eq. (2.39). The quantity $|\lambda_{ij}|^2 (f(\varepsilon_i) - f(\varepsilon_j))$ is denoted the relevant matrix elements here. In the perturbative case of section 4.2 the largest relevant matrix elements are of the order of $10^{-4}$ eV$^2$, and these are concentrated in the e-h pair energy range between 0 and 1 eV, decreasing rapidly with

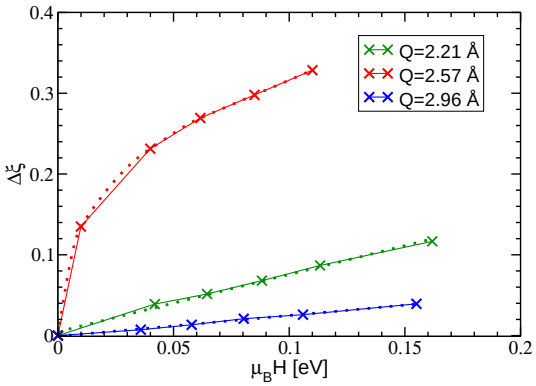


Figure 4.16: Local spin polarization in excess of the adiabatic part $\Delta\xi$ vs. magnetic energy $\mu_B H$, for 3 different positions of the H adsorbate. The middle (green) graph is for a distance of 2.21 Å between adsorbate and substrate. The adsorbate is closer to the surface than the adiabatic spin transition point. The upper (red) graph is for a distance of 2.57 Å, which is at the adiabatic spin transition point. The lowest (blue) graph is for the adsorbate far away from the surface with a distance of 2.96 Å. While there is a nonlinear dependence of the spin polarization for the adsorbate at the adiabatic spin transition point, the spin polarization is linear (with respect to the magnetic field) close to and far away from the surface. Also it requires a much lower magnetic field to change the adsorbate's spin polarization close to the adiabatic spin transition point. The straight lines are a guide to the eye, and the dotted lines are regression curves in the two linear cases and a spline interpolation for the nonlinear case.

energy. In the GS-like case, however, the largest relevant matrix elements are of the order of $10^{-3}$ eV$^2$. The relevant matrix elements are much slower decaying with energy, and matrix elements of the order of $10^{-5}$ eV$^2$ are found even close to e-h pair energies of 5 eV. Fig. 4.15 shows a comparison of both cases.
To evaluate the spectrum (2.39), however using the GS matrix elements, it is necessary to select a geometry where the eigenenergies appearing in that equation are taken from. It was found that the chosen geometry plays a minor role for the spectra, and can certainly not explain the huge discrepancies to the experiment, cf. section 3.6.3. However, the naive conclusion that the GS-like perturbation theory is not applicable here seems unlikely, as MHRT should be a limiting case of the GS-like approach. Instead, the characteristics of the matrix elements hint towards the fact that the mapping of the wavefunctions is inherently flawed, cf. section 3.6.2. It is thus proposed to avoid the suggested mapping.
While the high-energy tail of the spectra is not described satisfyingly by the GS-like approach, the dissipated energy is closer to other theoretical results. Thus the low-energy part of the spectra, which dominates the dissipated energy, may be described better by the GS-like approach. In this work, the main focus is on the high-energy tail of the spectra, mainly due to its experimental accessibility. Thus this approach was not investigated further.

### 4.3.2 Spin Case Ib: Nonadiabatic Spin Transition

In Fig. 4.4 the adiabatic spin transition from adiabatic calculations of the ground state is shown. However, the spin transition depicted in the figure leads to divergencies in the theory of electronic friction [27]. It is possible to include a nonadiabatic spin dynamics via a nonadiabatic spin transition as presented in section 3.3. Such a nonadiabatic 'smooth' spin transition is defined within the present work as the transition from the spin-polarized case to the unpolarized case, and does not necessarily include divergencies.
The dynamics requires knowledge of the dependence of $H(\xi_{ads} - \xi_{ads}^{\text{adiabatic}})$. This was calculated as follows: The system is the same as in section 4.2, but the total number of spin up and spin down electrons is constrained in the calculations. The wavefunctions are relaxed until self-consistency is reached. It is then possible to calculate the adsorbate's spin polarization $\xi_{ads}$ of the adsorbate through Eq. (3.14). In the constrained calculations, separate Fermi energies for the spin up and spin down electrons are given. It is thus possible to define the

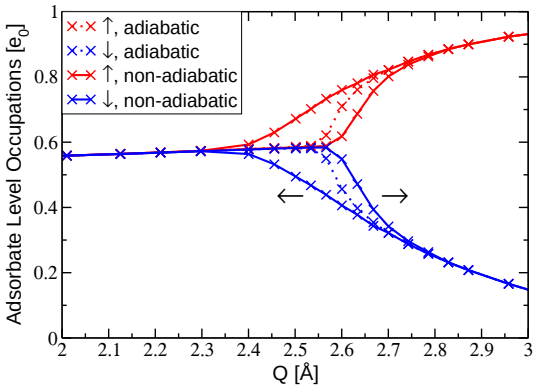


Figure 4.17: Occupation of the spin up and spin down states of an approaching H atom with an incident kinetic energy of 60 meV vs. its distance from an Al(111) surface in the nonadiabatic case. Far away from the surface there is a local spin polarization of the adsorbate of approximately 1, which will eventually become 0 somewhere after the adibatic spin transition point, where it vanishes in the adiabatic case (dotted lines). A $\sqrt{Q}$-dependence of the polarization can be observed. The nonadiabatic behavior smears this transition out over a certain range of about 0.3 Å.

magnetic field through Eq. (3.17). Results for the system H/Al(111) are shown in Fig. 4.16. One observes that the behavior of the magnetic field with respect to the excess spin polarization $\Delta\xi$ is nonlinear around the adiabatic spin transition point, and approximately linear far way from it.
To calculate the local non-adiabatic spin polarization requires knowledge of the adsorbate's velocity, according to Eq. (3.26). The velocity is nearly unperturbed by energy dissipation into the electronic system in the trajectory approximation. Thus it may be directly taken from adiabatic calculations.
The result for the nonadiabatic occupation of the adsorbate's orbital for a full round trip is shown in Fig. 4.17. Comparing this result to the literature [6, 30], one finds that for the way towards the surface the agreement is very good quantitatively. For the way back the agreement is not good, however.
This nonadiabatic reoccupation of the Kohn-Sham states, following Eq. (3.24), is then used to calculate the effective potential, and the spectra in the perturbative approach. The result for the dissipated energy is 0.035 eV for hydrogen in spin case Ib, in contrast to 0.023 eV in spin case Ia. The result for the spectrum is shown in Fig. 4.18 for hydrogen, where it is compared to the spectrum without reoccupation, Fig. 4.6. In the energy range below 0.5 eV from the Fermi energy the spectrum is similar in both cases. After this energy an underlying structure appears, which decays differently. Investigation of the isotope effect for the nonadiabatic reoccupation showed that it can not explain the experimental values, since the high-energy tail is very similar for H and D adsorption. The probable reason was already explained in section 3.6.1. There it was mentioned that a localized reoccupation of only the adsorbate orbitals is very difficult to implement in a plane-wave approach.
Note that the non-selfconsistency is not the only or main reason for failure. To prove this, a self-consistent scheme, without taking into account the spin dynamics, is investigated in section 4.3.3.

### 4.3.3 Spin Case IIa: Constrained Spin Polarization

A much simpler approach to deal with the nonadiabatic spin transition than presented in section 4.3.2 is the constrained spin approach. The purpose of this approach is to get a spin transition which does not show the observed $\sqrt{Q}$-behavior observed in Fig. 4.4. This approach has been used before for the electronic friction approach in order to work around the problem that the $\sqrt{Q}$-behavior leads to an infinite friction coefficient in DFT calculations [5]. Its main idea is to constrain the spin of the whole system. In order to achieve this, the spin polarization of the adatom far away from the surface is assumed to be correct, in this case defining a spin polarization of the total system of 1. The spin polarization of the total system is the constraint for all subsequent calculations. While the adatom is far away from the surface, this does not lead to notable changes in

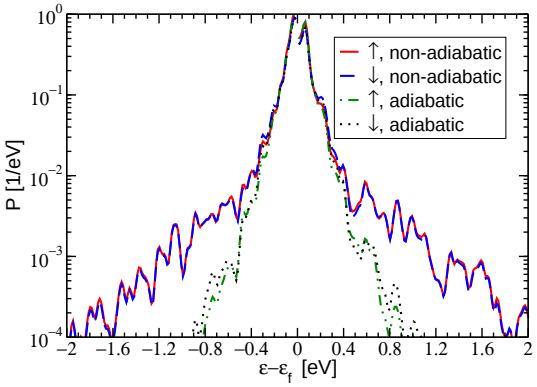


Figure 4.18: Spin-resolved excitation spectrum of electrons and holes for an impinging H atom with an initial kinetic energy of 60 meV on the on-top position of an Al(111) surface after one half round trip in the chemisorption well, demonstrating the effect of a nonadiabatic occupation of the wavefunctions. The solid lines show the spectrum when including reoccupation of the adiabatic wavefunctions, and the dotted lines show the spectrum without reoccupation (taken from Fig. 4.6). Excitations with energies in the range of the smearing parameter ($\varepsilon < 0.0136$ eV) have been left out of the calculations. There is nearly no effect of the reoccupation when taking a look at the low-energy part of the spectrum, where the values of $P(\varepsilon)$ are large in comparison to those at high energies. The effect of the reoccupation is obvious at the tails of the spectra, where there seems to appear an underlying structure, which has a different decay than the low-energy part.

the calculations. Close to the surface there is no local spin polarization of the adatom, but the spin polarization is spread over the whole slab. Close to the adiabatic spin transition point, however, there is a small area in which the adsorbate's local spin polarization is reduced smoothly (in contrast to the abrupt transition shown in Fig. 4.4). In TDDFT calculations the total spin has also been constrained, introducing a broken symmetry [6]. The main purpose for the constraint in TDDFT calculations was, however, not the unphysical result of the spin polarization vanishing with a $\sqrt{Q}$-behavior. Instead it was necessary for numerical definiteness of the calculations.

As intended, this approach leads to a smooth spin transition scheme, shown in Fig. 4.19. One can observe the smooth transition around the adiabatic spin transition point. With the $\sqrt{Q}$-like behavior missing, there is no divergence in the derivative of the effective potential any more. However, the spin now survives longer on its way towards the surface. This results in a larger energy dissipation due to a comparatively larger change of the potential over a wider area (in contrast to a sharp peak close to the transition point), see Fig. 4.20. This also has consequences for the decay of electron and hole spectra. The newly derived spectra are shown in Fig. 4.21 for different isotopes.

Although fitted temperatures are now closer to the experimental values, they can still be changed over a wide range by varying the fitting window. Therefore the excitation probability over the Schottky barrier is still the better way to compare experimental and theoretical results. Unfortunately, it is now no longer possible to explain the experimental isotope effect: The detection ratios for holes (with an energy larger than 0.48 eV) with respect to H are $1.76$, $8.06$, and $32.39$, for the isotopes D, $\mathrm{H}_{0.1m_H}$ and $\mathrm{H}_{0.01m_H}$, respectively. If self-consistency alone could explain the inability of the nonadiabatic reoccupation scheme of section 4.3.2, spin case Ib, to describe the experimentally measured isotope effect, the approach of the present section, spin case IIa, should be able to calculate this effect within experimental error bars, as was done in section 4.2 for spin case Ia. However, this is not the case. Thus neglection of self-consistency alone is not responsible for failure of the nonadiabatic reoccupation scheme of section 4.3.2.

The squared absolute values of the matrix elements (2.35) of the unperturbed case of section 4.2 and this section, times the occupation function $f(\varepsilon_i) - f(\varepsilon_j)$, are compared in Fig. 4.22. It is shown that the matrix elements of the unconstrained case decay much faster with respect to energy than in the constrained case.

This result is interpreted in the way that the delocalization the spin plays an important role: When constraining

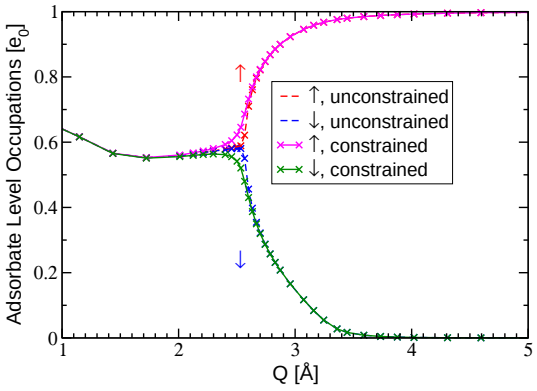


Figure 4.19: Ground-state occupation of the spin-up and spin-down orbital of an approaching H atom vs. its distance from an Al(111) surface. Compared are the case of a system with total spin polarization constrained to the initial value, and the unconstrained case. Far away from the surface, the electronic charge at the H atom, corresponding to one electron, is fully spin-polarized in both cases. Both spin-up and spin-down orbitals become equally populated after a spin transition point. In the unconstrained case, there is a sharp $\sqrt{Q}$-behavior close to the adiabatic transition point, in the constrained case this transition is smeared out.

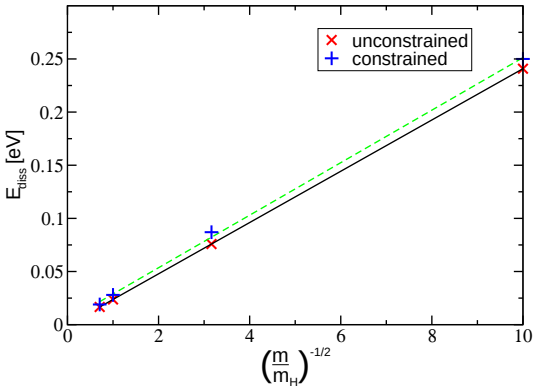


Figure 4.20: Total energy loss vs. the mass scaling parameter $1/\sqrt{m/m_H}$. $m$ denotes the mass of the adsorbing atom. Compared are the case of a system with total spin polarization constrained to the initial value and the unconstrained case. The lines are linear fits to the data. The energy loss for the constrained case is systematically higher than for the unconstrained case.

the total spin of the system, part of it will spread over the whole slab, leading to small perturbations of the effective potential within the slab when the adsorbate is approaching the surface. This results in small excitations, observable in Fig. 4.22 through the large-energy matrix elements, leading to a background signal in the spectrum. In TDDFT calculations this signal does not appear, because the spin is more localized at the surface, when the particle approaches the surface rapidly.

The results of the spin-constrained approach still shows no relevant sign of spin-dependent features in the spectra. However, this section, in conjunction with section 4.3.2, is able to explain partially the important difference in the total energy loss per round trip between spin-polarized TDDFT results [6] and the perturbative approach of this work: If the spin polarization exists closer to the surface, this has the consequence of larger changes of the effective potential there. Thus the difference in the total energy loss per round trip between Ref. [6] and this work (Fig. 4.11) can partially be explained through the existence of a spin polarization closer to the surface in the TDDFT case. However, since the perturbative approach is not valid for the low-energy regime of the spectra, this will also play an important role. Here the GS-like approach may be better. Assuming an additional energy dissipation of 50 % due to the nonadiabatic spin transition, following the results of section 4.3.2, the GS-like approach should result in an energy loss of roughly 0.1 eV for the half round trip, which is the number

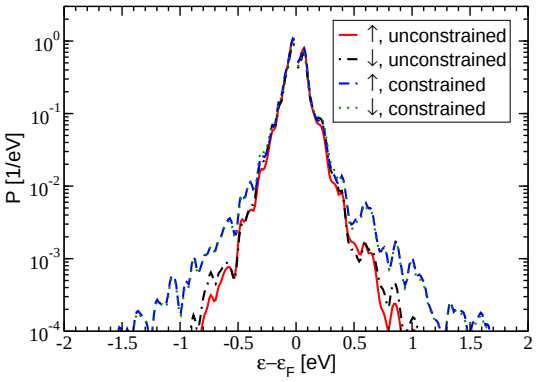


Figure 4.21: Spin-resolved excitation spectra of electrons (positive energies) and holes (negative energies) for an impinging H atom with an initial kinetic energy of 60 meV on the on-top position of an Al(111) surface after one half round trip in the chemisorption well. Compared are the case of a system with total spin polarization constrained to the initial value, and the unconstrained case. Both spectra look qualitatively similar, but a slower decay of the flanks can be observed in the unconstrained case. Values close to the Fermi energy ($|\varepsilon - \varepsilon_F| < 0.0136$ eV) are not plotted because of numerical inaccuracies in this energy range.

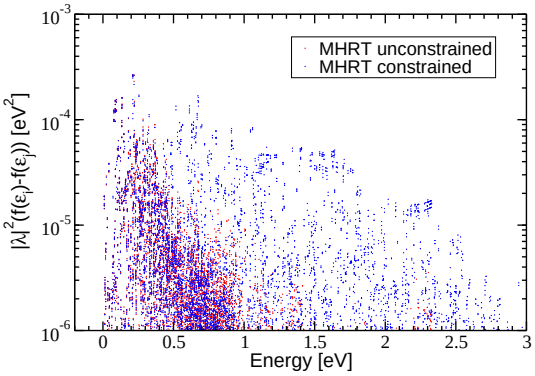


Figure 4.22: Comparison of the squared absolute values of the matrix elements (2.35), times the occupation function $f(\varepsilon_i) - f(\varepsilon_j)$, for the 1st order perturbation theory of section 4.2, labeled MHRT unconstrained, and the constrained theory of section 4.3.3. The matrix elements in the unconstrained case decay much stronger with energy than those in the constrained case.

from TDDFT calculations.
One may conclude that, if one had a description of the spin polarization resembling the TDDFT case, the total energy loss would be much larger in the perturbative approach, too. From TDDFT results one gets a factor of three to four for the dissipated energy between the spin-polarized and unpolarized case [6, 63]. In section 4.3.2 a difference of 50 % was found. Therefore the present theory is probably sufficient to describe the high-energy tails of the spectra, with the possible exception of spin effects.

### 4.3.4 Spin Case IIb: Spin Unpolarized System

Having discussed the effects of constrained spin polarization calculations on the spectra, the question arises what happens, when there is no spin in DFT calculations, i.e. to what amount is the effective potential determined by the difference in the spin channels.
In order to answer this question, the DFT chemisorption potential was calculated without using the spin-density approximation; this means without introducing the spin degree of freedom in DFT calculations. The result is

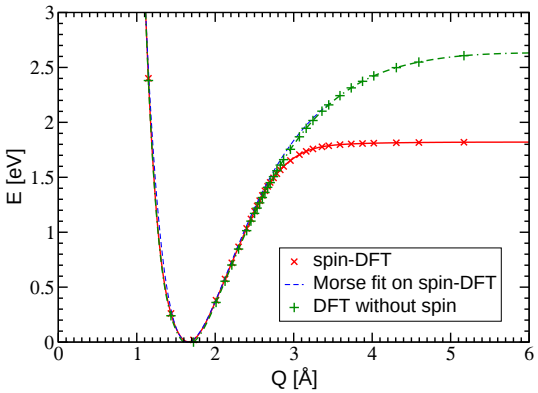


Figure 4.23: Comparison of the chemisorption potentials of an H atom above the on-top position of an Al(111) surface in the spin-DFT and spinless DFT case. Both potentials merge around 2.8 Å, while the spin polarization in the spin-DFT calculations vanishes at about 2.6 Å. Shown is also a fit on the spin-DFT potential for the chemisorption well. This fit falls nearly on-top the spinless DFT potential.

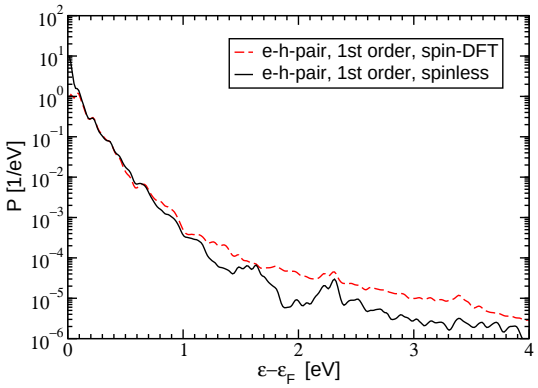


Figure 4.24: Comparison of the e-h pair spectra on the spin-DFT and spinless DFT case. Although the initial energy in the spinless DFT case is slightly larger for the investigated trajectory, the excitation probability of e-h pairs is larger in the spin-DFT case for high energies. Both spectra are similar on this scale.

shown in Fig. 4.23. Compared is the calculated 'spinless' potential to the GGSDA result of Fig. 4.3. One observes that the fit to the Morse potential for the potential well of Fig. 4.3 describes the whole chemisorption curve in the non-GGSDA case. While there are differences between the spin-DFT and spinless DFT case in the total energy further away from the surface, when electron-hole pair excitations are improbable, close to the surface both calculations yield very similar results. One may expect that this has the consequence that the spin plays a minor role for the excited electron-hole pairs.

However, a straightforward comparison of the spin-DFT and spinless DFT results by just calculating the trajectory in the spinless chemisorption well, and then applying perturbation theory, is not advisable, since the velocity in the wells will be different then. So the results will be dominated by the different velocity of the hydrogen atom in the chemisorption well. This comparison, however, is not the goal of this section, and does not answer the question whether the spin plays an important role: If the only difference is due to a change of velocity in the chemisorption well, then the spin is only important to calculate the forces on the adsorbate, but not in any other respect.

Instead, the adsorbing H atom was put at the same starting position and the same starting velocity in the chemisorption well as in the spin-DFT case. The potential energies in the spin-DFT and spinless DFT case are similar at the starting position Q=3.16Å, with a difference of just 0.2 eV in favor of the spin-DFT case, instead of 0.8 eV at $Q = 6$Å. The trajectory and electron-hole pair spectra, as well as the total energy dissipated into

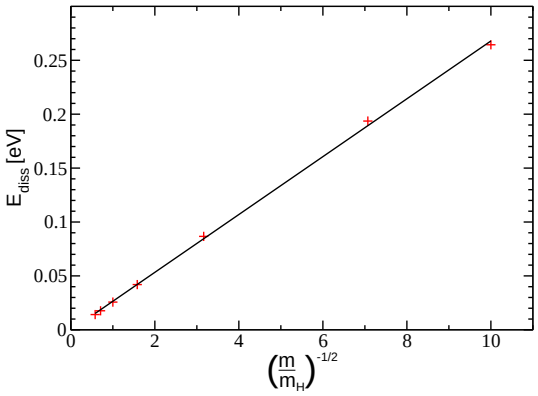


Figure 4.25: Total energy loss per half round trip in the chemisorption well vs. the mass scaling parameter $1/\sqrt{m/m_H}$. $m$ denotes the mass of the adsorbing atom. The dissipated energy is shown in the case of spinless DFT. Fig. 4.11 shows the corresponding graph in the spin-DFT case.

the electronic system, were then calculated as in section 4.2. The electron-hole pair spectra for the spinless and spin-containing case are compared in Fig. 4.24. One observes that both spectra are practically on-top each other on the shown scale.
The dissipated energy for the spinless DFT case is shown in Fig. 4.25. The corresponding graph for the spin-DFT case is Fig. 4.11. Both graphs are very similar.
One must conclude that the (possibly unphysical) spin transition of spin case Ia does not dominate the dissipated energy. Instead, the spin plays a minor role for it, and electron-electron interaction is more important. However, results from TDDFT of Refs. [6, 63] show that the spin dynamics is indeed essential for the dissipated energy, since a factor three to four for the energy loss appears between the unpolarized and spin-polarized calculations, with the dissipation in the spin-polarized case being larger. This point was investigated in sections 4.3.2 and 4.3.3, spin cases Ib and IIa. The energy loss is systematically larger in both cases than in spin case Ia. Thus the increase in the dissipated energy can partially be traced back towards the influence of the spin dynamics on the effective potential close to the surface: If the spin polarization of the adsorbate changes close to the surface, the dissipated energy is larger. Therefore a *nonadiabatic* treatment of the spin dynamics leads to an increase in the energy dissipation.

## 4.4 Discussion

At present, the possibilities to test the present results against experiment are rather limited. Quantitative comparison is possible so far only for the isotope effect: Here, the results of the perturbative approach for Al are in good agreement with the measurements using Ag/Si-Schottky diodes [72, 22] and MIM sensors [3]. Some experimental information is also available about the slopes of the excitation spectra from measurements with Schottky diodes made from the same material but with slightly different *I-V*-characteristics. The temperatures estimated from these measurements are in reasonable agreement with the slopes of the calculated spectra. However, the author is quite sceptical whether a single temperature would still be a good description if one had better experimental access to the spectrum.
A more detailed comparison of the present results is possible with previous TDDFT calculations for the same system, H on Al(111). In non-spinpolarized calculations, a total energy loss of 30 meV and 40 meV was found after a half and a full round trip, respectively [63]. This is in reasonable agreement with the values of 23 meV and 46 meV calculated in the perturbative approach of this work. In addition, the linear dependence of the energy loss on the mass scaling parameter (cf. Fig. 4.11), and the effective temperatures of the spectra (cf. Tab. 4.1) obtained in both theories are consistent. However, more recent spin-polarized TDDFT calculations yielded energy losses of about 100 meV and 185 meV for the half and full round trip, respectively [6]. These findings

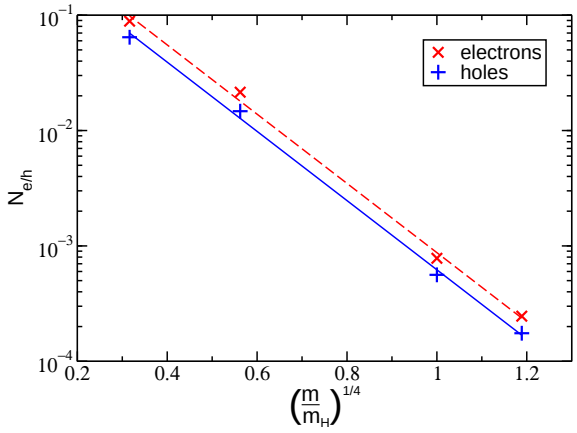


Figure 4.26: Yield of the electron (red, upper curve) and hole (blue, lower curve) excitation spectra plotted versus the scaling variable $(m/m_H)^{1/4}$ for the system H/Al(111). $m$ denotes the mass of the adsorbing atom. The lines are linear fits to the data.

from the TDDFT calculations suggest that the spin transition is quite important for the energy loss. While the perturbative approach of this work in principle includes the spin transition, it seems to underestimate its role in the energy dissipation. This was investigated in section 4.3.4, where it was shown that the spin plays a minor role for the total energy dissipation and the spectra in the perturbative approach, if the spin dynamics of the H atom follows the adiabatic dynamics (case Ia). Calculations using a smoothened and delayed spin transition (similar to the findings of Ref. [6]) instead of an abrupt one show a higher energy loss in perturbation theory, too, see sections 4.3.2 and 4.3.3. Such a smooth spin transition does not lead to spin-dependent features in the excitation spectra in the perturbative approach, but has the consequence of a larger energy loss. It is probable that the larger energy loss in recent TDDFT calculations is partially caused by the spin polarization existing closer to the surface, which is due to the nonadiabatic description of the spin transition. However, the perturbative approach is only valid for the high-energy tail of the spectra, while the GS-like approach is probably better for the low-energy regime of the spectra. The low-energy regime dominates the dissipated energy. In the spin-polarized case this probably plays a more important role than in the unpolarized case, and accounts for the other part of the difference in the energy loss.

Both a perturbative (non self-consistent) approach for a smoother spin transition and a non-perturbative approach using constrained total spin lead to the appearance of a background contribution in the spectra. This is a strong hint towards the explanation that, in standard DFT, the spin must be localized at the adsorbate in order to get a correct description of the nonadiabatic transition.

In the TDDFT calculations, it was assumed for technical reasons that the total spin polarization (integrated over both the hydrogen atom and the substrate) is conserved, while in the ground-state DFT calculations of this work (section 4.2) the total spin polarization changes from about one electron for the hydrogen far away from the surface to zero after hydrogen adsorption. In accordance with section 4.3.3 this methodological difference could not explain why an energy shift between the spin-up and spin-down spectra is found in Ref. [6] after a half round trip, while the spectra of this work are almost identical for both spins. However, this discrepancy does not arise after a full round trip, where spin-dependent features are absent in both methods. This gives rise to the question, how much of these effects are introduced by the numerical method to calculate the spectra, and how much describe real physics. In recent publications it was shown, that the spin is not described accurately within the framework of DFT when using present-day XC functionals, cf. Ref. [38] and references therein. In an accurate quantum mechanical description a superposition of H atomic orbitals only differing in the spin quantum number should give the same energy, provided normalization is taken into account. Consequently this must be true for the superposition of spin up and spin down densities within the framework of DFT as well. However, for present-day XC functionals this is not the case. So a correct description of the spin is not possible with present-day XC functionals. Since the experiments are done without prescribing a preferred

spin direction, which in turn leads to an unpolarized atomic beam, electronic excitation spectra will show no spin-dependent features. However, in DFT calculations a spin polarization necessarily occurs, if one wants to calculate chemisorption energies correctly, thereby defining a preferred spin direction. The reason behind this is found in the foundations of DFT: In principle, there exists no 'small parameter' of any kind, which justifies the spin density approximation [33]. It is only justified by comparison with the experiment. However, in the case of atomic adsorption, one treats two very different cases. One case is the atom far away from the surface. In this case, the energy is described well by spin-DFT. However, one must be careful when interpreting the Kohn-Sham wavefunctions at this point in terms of quantum mechanical observables, like the spin. It is this case, where previous work has shown that present-day XC functionals fail [38]. Another point is, that describing atoms using DFT is difficult. Taken together, the case 'adsorbate far away from the surface' is not very well defined within the framework of DFT, especially when using GGSDA or LDA, although the calculated energy is closer to experimental findings.
On the other hand, when the adsorbate is close to the surface, its electrons are in the (nearly) free electron gas of the metal. For this case the spin density approximation was introduced. It is rather obvious that one should not trust a straighforward interpretation of the calculational results with respect to spin, when considering a transition between these two cases. So the spin effects found in previous works can be an artifact of a failure of present-day XC-functionals. Even if one had a spin-polarized atomic beam in the experiments, present-day XC-functionals might not be well-suited to describe it correctly, due to the aforementioned problems.
Another explanation of the spin features in different publications is possible by taking into account the different definitions of excitations. While this work calculates excitations directly, Refs. [6, 30] calculate them by comparing a nonadiabatic occupation of wavefunctions with the adiabatic case. Especially close to the surface spin-dependent features may be present for such a definition which rely on reversible changes of the electronic structure during adsorption, but are not, strictly spoken, excitations. While the present theory describes a clean surface, which is perturbed by an approaching adsorbate, this other definition describes surfaces with an adsorbate, where electronic excitations have been introduced. When the adsorbate moves back from the surface again, spin-dependent features may disappear, due to these reversible changes. Such reversible changes were observed in recent calculations for H on silicon [25]. The author believes that such a behavior is observed in TDDFT calculations. However, the definition of excitations within this work gives the correct limit if the particle is scattered back into the gas phase. The alternative approaches try to include some of the localized electronic excitation that results from forming a chemical bond between substrate and adsorbate. This point is also discussed in section 5.4 for the system H/K(110).
The present results may also be compared to earlier work on H/Cu(111) using the electronic friction / forced oscillator formalism [5, 26, 27], described in section 2.5. This theory assumes that the energy loss proceeds through multiple excitation of very small energy quanta, with the excitation energy of a single quantum ultimately tending to zero. Note that the total energy loss remains finite in this limit. Under this assumption, the energy loss due to friction can be described by an instantaneous friction force in each moment of time, and the materials properties of the substrate only need to be known in vicinity of the Fermi energy in order to calculate the friction coefficient. This is different from the present approach, where the probability to deposit a finite amount of energy to the substrate within a single excitation is calculated. In order to obtain the excitation spectra from the electronic friction approach, additional assumptions need to be made, such as the separability of matrix elements, and the statistical independence of multiple excitations. The spectra (for H/Cu(111)) obtained after making these approximations are essentially exponential distributions. The present results from first-order perturbation theory are qualitatively similar, but cannot be fit by a single exponential. This implies that the picture of multiple excitations made up from energy quanta close to zero may be an oversimplification. This point is investigated in chapter 5, too, and it is found, that the forced oscillator model is not justified.
The functional relationship between the excitation yield above the Schottky barrier and the isotope mass, Eq. (3.8), is discussed now. For the system H/Al(111) it was shown that the data is compatible with (3.8), where $\gamma = 1/2$, cf. Fig. 4.12. For H/K(110), in chapter 5 it is found that $\gamma = 1/6$ describes the data well. This motivated the author to re-visit the results for H/Al(111). While in section 4.2 the goal was to show that FOM scaling (i.e. $\gamma = 1/2$, Eq. (2.57)) is compatible with the data, which is still correct, it is found that $\gamma = 1/4$

describes the data better, see Fig. 4.26. Thus, the FOM does not apply to H/Al(111). It is noted that previous work [63] claiming FOM scaling for H/Al(111) is not conclusive in this respect, since the large error bars of the numerical data presented there are compatible with a wide range of possible values for $\gamma$. This is also true for Fig. 4.9.
Taking into account results for H/K(110), a thorough discussion of this point is found in section 5.4.
It is noted that a connection between the electronic friction and the perturbative approach can be made on the basis of the overall energy loss per round trip they predict. From the more detailed spectra obtained from the present approach, it is in principle possible to determine *a posteriori* an effective friction coefficient that would lead to the same amount of energy loss as obtained by integrating over our excitation spectra. This effective friction coefficient could then be used to re-run the trajectory to obtain new spectra, and the procedure could be iterated until consistency between the energy loss of the trajectory and the loss implied by the spectra has been reached.
Recently, non-adiabatic effects in adsorption have been studied in the framework of a time-dependent Newns-Anderson model treated in mean-field approximation [28, 29, 30, 31]. While this model is originally motivated by the surface chemistry of transition metals and noble metals, it may still make sense to compare the results to the present calculations for H on Al(111). The model requires a fit to the data supplied by DFT calculations, i.e. the projected density of states onto the H orbitals. In Ref. [30], spectra for H/Al(111) were obtained that show clear differences between electrons and holes, and between both spin orientations. However, the results are rather sensitive to the model parameters. One can observe that the parametrization of the values needed for the model calculations does not fit perfectly. This is especially the case far away from the surface where ionization and affinity level of H are about equally far below or above the Fermi energy of Al [30]. For this case, electron and hole spectra are predicted that are approximately equal. The spectra then have no important spin characteristics, cf. Ref. [31] for metals other than Aluminium. The author believes that it can be justified to argue that H on Al(111) also corresponds, in the language of this model, to such a system, so that one would expect electron and hole spectra that are approximately equal. This is found in the present calculations, too. However, the Newns-Anderson model also predicts that electron and hole spectra may be strongly different for other combinations of substrate and adsorbate. In order to probe the different regions of the parameter space of the Newns-Anderson model discussed in Ref. [29], i.e., strongly electronegative or electropositive adsorbates, additional DFT studies for such material systems would be desirable.

## 4.5 Conclusions

In this chapter, a first-order time-dependent perturbation theory was implemented to calculate excitation spectra of electrons and holes in a metal substrate due to non-adiabatic effects in adsorption, starting from the ground-state electronic potential and wavefunctions obtained from density functional theory. The calculated results for adsorption of hydrogen on aluminium are consistent with the experimental data obtained for hydrogen on noble metals. In particular, the present theory reproduces the observed isotope effect. In contrast to the electronic friction formalism, the present approach includes excitations over finite energy differences, and thus takes the effects of single-particle band structure into account in the excitation spectra.
The results of the perturbative approach are in agreement with results from the (computationally much more demanding) TDDFT method, with the notable exception of spin effects. On the other hand, the perturbative approach is much faster and affordable for a wider range of systems, as it requires only ground-state DFT calculations. These calculations are widely used in the scientific community, e.g. in the calculation of potential energy surfaces within the Born-Oppenheimer approximation.
So it is concluded that this description gives rise to hopes for a simple and affordable possibility to calculate electronic excitation spectra for moving particles, without using oversimplifying approximations. The author also speculates that this description is able to overcome its problems when using localized orbitals for localized dynamic effects, e.g. the spin transition.
Whether or not spin-dependent features are present in experiments is still under debate. Even if a spin-polarized atomic beam existed in the experiments, it is not a foregone conclusion that present-day DFT calculations de-

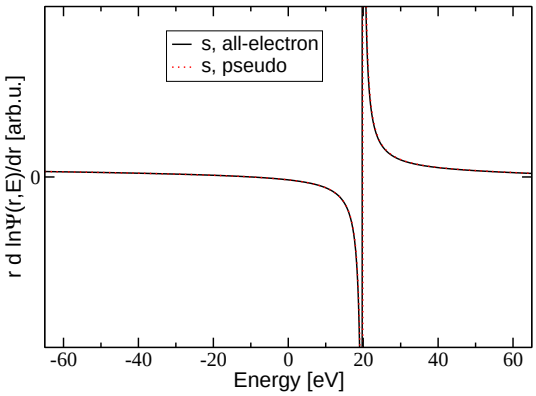


Figure 4.27: Comparison of the logarithmic derivatives of the all-electron and pseudo wavefunctions for the H pseudopotential. This energy range of validity of the pseudopotential is not truncated here, since the pseudopotential is the same as the all-electron potential after a cutoff radius of 0.53 Å (1 bohr).

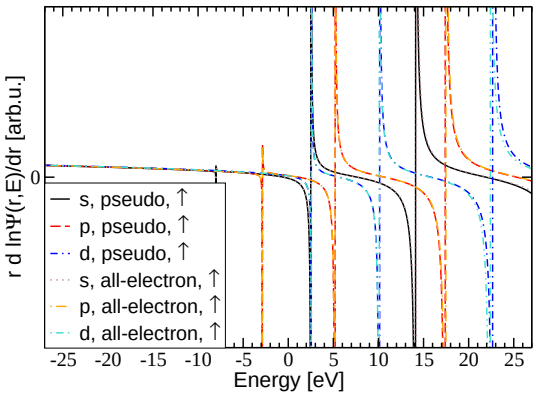


Figure 4.28: Comparison of the logarithmic derivatives of the all-electron and pseudo wavefunctions for the Al pseudopotential. The comparison was done using a spin-polarized calculation. For simplicity of the figure, only the spin-up part is shown. The spin-down part is very similar. Over a range of approximately 30 eV, between -9 and 21 eV, the logarithmic derivatives of both wavefunctions are on-top each other. This gives an approximation for the energy range of validity of the pseudopotential.

scribe this experiment correctly. Due to the different definitions of electronic excitations in the several approaches, it may well be that spin-dependent features of the spectra are artifacts of these definitions. Thus reversible effects may be regarded as measurable electronic excitations in other approaches. Since the present theory avoids such problems, the author believes it is thus better suited to describe measurable excitations.
While this chapter investigated the spin transition and different perturbative approaches to calculate electronic excitations, in the forthcoming chapters the atomic isotope effect and effects of the bandstructure are investigated more thoroughly.
In most theoretical approaches, the atomic band structure is not taken into account, when using the wide-band limit. The present approach includes it by definition.
Since the isotope effect is currently the best test of theoretical approaches, and the best way to compare to experiments, the author believes that any theory of electronic excitations should describe it well. It is proposed that theoretical approaches should be tested by this effect, and be compared on the basis whether they can describe it.

## Appendix 4.A Pseudopotential Generation and Tests

An elaborate description of the generation of a pseudopotential can be found in section 5.A. In the present section the most relevant facts are mentioned for the pseudopotential generation for H, and the tests for the H and Al pseudopotentials. For H a PBE-GGA [39] pseudopotential was constructed, using the *atomic* code of the PWSCF package [41]. Only the (1s) orbital was taken into account for the pseudopotential, and is therefore the local potential, since non-local parts are nonexistent. The pseudopotential was constructed following the Rappe-Rabe-Kaxiras-Joannopoulos (RRKJ) scheme [77]. The scalar-relativistic method was used for the generation of the pseudopotential. A radial cutoff of 0.53 Å (1.00 bohr) was chosen.
In Fig. 4.27 the logarithmic derivatives of the all-electron wavefunctions are compared to the logarithmic derivatives of the pseudo wavefunctions, for a radius of 0.8 Å (1.5 bohr). They are on-top each other over the total range printed here. Therefore problems for the range of validity from this pseudopotential are not expected. By definition the slope of the pseudopotential is the same as a simple 1/r potential after the radial cutoff. Besides reducing the plane-wave energy cutoff for the calculations, there is no notable effect of the pseudopotential. However, a simple 1/r potential is not envisioned in the code, which is the reason why a pseudopotential was used at all. The Al pseudopotential was downloaded from the *PWSCF* website [41], named 'Al.pbe-rrkj.UPF'.
To determine the energy range of validity, the logarithmic derivatives of the all-electron wavefunctions are compared to the logarithmic derivatives of the pseudo wavefunctions in Fig. 4.28. The calculations of the derivatives were done using a spin-polarized calculation. For reasons of simplicity only the spin-up part of the results is shown in the figure. The spin-down part of the figure is very similar, and does not give new insight here, but the infinities of the derivatives are located at slightly different energies, with a distance of a few eV. Over an energy range of 30 eV, between -9 eV and 21 eV, in both the spin-up and the spin-down cases, the logarithmic derivatives are on-top each other, giving an approximation for the energy range of validity, i.e. transferability, of the pseudopotential.

# Chapter 5

# Results: H on K(110)

In chapter 3 a new approach to calculate excitation spectra in adsorption was introduced. The approach was tested and investigated in chapter 4. Some possible variations of the presented method were tested, compared to previous theoretical approaches, and it was concluded that the new perturbative method can explain the experimental data. While the developed method incorporates effects of the bandwidth of the conduction band, the order of magnitude of such effects is unknown. This is investigated in this chapter. Since the role of a highly reactive substrate, such as K, for chemicurrents is elusive, the perturbative method is extended to H/K, and compared to results for H adsorption on Al, chapter 4.

In most chemicurrent experiments, the kinetic energy of the adsorbing particle is small, of the order of a few 10 meV. The potential energy of the adsorbate is dominating. It is determined by the chemical binding energy, i.e. the depth of the chemisorption well, which is of the order of 1 eV. Hence the adsorbing particle's velocity in the chemisorption well is determined by its mass and the chemical binding energy.

To date, the experimentally determined dependence of the measured chemicurrent on the isotope mass is the only reliable test of theoretical approaches to chemicurrents. Therefore the influence of the isotope mass on the detected chemicurrent is of considerable interest, and should be described well by theories. In order to predict the order of magnitude of the chemicurrent for adsorbates of different mass, two major scenarios can be imagined: In one scenario, a general scaling law exists for a wide range of adsorbates and substrates, where the chemicurrent is only dependent on the mass of the adsorbate, but independent on the exact chemical properties of the adsorbate-substrate-system. In the other scenario, the detected chemicurrent is strongly dependent on the chemical properties of the investigated system, and no general law can be found. Whatever scenario is true, the importance of the electronic energy dissipation channel for the total energy dissipation is strongly dependent on the answer to this question.

Currently, the forced oscillator model (FOM) is the theoretical description of the chemicurrent usually employed by experimentalists [65]. Here, measured currents for H systems are scaled using the root of the adsorbate's mass [27, 63], see section 2.5. Obviously, the use of FOM is justified only if a scaling law exists, and if FOM describes this law correctly.

Recent experimental studies of Mg adsorption on a Mg surface [65] have shown that even for systems, where the adsorbate has a comparatively large mass, and hence a low velocity in the chemisorption well, a chemicurrent can be measured. The chemicurrent measured is approximately two orders of magnitude larger than was expected from a FOM extrapolation of the measured currents for hydrogen adsorption on metal surfaces [72, 22]. Larger chemicurrents than expected might have various reasons, e.g. different excitation mechanisms, one of them being charge transfer. For heterogeneous systems, especially adsorption of highly reactive molecules, such as $O_2$, on reactive alkali, this may indeed be the case. However, in homonuclear systems, such as Mg/Mg, no charge transfer is to be expected between substrate and adsorbate. In this chapter, it is found that the simple extrapolation of the detected chemicurrent using the FOM does not work, and instead a weaker dependence of the chemicurrent on the particle's mass is found. This results in the prediction of larger chemicurrent for particles with large masses.

As a second point in this chapter, the effect of the band structure on the isotope effect is investigated. In order

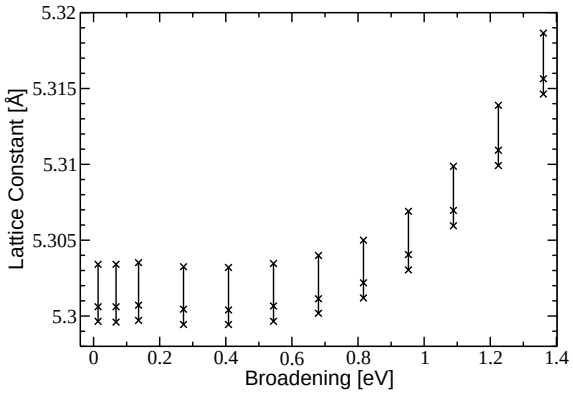


Figure 5.1: Convergence tests for K pseudopotential, using a Monkhorst-Pack grid of $30 \times 30 \times 30$ k-points. Tested are the broadening (x-axis) of the Methfessel-Paxton occupation scheme and energy cutoff vs. the calculated equilibrium lattice constant using the Murnaghan equation of state. Cutoff energies were 136, 272 and 408 eV. The largest lattice constant for each broadening belongs to a cutoff of 136 eV, the medium to 272 eV, and the lowest lattice constant belongs to 408 eV cutoff. Over a wide range for the broadening the lattice constant does not change significantly, defining the converged result.

to point out differences between the substrates K and Al, previous results of chapter 4 are compared to results for the system H/K(110) whenever applicable. The band structure of K is qualitatively different from the band structure of Al. Due to details of the band structure below the Fermi energy, one may expect that the isotope effect for holes and for electrons should be different. It is found that this expectation holds. This is the first time such a difference is predicted, and it has not been investigated yet within chemicurrent experiments.
The chapter is organized as follows: Section 5.1 contains tests of the pseudopotential, and sets numerical parameters. In section 5.2 the stable surface for K is determined, being K(110), and the surface band structure and density of states are shown, demonstrating huge differences to Al(111). The results are put together in section 5.3, treating the adsorption of H/K(110). It is shown that the forced oscillator model is not applicable in this case, and band structure effects are observable. Discussion and conclusions are found in section 5.4.
The appendix of this chapter in section 5.A contains considerations for pseudopotential generation for K. This section is technical.

## 5.1 Convergence Tests

In this section results for the calculation of the equilibrium lattice constant and the bulk modulus are presented. Thereby the k-point set and the cutoff energy with respect to the convergence of lattice constant and bulk modulus are tested, as well as the broadening of the occupation functions.
Calculations for the total energy were done using a Monkhorst-Pack k-point grid of $30 \times 30 \times 30$, and cutoffs of 136, 272 and 408 eV (10, 20 and 30 Ry), respectively, using different lattice constant. The equilibrium lattice constant was calculated by fitting this data to the Murnaghan equation of state. Results are show in Fig. 5.1. Here a broadening between 0.01 and 1.36 eV, was used for the Methfessel-Paxton occupation function [49]. The largest lattice constants belong to a cutoff of 136 eV, the intermediate ones to a cutoff of 272 eV, and the lowest ones to a cutoff of 408 eV. Calculations using a larger cutoff energy give essentially the same as a cutoff of 408 eV, cf. Fig. 5.2. The relative convergence errors for the lattice constant $a$ with respect to the plane-wave cutoff, $\Delta a(\mathrm{E_{cut}}) = (a(\mathrm{E_{cut}}) - a_{\mathrm{converged}})/a_{\mathrm{converged}}$, with $a_{\mathrm{converged}} = a(\mathrm{E_{cut}} = 408\,\mathrm{eV})$, are $\Delta a(10\,\mathrm{eV}) = 7\ ‰$ and $\Delta a(20\,\mathrm{eV}) = 2\ ‰$. Therefore it is sufficient to use a cutoff of 272 eV in order to regard the system as converged. One can observe that a large broading has an effect on the lattice constant, which is not what is wanted here. This means that the lattice constant using the numerical parameters chosen below should be slightly less than 5.30 Å.

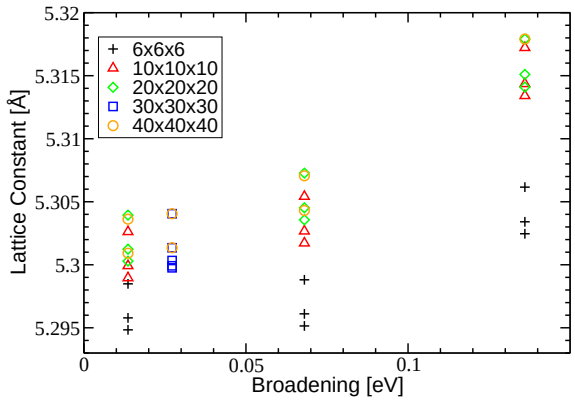


Figure 5.2: Convergence tests for K pseudopotential, using different Monkhorst-Pack grids and a broadened Fermi-Dirac occupation function. Additional data includes variation of the energy cutoffs (136, 272, 408, 544 and 680 eV). The largest lattice constants for each smearing belong the lowest cutoffs. Usually only 2 or 3 cutoff energies were tested, but at a broadening of 27 meV all five cutoff energies were tested, using a $30 \times 30 \times 30$ k-point grid. The calculated lattice constants of the larger cutoffs are essentially on-top each other.

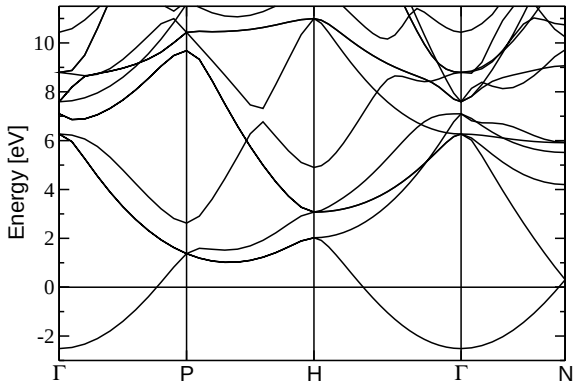


Figure 5.3: Kohn-Sham bulk band structure of K, calculated using a Monkhorst-Pack k-point grid of $30 \times 30 \times 30$, a Fermi-Dirac broadening of 27 meV and a cutoff energy of 408 eV. Good agreement with theoretical literature is achieved [78].

The broadening parameter resembles a physical temperature if a Fermi-Dirac occupation function is chosen for the substrate. Since the Fermi-Dirac occupation function is relatively sensitive to the broadening energy in comparison to a Methfessel-Paxton occupation function, it is necessary to compare the results to those of Fig. 5.1. Convergence tests using the Fermi-Dirac occupation function are shown in Fig. 5.2. Here, different k-point sets, different broadenings and different cutoff energies are tested with respect to the converged result for the equilibrium lattice constant. Consecutively smaller lattice constants within one broadening energy belong to cutoff energies of 136, 272, 408, 544 and 680 eV (10, 20, 40, 40 and 50 Ry), respectively, where often only the two or three first of these energies are shown. However, for k-point set $30 \times 30 \times 30$ all five cutoff energies are used, but the last three are nearly on-top each other. The graph shows that a k-point set of $20 \times 20 \times 20$ is sufficient to be converged, when comparing to $40 \times 40 \times 40$. A broadening of 27 meV can be used, but should not be increased. While a cutoff energy of 408 eV gives a small increase in the accuracy of the lattice constant when comparing to 272 eV, the additional computation time is probably not worth the effort, since the error is of the order of 2 ‰. Even a cutoff energy of 136 eV is sufficiently high. The calculated lattice constant is then 5.30 Å. Experimental literature gives a lattice constant of 5.23 Å at 5 K, and 5.25 Å at 78 K [79], which shows a difference of 1.3 % and 0.9 %, respectively, to the calculated values. The experimental bulk modulus is 3.70 GPa [79], which compares well to the calculated result of 3.5 GPa, i.e. a difference of only 5 % exists.

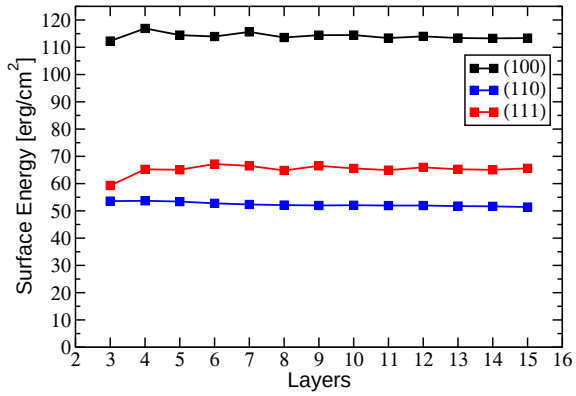


Figure 5.4: Surface energies of a K slab in (100), (110) and (111) direction. Shown is the convergence with the number of layers. For the most stable (110) surface 8 layers are sufficient to achieve convergence on this scale, but the energy differences are already tolerable from the beginning.

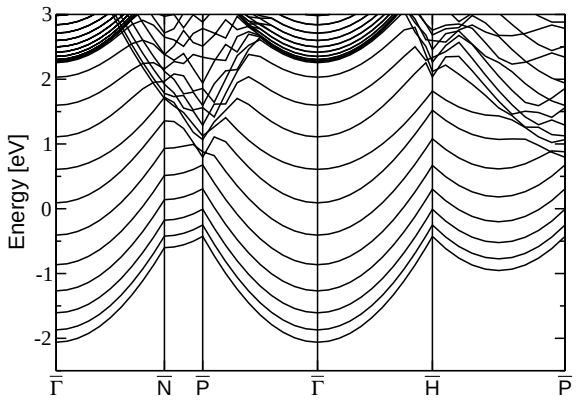


Figure 5.5: Kohn-Sham surface band structure of a $(1 \times 1)$ K slab of 8 layers in (110) direction calculated using PBE-GGA. The cutoff was 272 eV, the k-point set was $20 \times 20 \times 1$ and a Fermi-Dirac broadening of 27 meV was used. The band structure is largely independent of these convergence parameters.

These comparisons show that the pseudopotential matches the experimental data well. It is concluded that a broadening energy of 27 meV for the Fermi-Dirac occupation function, a k-point set of $20 \times 20 \times 20$, and a cutoff energy of 272 eV is sufficently accurate for this work.
The calculated bulk band structure is shown in Fig. 5.3, where the Fermi energy is set to zero. Comparison to the literature shows good agreement [78], over a range of about 10 eV. The lowest state is only about 2 eV below the Fermi energy. Therefore, large energy excitations should behave differently for electrons and holes, and such differences may possibly be observed in experiments, see section 5.3.
To summarize this section, convergence tests for the self-constructed K pseudopotential of section 5.A were done. It was shown that a cutoff of 272 eV is sufficient for the calculations of this work, and a k-point set of $20 \times 20 \times 20$ can be used. A broadening of the Fermi-Dirac occupation function of 27 meV is sufficient to guarantee numerical convergence. Lattice constant, bulk modulus and bulk band structure from DFT pseudopotential calculations agree well with experimental data. This proves that the pseudopotential is constructed well.

## 5.2 Surface Energy and Band Structure

The Schottky diodes of Ref. [80] showed no long-range crystalline order in the metal films. Due to limitations in the experimental setup, detailed information about the K film is not available. The Schottky diodes are manufactured by evaporating K atoms onto a p-doped Si substrate. The experimentalists observe layer-by-

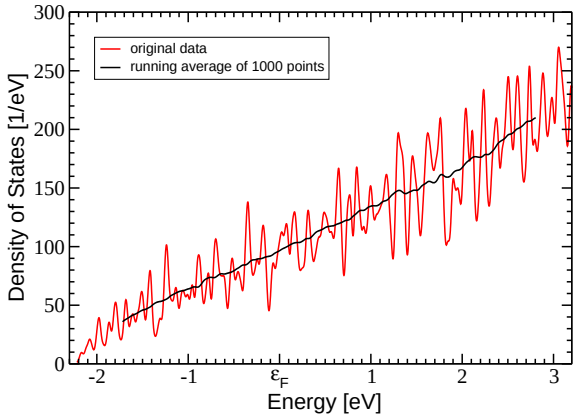


Figure 5.6: Density of states of a clean K(110) slab of 8 layers. The Fermi energy $\varepsilon_{\mathrm{F}}$ is set to zero. The oscillating part is directly taken from the data of the DOS calculation, but a running average of 1000 points is additionally shown in the graph, in order to show the general trend. The H atomic orbital has an energy of -6.49 eV in DFT calculations. The K work function is 2.37 eV in the calculations.

layer growth, indicative of a polycrystalline potassium film. The largest fraction of the surface area will consist of the surface with the lowest surface energy. Consequently, the most stable crystalline K surface will probably provide the most important contribution to the chemicurrent. Therefore the surface energies of a clean K slab for the (100), (111) and (110) directions were calculated. It was found that the K(110) surface is the most stable one. For the stable (110) surface a surface energy of 52 erg/cm$^2$ was calculated, i.e. good agreement was reached with the experimental literature value of 49 erg/cm$^2$ [81]. The surface energy was converged for 8 layers of the K slab. For the (100) surface an energy of 114 erg/cm$^2$ was found, and for the (111) surface an energy of 65 erg/cm$^2$ was calculated. The energies are quite small in comparison to transition metals (about a factor of 10 smaller).
Figure 5.5 shows the surface band structure of a $(1 \times 1)$ K slab of 8 layers in (110) direction. The Kohn-Sham conduction band of K extends up to 2 eV below the Fermi energy. For comparison, in Al(111) the author previously found Kohn-Sham energies in the conduction band up to 11 eV below the Fermi energy, Fig. 4.1. In the computational setting used for K, the bulk-projected bands (see Fig. 5.5) are rather close. Indeed, the energy spacing of these bands is much closer than with the previous settings for Al(111). Convergence tests with respect to the k-point set in Fig. 4.6 showed that such a smaller energy spacing will lead to smoother spectra, but not to notable changes in any other respect.
Finally the author decided to use a supercell of $(4 \times 4)$ K atoms for his calculations, with 8 layers of K. The uppermost 3 layers of the slab were relaxed with respect to interatomic distances. Only the first layer showed minor inward relaxation of $\mathrm{d}_{12} = -1.3\%$. The vacuum region was 20.45 Å between slab images. Increasing the size of the vacuum region to 37.41 Å did not change the chemisorption potential (Fig. 5.7) and adsorbate level occupations (Fig. 5.9) within numerical accuracy. A compensating dipole field to get rid of dipoles in the system was not used.
The density of states of the K slab is shown in Fig. 5.6. It is increasing roughly linear with energy, except very close to the conduction band minimum. Such a linear behavior is untypical for metals. One may observe that the density of states increases by 50 % from -0.55 eV below the Fermi energy to 0.55 eV above. Since 0.55 eV is the Schottky barrier, taken from experiment [80], one may expect that the probability for electron and for hole excitations may display a different energy dependence.

## 5.3 Results

The author then calculated a H atom at 35 different distances $Q$ from the surface, with the H atom on-top a K atom, and a rigid surface approximation for the substrate. The resulting chemisorption potential is shown in

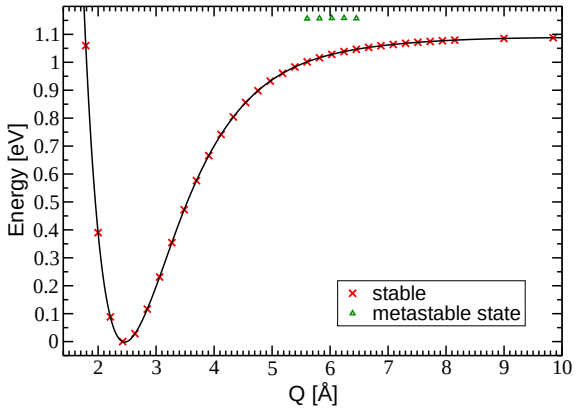


Figure 5.7: Chemisorption potential of a H atom above the on-top position of a K(110) surface. The spin transition is around 3.1 Å in this system, much closer to the minimum of the potential than in the case H/Al(111), cf. Figs. 5.9, 4.4 and 4.3. A metastable state appears further away than about 5.5 Å above the surface. This state has a total Löwdin charge of one and is fully spin-polarized, with the spin minority (down) channel fully depleted.

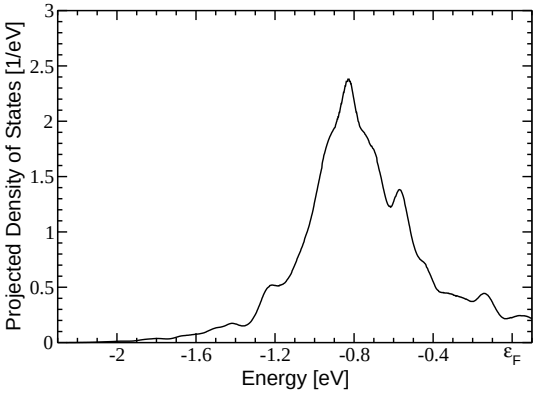


Figure 5.8: Projected density of states of an H atom adsorbing on-top a clean K(110) surface at the equilibrium geometry. The Fermi energy $\varepsilon_{\mathrm{F}}$ is set to zero.

Fig. 5.7.
The orbital character (with respect to the adsorbate atomic orbitals) of the energy levels was analyzed using the Löwdin charge method implemented in *PWSCF*. It is found that the number of electrons in the two spin states of the H atom sum up to a value notably larger than one. This holds even in a large supercell with a large vacuum region above the slab, and between the H atom and the periodic image of the surface. Calculations using a fixed spin moment for the total system did not change this behavior. However, also a metastable state with a Löwdin charge of one at the adsorbate further away than about 5.5 Å above the surface is found, even in the case without fixed moment. This state is fully spin-polarized in DFT calculations. The solution of the Kohn-Sham equations containing an adsorbate with a total Löwdin charge larger than one possesses a lower ground-state energy than the solution for an adsorbate with a Löwdin charge of one, with an energy difference of about 0.05 eV.
Comparing the work function of K of 2.25 eV, which is also found in the experiments characterizing Schottky diodes [82, 83], with the electron affinity of H, which is 0.75 eV [84], one would not expect such a charge transfer. In the calculations a K work function of 2.37 eV is found. So the author believes that the additional fractional charge found on the H atom far away from the surface is an artifact of density-functional theory (DFT), explained by the so-called delocalization error of DFT [38].
The projected density of states (PDOS) onto the atomic H (1s) orbital is shown in Fig. 5.8, with the H atom at

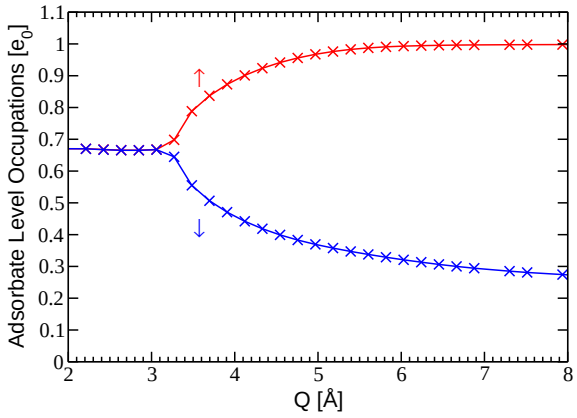


Figure 5.9: Occupation of the spin-up and spin-down orbital of an approaching H atom vs. its distance from a K(110) surface. Far away from the surface the electronic charge at the H atom is greater than 1. While the spin-up orbital is fully occupied there, the spin-down orbital is still partially occupied, even at a distance of 10 Å from the surface. Both spin-up and spin-down orbitals become equally populated after the spin transition point at about 3.1 Å. The spin polarization shows a $\sqrt{Q}$-behavior close to the transition point.

| Isotope | Electrons, $\uparrow + \downarrow$ | | Holes, $\uparrow + \downarrow$ | |
|---|---|---|---|---|
| | A(m) [1/eV] | $T_{\text{eff}}^{\text{m}}[K]$ | A(m) [1/eV] | $T_{\text{eff}}^{\text{m}}[K]$ |
| T | 0.018 | 1121 | 0.022 | 1031 |
| D | 0.010 | 1500 | 0.013 | 1291 |
| H | 0.003 | 2641 | 0.007 | 1783 |
| $H_{0.1m_H}$ | 0.119 | 2156 | 0.317 | 1533 |

Table 5.1: Numerical parameters corresponding to the fits in Fig. 5.11 using Eq. (2.55). The fits have been done over an energy range of $0.5\,\text{eV} < |\varepsilon| < 0.9\,\text{eV}$.

the equilibrium geometry. One observes that the atomic (1s) orbital is broadened close to the surface, due to the interaction with the bulk material, and has also shifted. Both the spin up and spin down PDOS are the same. Comparing Figs. 5.8 and 4.5 shows, that in the K case the H maximum value of the PDOS is much closer to the Fermi energy than in the Al case.

As explained in the introduction of this chapter, the author is interested in situations where the total energy of the adsorbate is dominated by the depth of the chemisorption potential. Consequently, a maximum energy of 1.1 eV is available for electronic excitations. A difference in the potential energy of 0.05 eV far away from the surface would decrease the time for a round-trip in the chemisorption well by about 2-3 %. Only very minor quantitative differences in the electronic excitation spectrum can be expected from such a difference. Therefore the potential energy surface (PES) of the DFT ground state may be used to calculate properties of the system, despite the somewhat unphysical Löwdin charge of the H atom.

The adsorption geometry considerably affects the depth of the chemisorption potential. In the rigid surface approximation, the K hollow position is preferable for the adsorbate, the energy difference being 0.86 eV in favor of hollow position compared to the on-top position. The total energy available for electronic excitations is then approximately 2 eV. Nonetheless the on-top position was chosen, because it was the goal to compare with the previous results for H/Al(111) of chapter 4. If the H atom is far away from the surface, the DFT ground state is found to be spin-polarized. An initial spin-up polarization of the H atom was chosen, hereby defining the spin majority part. (Consequently, spin-down is the minority spin.) Fig. 5.9 shows the result of an occupation analysis of the spin-up and spin-down orbitals of the H atom, calculated using the Löwdin approach implemented in *PWSCF*. The DFT ground-state wavefunctions of either spin for each position along the trajectory were projected onto the H (1s) orbital. Below the spin transition point at about 3.1 Å both the spin-up and the

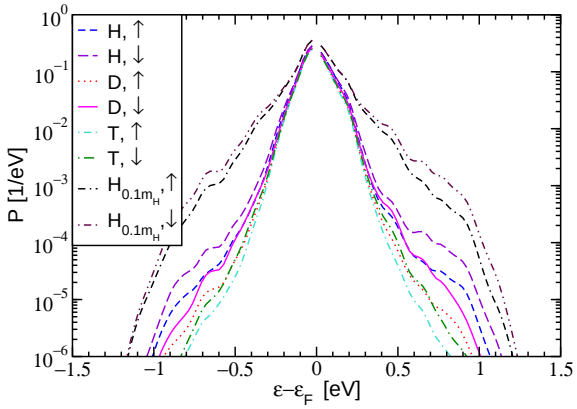


Figure 5.10: Spin-resolved excitation spectra of electrons (positive energies) and holes (negative energies) for four H isotopes with an initial kinetic energy of 30 meV on the on-top position of an K(110) surface after one half round trip in the chemisorption well. A observe small spin effect is observed, with the spin minority (down) part being slightly enhanced. There are perceptible differences between electrons and holes, compare also Fig. 5.13. Values close to the Fermi energy ($|\varepsilon - \varepsilon_F| < 0.027$ eV) are not plotted because of numerical inaccuracies in this energy range. The maximum energy available for e-h pair (and such electron and hole) excitations is 1.1 eV.

spin-down orbitals show a population of about 0.65 electrons. Further away from the surface, the H atom is partially spin-polarized and has a Löwdin charge larger than one. Here the spin-up orbital gets fully populated while the spin-down orbital gets only partially depleted. Right above the transition point the spin polarization shows a sharp, square-root-like increase. Qualitatively the behavior of the occupation is similar to the one in H/Al(111), Cf. Fig. 4.4: A spin polarization far away from the surface vanishes at a certain point above the surface, where a $\sqrt{Q}$-behavior for the occupation of the spin states, and correspondingly of the effective potential, occurs [27].

Comparing Figs. 5.7 and 5.9 with Figs. 4.4 and 4.3 one may note that the spin transition appears to happen much closer to the equilibrium adsorption point than in the case H/Al(111). Around the spin transition point $V_{\text{eff}}(Q)$ changes rather rapidly. If a model of an adsorbate oscillating many times within the adsorption well is correct, then spin features of the spectra and effects on energy dissipation - if present - should be greatly enhanced, cf. [6, 30]. However, in section 4.3.4 it was shown that the spin plays a minor role in the perturbative approach, when following adiabatic spin dynamics on the PES.

The classical trajectory for vertical impact of the H atom onto the on-top site of K(110) is calculated from Newton's equations for an initial kinetic energy of 30 meV, and starts 8 Å above the surface. The small effect of electronic friction on the trajectory is neglected. The total time needed for one half round trip in the chemisorption well is 123 fs. The mass of the approaching adsorbate was changed in the equations of motion between different calculations, thereby also changing the initial velocity of the particle.

The non-adiabatic electronic excitations in the substrate are calculated perturbatively using essentially the same formalism as described in section 3.2. However, the efficiency in evaluating the matrix elements $\lambda_{ij}$ was improved. The reader is reminded that the $\lambda_{ij}$ are the coupling matrix elements between unperturbed states of the clean slab, from which the excitation spectra of electrons and holes are calculated. Details of the improvement are found in section 3.2.1. The maximum energy available for electronic excitations in Eq. (3.12) is $E_{\max} = 1.1$ eV.

The main result of the calculations are the spectra of the electrons and holes excited in the potassium film by a hydrogen atom impinging with thermal kinetic energy. From the part of the spectra exceeding the Schottky barrier, the predicted yield of the measured chemicurrent can be directly derived. In order to study the isotope effect systematically, not only calculations for H, D and T are carried out, but also for a fictitious H atom of mass $0.1m_H$, where $m_H$ is the ordinary hydrogen mass. The fictitious light isotope is labeled $\text{H}_{0.1m_H}$ within this work. The spectra are shown for a half round trip in the adsorption potential (until the particle has reached

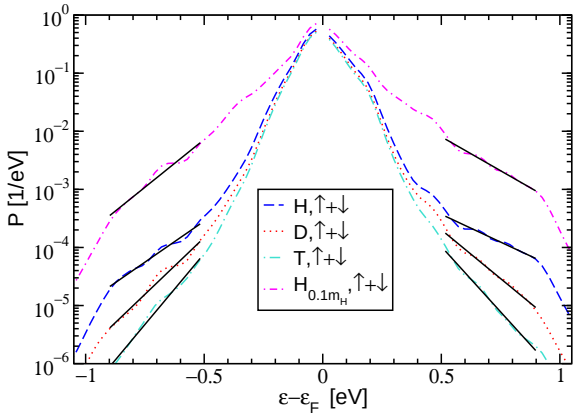


Figure 5.11: Excitation spectra of electrons and holes for all investigated isotopes, including an exponential fit in the energy range $0.5\,\mathrm{eV} < \varepsilon < 0.9\,\mathrm{eV}$. The fit is done using Eq. (2.55), resulting in the parameters of Table 5.1.

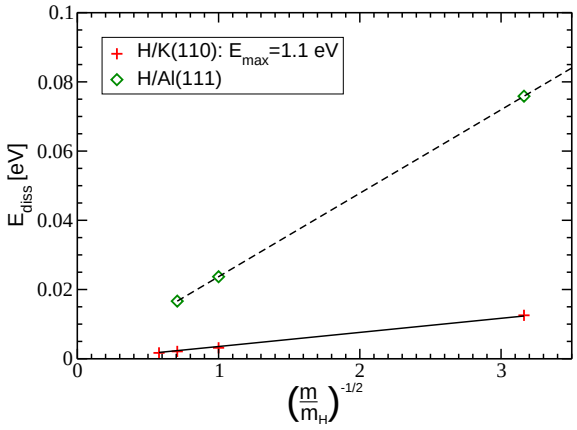


Figure 5.12: Total energy loss per half round trip in the chemisorption well vs. the scaling variable $1/\sqrt{m/m_H}$. $m$ denotes the mass of the adsorbing atom. The lines are linear fits to the data, where the dashed line corresponds to the system H/Al(111), and the straight line corresponds to H/K(110). The fitted linear dependency of the energy loss on the root of the mass is compatible with the data. The absolute values for H/K(110) are about a factor 5 smaller than in the system H/Al(111), demonstrating a less effective electron-hole pair excitation mechanism.

the turning point on the repulsive branch of the PES), to be able to compare with earlier results of section 4.2. Fig. 5.10 shows the spectra of electrons (positive energies) and holes (negative energies) for a half round trip of H, D, T and $H_{0.1m_H}$. Despite the $\theta$-function in (3.12), excitation energies larger than 1.1 eV appear in the figures due to the broadening of energy levels used for plotting. It is noted that e-h pair excitations of an energy larger than 1.1 eV are physically meaningful if H adsorption at the K hollow position is considered. Unlike in the system H/Al(111), there is a notable difference between the spin channels, with the spin minority (down) channel slightly enhanced. (Note that in this work a spin down hole is a missing spin down electron. This is in accordance with previous literature on this subject [6, 63, 29].)

In Fig. 5.10, the electron and hole parts of the spectra differ, best observable at large excitation energies $\varepsilon \gtrsim 0.5$ eV. The electron part of the spectra is decaying slower than the hole part. The hole part of the spectra is more concentrated close to the Fermi energy. This is best observable for light isotopes of mass $m \leq m_H$, and can be attributed to the K band structure and density of states (Figs. 5.5 and 5.6): At 0.5 eV below the Fermi energy the density of states of the K conduction band is about 50 % lower than at 0.5 eV above the Fermi energy. At an energy of 1 eV below the Fermi energy the band structure shows no electronic states in large parts of the

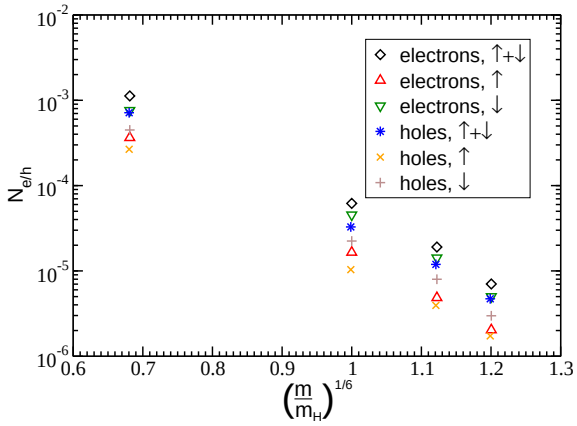


Figure 5.13: Spin-resolved yield of the electron and hole excitation spectra plotted versus the scaling variable $(m/m_H)^{1/6}$. $m$ denotes the mass of the adsorbing atom. Linear scaling of the excitation probability over the Schottky barrier is found only if plotted over $(m/m_H)^{1/6}$, but not for $(m/m_H)^{1/2}$. There is a noticable difference between the two spin channels.

| Isotope | Electrons | | | Holes | | |
|---|---|---|---|---|---|---|
| | $\uparrow+\downarrow$ | $\uparrow$ | $\downarrow$ | $\uparrow+\downarrow$ | $\uparrow$ | $\downarrow$ |
| $N(T)\times 10^6$ | 7.03 | 2.03 | 5.00 | 4.71 | 1.73 | 2.98 |
| $N(H)/N(T)$ | 8.79 | 8.13 | 9.06 | 6.94 | 5.95 | 7.52 |
| $N(D)\times 10^5$ | 1.90 | 0.48 | 1.42 | 1.19 | 0.39 | 0.80 |
| $N(H)/N(D)$ | 3.25 | 3.44 | 3.19 | 2.75 | 2.64 | 2.80 |
| $N_H\times 10^5$ | 6.18 | 1.65 | 4.53 | 3.27 | 1.03 | 2.24 |
| $N(H_{0.1m_H})\times 10^3$ | 1.12 | 0.36 | 0.76 | 0.72 | 0.27 | 0.45 |
| $N(H_{0.1m_H})/N(H)$ | 18.1 | 21.8 | 16.8 | 22.0 | 26.2 | 20.1 |

Table 5.2: Average number of electrons and holes $N(m)$ above the Schottky barrier, created per impinging H isotope ($T, D, H, H_{0.1m_H}$) with an initial kinetic energy of 30 meV, per half round trip. The spin channel is denoted by $\uparrow$ and $\downarrow$. The excitation efficiency is about an order of magnitude smaller than for H/Al(111), and the difference in the yield of electrons and holes (above the Schottky barrier) is more pronounced for H/K(110) in comparison to H/Al(111).

Brillouin zone.

When comparing to the system H/Al(111), the excitations are about one order of magnitude smaller for H/K(110). Although the present calculations are not directly comparable to the experiments, the author thinks that it is safe to predict that measurements of the chemicurrent should give a current which is about one order of magnitude smaller than for H/Al(111) under the same experimental conditions, and assuming similar Schottky barriers.

The spectra of the electron-hole pairs have also been calculated. The results of first-order perturbation theory are compared to the treatment by Müller-Hartmann and co-workers [56] that sums up all orders in the perturbation expansion. As in the system H/Al(111) it is found that the two approaches yield very similar spectra when plotted on a logarithmic scale. In the case of H/K(110), both curves fall essentially on-top each other, and deviations are much smaller than in the case H/Al(111). Again, first-order perturbation theory proves to be sufficient. The absence of higher order transitions is consistent with the smaller energy loss of the system H/K(110) per round trip, which is in general about a factor 5 smaller than H/Al(111) (see below).

Next it is tested if the results from the DFT plus perturbation theory are compatible with scaling. Following the ideas of the FOM, the high-energy tails of the spectra of Fig. 5.10 were fitted to an exponential of the form (2.55), separately for electrons and holes, where both $A(m)$ and the effective temperature $T_{\text{eff}}(m)$ are allowed

to be dependent on mass. It was mentioned in chapter 4 that the absolute value of an effective temperature to describe the slope of the spectra is dependent on the fitting window, cf. also Ref. [63], where large error bars are found by varying the fitting window. This still holds in the present case, but it is found that part of the exponential high-energy tail in Fig. 5.10 can be fitted to such an effective temperature here, with acceptable error bars. Eq. (2.55) was fitted in the energy range $0.5\,\mathrm{eV} < |\varepsilon| < 0.9\,\mathrm{eV}$ to the spectra of Fig. 5.10. The numerical values of $A(m)$ and $T_{\mathrm{eff}}^{\mathrm{m}}$ have been collected in Table 5.1. The spectra including the exponential fits are collected in Fig. 5.11. In the energy range $|\varepsilon| > 0.9\,\mathrm{eV}$ the maximum excitation energy $E_{\max}$ changes the slope of the excitation spectra notably, thereby making a fit following (2.55) impractical.
Note that the upper bound for the energy of e-h pair excitations set by the adsorption energy has a distinct influence on the spectra. If more energy was available, e.g. considering the K hollow adsorption site, marked changes of the spectra must be expected, expecially close to $E_{\max}$. One may lift the restriction of the $\theta$-function in Eq. (3.12) to investigate such behavior, and find that this is indeed the case. For the physical isotopes H, D and T (only) it was found that $A(m) \sim (m/m_H)$ and $T_{\mathrm{eff}}^{\mathrm{m}} \sim (m/m_H)^{-1/2}$ roughly captures the trend. However, the data for $\mathrm{H}_{0.1m_{\mathrm{H}}}$ deviates, indicating that the FOM scaling cannot be generalized. There is a linear relationship between the total energy loss and the mass scaling variable $(m/m_H)^{-1/2}$ for all four isotopes, as shown in Fig. 5.12 and expected from the electronic friction model (2.52). The total dissipated energy per half round trip is about a factor 5 smaller than for H/Al(111), Fig. 4.11, and amounts to 0.2 % of the total adsorption energy for H/K(110).
The total number of excited charge carriers $N_{e/h}^{\varepsilon_{\mathrm{S}}}(m)$ above the Schottky barrier $\varepsilon_{\mathrm{S}} = 0.55$ eV, whose value was taken from experiment [80], was evaluated numerically following (2.56). The results are fitted to Eq. (3.8). In contrast to the prediction of the FOM, $\gamma = 0.18$ is found for electrons and $\gamma = 0.17$ is found for holes. Using $(m/m_H)^{1/6}$ as a new, approximate scaling variable, an almost linear relationship for $\ln(N_{e/h}^{\varepsilon_{\mathrm{S}}}(m))$ and the scaled isotope mass is found, as shown in Fig. 5.13. However, the scaling exponent $\gamma$ is dependent on the Schottky barrier height. So far, the experiments are not sensitive to excitations close to the Fermi energy. If all excited quasiparticles could be detected, the dependence of the yield on isotope mass would be even weaker, and $\gamma \sim 1/15$ would be appropriate. This weak dependence is obvious already from the spectra, Fig. 5.10.
The ratio of the integrated probabilities $N_{e/h}^{\varepsilon_{\mathrm{S}}}(m)$ for H and D atoms is about 3.25 for electrons, and 2.75 for holes, see Table 5.2. One may lift the restriction of the $\theta$-function in Eq. (3.12), thereby getting 3.60 for electrons, and 3.12 for holes. Therefore, the author predicts that the isotope effect will be different for electrons and holes (even if more energy is released, e.g. due to adsorption at a more strongly bound site), with the hole part showing a smaller ratio. The calculated isotope effect is not within available experimental error bars for the system H/Ag, where a ratio of $3.7 \pm 0.7$ was measured in H vs. D adsorption for holes [72, 22]. This is the only system where experimental data is available at the moment. However, the K and Ag band structures are very different.
One may also observe that the spin minority channel contributes about a factor 2–3 times more to the total number of excited charge carriers above the Schottky barrier than the spin majority channel. This difference is the more pronounced the heavier the isotopes.

## 5.4 Discussion and Conclusions

Remarkably, electron and hole excitations occur with different probabilities due to the electronic structure of the potassium substrate: One may observe that the probability for hole excitations drops off more steeply with energy as compared electron excitations (Fig. 5.11). This is to be expected, since the density of states in the energy range below 0.5 eV below the Fermi energy is lower than the corresponding DOS above the Fermi energy (Fig. 5.6). The visible difference in slopes, see Fig. 5.11, is confirmed by the numerical values of the exponential fits shown in Table 5.1: Electrons have a systematically higher temperature there, indicating a slower decay of the spectra.
To the author's knowledge, this is the first calculation clearly demonstrating an influence of the band structure on the spectra: The FOM [5] explicitly assumes electron-hole symmetry. Previous Newns-Anderson (NA) model calculations [28], and time-dependent tight-binding [32] relied on the wide-band approximation. Only

the TDDFT calculations for H/Al(111) [6] incorporated band structure data, but differences between electrons and holes are not very pronounced for this system.
As a first step towards an experimental investigation of this behavior, one might make use of exoelectron emission. The work function of K is 2.25 eV [82]. If experiments are able to detect exoelectrons and hole currents in the diode simultaneously, using *p*-type Schottky diodes, this should confirm that the spectra for electron and holes are indeed different. However, one has to make sure that $E_{\max}$ is sufficiently low, so that excitation of holes in the highest fully occupied K band (the one below the conduction band) can be excluded.
While in chapter 4 for H/Al(111) the spectra for electrons and holes of both spin directions were almost identical, for H/K(110) a higher excitation in the spin minority channel is found for both electrons and holes. The results of this work for this spin effect are different from results of TDDFT and NA model calculations [6, 29]: These other approaches obtain a higher excitation in the spin majority channel for electrons, and in the spin minority channel for holes, especially for H/Al(111). Although the system H/K(110) was not investigated within the NA approach, it appears to be a general feature of this model that electrons (holes) are more excited in the spin majority (minority) channel, since this conclusion only relies on the relative position of the adsorbate affinity level with respect to the Fermi energy of the metal [29]. However, the discrepancy can be reconciled by recalling that different quantities are calculated in either approach. During adsorption, the electronic states of the clean surface are transferred into electronic states of an adsorbate-covered surface. This means that two different state spaces may serve as a starting point for calculation of electronic excitations. The excitation probability in both the TDDFT and NA model calculations is calculated from the non-adiabatic wave function, and thus the excitations include the changes in the Hilbert space of electronic states for the clean and adsorbate-covered surface. In contrast, in this work the excitation probability is calculated by integrating the excitation rate (defined relative to the electronic states of the clean surface) over the time interval of impact, thus excluding changes in the functions spanning the Hilbert space. Thus, the definition of excitations within this work gives the correct limit if the particle is scattered back into the gas phase, while the alternative approaches try to include some of the localized electronic excitation that results from forming a chemical bond between substrate and adsorbate.
Regarding experimental investigation of this behavior, if a suitable experimental setup existed, which is able to detect spin-polarized currents from a spin-polarized beam, this experiment could be able to decide which of the theoretical approaches is the best to describe experiments: In the TDDFT and NA model approaches spin effects are more pronounced than in the perturbative approach.
As mentioned in section 4.4, the functional relationship between the excitation yield above the Schottky barrier and the isotope mass, Eq. (3.8), was also investigated in the case H/K(110). It is found that $\gamma = 1/6$ describes the data well. Following section 4.4, where $\gamma = 1/4$ is found for H/Al(111), the FOM neither applies to H/Al(111) nor to H/K(110). In section 3.1.4 it has been mentioned that model calculations for H/Cu [51] found a cross-over from $\gamma = 1/4$ for slow velocities of the impinging H atom (up to approximately 1 Å/fs) to $\gamma = 1/2$ for higher velocities. The author concludes that using the FOM to calculate excitation spectra for electrons and holes is inappropriate for these small velocities.
Based on these findings, the author suggests a modified interpretation of the notion of 'electronic friction'. The energy dissipation of the adsorbate into the electronic system in this picture is given by (2.51), and scales according to (2.52). Indeed, this is what is observed here. The picture of electronic friction is still valid. However, this does not justify the use of the FOM for calculating excitation spectra. The FOM implies a scaling law, Eq. (2.57), of the spectra with adsorbate mass, with exponent 1/2. The results of this work do not support (2.57). Instead, assuming a typical Schottky barrier of about 0.5 eV, the author tentatively proposes a new scaling law, Eq. (3.8), with $\gamma = 1/4$ for H/Al(111), and $\gamma = 1/6$ for H/K(110). In Ref. [51] a scaling with $(m/m_H)^{1/4}$ for model systems is found. In summary, a scaling law of this type, if applicable at all, requires a system-dependent exponent $\gamma$, which is found to be distinctly smaller than $1/2$. At the moment one can only speculate on the physical grounds for such behavior.
The present results, which contest the FOM scaling, lead to an important prediction: The number of excited electrons and holes (above a certain detection barrier) is most probably not as dependent on the adsorbate mass as is believed up to now. It is deduced that a larger chemicurrent can be measured even for very massive par-

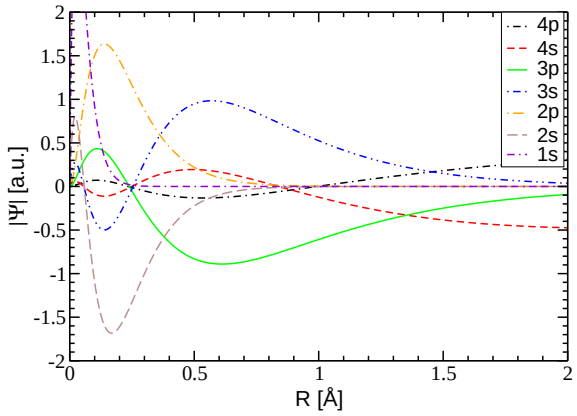


Figure 5.14: Wavefunctions for the neutral K atom, close to the atomic core. Nearly all wavefunctions disappear before or around 2 Å, which is much less than the nearest-neighbour distance of 3.7 Å in experiments. Only two wavefunctions reach further out, namely 4s and 4p, the last one representing an unoccupied state of the atom. A radial cutoff of 1.59 Å for these two wavefunctions is before their maximum, being sufficiently (but not too) small for the pseudopotential generation.

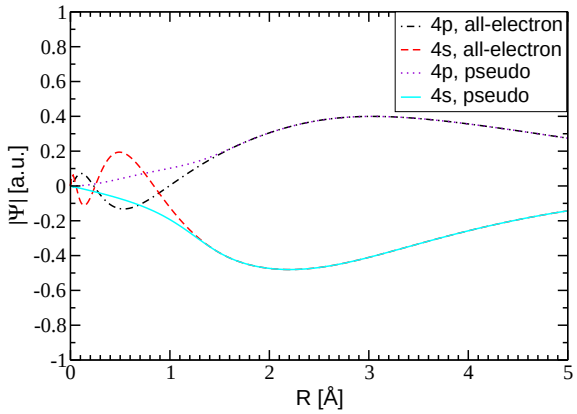


Figure 5.15: The two wavefunctions used in the pseudopotential. The all-electron wavefunctions are compared with the pseudo wavefunctions. After the radial cutoff of 1.59 Å, both kinds of wavefunctions are on-top each other.

ticles impinging at thermal velocities. This explains qualitatively the magnitude of the chemicurrent measured for Mg/Mg adsorption [65, 66].
To summarize, it is found that non-adiabtic effects in the adsorption of H/K(110) are qualitatively similar to, but quantitatively different from H/Al(111). For K, the band structure has a notable influence on the isotope effect. It is found that the number of excited particles above the Schottky barrier is much less dependent on the mass than expected from the forced oscillator model. The author concludes that electronic excitations are more important for slow and heavy elements than was expected before.

## Appendix 5.A Pseudopotential Generation for K

As an example it is demonstrated in this chapter how the pseudopotential for K was generated in this work, and how it was tested. This tedious task is described only once in this length, since the procedure is the same every time.
For generation of the pseudopotential the *atomic* code delivered with *PWSCF* was used [41]. The pseudopotential was constructed following the Troullier-Martins scheme [43].

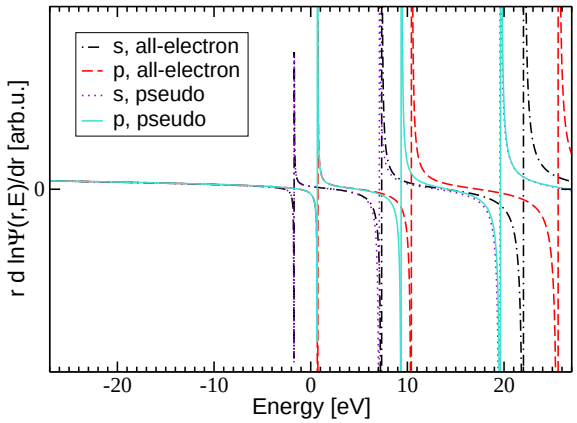


Figure 5.16: Comparison of the logarithmic derivatives of the all-electron and pseudo wavefunctions. Over a range of approximately 10 eV, between -3 eV and 7 eV, the logarithmic derivatives are on-top each other. This gives an approximation for the energy range of validity of the pseudopotential.

The improved code from section 3.2.1 can not treat ultrasoft pseudopotentials. A perturbation theory for non-orthogonal states defined by a generalized Schrödinger equation is extremely difficult to implement, and standard literature stays quiet on this subject. So although ultrasoft pseudopotentials could achieve a smaller energy cutoff, it remained conceptionally unclear, how they could be correctly implemented within perturbation theory [85].
Due to this limitation the generation of a norm-conserving pseudopotential is preferable. Scalar-relativistic effects were taken into account. The configuration chosen was '[Ar] $4s^1$ $4p^0$', i.e. the neutral K configuration, but including an unoccupied orbital. A nonlinear core correction was used [44]. The pseudopotential was generated using a single-projector per channel. Since surface calculations had to be done with this pseudopotential, gradient effects of the density should be taken into account. Therefore the gradient-corrected density functional PBE-GGA [39] was chosen. The result of the all-electron wavefunction calculation for the atomic K is shown in Fig. 5.14. For calculation of electronic excitations, only the long-range wavefunctions are necessary. For K only the (4s) and (4p) wavefunctions possess such a long-range behavior, and so only they need to be taken into account for the pseudopotential. A radial cutoff of 1.59 Å (3.00 bohr), which is smaller than necessary, was chosen, in order to have a security reserve for the calculations of matrix elements later on. A comparison of pseudowavefunctions and all-electron wavefunctions is found in Fig. 5.15.
These considerations have shown that the pseudopotential calculations only need to take into account 2 wavefunctions ((4s) and (4p)), and that the pseudopotential calculation seems to give decent wavefunctions. However, a check for ghost states must be made, too. In Fig. 5.16 the logarithmic derivatives of the all-electron wavefunctions are compared to the logarithmic derivatives of the pseudo wavefunctions, for a radius of 4.23 Å (8 bohr). The derivatives are on-top each other in a range of approximately 10 eV. So as long as the Kohn-Sham energies from substrate calculations do not span an energy range larger than 10 eV (from lowest to highest state), no ghost states appear.
Finally, the pseudopotential has to be tested by calculating the equilibrium lattice constant of bulk K, its bulk modulus, and the band structure. Only if these tests all give reasonable results can the pseudopotential be regarded as suitable for the calculations. Such calculations are done in section 5.1.

# Chapter 6

# Results: Mg on Mg(0001)

Experimental results have proven that during deposition of Mg on a Mg/*p*-Si(001) Schottky diode a current can be measured between the front- and backside of the diode [66, 65]. In these works the experimentalists concluded that during metal epitaxy - at least in the system Mg/Mg - electronic charge carriers are excited sufficiently high to overcome the inherent energy barrier in the diode. In this chapter it is investigated whether it is possible to describe this effect within the framework of the perturbation theory developed in this work. It is found that particle adsorption on ideal surface terraces can probably not explain the observed chemicurrent. Instead, surface defects are important for the measured electronic excitations. Nonetheless theory predicts that observation of chemicurrents may be possible in metal epitaxy. For a detailed theoretical investigation exact knowledge of the surface structure is necessary. Electronic nonadiabaticity during surface diffusion may be dominating the chemicurrent. From the perturbation theory point of view, the current is at least two orders of magnitude smaller than in the case of hydrogen adsorption on metals. This is what is found in the experiments. To the author's knowledge this is the first time a theoretical description of electronic excitations in metal epitaxy is published.

## 6.1 Convergence Tests

In order to determine the numerical parameters for the DFT calculations, in principle the same tests were done as in the K case in section 5.1. For the bulk system an energy cutoff of 272 eV (20 Ry) was found to be sufficient, with a k-point set of $20 \times 20 \times 20$. A Fermi-Dirac broadening of 0.0136 eV (1 mRy) was used.
Using these parameters, and the hcp crystal structure with 2 atoms per unit cell, a lattice constant of 3.24 Å was calculated, with a height of the unit cell of 1.624 lattice constants. A bulk modulus of 33 GPa was calculated by fitting calculations of the total energy with varying lattice constants to the Murnaghan equation of state. These results can be compared to literature values, where the augmented plane wave (PAW) method was used for calculations of these constants [86]. In these calculations the height of the unit cell was fixed at 1.621 lattice constants. A lattice constant of 3.18 Å was calculated, with a bulk modulus of 36 GPa at 0 K, and a lattice constant of 3.21 Å and a bulk modulus of 33 GPa at a temperature of 298 K. Experimental values are 3.20 Å and 37 GPa, respectively, at a temperature of 298 K, taking into account vibrational effects within the quasi-harmonic approximation. The difference between the calculated values with the present pseudopotential and theoretical literature values is 2 % for the lattice constant, and 8 % for the bulk modulus. The difference between literature values and calculated values is caused by the fact that in the newly constructed pseudopotential only the (3s) electrons were used as valence electrons, cf. appendix 6.A. Anyway, the error is tolerable.
The pseudopotential was tested by calculating the band structure of Mg, which is shown in Fig. 6.1. Excellent agreement with theoretical literature is achieved [87]. The author concludes that the electronic properties of Mg, which are most important for the present calculations, are described well, which makes him confident that the pseudopotential is well suited for his purposes.

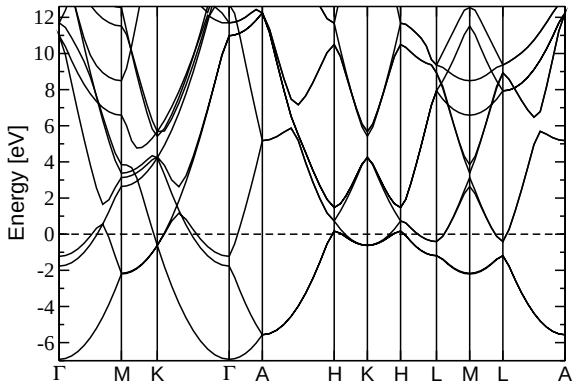


Figure 6.1: Kohn-Sham bulk band structure of Mg. The Fermi energy is set to zero. Excellent agreement with other theoretical literature is achieved [87].

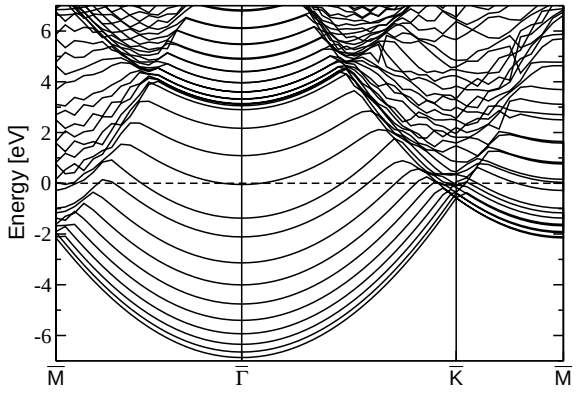


Figure 6.2: Kohn-Sham surface band structure of a $(1 \times 1)$ Mg slab of 9 layers in (0001) direction calculated using PBE-GGA. The cutoff was 272 eV, the k-point set was $16 \times 16 \times 1$ and a Fermi-Dirac broadening of 13.6 meV was used. The Fermi energy is set to zero.

## 6.2 Surface Morphology and Band Structure

The experiments done make use of Mg/*p*-Si(001) Schottky diodes [66, 65]. After deposition of Mg at a temperature of 120 K, these diodes are annealed at room temperature, and cooled down to 120 K again. Due to limitations in the experimental setup, it was not possible to investigate the surface structure of these diodes, but the experimentalists claim that the diodes have a rather rough surface. It is plausible to assume that the surface is polycrystalline, but it may contain defects.

The Mg(0001) surface was investigated, since it is energetically the most stable one [87]. Therefore a polycrystalline surface will contain a large fraction of (0001) facets, and will probably be most important for the chemicurrent. A slab of 9 Mg layers of Mg in (0001) direction was relaxed with respect to interlayer distance, keeping the lowest three layers fixed, thereby finding a generally outward relaxation of $\mathrm{d}_{12} = 1.9\%$, $\mathrm{d}_{23} = 0.9\%$ and $\mathrm{d}_{34} = 0.1\%$ for the uppermost three interlayer distances. Good agreement is reached with theoretical and experimental data on this subject [88, 89].

Fig. 6.2 shows the surface band structure of the relaxed slab. Good agreement with the literature is achieved [87], including several fine details. There are states up to 6.65 eV below the Fermi energy, but also small gaps in the band structure in parts of the Brillouin zone around the Fermi energy. In other parts of the Brillouin zone, around the $\overline{K}$ point, the density of states (DOS) is reduced below the Fermi energy.

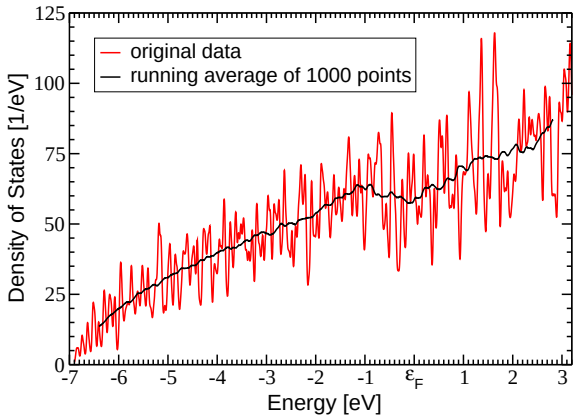


Figure 6.3: Density of states of a clean Mg slab of 9 layers, including a surface vacancy. The Fermi energy $\varepsilon_{\mathrm{F}}$ is set to zero. The oscillating part is directly taken from the data of the DOS calculation, but a running average of 1000 points is additionally shown in the graph, in order to show the general trend. The Mg atomic (3s) orbital has an energy of -4.71 eV, and the unoccupied (3p) orbital has an energy of -1.33 eV within DFT calculations. The Mg work function is 3.67 eV in the calculations, and 3.66 eV in experiments.

## 6.3 Results

For the calculations a supercell with lateral periodicity of $4 \times 4$ atoms was used, with 9 layers of Mg for adsorption on the hollow, bridge and top sites, but see below for the kink and vacancy geometries. The k-point set used was $4 \times 4 \times 1$, the plane-wave cutoff energy 272 eV (20 Ry), and a broadening of the Fermi-Dirac occupation function of 0.0136 eV (1 mRy) was used.
The surface morphology changes during adsorption. It turns out that a possible chemicurrent observable in experiments is strongly dependent on the exact environment of an adsorbing atom on the surface. Thus four representative sites, top, hollow fcc, kink, and vacancy adsorption, are studied in more detail.
As a first step the chemisorption energy of a single Mg atom was calculated on several adsorption sites of the clean perfect Mg (0001) surface in the rigid surface approximation. A chemisorption energy of 0.43 eV for the on-top position, and 0.56 eV for the hollow hcp position was found. Note there are two hollow positions, one with an Mg atom positioned in the second layer below the adsorbate atom in (0001) direction, which is the hollow hcp site, and one without an atom below the adsorbate atom in (0001) direction, the hollow fcc site. Additional tests using pseudopotentials from the *PWSCF* website [41] confirmed the calculated energies. Lifting the restriction of the rigid surface approximation, chemisorption energies of 0.460(9) eV for the top and 0.576(1) eV for the hollow hcp site were found. For the hollow fcc site an energy of 0.591(9) eV was determined. The bridge site, between two surface atoms, possesses a chemisorption energy of 0.573(4) eV after relaxation. Taking into account the thermal energy available for diffusion at a temperature of 120 K, which is 0.010 eV, it is obvious that diffusion processes on the surface may appear during adsorption: The energy barrier between the fcc hollow site and the bridge site is $\Delta E_{\mathrm{diff}}$ =0.018(4) eV, which is roughly twice the thermal energy at 120 K. The jump rate $\Gamma$ between two sites is then given by $\Gamma = \Gamma_0 \exp(-\Delta E_{\mathrm{diff}}/k_B T)$. The attempt frequency $\Gamma_0$ is typically taken to be a phonon frequency, often the vibrational frequency of the adatom. For Mg these are of the order of a few $10^{12}$/s [90]. Thus is follows $\Gamma = 0.15 \times 10^{12}$/s for the jump rate. However, this is only a rough estimate for the jump rate, since the used exponential law is only reliably valid for $\Delta E_{\mathrm{diff}} > 4k_B T$. This is not the case for Mg at 120 K. Nonetheless this approximation gives a first estimate.
The height of the Schottky barrier was determined experimentally, being 0.5 eV [66]. In the experiments, the kinetic energy of the adsorbing atom is quite low initially, of the order of a few 10 meV. When the Mg atom adsorbs at the surface, several energy dissipation channels contribute to the total energy dissipation, among these the electronic and phononic channels. Chemicurrents belong to the electronic channel. However, the phononic

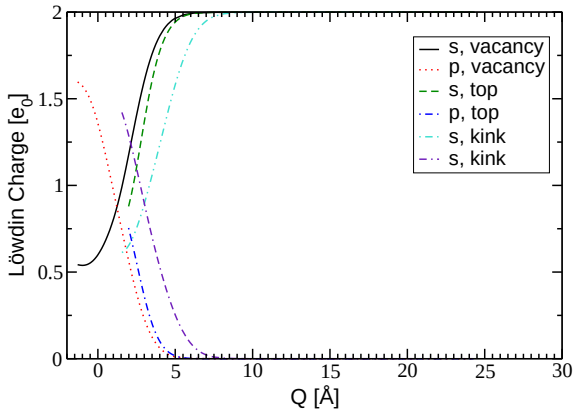


Figure 6.4: Number of electrons in the Mg (3s) and (3p) state during adsorption on an Mg(0001), for the on-top, kink and vacancy positions. Q denotes the distance from the surface. One observes an sp-hybridization, where the number of electrons in the s-state decays, while the number of electrons in the p-state rises. It seems that a saturation value appears. The bulk values are $0.5e_0$ for the (3s) state and $1.5e_0$ for the (3p) state, while for the surface atoms the values are approximately $0.6e_0$ for the (3s) state and $1.4e_0$ for the (3p) state, depending on the exact position of a surface atom.

channel is also important for the total energy dissipation. So the total energy available for chemicurrents will in these cases generally be not sufficient for electrons or holes to overcome the Schottky barrier.
However, the Mg particle beam deposits material, which in turn changes the surface morphology constantly during the measurements. Thus a multitude of processes may contribute to the chemicurrent, while adsorption on the perfect clean surface is probably irrelevant for the chemicurrent. Thus, two cases are additionally investigated, the kink and vacancy adsorption geometries.
For the vancancy, the equilibrium geometry of a clean Mg slab of 9 layers was calculated, where a single vacancy has been introduced in the first layer of the perfect Mg(0001) surface, afterwards relaxing the atomic positions, while keeping the lowest three layers of the slab fixed. The chemisorption energy of a Mg atom adsorbing into this vacancy, where the slab is kept rigid during adsorption, is 1.97 eV. After relaxation an energy of 2.00 eV is obtained. In both cases the energy is in principle large enough to be able to explain the excitation of electrons and holes to energies larger than the Schottky barrier.
For the kink geometry, starting from a $4 \times 4$ supercell, a slab of eight layers of Mg was defined. An ninth layer consisted of $2 \times 4$ Mg atoms, and an additional atom in front of these two rows. This slab was relaxed, with the exception of the lowest three layers, and serves as the unperturbed surface for electronic excitations during adsorption on the kink site. For calculation of the chemisorption energy an additional atom was put into the supercell, either far away from the surface, or beneath the single atom, close the the complete Mg row, on the slab. The slab was relaxed again, with the exception of the lowest three layers. The chemisorption energy calculated is 1.375 eV. In the rigid surface approximation, the position of the adsorbate in the surface plane, i.e. parallel to the surface, can be chosen. The adsorbate's position in the surface plane of the completely relaxed case was chosen for this purpose, and only the position perpendicular to the surface plane was changed to calculate the particle's trajectory. In the rigid surface approximation, with the unperturbed kink surface kept rigid, the energy is just 1.35 eV. In both cases the energy is sufficient to overcome the Schottky barrier.
From a physical point of view, these larger energies than for the ideal surface are to be expected: When a Mg atom adsorbs at a clean surface, it will bond with three surface Mg atoms in the hollow positions, yielding 0.576 eV in the hollow hcp case and 0.592 eV in the hollow fcc case. Roughly spoken, from simple geometry considerations, in a surface vacancy it will bond to 9 Mg atoms, thereby gaining about three times this energy. In the kink site it will bond to 6 atoms, thereby gaining about two times the energy of one the hollow sites. Already this very simple picture can provide a semiquantitative explanation for the 2.00 eV and 1.375 eV gained by adsorbing into the vacancy or kink position, respectively.

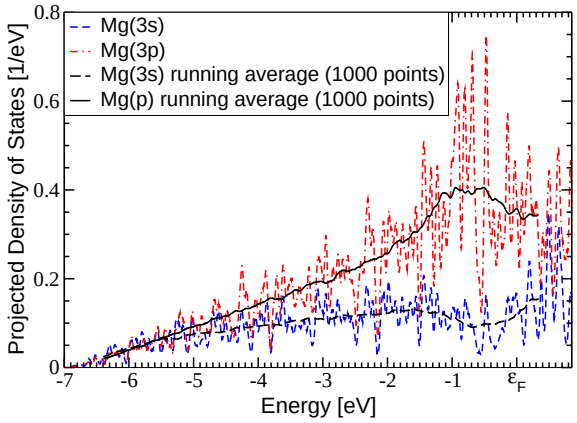


Figure 6.5: Projected density of states of an Mg atom adsorbing in the vacancy position of a clean Mg slab of 9 layers at the equilibrium geometry. The Fermi energy $\varepsilon_{\mathrm{F}}$ is set to zero. The oscillating part is directly taken from the data of the DOS calculation, but a running average of 1000 points is additionally shown in the graph, in order to show the general trend.

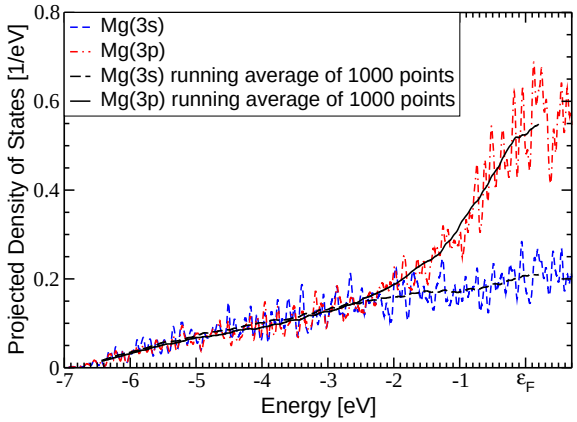


Figure 6.6: Projected density of states of an Mg atom adsorbing in the kink position of a clean Mg slab in the kink equilibrium geometry. The Fermi energy $\varepsilon_{\mathrm{F}}$ is set to zero. The oscillating part is directly taken from the data of the DOS calculation, but a running average of 1000 points is additionally shown in the graph, in order to show the general trend.

Thus, if the detected chemicurrents can be explained by the present theory, in a general sense defects in the Mg slab are important, e.g. steps, or already adsorbed atoms. However, in addition to direct adsorption, other processes may also be relevant for the chemicurrent generation. Since the diffusion barrier is of the order of the thermal energy, surface diffusion will play an important role in the experiments. Thus an adsorbing atom on a terrace, e.g. in one of the hollow positions, might move rather rapidly on the surface until it hits a surface vacancy, or a kink or step edge. For instance, the energy gain between a hollow hcp and kink site is still 0.799 eV, which is in principle sufficient to pass the Schottky barrier.
A general investigation of all possible processes is beyond the scope of this work, but four geometries shall be investigated in more detail. The on-top position was chosen, since it was already investigated in previous chapters. The vacancy geometry was chosen, since it will probably be the geometry yielding the largest chemisorption energy. Following the terrace ledge kink model [91, 92], the chemisorption energy of a kink is the sublimation enthalpy within this model. Thus the kink geometry was chosen, and its chemisorption energy is indeed close to the measured sublimation enthalpy of 1.3 eV [65, 66]. The kink geometry may be representative for the current, if only the sublimation enthalpy is important for chemicurrent generation. As a fourth geometry the hollow fcc site was considered, since this geometry gives the largest chemisorption energy for the

ideal flat Mg(0001) surface.
The density of states (DOS) for a clean Mg slab, including a vacancy, is shown in Fig. 6.3. Around the Fermi energy $\varepsilon_{\mathrm{F}}$, which is the most important part of the DOS for chemicurrent generation, the DOS is decreasing slightly, which has been found in previous work, too, when investigating the surface band structure [93]. The square-root like behavior is typical for free-electron metals. For the kink position, the DOS is similar.
When adsorbing on an Mg surface, the adsorbate Mg's (3s) state hybridizes with the (3p) state. The projected density of states onto these two states was calculated, using the Löwdin method, which is implemented in *PWSCF* [41], for the on-top, kink and vacancy adsorption geometries on Mg(0001). The number of electrons in the s- and p-type orbitals during adsorption were extracted. The results are shown in Fig. 6.4. The hybridization is nicely shown: During adsorption, the number of electrons in the s-type Mg orbital decays, and the number of electrons in the p-type orbital rises. The bulk values are approximately 0.5 electrons in the s-orbital, and 1.5 electrons in the p-orbital, while the values for the surface atoms of the Mg(0001) geometry are roughly 0.6 $e_0$ and 1.4 $e_0$, repectively, depending on the exact position of the surface atom. During adsorption at the vacancy position, the number of electrons in the two orbitals seem to approach a saturation value, which roughly resembles the bulk values. Quantitative differences between the on-top, kink and vacancy positions exist, but the qualitative behavior stays the same in the plotted range. Note that the zero in the kink case is different from the other two cases.
In the case of the surface vacancy, the zero for the distance Q of the adsorbate atom from the surface, which is not flat, was taken as the mean average of all heights of the 15 atoms in the outermost layer of the (0001) surface in the supercell. The maximum absolute deviation from the average is 0.025 Å, and the root mean square deviation is 0.004 Å. A similar definition was used for the zero for the distance Q adsorbing on-top an ideal Mg(0001) surface, where the outermost (ninth) layer defines the Q zero. However, in the top case there is no deviation from the average value for the surface atoms.
In the case of the kink, the zero for the distance Q of the adsorbate atom from the surface was taken as the mean average of all heights of the 16 atoms in the outermost complete (i.e. eighth) layer of the (0001) surface in the supercell. The maximum absolute deviation from the average is 0.163 Å, and the root mean square deviation is 0.026 Å.
This explains the distance shift of the kink curve in Fig. 6.4 with respect to the other two curves.
The projected density of states (PDOS) of the Mg atom adsorbing into the surface vacancy and kink position onto its (3s) and (3p) orbitals is shown in Figs. 6.5 and 6.6, respectively, with the Mg atom at the equilibrium geometry in the rigid surface approximation. For the surface vacancy, features in the plot, for instance the dip close to the Fermi energy in the (3s) case, closely resemble those of the Mg bulk DOS of Fig. 6.3. This was expected: Since the Mg atom fills the vacancy at this position, its DOS should be similar to the DOS of the bulk metal. For the kink position one observes a broadened (p)-type orbital around the Fermi energy, and there is no dip in the PDOS of the (3s) state around this energy. The kink geometry is closer to the case of an atom in front of the surface than the vacancy case, so that this difference to features of the Mg bulk DOS of Fig. 6.3 is expected.
The chemisorption potentials of an Mg atom adsorbing into a surface vacany and kink are shown in Fig. 6.7. The Q zero has been defined as explained above. The adsorbate will move into the surface when adsorbing, repairing the surface vacancy if enough time passes, and the full dynamics is taken into account. However, in the calculations a rigid surface approximation is used. In the case of the kink, note that for calculation of the spectra the rigid surface approximation is used, too. Thus the chemisorption energy in the kink case is only 1.35 eV in the following calculations.
Including a small kinetic energy of 30 meV, the total energy available for the excitation of electron-hole pairs is $E_{\max} = 2$ eV (3.12) in the vacancy case, and $E_{\max} =$1.38 eV in the kink case.
In the present calculations the movement of the Mg adsorbate starts with a kinetic energy of 30 meV, straight towards the surface. In the case of adsorption into the surface vacancy the trajectory starts at 8.15 Å above the surface, and in the case of adsorption at the kink site it starts at 10.11 Å above the surface (using the definition of Q=0 as mentioned above). The classical trajectory for vertical impact of the $^{24}$Mg isotope onto the vacancy and kink position of a relaxed Mg(0001) surface was calculated from Newton's equations. The small effect of

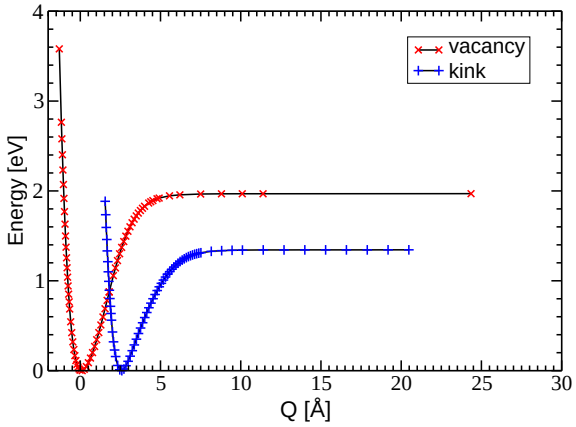


Figure 6.7: Chemisorption potential of a Mg atom above the vacancy and kink positions in a relaxed Mg (0001) surface. The chemisorption energy is strongly dependent on the adsorption site. The crosses mark the positions where the geometry was calculated. The lines are interpolations of these points.

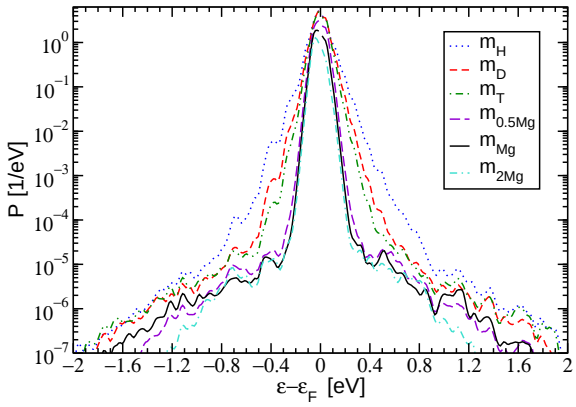


Figure 6.8: Excitation spectra of electrons and holes for impinging (fictitious) Mg isotopes with an initial kinetic energy of 30 meV impinging into the surface vacancy of a relaxed Mg(0001) surface after one half round trip in the chemisorption well.

electronic friction on the trajectory was neglected. The total time used for one half round trip in the chemisorption well is 879 fs in the vacancy case, and 1014 fs in the kink case. This time is much larger than for previous calculations of H/Al(111) in section 4.2, which is mainly due to the much larger mass of Mg, but also due to different starting positions of the trajectory and a different chemisorption potential. A fictitious Mg isotope of hydrogen mass needs a time of 179 fs for the round trip in the vacancy case, where the chemisorption energy is approximately equal to the case H/Al(111), and 204 fs in the kink case. In order to be able to compare with results from chapter 5, the scaling of the detected chemicurrent with the mass was investigated. In order to do so, the Mg mass was scaled, so that fictitious Mg isotopes of different masses could be investigated in the calculations. In order to observe notable differences in the spectra for different masses, judging from previous results of chapter 5, the mass *ratio* must change notably, not only the absolute differences. Thus large absolute differences for the masses have to be chosen for the calculations.
The main results of the perturbation theory are the spectra of the electrons and holes excited by the impinging Mg atom. In this chapter it was not necessary to do a spin-polarized calculation, since tests showed that such a polarization does not occur in the system. This is not surprising: Mg has a closed (3s) shell as valence far away from the surface, which will usually not polarize. Close to the surface, hybridized states appear. However, these turn out to be unpolarized also. Since Mg is not a ferromagnetic material, a spin polarization of an Mg crystal is not expected.

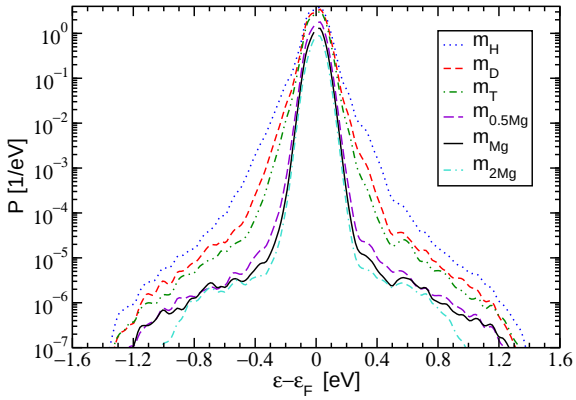


Figure 6.9: Excitation spectra of electrons and holes for impinging (fictitious) Mg isotopes with an initial kinetic energy of 30 meV impinging into a kink on a relaxed Mg(0001) surface after one half round trip in the chemisorption well.

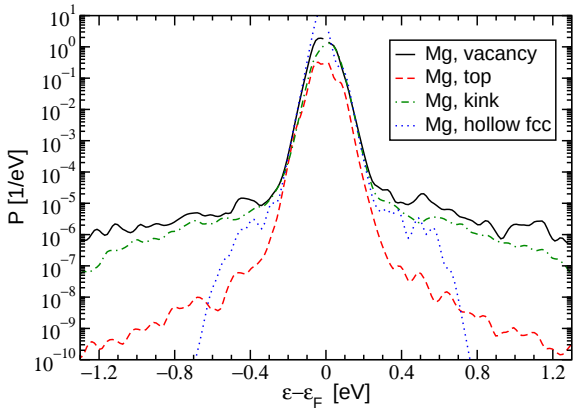


Figure 6.10: Excitation spectra of electrons and holes for an approaching Mg atom with an initial kinetic energy of 30 meV impinging onto the on-top, hollow fcc, kink and vacancy positions of a relaxed Mg(0001) surface after one half round trip in the chemisorption well. The excitation probability in the high-energy tail of the spectra is the larger the larger the chemisorption energy in these three cases. For the top position, the curve is shown without the energy-conserving $\theta$-function.

Spectra for fictitious Mg isotopes of mass $m_{\mathrm{H}}$, $m_{\mathrm{D}}$, and $m_{\mathrm{T}}$, which are the masses of hydrogen, deuterium and tritium, were calculated, and of masses $m_{0.5\mathrm{Mg}}$ and $m_{2\mathrm{Mg}}$, which are Mg isotopes which have half and double the mass of $^{24}$Mg. The isotopes are labeled $\mathrm{Mg}_{m_{\mathrm{H}}}$, $\mathrm{Mg}_{m_{\mathrm{D}}}$, $\mathrm{Mg}_{m_{\mathrm{T}}}$, $\mathrm{Mg}_{0.5m_{\mathrm{Mg}}}$, $\mathrm{Mg}_{2m_{\mathrm{Mg}}}$, and Mg, respectively. The spectra are shown for a half round trip in the adsorption potential in Fig. 6.8 for the vacancy case. As in chapter 5, one can clearly distinguish two separate energy ranges: one close to the Fermi energy, where the decay of the number of excited electrons and holes ist very strong, and one further away from the Fermi energy, where the spectra decay more slowly. All spectra are qualitatively similar. Especially in the energy range above the Schottky barrier the spectra for $\mathrm{Mg}_{0.5m_{\mathrm{Mg}}}$, $\mathrm{Mg}_{2m_{\mathrm{Mg}}}$, and Mg are very close to each other on a logarithmic scale.

For the kink case the spectra are shown in Fig. 6.9. The spectra are similar to those of the vacancy case. Differences appear for large energies close to $E_{\max}$, which were expected. Also the excitation probability for electrons and holes is systematically smaller than in the vacancy case, see also Fig. 6.10 below.

Spectra from calculations of Mg/Mg(0001) with Mg adsorbing on the on-top position can also be investigated. One may lift the restriction of the $\theta$-function in (3.12) for the on-top case, in order to be able to compare the numerical results with the vancancy and kink geometries. Such a comparison in done in Fig. 6.10, where also a spectrum for Mg adsorption into the hollow fcc site is shown. For the hollow fcc site a maximum energy of

$E_{\max}$ =0.605 eV was used, which corresponds to the particle's initial kinetic energy, plus the chemisorption energy in the rigid surface approximation. One then observes that especially the high-energy tails of the spectra are different, with that for the on-top position decaying faster and being several orders of magnitude smaller than those for the kink and vacancy positions, while the spectrum for the hollow fcc position is in between the top and kink spectra around the Schottky energy. The spectrum for the on-top position always has the smallest excitation probabilities, and the spectrum for the surface vacancy always has the largest excitation probabilities, with the notable exception of energies close to zero, where the spectrum for the hollow fcc site becomes larger. The kink and hollow fcc geometries are in between these two extrema. Close to 0.6 eV the spectrum for the holow fcc site is dominated by the available excitation energy $E_{\max}$, so that the excitation probability of electrons and holes close to this energy is impaired.
The excitation probability in the four cases can be traced back to the movement of the adsorbing atom through the electron sea at the surface of the slab: The electron density close to the turning point of the trajectory is notably larger in the kink and vacancy cases than in the top case, with the density in the vacancy case being slightly larger than in the kink case. The electron density in the hollow fcc case close to the turning point of the trajectory is larger than in the top case, and should be closer to the kink and vacancy cases, than to the top case. It is expected that excitation of electrons and holes during adsorption on other sites of an ideal surface are between the on-top case and the hollow fcc case, and do not resemble the kink and vacancy cases.
It is noted that the spectrum for the on-top position is several orders of magnitude smaller than the spectra for the kink and vacancy positions in Figs. 6.8 and 6.9. This is also true for the hollow fcc spectrum in Fig. 6.10, although the spectrum in the hollow fcc case is closer to the on-top case than the two other cases. It is also influenced by the available excitation energy. Due to the difference in the order of magnitude of the excitation probability, numerical accuracy issues were excluded, which could otherwise explain the slope of the high-energy tails of the spectra through noise. Since all spectra behave similarly, it is concluded that numerical noise issues are not important for all four adsorption geometries. Additionally the evaluation of the integrals of Eq. (3.12) was tested with respect to the number of timesteps and the energy spacing. Also it was tested whether calculation of a full round trip, or a different starting point for calculation of the trajectory, leads to qualitative changes of the spectra, and it was found that this is not the case. (Quantitative differences appear, of course, but are in the expected range.) No evidence was found that numerical issues play an important role in the present calculations. Instead, the high-energy tail of the spectra is interpreted as a physical property.
Fig. 6.11 shows the spectrum of the electron-hole pairs for the surface vacancy, which yields the largest dissipated energy. The results of first-order perturbation theory, Eq. (2.37), are compared to the treatment by Müller-Hartmann and co-workers [56] that sums up all orders in the perturbation expansion. As in the previous chapters 4 and 5 it is found that the two approaches yield similar spectra when plotted on a logarithmic scale. There are minor differences in the energy range 0.2-0.4 eV. For larger energies than the Schottky barrier the agreement is quite good again. Thus the perturbative approach is still sufficient for calculation of chemicurrents.

Fig. 6.12 shows the total energy loss of an impinging Mg atom for the surface vacancy and the kink, using different masses for the Mg atom. The amount of energy dissipated into the electronic excitation channel is rather small, just like in chapters 4 and 5. This justifies the use of the perturbative approach a posteriori.
For the kink case a linear dependence of the total dissipated energy with $(m/m_H)^{-1/2}$ over the whole range of masses considered is found, just like in the case of H adsorption on metal surfaces in chapters 4 and 5. For the vacancy case, there is no such linear dependence over the whole range of masses considered. Instead, there appear two regions, one for large masses, and one for low masses. The border between the regions is around 10 atomic mass units (amu). Although a linear behavior is found in each of the regions, such a behavior can not be extended to the whole range of investigated masses. The reason for this is found considering the low-energy regime of the spectra ($\varepsilon < 0.3$ eV) in Figs. 6.8 and 6.9, which dominates the dissipated energy. In the kink case the height-width ratio of the central peak is smaller than in the vacancy case. Thus in the kink case large e-h pair energies are more important than in the vacancy case. This means that the dissipated energy is dominated by a smaller energy range in the vacancy case than in the kink case. Depending on whether or not electron and hole states are found in this energy range around the Fermi energy, excitation of electron-hole pairs may be

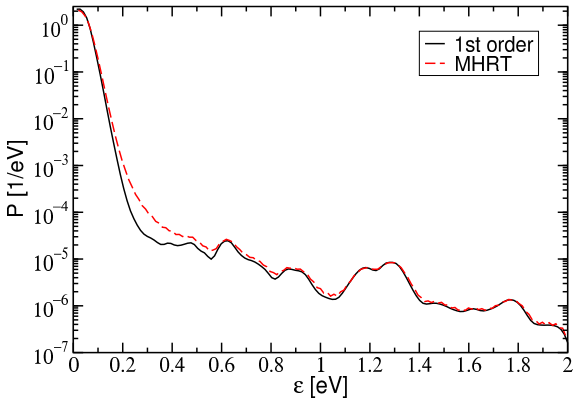


Figure 6.11: Excitation spectra of electron-hole pairs for an impinging Mg atom with an initial kinetic energy of 30 meV impinging onto the vacancy position of a relaxed Mg(0001) surface after one half round trip in the chemisorption well. The curve calculated in first-order perturbation theory is compared with the curve obtained by a resummation of the perturbation expansion following Müller-Hartmann *et al.* (MHRT). The spectra are close enough for the perturbative approach still being sufficient in the energy range above 0.5 eV, which is the important region for calculating the particle yield. Values close to zero energy ($\varepsilon < 0.0136$ eV) are not plotted (and omitted in the calculations) because of numerical inaccuracies in this energy range.

not possible. Keeping in mind that the surface band structure (Fig. 6.2) has gaps in parts of the band structure close to the Fermi energy, such a loss of mass-scaling for the vacancy case may be explained. The yield of electrons and holes above the Schottky barrier is shown per impinging Mg isotope for the first half round trip in the chemisorption well in Fig. 6.13 for the kink and vancancy case. A generalized scaling law (3.8) has already been introduced for H adsorption. If such a scaling law is also applicable for Mg adsorption, then the exponent in (3.8) can be determined by plotting $\ln\left|\ln(N_{e/h}^{\varepsilon_S})\right|$ vs. $\ln(m/m_H)$. This is done in Fig. 6.13. For the three heavy isotopes a linear relationship is found, yielding $\gamma \approx 1/28$ in the vacancy case, and $\gamma \approx 1/44$ in the kink case. This means, that the particle yield for heavier three isotopes is nearly independent on their mass. This was expected from the spectra of Figs. 6.8 and 6.9, since they are very similar above the Schottky barrier. Nonetheless a small effect still exists. For the three light isotopes no $\gamma$ is found in the vacancy case. In the kink case a fit is possible, yielding $\gamma \approx 1/6$, but not convincing due to comparatively large deviations of the data from the fit. In both cases the fit for the three light masses has a strongly different slope than the fit for the three large masses. This is explained by the importance of the central peak. For the low-mass isotopes, it is dominating the particle yield. For the large-mass isotopes, the central peak has diminished. A transition between the two regimes already begins around the tritium mass.

The yield of detected particles has also been tabulated in Table 6.1.

| | Vacancy | | Kink | |
|---|---|---|---|---|
| Isotope | Electrons | Holes | Electrons | Holes |
| $N(\mathrm{Mg}_{m_\mathrm{H}})$ | $8.095 \times 10^{-5}$ | $4.436 \times 10^{-5}$ | $2.744 \times 10^{-5}$ | $3.309 \times 10^{-5}$ |
| $N(\mathrm{Mg}_{m_\mathrm{D}})$ | $1.235 \times 10^{-5}$ | $0.865 \times 10^{-5}$ | $0.774 \times 10^{-5}$ | $0.836 \times 10^{-5}$ |
| $N(\mathrm{Mg}_{m_\mathrm{T}})$ | $8.34 \times 10^{-6}$ | $7.06 \times 10^{-6}$ | $5.17 \times 10^{-6}$ | $4.60 \times 10^{-6}$ |
| $N(\mathrm{Mg}_{0.5m_\mathrm{Mg}})$ | $4.15 \times 10^{-6}$ | $2.89 \times 10^{-6}$ | $1.23 \times 10^{-6}$ | $1.10 \times 10^{-6}$ |
| $N(\mathrm{Mg})$ | $3.27 \times 10^{-6}$ | $2.20 \times 10^{-6}$ | $0.98 \times 10^{-6}$ | $0.98 \times 10^{-6}$ |
| $N(\mathrm{Mg}_{2m_\mathrm{Mg}})$ | $2.20 \times 10^{-6}$ | $1.90 \times 10^{-6}$ | $0.64 \times 10^{-6}$ | $0.71 \times 10^{-6}$ |

Table 6.1: Average number of electrons and holes $N(m)$ above the Schottky barrier, created per impinging Mg isotope ($\mathrm{Mg}_{m_\mathrm{H}}, \mathrm{Mg}_{m_\mathrm{D}}, \mathrm{Mg}_{m_\mathrm{T}}, \mathrm{Mg}_{0.5m_\mathrm{Mg}}, \mathrm{Mg}, \mathrm{Mg}_{2m_\mathrm{Mg}}$) with an initial kinetic energy of 30 meV, per half round trip. Both the results for the vacancy and kink cases are shown.

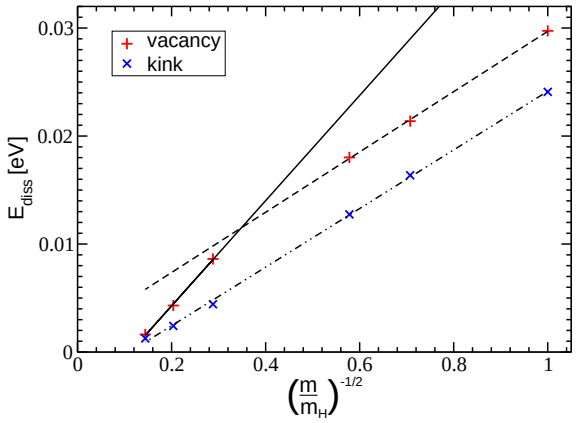


Figure 6.12: Total energy loss vs. the mass scaling parameter $1/\sqrt{m/m_H}$ for the kink and vacancy case. $m$ denotes the mass of the adsorbing atom. The lines are a linear fits to the data. On the data for the vacancy case, two lines are fitted, one for the limits of high mass, where the $^{24}$Mg isotope is found, and one for the regions of low mass, where fictitious isotopes of Mg with the masses of H, D and T are found. The fitted linear dependences are locally applicable, but not globally for all the masses in the vacancy case. For adsorption in the kink geometry, a linear dependence is found over the whole range of masses.

## 6.4 Discussion and conclusions

In previous chapters it was proposed that a generalized scaling law exists for adsorbates of low mass. In this chapter, the question whether a generalized scaling law for the chemicurrent exists for adsorbates of large masses can be decided.
In order to do so, it is assumed that the yield can be calculated using Eqs. (2.55) and (3.8), i.e.

$$N_{e/h} = A \exp\left(-\frac{\varepsilon_S}{k_B T_{\text{eff}}^H}\left(\frac{m}{m_H}\right)^{\gamma}\right). \tag{6.1}$$

Here, $A$ is a constant, $\varepsilon_S$ is the Schottky barrier, and $T_{\text{eff}}^H$ is an effective temperature fitted onto the slope of the Mg spectrum of the fictitious $\mathrm{Mg}_{m_\mathrm{H}}$ isotope (cf. Fig. 6.8). Also $\gamma$ is a parameter. For the surface vacancy, in the energy range $0.5\mathrm{eV} < |\varepsilon| < 2\mathrm{eV}$, for this isotope the effective temperature is 2359 K for electrons, and 2238 K for holes. For the kink, a temperature of 1647 K for electrons, and 1550 K for holes is obtained in the energy range $0.5\mathrm{eV} < |\varepsilon| < 1.2\mathrm{eV}$. If a generalized scaling law exists, then the data of Fig. 6.13 must fall onto a line for a single adsorption geometry. This is not the case.
So, unlike the case of H adsorption on metals, such a generalized scaling law for the chemicurrent is not found for adsorbing particles of large mass. Although (6.1) may be applicable in certain systems or in different regimes (here in a certain mass range), the equations seem not to be applicable generally. Instead it is found that every system should be investigated separately, especially when adsorbates of large masses are considered.
It is now the goal to compare predicted yields for hydrogen adsorption on metals with predicted yields for Mg adsorption on Mg. The yield is strongly dependent on the exact environment of the adsorbing atom. For instance, lifting the restriction of the $\theta$-function in (3.12), the yield of detected particles is only $N_e = 6.3 \times 10^{-6}$ and $N_h = 5.7 \times 10^{-6}$ for $\mathrm{Mg}_{m_\mathrm{H}}$ on-top, and $N_e = 4.2 \times 10^{-9}$ and $N_h = 3.0 \times 10^{-9}$ for Mg on-top, i.e. the yield is one order of magnitude ($\mathrm{Mg}_{m_\mathrm{H}}$) or three orders of magnitude (Mg) smaller than for the surface vacancy, cf. also Tab. 6.1 for comparison of the kink and vacancy case (including the $\theta$-function). The excitation probabilities for the hollow fcc case are $N_e = 1.6 \times 10^{-6}$ and $N_h = 0.9 \times 10^{-6}$ for $\mathrm{Mg}_{m_\mathrm{H}}$, and $N_e = 1.6 \times 10^{-7}$ and $N_h = 1.3 \times 10^{-8}$ for Mg. Thus a detailed comparison would require a detailed knowledge of the surface structure, so that an importance sampling of the data would be possible. Also it requires knowledge of all possible excitation mechanisms. As mentioned before, surface diffusion and subsequent electronic excitations when approaching steps and kinks may also play an important role. Also, it is not a foregone conclusion that the half

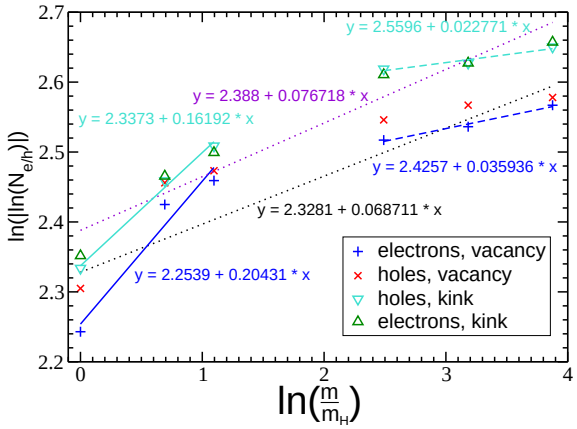


Figure 6.13: Yield of the electron and hole excitation spectra of the kink and vacancy positions plotted versus the mass $m$ of the adsorbing atom. Several fit lines are shown in the graph for the holes in the kink and vacancy geometries. In the vacancy case, the relation between the double-logarithm of the particle yield and logarithm of the scaled mass is linear for $\mathrm{Mg}_{2m_{\mathrm{Mg}}}$, $\mathrm{Mg}$ and $\mathrm{Mg}_{0.5m_{\mathrm{Mg}}}$ here, yielding Eq. (3.8) with $\gamma \approx 1/28$. It is not possible to find such a linear behavior for the lower three masses. For the kink case, the result is qualitatively similar, with $\gamma \approx 1/44$. However, the fit for the lower three masses is better than in the vacancy case.

round trip is representative for excitations of electron-hole pairs. But even if such a detailed study of excitation mechanisms was done, a similar study was required for hydrogen adsorption. Thus such a comparison is extremely involved. A direct comparison between theory and experiment is not possible at the moment, since the surface structures of the substrates are not well-known. However, solely within the theory, some conclusions may be drawn under certain assumptions.

The first assumption is, that the half round trip is representative for the excitation. The second is, that the exact excitation mechanism is not of further interest. In the long run, all adsorbates must dissipate the sublimation enthalpy into the system, at least on average. This may lead to similar electronic excitations. The third is, that e-h pair excitations in the case of H adsorption on metals are well-described by the on-top adsorption site. Note that this assumption is probably not well-justified [94]. However, a thorough investigation of this point remains to be done.

Regarding experimental results, experimentalists have measured a chemicurrent efficiency of around $10^{-3}\mathrm{e}_0$/atom for H/Ag [22] and $3.5 \times 10^{-5}\mathrm{e}_0$/atom for Mg/Mg [65]. However, since calculations for H/Ag were not done within this work, it is further not possible to compare directly to results for this system.

The following is a 'best-case' scenario, in terms of comparability.

In the case of hydrogen adsorption on Al(111) the chemisorption energy, 1.83 eV, was comparable to Mg adsorption on Mg(0001) in the surface vacancy case, 2 eV. This is also approximately true for the kink case in Mg and H/K(110), with 1.38 eV vs. 1.1 eV, respectively. However, Mg is much heavier than H, and moves slower in the chemisorption well. This has a direct influence on the spectra. In order to take this into account, the results for $\mathrm{Mg}_{m_{\mathrm{H}}}$/Mg(0001) adsorption are considered for comparison of Mg adsoprtion vs. hydrogen adsorption. The vacancy case is taken to compare results for H/Al(111) and Mg/Mg(0001). The kink case is taken to compare results for H/K(110) and Mg/Mg(0001). In the vacancy case, the particle yield in the $\mathrm{Mg}_{m_{\mathrm{H}}}$ case is approximately one order of magnitude smaller than for H/Al(111). In the kink case, the particle yield is of the same order of magnitude as in the case H/K(110). This yields between zero and one orders of magnitude for the chemical environment. Since the electronic structure of silver is more similar to Al than to K, one order of magnitude should be appropriate. From Tab. 6.1 the particle mass of $\mathrm{Mg}$ yields another one or two orders of magnitude. Thus the chemicurrent for Mg adsorption on Mg(0001) is at least two orders of magnitude smaller than in the case of H adsorption on metals. Considering H adsorption in the hollow position [94], and the assumptions of the 'best-case' scenarios above, it is probable that even a larger difference appears.

When calculating chemicurrents for Mg/Mg(0001) on-top adsorption, one finds that the chemisorption energy

is not sufficient to explain excited charge carriers. Lifting the restriction of the $\theta$-function in (3.12), a comparison between $\mathrm{Mg}$ and $\mathrm{Mg}_{m_\mathrm{H}}$ is possible for the on-top case too. It is found that the particle yield is three orders of magnitude smaller for $\mathrm{Mg}$ adsorption than for $\mathrm{Mg}_{m_\mathrm{H}}$ adsorption. Comparing absolute numbers for the on-top adsorption sites of Mg/Mg(0001) and H/Al(111), the chemicurrent efficiency for Mg adsorption on Mg may be up to six orders of magnitude smaller than in the case of hydrogen adsorption on metals. Such could not explain the experimentally observed current.
Finally, taking into account the hollow fcc site, the chemisorption energy is barely sufficient for excited charge carriers to pass the Schottky barrier. In order to compare to the above cases, one might assume that the chemisorption energy is fully transferred into electronic excitations of the metal slab. This is probably not justified for this homonuclear system, since phonons will be important. Neglecting this point, it is found that the chemicurrent is one (electrons) or two (holes) orders of magnitude lower than in the kink and vacancy cases. Thus, adsorption into the hollow fcc site can also not explain the measured chemicurrents.
Increasing evidence is found that the electronic excitation spectra consist of (at least) two parts. One part exists for small excitation energies, i.e. close to the Fermi energy for electrons or holes, or small energies of e-h pairs. This part lasts up to around a few tenths of an eV in the investigated cases. The other part is visible from this point on. It is decaying more slowly. Considering data for on-top adsorption in Fig. 6.10, where the decay of the spectra is much faster than in the vacancy and kink cases, and the resulting particle yield is much lower, it is found that the high-energy tails of the spectra are not dominated by numerical noise.
A possible interpretation of the form of the spectra is given by considering two distinct cases. Excitations of low energy are always possible in metals, and the effective potential is perturbed slightly over a wide area. Thus a large central peak with electronic excitations of low energy may be expected. Large-energy excitations are not as probable, and they require a hard impact of the adsorbate on the surface, i.e. they appear only close to the impact point. This means that two different excitation mechanisms may play a role in the nonadiabatic processes on the surface, which are both combined in the matrix elements. Also note the analytical considerations for the general form of the high-energy tail of the spectra, section 3.1.4.
It would be nice if a comparison could be done between theory and experiment with respect to the slope of the spectra in the total energy range. However, experimental measurements of the spectra have not been done up to now, which is, according to experimentalists, mainly due to the difficulties in changing the Schottky barrier in a metal-semiconductor diode.
The cohesive energy of bulk Mg is 1.51 eV [86], while the experimental sublimation enthalpy is 1.3 eV [65]. For comparison with theoretical numbers, the chemisorption energy of a kink was calculated, yielding 1.375 eV. Following the terrace ledge kink model [91, 92], this energy should be close to the sublimation enthalpy, and this is indeed the case. Also note that the mean average of adsorption energies for the hollow hcp site on the clean surface and the vacancy position is 1.27 eV, which corresponds well to the experimental sublimation enthalpy, too. Following the terrace ledge kink model this may be expected, since the model is based onto the number of nearest neighbours, which is 9 in the case of a surface vacancy, 3 in the case of a hollow site, and 6 for the kink. The mean average of 9 and 3 neighbours is 6.
To summarize, electronic excitations in adsorption of (fictitious) Mg isotopes on a Mg(0001) surface were calculated. It is found that adsorption on a perfect, clean surface can not describe the measured chemicurrents due to the limited energy available for the excitation of chemicurrents; however, introducing a defect, the chemisorption energy of an Mg atom adsorbing at this defect is sufficient to excite electrons and holes over the Schottky barrier. The experimental sublimation enthalpy corresponds well to calculations following the terrace ledge kink model.
A generalized scaling law for the chemicurrent was suggested from results of chapters 4 and 5 for low-mass particles. Results from the current chapter can not confirm its existence for different adsorbates of large masses. Instead the author must propose to calculate excitation spectra for every system under investigation separately.
A direct comparison is not possible between the predicted particle yield of the present chapter and experimental observations. Assuming a best-case scenario in terms of comparability between theory and experiment, the particle yield is at least two orders of magnitude smaller than in the case of hydrogen adsorption on metals. A less optimistic comparison even yields a difference of six orders of magnitude. However, judging from theoretical

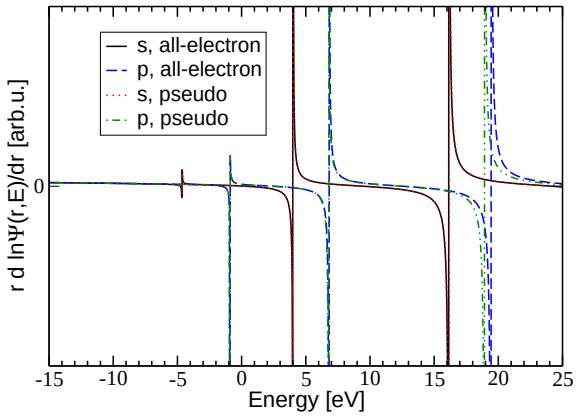


Figure 6.14: Comparison of the logarithmic derivatives of the all-electron and pseudo wavefunctions for the Mg pseudopotential. Over a range of approximately 22 eV, between -5 eV and 17 eV, the logarithmic derivatives of both wavefunctions are on-top each other. This gives an approximation for the energy range of validity of the pseudopotential.

results, observation of chemicurrents in metal epitaxy is in principle possible.

## Appendix 6.A Pseudopotential generation for Mg

For the plane-wave calculations of the present code, a PBE-GGA [39] pseudopotential was constructed, using the *atomic* code of the PWSCF package [41], and following the Troullier-Martins scheme [43]. For this potential, the '[Ne] $2s^2$ $2p^0$' configuration was chosen, including a nonlinear core-correction [44]. Relativity was taken into account using the scalar-relativistic method for the generation of the pseudopotential. The unoccupied p orbital was taken as the local channel. A radial cutoff of 1.06 Å (2.00 bohr) was chosen.
In order to check for ghost states, in Fig. 6.14 the logarithmic derivatives of the all-electron wavefunctions are compared to the logarithmic derivatives of the pseudo wavefunctions, for a radius of 4.23 Å (8 bohr). They are on-top each other in a range of approximately 22 eV, between -5 eV and 17 eV, so this energy range is probably okay for substrate calculations.

# Chapter 7

# Results: $Cl_2$ on K(110)

Chlorine itself is very reactive. Thus, when a Chlorine molecule adsorbs on a metal surface, measurement of huge chemicurrents is expected. This is especially the case for adsorption in alkali. For $Cl_2$ adsorption on potassium the chemical reaction $Cl_2 + 2\ K \rightarrow 2\ KCl$ is expected to happen. The chemicurrent might then show time-dependent features which identify this reaction. Thus in this chapter chlorine adsorption on a potassium surface is investigated.
Similar to chlorine, also oxygen is very reactive. Oxygen adsorption on alkali metal surfaces, with respect to chemicurrent generation, has already been investigated experimentally [83, 80]. Huge chemicurrents were measured. However, it is difficult to treat oxygen molecules on metal surfaces within the framework of DFT [69].
Some experiments have already been done on the adsorption of $Cl_2$ molecules on a potassium surface [82, 95, 96, 97]. It was found that even for low kinetic energies of the order of 0.1 eV of the $Cl_2$ molecule a reaction heat of at least 6 eV may be expected from such a reaction. The final result were (usually) $Cl^-$ atoms embedded in the potassium surface; however, emission of ions has also been observed [95]. Exoelectron emission has been observed during adsorption, and its probability is of the order $10^{-3}/Cl_2$ for these low kinetic energies.
The emission of exoelectrons was explained by the Nørskov-Newns-Lundqvist (NNL) model first developed in Ref. [98], and extended in subsequent work [99, 10, 96]. In this model, it was shown how molecular orbital correlation diagrams can be used to give a picture of halogen dissociation on alkali, and describe the measured chemiluminescence spectra during adsorption of $Cl_2$ on sodium [100]. Note that the jellium model for the K surface was used in this work. The chemiluminescence spectra were investigated further in Ref. [97].
In the following paragraph, the tentative picture of $Cl_2$ adsorption as suggested by the NNL model is recapitulated: According to the NNL model and its extensions the $Cl_2$ affinity level is not filled adiabatically. Instead, when the molecule is approaching the potassium surface, the $Cl_2$ molecule gets ionized only close to the surface, and starts to dissociate immediately thereafter. Through a combination of the increased nuclear separation and the increased screening of the ionic part of the molecular ion (the one closest to the surface), the affinity level of the neutral part of the molecular ion is shifted rapidly below the Fermi energy, and then below the bottom of the metallic band. This is comparatively easy in the case of a potassium substrate (in comparison to other metals with a broad conduction band below the Fermi energy, e.g. aluminium), since the bandwidth of the metallic band below the Fermi energy is small, just 2.1 eV. A second electron transfer is possible in this energy range, but not contributing to the exoelectron emission. Below the metallic band, the resonant filling of the affinity hole ceases, and only less-frequent non-adiabatic transitions from higher-lying states are possible. Therefore there is ample time for the affinity level to shift further downward, attaining a high excitation level resulting in high energetic (photons and) electrons, which may then be emitted [82]. The second electron is transferred into a molecular affinity level around 2-2.5 eV below the K band edge. Taking into account the bandwidth of 2.1 eV below the Fermi energy, this indicates a hole energy of 4.1-4.6 eV.
Far away from the surface, the $Cl_2$ molecule in its ground state has an affinity level which is about 0.1 eV below the K Fermi energy. Therefore ionization is energetically allowed at any distance, and the molecule should be ionized in adiabatic calculations. However, the $Cl_2^-$ bond length is about 2.5 Å, which is 0.5 Å larger

than the $Cl_2$ bond length. Thus the vertical affinity is about 1.3 eV above the Fermi energy of potassium, and transition of an electron from the K surface to the affinity level is energetically prohibited. The electron transfer is suppressed until the molecule is around 4 Å from the surface. At this moment, the vertical affinity of the $Cl_2$ molecule is shifted below the Fermi energy of potassium, and an electron is transferred to the molecule. This process is called 'harpooning' of the image-shifted molecular $Cl_2$ niveaus. For $Cl_2$/Na this was also commented upon in Ref. [101]. The distance at which the harpooning happens is dependent on the velocity of the $Cl_2$ molecule.
In Ref. [95] it was shown that abstraction and ballistic motion may appear during adsorption of the $Cl_2$ molecule, where both neutrals and charged particles may be emitted from the surface. The NNL model was further applied to $O_2$ adsorption on Li surfaces, with reasonable results [102, 103].
In this chapter it is investigated whether the perturbative approach of the present work can explain the amount of chemicurrent generated in adsorption of $Cl_2$ on K(110), and possibly give an alternative explanation for the observation of exoelectrons. The number of electrons per molecule is estimated, which should be observed in the experiments. However, since the amount of energy set free during adsorption is very large, it turns out that this system lies outside the range of validity of the perturbative method. The method is further restricted by the use of the unperturbed electronic structure of the clean surface for calculation of electronic excitations, since at the point where the constituents of the molecule come to rest, the electronic structure is not similar to that of the clean surface. Since the perturbative approch relies on the adiabatic PES, it does not taken into account the claim that the $Cl_2$ molecule behaves strongly nonadiabatic [82, 95, 96]. Therefore a diabatic picture, taking the potential energy surfaces (PES) of the $Cl_2$ and $Cl_2^-$ molecules into account, may provide a better picture of the adsorption process.
The involved dynamics at the surface during adsorption is a hint towards time-delayed chemical reaction, i.e. a chemical reaction long after the initial impact of the particle, leading to possible peaks in the chemicurrent long after the initial reaction. For $O_2$ adsorption on a potassium-covered Pd film such peaks appeared up to 100 s after the initial reaction [83]. Some general conclusions regarding the dynamics of the system $Cl_2$/K may be drawn.
Some general remarks on the constituents of the system $Cl_2$/K are found in section 7.1. A trajectory of a $Cl_2$ molecule adsorbing at the K(110) surface is calculated in section 7.2. The change of the Löwdin charge of the two atomic orbitals during adsorption is investigated, and it is estimated when ionization occurs. Also the trajectory itself is described. It is found that the jellium approximation for the K surface is probably very bad. In section 7.3 the results of the perturbative approach are presented, and it is demonstrated that a perturbative approach of higher order is needed to treat the electronic excitations of this system properly. Conclusions are drawn in section 7.4, where it is proposed that the excitation spectra follow a Lorentzian rather than exponential, which may be observable for slow and heavy molecules. Some remarks on the pseudopotential for Cl are found in section 7.A.

## 7.1 General Remarks on K, Cl and $Cl_2$

For the calculations in this chapter, adsorption of a $Cl_2$ molecule on a clean, perfect K(110) surface was considered. Results for the clean K surface have already been shown in sections 5.1 and 5.2. The calculated numerical convergence parameters are used within this chapter, too. Numerical calculations for the bond length and binding energy of the $Cl_2$ molecule are found in 7.A. The calculated bond length of the unperturbed molecule is 2.04 Å. Also the the lattice constant and bulk modulus of the KCl crystal is investigated there.
The calculated atomic energy levels for the Cl atom are -13.85 eV for the (3s) niveau, and -2.13 eV for the (3p) niveau, as a joint notation of the ($3p_x$), ($3p_y$) and ($3p_z$) orbitals. The molecular energy levels of the $Cl_2$ molecule are -23.2 eV, -19.3 eV, -11.8 eV, -9.8 eV, -9.8 eV, -7.4 eV and -7.4 eV in DFT calculations using the calculated bond length. According to Ref. [104], these can be attributed to the molecular orbitals $4\sigma_g(3s\sigma_g)$, $4\sigma_u(3s\sigma_u)$, $5\sigma_g(3p\sigma_g)$, $2\pi_u(3p\pi_u)$ twice and $2\pi_g(3p\pi_g)$ twice, respectively. An additional unoccupied molecular orbital, not calculated here, is labeled $5\sigma_u(3p\sigma_u)$. Here, the energy zero was determined as the Kohn-Sham potential far away from the molecule.

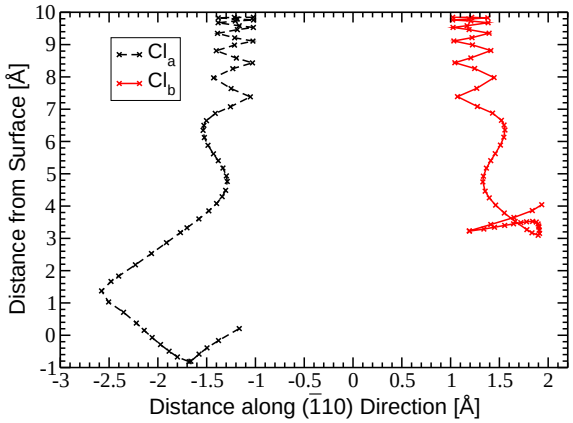


Figure 7.1: Adsorption trajectory of a $Cl_2$ adsorbing on a clean K(110) slab in MD. On the abscissa the distance between the molecule along the ($\bar{1}$10) direction is shown, i.e. along the long axis of the diamond-shaped bcc(110) unit cell. The axis of ordinate shows the distance of the atoms from the initial K surface. One of the Cl atoms ($Cl_a$) penetrates the surface, while the other atom ($Cl_b$) does not.

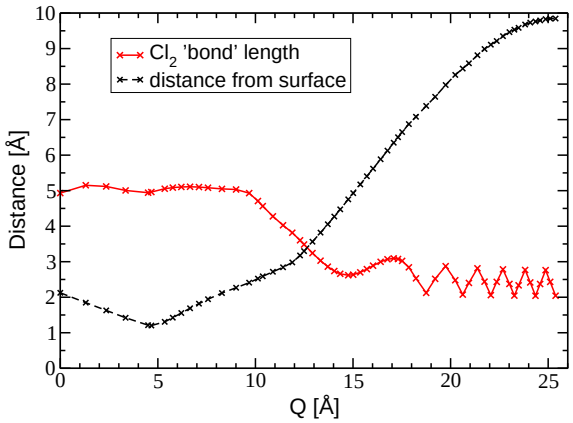


Figure 7.2: 'Bond' length and distance of the centre of mass-coordinate from the initial K surface for the impinging $Cl_2$ molecule versus the arc length $Q$. The Cl atoms are not bound to each other over the whole length of the trajectory, but only up to $Q \approx 13$ Å. The trajectory for calculations of the matrix elements (3.12) ends when the centre of mass speed changes its sign, similar to investigations of atomic adsorbates.

The equilibrium distance, centre of mass-coordinate and adsorption energy of a $Cl_2$ molecule standing upright on the K surface has been determined for the on-top and hollow positions in the rigid K surface approximation. In the calculations the $Cl_2$ molecule is relaxed until the final adsorption site reached. For the on-top position the equilibrium distance is 6.07 Å, the centre of mass is 2.80 Å above the surface, and the chemisorption energy, with respect to a molecule of the calculated equilibrium bond length far away from the surface, is 2.31 eV. For the hollow position the equilibrium distance is 3.29 Å, the centre of mass is 0.65 Å above the surface, and the chemisorption energy is 5.54 eV.

## 7.2 Adsorption Kinetics and $Cl_2$ during Adsorption

For calculation of the adsorption trajectory, one of the Cl atoms ($Cl_a$) was put above the hollow position 9.85 Å above the surface. The other Cl atom ($Cl_b$) was put at the equilibrium molecular distance of 2.04 Å in ($\bar{1}$10) direction, so that one of the Cl atoms is in the middle of the diamond-shaped unit cell of the bcc(110) surface,

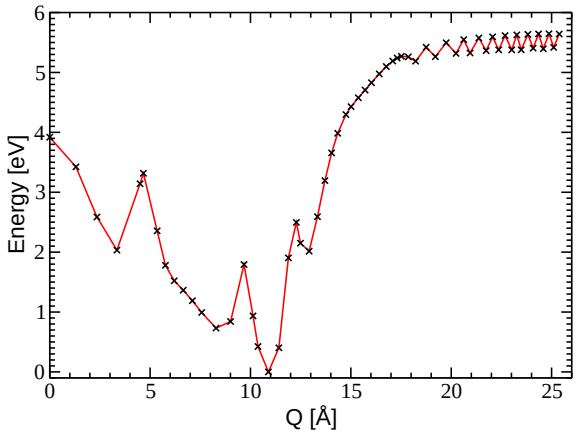


Figure 7.3: Adsorption energy of an impinging $Cl_2$ molecule on a K(110) surface for the trajectory of Figs. 7.1 and 7.2. One may observe several kinks in the energy curve, which are due to features of the trajectory. The energy difference between the largest and lowest points of the curve is 5.64 eV.

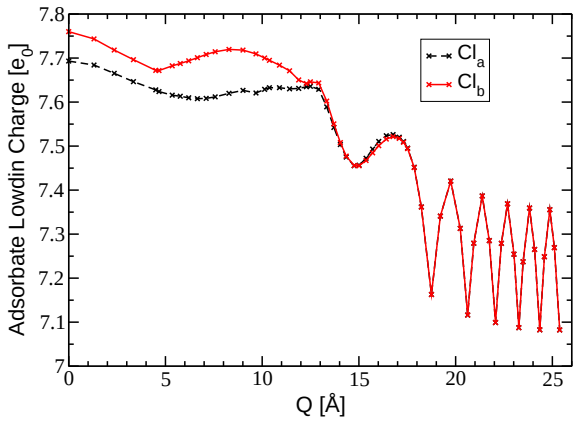


Figure 7.4: Occupation analysis of the Cl (3s) and (3p) (sum of ($3p_x$), ($3p_y$) and ($3p_z$)) atomic orbitals, together, for an approaching $Cl_2$ molecule vs. the arc length $Q$. The total Löwdin charge on the molecule is always greater than 14 electrons, depending on the distance between the atoms, and the distance from the surface. The point where the two atoms have different charge on them for the first time at $Q \approx 13$ Å is considered to be the point where the molecule breaks up.

and the molecular bond is pointing to a K atom on the 'long' edge of the unit cell. The atom then started moving towards the surface.

It was found that the chemisorption energy of $Cl_2$/K(110) is larger than 5 eV for adsorption for this geometry. The cohesive energy of K is around 0.8 eV [105]. A Cl atom has a mass of 35.4530 amu, and a K atom has a mass of 39.0983 amu.

Since the chemisorption energy is much larger than the K cohesive energy, and the mass of both nuclei are approximately equal, the frozen surface approximation for K is deemed to be insufficient for adsorption calculations. Therefore the trajectory of $Cl_2$ must be calculated by a direct approach. A possible approach is to calculate a multidimensional potential energy surface (PES) for $Cl_2$. However, from molecular dynamics calculations it can be shown that such a trajectory must be at least 2-dimensional for each Cl atom, and additionally at least 4 K atoms must be incorporated with at least 6 dimensions of movement, i.e. the resulting PES must be at least 10-dimensional. To calculate such a high-dimensional PES is too expensive even nowadays. So the trajectory was calculated using molecular dynamics (MD), which is implemented in the *PWSCF* package [41]. Using the initial geometry described above, the starting kinetic energy was chosen to be 0 meV, since it is usually negligible within the experiments.

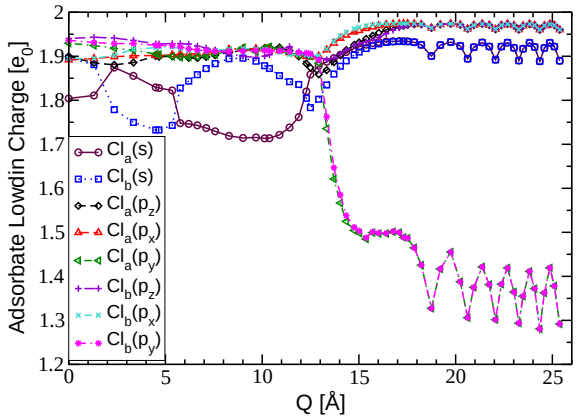


Figure 7.5: Occupation analysis of the Cl (3s) and ($3p_x$), ($3p_y$) and ($3p_z$) atomic orbitals, for an approaching $Cl_2$ molecule vs. the arc length $Q$. The charge has been calculated by integrating the PDOS up to the Fermi energy. Due to numerical inaccuracies the sum of the partial charges is lower than in Fig. 7.4. At $Q \approx$13 Å the molecule breaks up.

If adsorption was on a Na surface, according to previous work, the $Cl_2$ molecule is ionized by a harpooning process approximately at a distance of 10 Å from the surface [101]. The employed MD is not able to describe the transfer of a full electron from the surface to the molecule. Thus this process may lead to deviations of the calculated trajectory from the physical one. Therefore a simulation taking into account the diabatic PES of an ionized and non-ionized molecule, and a transition probability between the two PES, should be more appropriate. Such may be done in principle, e.g. within the framework of the 'fewest switches' algorithm [50]. Using the NNL model, for the K surface it is claimed that the harpooning process happens at around 4 Å from the surface, in a K jellium model [96]. Comparing the electron work functions for Na, which is 2.75 eV [106], and K, which is 2.25 eV [82], such a difference appears unlikely - it appears more likely that such an ionization should happen further away from the surface. However, taking into account the vertical affinity levels, this difference may be explained.
For the MD calculations, a fixed timestep of 5 fs was chosen. 48 K atoms in the 3 uppermost layers of a K slab were allowed to move, while the lower 5 layers remained fixed. The Cl molecule then started moving towards the surface, thereby oscillating. For different molecular bond lengths, the ionization and potential energy of the moving adsorbate changed. Although they were allowed to move freely, the Cl atoms only moved along the molecular bond length ($\bar{1}10$ direction, y) and towards the surface ($\overline{11}0$ direction, z), which is due to the symmetry of the calculation. The two coordinates (y, z) of each atom are shown in Fig. 7.1.
Along this trajectory 60 geometries were chosen and calculated using standard DFT. These geometries serve as the basis for further calculations.
The position of the atoms along the trajectory have been distilled into a single coordinate, the arc length $Q$, following (3.28). The number $N_{ad}$=50 of Eq. (3.28) is defined by the two adsorbing Cl atoms, plus the 48 moving K atoms. Of the 48 K atoms, most remain at their approximate starting position throughout the adsorption process, but some are experiencing a quite sizable change in their positions of the order of a few Å. The arc length is measured in such a way that a small number is close to the end of the trajectory, in the present case close to the surface. The distance between the two atoms and the distance of the centre of mass of the molecule from the (initial) K(110) surface are shown in Fig. 7.2. The oscillation amplitude of the molecule far away from the surface is roughly 0.4 Å. The classical trajectory of the impinging $Cl_2$ molecule for the calculations of the matrix elements (3.12) is calculated until the turning point for the centre of mass-coordinate is reached. This roughly resembles a single atom scattered back from the surface.
Several snapshots of the system along the trajectory are shown in Fig. 7.9 from different directions. One may observe that the dynamics is quite complex and involved.
The potential energy of the system along $Q$ is shown in Fig. 7.3. The potential energy is oscillating due to the

molecule's oscillations, with twice the frequency.
An occupation analysis of the Cl atomic orbitals was done using the Löwdin approach implemented in *PWSCF*. The result is shown in Figs. 7.4 and 7.5. While the total charge in Fig. 7.4 may be obtained directly from the calculations, it is necessary to integrate the PDOS up to the Fermi energy to calculate the charges in each orbital. This leads to numerical inaccuracies, so that the sum of the charges in the atomic orbitals (Fig. 7.5) is smaller than the total charge on each atom (Fig. 7.4). The atomic ($3p_x$) orbital is in the initial bond direction of the molecule in the chosen geometry, while ($3p_z$) is pointing towards the surface, and ($3p_y$) is parallel to the surface, but perpendicular to the molecular bond. One may observe that the number of electrons located on the different Cl atoms is changing with the 'bond' length between them, as long as the molecule is far away from the surface, where a large 'bond' length gives room for additional electrons. The electrons are mostly added to or subtracted from the ($3p_x$) orbital, which points into the direction of the molecular bond. Note that the molecule is not bound any more close to the surface. Not considered here is a possible nonadiabatic occupation of the Cl atomic levels, e.g. due to a delayed harpooning due to the vertical affinity level. The Löwdin charge at the atoms gets larger when the atoms are close to the surface. A surprising result is that the (3s) orbitals seem to strongly change their occupation during the adsorption process. However, comparing to the PDOS calculations shown in Fig. 7.10 it may well be, that this is just a numerical issue, since at least the main parts of the (3s) orbitals are well below the Fermi energy.
Taking into account information from Figs. 7.1, 7.2, 7.3 and 7.4, around 7.5 Å from the surface, at $Q \approx 18$ Å, the $Cl_2$ molecule is accelerated very much, gaining a kinetic energy of roughly 3.5 eV up to $Q \approx 13$ Å. At $Q \approx 13$ Å, when one of the atoms ($Cl_b$) is about 3 Å from the surface, the molecule seems to break up, so that the molecule does not exist in a strict sense any more.
The Löwdin charge still behaves similar for both atoms from this point on. However, the $Cl_b$ atom which is further away from the original (110) surface gets a larger Löwdin charge in adiabatic calculations. This is a direct contradiction to the claim of the NNL model that the charged particle is closer to the surface. However, the K atoms in the surface are also moving, which is not taken into account in the K jellium model employed in the NNL calculations. The other atom ($Cl_a$) penetrates the surface 0.8 Å deep, and is repelled at $Q \approx 5$ Å. This is the position where the calculation of the trajectory stops in the perturbative approach, since the centre of mass-coordinate of the $Cl_2$ molecule changes its direction of movement here, too. This point is labeled the first reflection point.
For curiosity, the MD has been continued for some time after this point. (This is not shown here.) The surface is heavily perturbed even after the first reflection point, experiencing an even more complex and involved dynamics. Generally spoken, the $Cl_a$ atom penetrates even further into the slab. The $Cl_b$ atom is involved in a dynamics with several K atoms at or above the surface, thereby slowly moving away from the original (110) surface in the median, but taking a few K atoms with it. It appears there is a certain chance that particles may be ejected from the surface again, which could be K atoms or even a KCl molecule, but also (ionized) atomic Cl. Such is also found experimentally in Ref. [95]. However, the jellium model employed for the K surface in Ref. [95] appears to be unjustified, due to the large perturbation of the surface. Judging from a thorough investigation of the MD results, it is well-justified to claim that the surface explodes after initial impact of the $Cl_2$ molecule.
The projected density of states (PDOS) on the Cl (3s) and (3p) (sum of ($3p_x$), ($3p_y$) and ($3p_z$)) atomic orbitals during adsorption of $Cl_2$ on K(110) is shown in Figs. 7.11 and 7.10. The PDOS is shown for several points along the adsorption trajectory, measured by the arc length $Q$. Far away from the surface, the PDOS of both atoms are on-top each other. At $Q \approx 13$ Å, the two PDOS start to differ. However, this is a continuous process. At the point of lowest energy, at $Q = 11$ Å, the PDOS of both atoms show significant differences. This finding strengthens the suggestion that the molecule breaks up at $Q \approx 13$ Å. The centre of mass-coordinate is 3.5 Å above the surface at this point, with both atoms being at approximately the same height. The 3.5 Å calulated here are in concordance with results from the K jellium model, where the molecule becomes ionized at around 4 Å from the surface [96], and dissociates thereafter. However, a first ionization of the molecule may still have happened before. It may also be observed that the (3p) states change from distinct molecular type states far away from the surface to a broadened merged state when the Cl atoms are close to the surface. For an

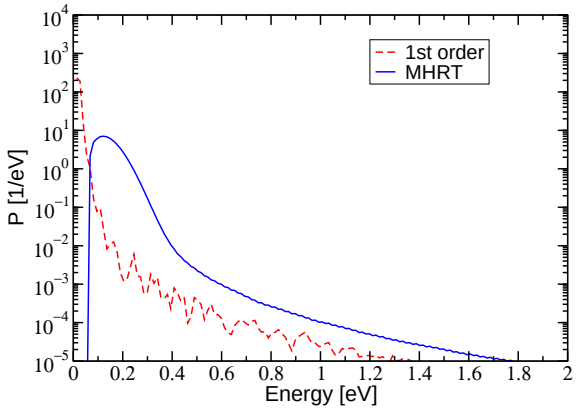


Figure 7.6: Comparison of the excitation spectra of electron-hole pairs for an impinging $Cl_2$ molecule onto the K(110) surface with an initial kinetic energy of 30 meV after the first backscattering of the molecule from the surface. The curve calculated in first-order perturbation theory is not similar to the one obtained by a resummation of the perturbation expansion following Müller-Hartmann *et al.* (MHRT). Values close to zero energy ($\varepsilon < 0.0136$ eV) are not plotted (and omitted in the calculations) because of numerical inaccuracies in this energy range. The MHRT-curve has been calculated by subtracting an overlying oscillation, caused by numerical evaluation issues, and is set to zero close to the energy zero ($\varepsilon < 0.06$ eV), justified by taking into account analytical results.

assignment of the peaks to the molecular orbitals, cf. section 7.1.

## 7.3 Results

The adsorbing molecule's trajectory was started at $Q$ =25.38 Å, with an initial kinetic energy of 30 meV towards the surface. The maximum energy available for excitation of electron-hole pairs is then $E_{\max}$ =5.67 eV. Note that this initial kinetic energy has negligible influence on the trajectory, but is introduced for numerical stability. The trajectory was defined by the 60 geometries calculated using standard DFT, which were in turn distilled from the molecular dynamics calculation of section 7.2. The velocity along the arc length was calculated following section 3.4. The calculation stops at the first reflection point, where the centre of mass-coordinate of the molecule is moving away from the initial surface for the first time, at $Q$ =4.69 Å.

In previous chapters the reflection point of the trajectory was a well-defined quantity, resting on the rigid surface approximation for the substrate, and an atomic adsorbate. For the complex dynamics of molecular $Cl_2$ adsorption on K(110), this no longer holds. However, observing the centre of mass-coordinate of the molecule, and defining reflection points using this coordinate, is reasonable.

An important result of the calculations is the comparison between the perturbative approach and the treatment by Müller-Hartmann (MHRT) and co-workers [56] that sums up all orders in the perturbation expansion, Fig. 7.6. Since the two approaches yield different results, it is found that first-order perturbation theory is not sufficient to describe the excitation spectrum of e-h pairs.

Such a finding could be expected from two considerations: First, the chemical binding energy of $Cl_2$ on K(110) is around 5.5 eV, being approximately 7 times larger than the cohesive energy of K. Therefore a large distortion of the surface should be expected during adsorption. Second, MD simulations demonstrated that the dynamics at the surface is very involved. Thus many opportunities exist to excite electron-hole pairs, when two atoms collide, many more than in 'simple' systems like H adsorption on metals with thermal kinetic energy. One must conclude that a low-order perturbative approach is unlikely to be close to a treatment that sums up all orders in the perturbation expansion in the case of $Cl_2$/K(110).

The energy dissipation into the electronic system is 0.12 eV within the perturbative and MHRT approaches.

Although the first-order approach is insufficient, one may get a rough impression on the importance of elec-

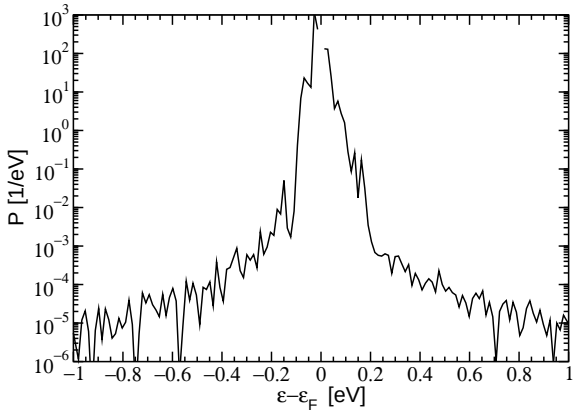


Figure 7.7: Excitation spectra of electrons and holes for $Cl_2$ with an initial kinetic energy of 30 meV adsorbing on the K(110) surface after the first backscattering of the molecule from the surface. Values close to the Fermi energy ($\varepsilon - \varepsilon_{\mathrm{F}} < 0.0136$ eV) are not plotted (and omitted in the calculations) because of numerical inaccuracies in this energy range. The more pronounced oscillations in the graph when comparing to spectra in previous chapters are caused by a reduction in the broadening of the $\delta$-function used for plotting. This was necessary due to numerical issues caused by the extremely large excitations close to the Fermi energy.

tronic excitations if one compares the perturbative results for adsorption of $Cl_2$/K(110) with results from chapter 5, where H adsorption on K(110) was investigated. Therefore the electron and hole spectra for adsorption of $Cl_2$, calculated by the perturbative approach, are shown in Fig. 7.7. The qualitative behavior is different than observed in the case H/K(110). The high-energy tail for $Cl_2$ may be roughly following a Lorentzian distribution, cf. section 3.1.4, while in the H case the high-energy tail of the distribution is roughly exponential on the investigated scale. The spectrum for $Cl_2$/K(110) is comparable to the spectrum in the case Mg/Mg(0001), Fig. 6.8. However, keep in mind that the calculated distribution in the $Cl_2$ case is not the distribution in experiments, since only the lowest order in the perturbation expansion is taken into account in the theoretical calculation. Taking into account higher orders in the perturbation expansion, the distribution should qualitatively follow the MHRT-case of Fig. 7.6.

Obviously very large excitations occur. Assuming a Schottky barrier height of 0.55 eV, taken from experiments, one gets a number of excited electrons (holes) of $N_e = 1.4 \times 10^{-5}$ ($N_h = 1.1 \times 10^{-5}$) in first order. These numbers are smaller by a factor of 4 for electrons and 3 for holes than in the case H/K(110). However, the excitation probability in the MHRT case of Fig. 7.6 is approximately a factor 10 larger than in the perturbative case around the Schottky energy. Therefore, these numbers should be multiplied by a factor of 10, too, to account for the higher orders in the perturbation theory. Thus the author believes that the number of detectable electrons or holes in the case $Cl_2$/K(110) will be about a magnitude larger than in the case H/K(110) until the first reflection point. However, real experiments may detect a current which is even larger, since the chemical reaction at the surface has just started at the point where the movement of the molecule is stopped in the theoretically investigated case here. The chemisorption energy is so large that multiple high-energy excitations may occur.

This is underlined by the perturbative result for exoelectron emission, where $3 \times 10^{-7} e_0/Cl_2$ are found above the work function of potassium. By simply integrating the MHRT curve of Fig. 7.6 one gets $9 \times 10^{-7}$ e-h pairs/$Cl_2$ above the work function. Both numbers are much smaller than the experimental result of approximately $1 \times 10^{-3} e_0/Cl_2$ [96]. According to Ref. [96], steering effects through orientation of the molecule play a dominant role for exoelectron emission. This may explain the quantitative difference, see discussion.

## 7.4 Discussion and Conclusions

In this chapter it was proven that the system $Cl_2$/K(110) lies outside the range of validity of the perturbative approach of first order. An exothermic chemical reaction occurs at the surface, when the $Cl_2$ bond is broken. This leads to the availability of a large amount of energy of the order of 5 eV for excitation of electron-hole pairs, and thus chemicurrents may be large in this case in comparison to the case of hydrogen adsorption on metals. In the case of $O_2$ adsorption on Na and K, different chemical processes contribute to the chemicurrent, leading to time-dependent changes in the chemicurrent [80, 83]. Thus for $Cl_2$ adsorption on K(110) also different chemical processes may contribute to the chemicurrent. This is underlined by calculation of the adsorption trajectory, where a very complex dynamics is found. Nonetheless some statements can be made for the system $Cl_2$/K(110), especially from calculation of the trajectory.

The potential energy of the $Cl_2$ molecule adsorbing at the surface is already so large that the surface can be massively perturbed, being roughly seven times the cohesive energy of K. Thus, even without a large initial kinetic energy of the molecule abstraction of particles from the surface may occur. This proves that the jellium approximation for K employed in previous approaches [95, 96] is unjustified here. It also leads to the problem of justification of taking the unperturbed electronic structure for calculation of excitations in the perturbative approach, since the final structure of the surface is very different from the unperturbed one.

Each of the two Cl atoms is ionized close to the surface. The Löwdin charge of the adiabatic ground state of the $Cl_2$ molecule is investigated in Fig. 7.4 at several positions above the surface. If one takes the sum of the Löwdin charges of the atoms, averaged over one oscillation if $Q >$18 Å, as the charge of the molecule, it already starts singly ionized far away from the surface. This is in accordance with the adiabatic affinity level being 0.1 eV below the Fermi energy of potassium. This summation is not reasonable any more, when the molecule breaks up at around 4 Å above the surface. Each of the atoms should be treated separately after this point. The Löwdin charge of every atom is close to 8 at this point. Therefore adiabatic calculations suggest that both atoms are negatively ionized from this point on. However, non-adiabatic electron transfer effects may play an important role here. Far away from the surface the vertical affinity of the molecule is larger than the Fermi energy, which means that the transition probability of an electron from the surface to the adsorbate is zero. In adiabatic calculations the transition probability is not taken into account. Therefore in adiabatic calculations such a forbidden transition can only be described by constraining the charge at the molecule. Nonetheless, at some point close to the surface the electron transfer happens. One way to describe this delayed charge transfer is the use of diabatic PES, where ionized and non-ionized PES of $Cl_2$/K are investigated, and calculation of a transition probability between the two states. It is claimed that such a treatment describes the system better than standard adiabatic calculations [95, 101]. However, a treatment where TDDFT is used, starting from a non-ionized $Cl_2$ molecule far away from the surface, might also work, if the low transition probability is respected within these calculations, and thus the transition of an electron only occurs close to $Q = 4$ Å.

Considering the differences between the perturbative and experimental results for exoelectron emission, it seems obvious that strong nonadiabatic effects are not taken into account in the perturbative approach. According to the NNL model, and its extensions [98, 99, 10, 96], the $Cl_2$ affinity level is not filled adiabatically; see the introductory part of this chapter for details.

Note that the probability for exoelectron emission depends on the orientation of the molecule on the potassium surface. When the molecular axis is parallel to the surface, as in the investigated case here, the probability for exoelectron emission is of the order $10^{-4}$ to $10^{-5}$/molecule in the NNL model, since the resonance filling of the $Cl_2$ affinity level is then very effective [96]. An order of $10^{-6}$/molecule is predicted by integrating the MHRT curve, for a trajectory which ends at the first reflection point. However, the trajectory of the $Cl_2$ molecule continues after this point, which is not close to the final configuration. Thus the results of the MHRT approach are at least comparable to the results from the NNL model calculations. For an oblique orientation in the range of $10 - 30$ degrees, the NNL model predicts an excitation probability of the order of $10^{-1}$/molecule. This larger probability is due to the faster approach of the $Cl^-$ close to the surface due to intramolecular repulsion within the $Cl_2^-$ molecule. Thus it is caused by the non-adiabatic excitation of holes by image-shifting the affinity level rapidly below the Fermi energy and metallic band edge. This mechanism is not included in the MHRT approach

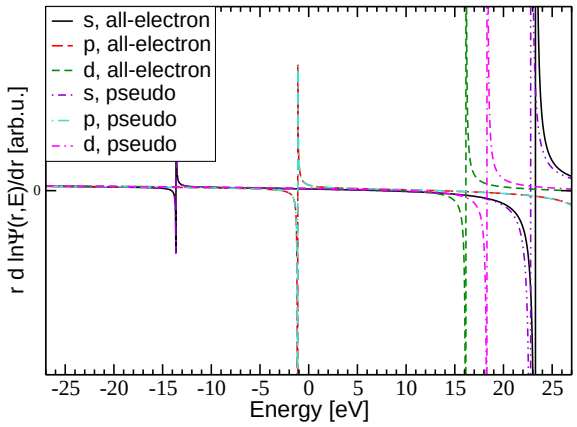


Figure 7.8: Comparison of the logarithmic derivatives of the all-electron and pseudo wavefunctions for the Cl pseudopotential. Over a range of approximately 26 eV, between -16 eV and 10 eV, the logarithmic derivatives of both wavefunctions are on-top each other. This gives an approximation for the energy range of validity of the pseudopotential.

of the present work, and thus results from the NNL model and the perturbative approach are probably not of a similar order of magnitude any more. However, this mechanism may not be dominating for all orientations of the molecule, especially when the molecular axis is parallel to the surface, as is the case in the present chapter. Additionally, in the model calculations the physical dynamics of the molecule-surface system was not taken into account. Instead, a rigid surface approximation, combined with intra-molecular Morse potentials and ion-surface image forces were used [95]. Taking into account the physical dynamics might change some results of the NNL model, especially with respect to the importance of the image-shifting of the affinity level, and is probably worth investigation.
The energy dissipation into the electronic system is of the order of 2 % of the chemisorption energy in the perturbative (and MHRT) approach until the first reflection point, but the absolute value is 0.12 eV. This is not small any more, and an additional indicative that the perturbative treatment fails.
The general form of the spectrum was found to be comparable to the case Mg/Mg(0001), being roughly Lorentzian rather than exponential, at least in the experimentally relevant energy range larger than the Schottky energy of roughly 0.5 eV. Results for H adsorption of chapter 5 are compatible with such a claim, if one takes the observable change of slope around 0.5 eV seriously. This justifies the tentative proposal of section 3.1.4, that the general form of the spectrum might be similar for all adsorbates, and be following a Lorentzian rather than an exponential with some temperature.
Generally the author proposes to treat $Cl_2$/K(110) with a method different from the perturbative approach of this work. One of these approaches might be implementation of a higher order in the perturbation theory. Such an approach must take into account the time-dependence of the electronic structure during adsorption, maybe similar to the approach presented in section 2.3.2. Alternatively, a non-perturbative approach, like TDDFT, may be thought of. Some possible approaches are shortly proposed in chapter 8.

## Appendix 7.A Pseudopotential construction and tests

The Cl pseudopotentials were constructed using the *atomic* code delivered within the *PWSCF* package [41] following the Troullier-Martins scheme [43]. Only the (3s) and (3p) states were taken into account as valence states. Since later calculations using a K surface were taken into account, the occupation of the (3p) states was chosen as 5.7 electrons instead of 5 electrons for the pseudopotential construction, i.e. an ionized Cl was taken as reference: [Ne] $3s^2$ $3p^{5.7}$. The cutoff radius was chosen as 0.85 Å (1.6 bohr). The PBE approximation was used for the exchange-correlation potential [39]. Relativity was taken into account using the scalar-relativistic method for the generation of the pseudopotential.

In order to check for ghost states, in fig. 7.8 the logarithmic derivatives of the all-electron wavefunctions are compared to the logarithmic derivatives of the pseudo wavefunctions, for a radius of 2.12 Å (4 bohr). They are on-top each other in a range of approximately 26 eV, so this energy range is probably okay for the present calculations.
The pseudopotentials were tested by calculating the lattice constant of KCl and its bulk modulus. The results for a cutoff of 272 eV (20 Ry) were 6.37 Å for the lattice constant and 17.3 GPa for the bulk modulus, which is compared to a cutoff of 408 eV (30 Ry), where 6.37 Å and 17.2 GPa were obtained, respectively. The experimental values are 6.20 Å and 20.8 GPa, respectively, and the calculated results are within the limits of other ab initio methods [107].
Using a cutoff of 340 eV (25 Ry), the binding energy of a $Cl_2$ molecule for the experimental molecular bond length of 1.99 Å in a large box was calculated. An energy of 65 kcal/mol (2.8 eV) was obtained. Calculations using the Vienna ab initio simulation package (VASP) [108] gave the same result [109]. Therefore the difference to the literature values for the PBE approximation, which gives a value of 63 kcal/mol [39], can be attributed to the pseudopotential approximation. The experimental result is 58 kcal/mol for this molecule. The relative difference of 12 % is not overly satisfying, but the PBE functional cannot do better.
The calculated bond length for the molecule was 2.04 Å. The relative difference of 2.5 % is acceptable.

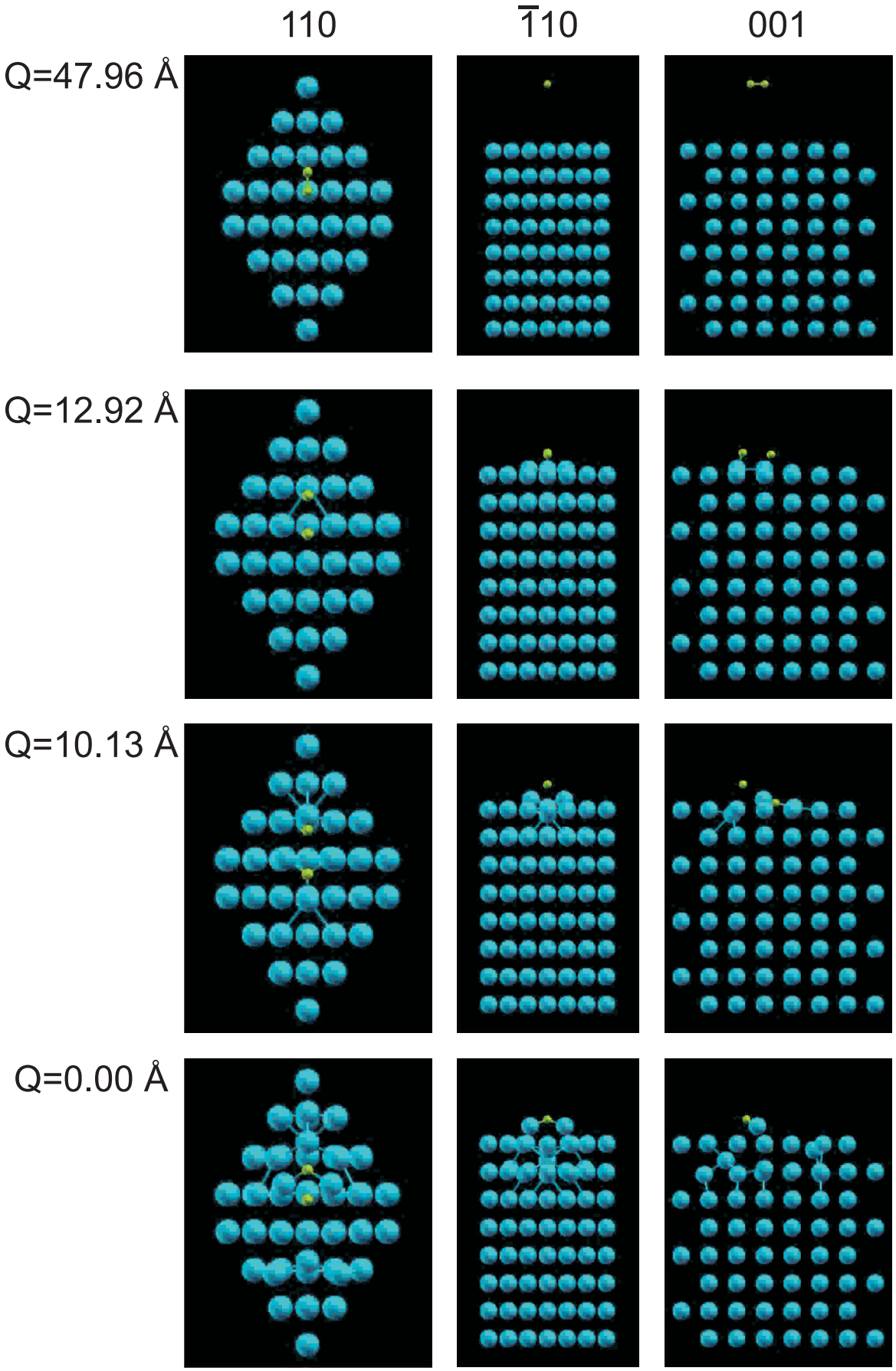


Figure 7.9: Several geometries of the $Cl_2$/K(110) system along the adsorption trajectory of $Cl_2$/K(110). The length of the trajectory is measured by the arc length $Q$, where $Q$=0 is the end of the trajectory. The system is shown from the (110), ($\bar{1}$10) and (001) directions.

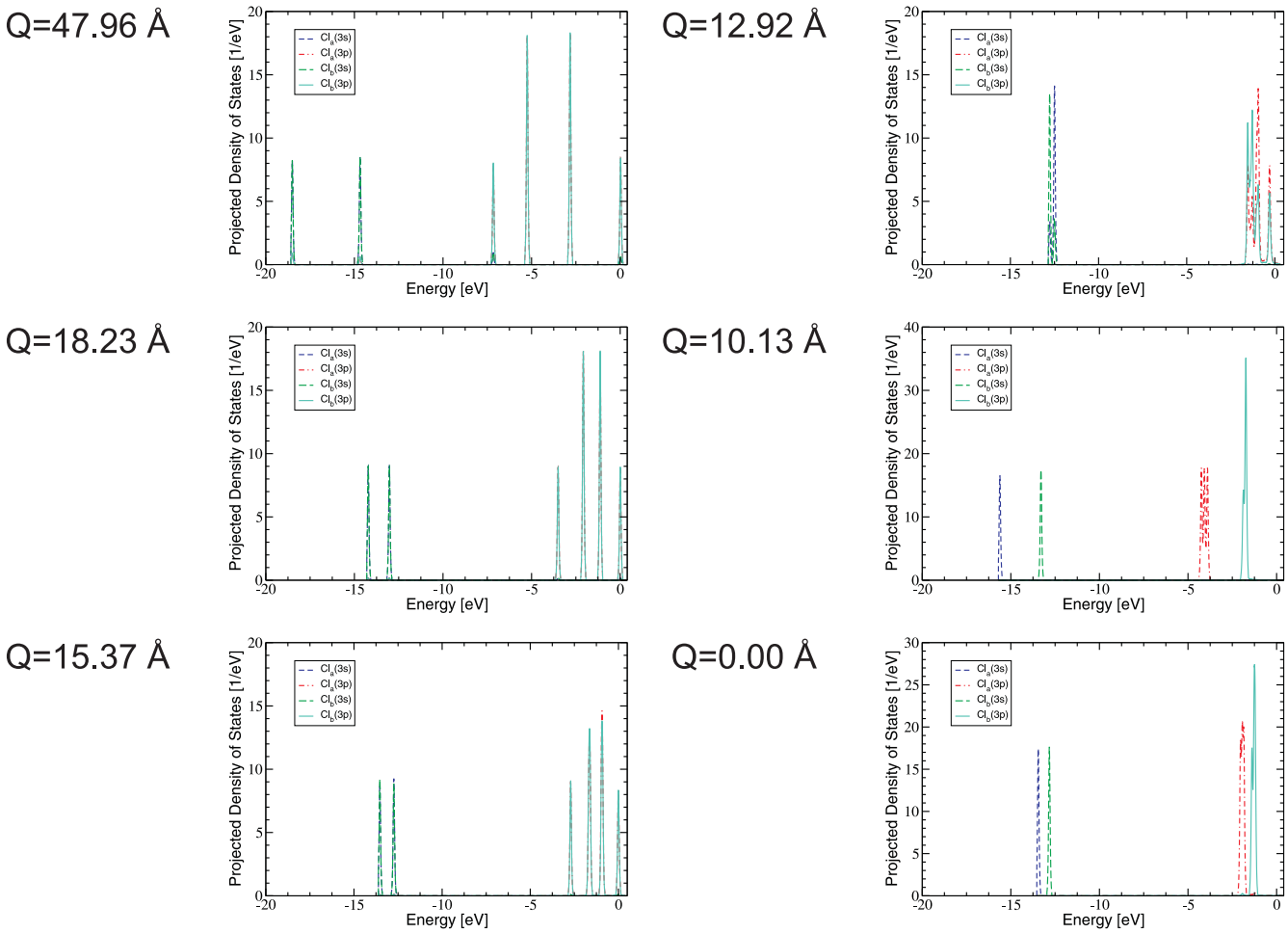


Figure 7.10: Projected density of states (PDOS) on the Cl (3s) and sum of the ($3p_x$), ($3p_y$) and ($3p_z$) atomic orbitals, labeled (3p), over the total energy range where Kohn-Sham energies are found in the calculations of $Cl_2$ on K(110). The PDOS are shown for several positions along the trajectory, measured by the arc length $Q$, where $Q$=0 is the end of the trajectory. The Fermi energy is set to zero. Note that $Q \approx$13 Å is considered to be the point where the molecule breaks up. The PDOS of the two Cl atoms are on-top each other up to the point where the molecule breaks up, but this is difficult to observe within this graph. Section 7.1 allows to assign molecular orbitals to the states, while the molecule is far from the surface. Fig. 7.11 shows the PDOS over the energy range of the K conduction band below the Fermi energy.

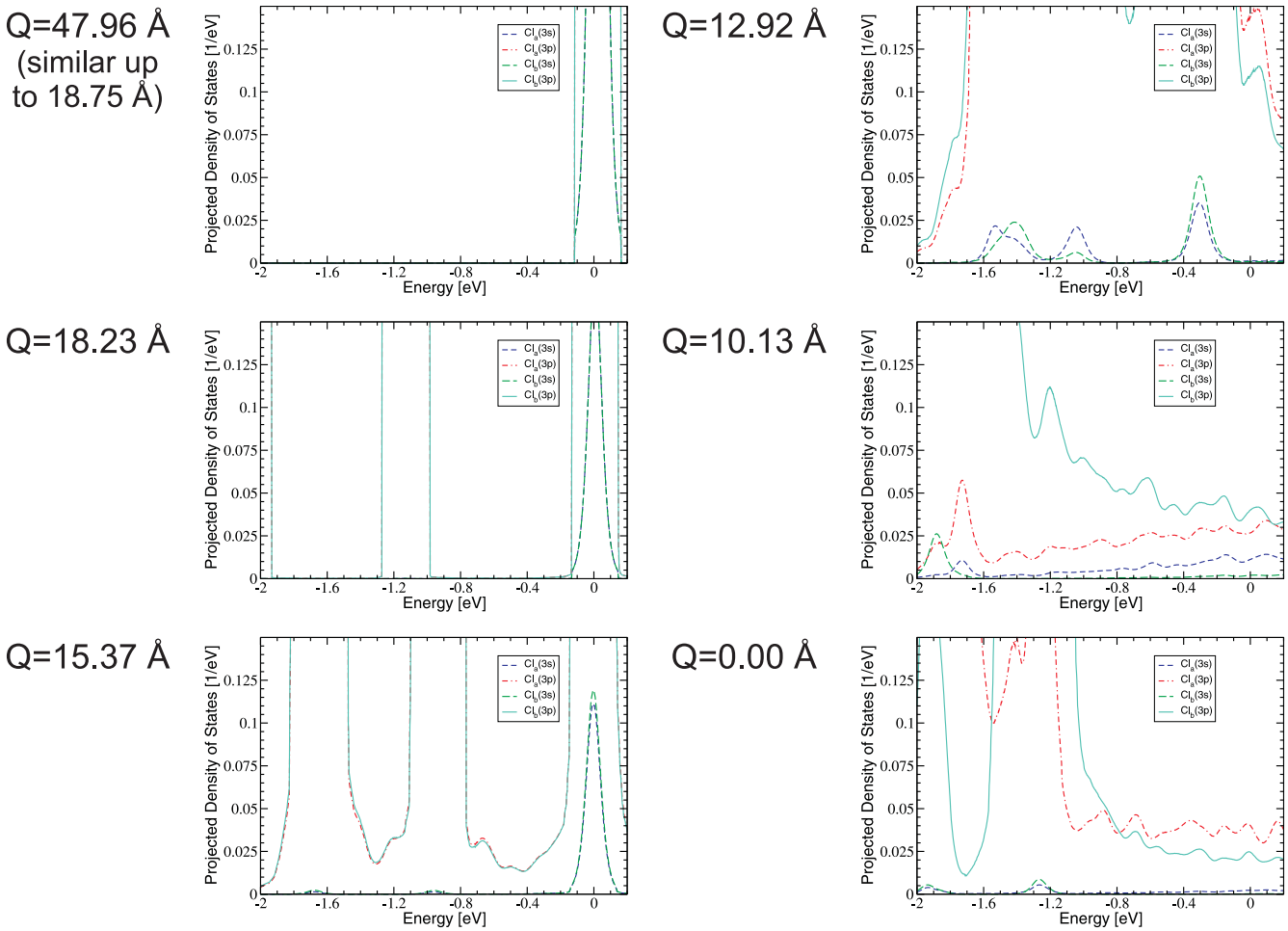


Figure 7.11: Projected density of states (PDOS) on the Cl (3s) and sum of the ($3p_x$), ($3p_y$) and ($3p_z$) atomic orbitals, labeled (3p), in the energy range of the K conduction band below the Fermi energy (Fig. 5.6), during adsorption of $Cl_2$ on K(110). The PDOS are shown for several positions along the trajectory, measured by the arc length $Q$, where $Q$=0 is the end of the trajectory. The Fermi energy is set to zero. Note that $Q \approx$13 Å is considered to be the point where the molecule breaks up. Up to $Q$ =18.75 Å the PDOS changes only slightly in this energy range. The PDOS of the two Cl atoms are on-top each other up to the point where the molecule breaks up, but this is difficult to observe within this graph. Fig. 7.10 shows the PDOS over a wider energy range.

# Chapter 8

# Discussion und Final Remarks

Within this work, several aspects of electronic excitations at surfaces during adsorption of particles have been treated. A perturbative approach to treat electronic excitations has been investigated thoroughly.
The results of this thesis are summarized within this chapter, and an outlook on possible future projects is given.
The perturbative approach can describe spectra for electron and hole excitations in adsorption.
The author has investigated hydrogen and deuterium adsorption on aluminium, as a system similar to hydrogen and deuterium adsorption on silver. The experimentally measured isotope effect of the latter system is theoretically found in the former system. Thus the isotope effect is described within experimental error bars.
For each system it is investigated whether the perturbative approach of first order is sufficient to describe the electron-hole pair excitation spectra, which may also be calculated by summing up all orders in the perturbative expansion. With the exception of molecular adsorption of $Cl_2$/K, for all investigated systems (H/Al, H/K, Mg/Mg) it was found that the perturbative approach of first order is already sufficient. For $Cl_2$/K the calculated dissipated energy into the electronic system is larger than in the other three investigated cases. Also the chemisorption energy for this system is roughly three times the chemisorption energy of the other cases, and seven times as large as the cohesive energy of potassium. It may be concluded that the perturbative approach of first order is insufficient if the investigated reaction is too exothermic. Comparing data for H/Al, Mg/Mg (vacancy case) and $Cl_2$/K, a chemisorption energy of up to roughly 3-4 eV marks the energy range of validity for the perturbative approach.
The energy dissipation is probably underestimated in the perturbative approach, when adsorption is considered. Taking into account results for the Gunnarsson-Schönhammer-like perturbation theory, in combination with results from spin-polarized TDDFT and model calculations, a correct description of the dissipated energy probably requires to take into account the changes in the Hilbert space of the system during adsorption. This should be irrelevant if the Hilbert space only changes slightly in a dynamic process, for instance considering vibrational excitations of an adsorbed molecule.
Spin effects may be underestimated within the perturbative approach.
Regarding the so-called spin transition, it was mentioned that DFT has principal problems describing the correct physical spin state of an adsorbing atom: The correct description for H in the investigated systems would include a superposition of the spin up and spin down states. This can not be described by present-day XC functionals. Instead, the hydrogen atom was in a spin-polarized state in most of the calculations of this work (with the exception of section 4.3.4). The resulting root-like behavior of the spin polarization, when the adiabatic potential energy surface is considered, then leads to unphysical divergencies in the derivative of the effective potential. This aspect is still under investigation, and probably needs fundamental work on XC functionals, which was outside the scope of this work. Within the framework of present-day functionals, a reliable description of the spin must be done non-adiabatically. However, nonadiabatic description of the transition requires a possibility to constrain the spin along the trajectory, and localize it in an atomic orbital. This is not possible within the employed code, but is a possible project for the future. It could be shown that the most important effect of a nonadiabatic description of the adsorbate's spin was a larger energy dissipation into the electronic system if the spin survives longer on its way to the surface.

It was also investigated to which amount the excitation probability of electrons and holes is spin-dependent. While the perturbative approach generally gives a rather small difference (factor 2-3 for H/K, or a very tiny difference for H/Al), in TDDFT and model calculations comparatively large differences appear. It is an unsolved question, whether they describe physical phenomena, or just contain DFT artifacts. If they are physical, the perturbative approach of this work underestimates them, while other approaches do show marked differences for excitations in the different spin channels, where one channel may be dominating the high-energy tails of the spectra. This discrepancy was resolved as follows: The definition of excitations within this work gives the correct limit if the particle is scattered back into the gas phase, while the alternative approaches try to include some of the localized electronic excitation that results from forming a chemical bond between substrate and adsorbate. Which way is better to describe experiments is not obvious, since, e.g., TDDFT calculations show spectra with spin features when the adsorbate is close to the surface, but these features are lost when the adsorbate is again far away from the surface. For multiple round trips in the chemisorption well either of the results may be more accurate. For instance, the localized excitations may be observable in chemicurrent experiments, if they decay into non-localized states on the timescale of the lifetime of an excited electron, and still possess an energy larger than the Schottky energy. Thus, the answer to this question is probably dependent on the system under investigation.

It was shown that differences for the isotope effect of electrons and holes must be expected, if the density of states of the substrate metal changes notably around the Fermi energy, in an energy range of about twice the Schottky barrier. If the density of states for, e.g., electrons is much larger than the density of states for holes, less hot holes can be detected, since most holes are excited between the Schottky barrier for holes and the Fermi energy. This has the consequence that the hole current is less dependent on the particle's mass, and thus the isotope effect for holes is less than the isotope effect for electrons.

Regarding metal epitaxy, for the first time it was shown in this thesis that electronic excitations might be measurable in experiments. On an ideal surface excitation of hot electrons and holes is unlikely, since the chemisorption energy is only just above the Schottky energy, or even below. Thus surface defects play an important role for chemicurrent generation in the system Mg/Mg(0001). Adsorption in a surface vacancy and a kink position have been investigated in detail, and it was shown that hot particles are excited, which may be detected. Due to the difference in mass between hydrogen and magnesium, the theory predicts that the particle yield is at least two orders of magnitude smaller than for hydrogen adsorption on metal surfaces. Within this thematic constellation, it was observed that the spectra do not decay exponentially, but in a more complex way. A possible description of the tail of the spectra is a Lorentzian distribution, valid from a certain minimum energy, which is for H adsorption larger than the Schottky energy, but less than this energy for heavy particles like Mg and Cl. Therefore an exponential fit to the tails of the spectra may be appropriate for light adsorbates, e.g. H, but such a fit is inappropriate for the heavier adsorbates. For adsorbates of mass considerably larger than the hydrogen mass distinct differences to an assumed Boltzmann distribution with some temperature are present, and should be in principle observable in experiments. The chemicurrent experiments for Mg/Mg adsorption may be considered as a hint towards a lower than exponential decay, since the measured chemicurrent is two orders of magnitude larger than was expected through naive extrapolation of exponentials, following the forced oscillator model. Further theoretical treatment of cases like Mg/Mg is necessary in order to support (or contradict) the suggestion of a Lorentzian form of the spectra, but a generally lower than exponential decay is probable.

For this purpose the form of the spectra can be investigated only if time-delayed chemical reactions do not play a dominating role for the chemicurrents. If the system changes chemically during the adsorption process, different excitation mechanisms play a role, which must be investigated separately. Thus the spectrum of the initial processes may not be observable. For the system $Cl_2$/K(110) a time-delayed chemical reaction is expected due to the formation of KCl. Time-dependent features have been observed in the case of oxygen adsorption, where the chemicurrent shows them 100 s after the initial impact of the first molecules [83].

It was shown that the simple jellium approximation is too simple for systems like $Cl_2$/K(110). The adsorption dynamics within this system is extremely involved. Although the NNL model, employing the jellium approximation, gives a reasonable explanation for excitation of hot exoelectrons, the non-adiabatic mechanism

proposed in that model may not be dominating in cases when the jellium approximation breaks down. Thus additional investigations with respect to the influence of the adsorption dynamics should be done.
The theory as presented is limited to small excitations, where the first order in perturbation theory dominates the system's behavior. For large excitations, a different approach must be taken. The author discusses three methods to move on:
The first method is a perturbative approach which takes into account higher orders in the perturbation theory, possibly also implementing a time-dependence of the electronic structure. While taking into account higher orders in the perturbation theory is possible in principle, the large computation time required makes this approach cumbersome and inefficient from a computational point of view. In addition, non-perturbative effects are missing in such an approach. Thus this approach is a possible first step to benchmark other methods, but not long-time strategy.
The second method makes use of a diabatic picture using constrained DFT, where particles are moving between two (or more) different PES, where one describes an excited (e.g., ionized) state, and the other a ground state (e.g., non-ionized). Approaches similar to the proposed one have already been investigated [50, 110]. The results of these investigations seem to imply that the approach is promising. Here some thoughts will be necessary on the topic how it is possible to take into account different trajectories belonging to the different PES, when the adsorbing particle behaves qualitatively different on the different trajectories. For instance, a particle may adsorb or be scattered back from the surface, and depending on the particle's velocity or excitation state close to the surface emission of atoms may or may not occur. These cases may require a large number of different PES, which is computationally demanding.
Therefore, the third possible method is direct calculation of the trajectory using TDDFT, calculating the particle's trajectory and evolution of the wavefunctions on the fly. The author proposes to introduce constraints in the standard TDDFT approach, so that ionization states of the adsorbing particles can be treated properly. The approach may then be labeled 'constrained TDDFT', and is a further development of the constrained DFT and TDDFT approaches [6, 69]. However, the author believes that this approach is extremely demanding from a fundamental and computational point of view, and thus would require a very considerable effort.
Taken together, the author proposes to move on using the diabatic method, which seems to be most promising, in contrast to the simple expansion of the perturbative approach. Also, in contrast to constrained TDDFT, it should still be affordable in terms of computational demand.
One principal problem of most present-day approaches is the trajectory approximation. If an electron-hole pair of an energy larger than the Schottky barrier is excited, the energy dissipated into that particle is *not* small any more, and considerable changes to the particle's velocity may be expected. However, the overall energy dissipation into the electronic system *is* small. The trajectory (in the case of an atomic adsorbate) usually does not change qualitatively, but only the particle's velocity along the trajectory changes. Therefore it is generally believed that the approximation works. However, a thorough investigation of this point, where the median of several calculations incorporating a realistic dynamics of the adsorbate, e.g. by using the 'fewest switches' algorithm, is still wished for.
Previous theoretical works on the problem of electronic excitations are considered within this work. It was found that the electronic friction model works in a wide range of adsorbates, but for certain adsorption geometries and certain systems results from the friction and perturbative approach differ. Within the present work the dissipated energy during Mg adsorption into a surface vacancy is not following the scaling law of the friction method over the whole range of masses considered.
It is also found that there is no justification to use the forced oscillator model for the high-energy tails of the spectra. For Mg adsorption the forced oscillator model predicts a current which is two orders of magnitude lower than the experimentally measured current. The scaling properties of the forced oscillator model also contradict results for the mass-scaling gained from the perturbative approach.
The perturbative approach is not as demanding as the TDDFT approach with respect to calculation time requirements. Often the effective potential is calculated when investigating the PES of an adsorbing system anyway, so that the present approach may be employed to calculate electronic excitations for a wide range of systems. The perturbative approach has the additional advantage that it can be done for nearly every system, while present-

day TDDFT calculations require low-mass adsorbates, and assume a scaling law of the calculated observables with the mass. However, within the present work it was found that such a scaling law does not necessarily exist for particles of large mass.

Model calculations are much faster from a computational point of view than the perturbative approach, but require fits of the model parameters. Such fits are nearly always ambiguous. An additional problem is that the models assume that they can neglect certain physical processes. Since theoretical investigation of electronic excitations is still an uncompleted field, important mechanisms may be left out of the model, or the wrong mechanisms may lead to fortuitous agreement of experiment and theory. Thus, additional calculations not based on model assumptions are required, such as in the present work.

The theoretical investigation of electronic excitations is far from being a completed field. A reliable and affordable theory of electronic excitations remains a goal for the future. The author believes that this work is one step towards such a theory.

# Chapter 9

# Acknowledgements

First I would like to thank my advisor Peter Kratzer for supervising my work, and for the many, and long, important discussions. Special thanks to him for letting me write my thesis with him.
Next, I have to thank the Deutsche Forschungsgemeinschaft (DFG), which financed my work through the Sonderforschungsbereich (SFB) 616, "Energy dissipation at surfaces".
Thanks are due to my fellow co-workers, post-docs and diploma students in the group, which, during my work, sometimes gave great advice, and sometimes just were there, providing me with a great atmosphere. I would like to mention Vladimir Fomin, Javad Hashemifar, Volker Pankoke, Sung Sakong, Benjamin Geisler, Johann Gutjahr and Hendrik Eilken.
Then there is the large group of collaborators in the SFB 616, who are too many to mention by name, but which provided many fruitful discussions, and always a great atmosphere, especially during the collaborator's workshops of the SFB.
I also have to thank David Bird, Eckhard Pehlke, Hermann Nienhaus, Matthew Mizielinksi, Michael Lindenblatt, David Krix, Jörg Meyer and Ulrich Hagemann for fruitful discussions. I acknowledge granted computer time from the John-von-Neumann center for scientific computing (NIC) in Jülich, Germany. Not to forget are the secretaries, especially Barbara Sacha and Maria Dunke, who always knew how to fend off the evils of bureaucracy.
Finally I would like to thank my parents for making a lot of things possible, and my fiancée, Nina, for just being there and reconstructing my enjoyment of my work when everything went wrong.

# Bibliography


[1] Kristian Laß, Xu Han, and Eckart Hasselbrink. The surprisingly short vibrational lifetime of the internal stretch of CO adsorbed on Si(100). *J. Chem. Phys.*, 123:051102, 2005.

[2] A. Bannani, C. Bobisch, and R. Möller. Ballistic electron microscopy of individual molecules. *Science*, 315:1824 – 1828, 2007.

[3] B. Mildner, E. Hasselbrink, and D. Diesing. Electronic excitations induced by surface reactions of H and D on gold. *Chem. Phys. Lett.*, 432:133–138, 2006.

[4] B. Gergen, H. Nienhaus, W. H. Weinberg, and E. W. McFarland. Direct detection of electron-hole pairs generated by chemical reactions on metal surfaces. *Science*, 294:2521–2523, 2001.

[5] J. R. Trail, M. C. Graham, D. M. Bird, M. Persson, and S. Holloway. Energy loss of atoms at metal surfaces due to electron-hole pair excitations: First-principles theory of 'chemicurrents'. *Phys. Rev. Lett.*, 88:166802, 2002.

[6] M. Lindenblatt and E. Pehlke. Ab initio simulation of the spin transition during chemisorption: H/Al(111). *Phys. Rev. Lett.*, 97:216101, 2006.

[7] S. Sakong, P. Kratzer, X. Han, K. Laß, O. Weingart, and E. Hasselbrink. Density-functional theory study of vibrational relaxation of CO stretching excitation on Si(100). *J. Chem. Phys.*, 129:174702, 2008.

[8] S. Sakong, P. Kratzer, X. Han, T. Balgar, and E. Hasselbrink. Isotope effects in the vibrational lifetime of hydrogen on germanium(100): Theory and experiment. *J. Chem. Phys.*, 131:124502, 2009.

[9] P. W. Anderson. Infrared catastrophe in Fermi gases with local scattering potentials. *Phys. Rev. Lett.*, 18:1049–1051, June 1967.

[10] T. Greber. Charge-transfer induced particle emission in gas surface reactions. *Surf. Sci. Rep.*, 28(1-2):1–64, 1997.

[11] H. Nienhaus. Electronic excitations by chemical reactions on metal surfaces. *Surf. Sci. Rep.*, 45:1–78, 2002.

[12] E. Hasselbrink. How non-adiabatic are surface dynamical processes? *Curr. Opin. Solid State Mater. Sci.*, 10(3-4):192 – 204, 2006.

[13] J. I. Juaristi, M. Alducin, R. Díez Muiño, H. F. Busnengo, and A. Salin. Role of electron-hole pair excitations in the dissociative adsorption of diatomic molecules on metal surfaces. *Phys. Rev. Lett.*, 100:116102, March 2008.

[14] P. Nieto, E. Pijper, D. Barredo, G. Laurent, R. A. Olsen, E.-J. Baerends, G.-J. Kroes, and D. Farias. Reactive and non-reactive scattering of $H_2$ from a metal surface is electronically adiabatic. *Science*, 312:86–89, 2006.

[15] A. C. Luntz, I. Makkonen, M. Persson, S. Holloway, D. M. Bird, and M. S. Mizielinski. Comment on "Role of electron-hole pair excitations in the dissociative adsorption of diatomic molecules on metal surfaces". *Phys. Rev. Lett.*, 102:109601, 2009.

[16] A. Duvenbeck, O. Weingart, V. Buss, and A. Wucher. Electron promotion and electronic friction in atomic collision cascades. *New J. Phys.*, 9(38), 2007.

[17] H.-C. Chang and G. E. Ewing. Lifetime of CO vibration on NaCl. *Phys. Rev. Lett.*, 65:2125, 1990.

[18] M. Morin, N. J. Levinos, and A. L. Harris. Vibrational energy transfer of CO/Cu(100): Nonadiabatic vibration/electron coupling. *J. Chem. Phys. 96 (5), 1 March 1992*, 96(5):3950 – 3956, March 1992.

[19] K. Laß, X. Han, and E. Hasselbrink. The surprisingly short vibrational lifetime of the internal stretch of CO adsorbed on Si(100). *J. Chem. Phys.*, 123:051102, 2005.

[20] Neil Shenvi, Sharani Roy, Priya Parandekar, and John C. Tully. Vibrational relaxation of NO on Au(111) via electron-hole pair generation. *J. Chem. Phys.*, 125:154703, 2006.

[21] Neil Shenvi, Sharani Roy, and John C. Tully. Nonadiabatic dynamics at metal surfaces: Independent-electron surface hopping. *J. Chem. Phys.*, 130:174107, 2009.

[22] D. Krix, R. Nünthel, and H. Nienhaus. Generation of hot charge carriers by adsorption of hydrogen and deuterium atoms on a silver surface. *Phys. Rev. B*, 75:073410, 2007.

[23] M. Persson. private communication. unpublished, 2009.

[24] Aron J. Cohen, Paula Mori-Sánchez, and Weitao Yang. Fractional spins and static correlation error in density functional theory. *J. Chem. Phys.*, 129(12):121104, 2008.

[25] G. Krugel, M. Grotemeyer, J. van Heys, M. Lindenblatt, and E. Pehlke. Ab initio molecular dynamics simulation of electronic energy dissipation: A comparison of H/Si(001), H/Al(111), and HCl/al(111). poster at the DPG spring meeting, Dresden, 2009.

[26] J. R. Trail, M. C. Graham, and D. M. Bird. Electronic damping of molecular motion at metal surfaces. *Comp. Phys. Comm.*, 137:163–173, 2001.

[27] J. R. Trail, D. M. Bird, M. Persson, and S. Holloway. Electron-hole pair creation by atoms incident on a metal surface. *J. Chem. Phys.*, 119:4539–4949, 2003.

[28] M. S. Mizielinski, D. M. Bird, M. Persson, and S. Holloway. Electronic nonadiabatic effects in the adsorption of hydrogen atoms on metals. *J. Chem. Phys.*, 122:084710, 2005.

[29] M. S. Mizielinski, D. M. Bird, M. Persson, and S. Holloway. Spectrum of electronic excitations due to the adsorption of atoms on metal surfaces. *J. Chem. Phys.*, 126:034705. Erratum in J. Chem. Phys. 126:229901, 2007.

[30] D. M. Bird, M. S. Mizielinski, M. Lindenblatt, and E. Pehlke. Electronic excitation in atomic adsorption on metals: A comparison of ab initio and model calculations. *Surf. Sci.*, 602:1212–1216, 2008.

[31] M. S. Mizielinski, D. M. Bird, M. Persson, and S. Holloway. Newns-Anderson model of chemicurrents in H/Cu and H/Ag. *Surf. Sci.*, 602:2617–2622, 2008.

[32] D. Bird. Coupling to electron-hole pairs during adsorption. private communication, 2009.

[33] R. M. Martin. *Electronic Structure - Basic Theory and Practical Methods*. Cambridge University Press, 2004.

[34] F. E. M. Charry. *First principles calculations of surfaces and layered materials*. PhD thesis, Universitat Autònoma de Barcelona, 2007.

[35] P. Hohenberg and W. Kohn. Inhomogeneous electron gas. *Phys. Rev.*, 136:B864, 1964.

[36] W. Kohn and L. J. Sham. Self-consistent equations including exchange and correlation effects. *Phys. Rev.*, 140:A1133, 1965.

[37] F. Aryasetiawan and O. Gunnarsson. The GW method. *Rep. Prog. Phys.*, 61:237 – 312, 1998.

[38] A. J. Cohen, P. Mori-Sánchez, and W. Yang. Insights into current limitations of density functional theory. *Science*, 321:792 – 794, 2008.

[39] J. P. Perdew, K. Burke, and M. Erzerhoff. Generalized gradient approximation made simple. *Phys. Rev. Lett.*, 77:3865, 1996.

[40] M. Städele, J. A. Majewski, P. Vogl, and A. Görling. Exact Kohn-Sham exchange potential in semiconductors. *Phys. Rev. Lett.*, 79(11):2089 – 2092, September 1997.

[41] Paolo Giannozzi, Stefano Baroni, Nicola Bonini, Matteo Calandra, Roberto Car, Carlo Cavazzoni, Davide Ceresoli, Guido L. Chiarotti, Matteo Cococcioni, Ismaila Dabo, Andrea Dal Corso, Stefano de Gironcoli, Stefano Fabris, Guido Fratesi, Ralph Gebauer, Uwe Gerstmann, Christos Gougoussis, Anton Kokalj, Michele Lazzeri, Layla Martin-Samos, Nicola Marzari, Francesco Mauri, Riccardo Mazzarello, Stefano Paolini, Alfredo Pasquarello, Lorenzo Paulatto, Carlo Sbraccia, Sandro Scandolo, Gabriele Sclauzero, Ari P. Seitsonen, Alexander Smogunov, Paolo Umari, and Renata M. Wentzcovitch. Quantum espresso: a modular and open-source software project for quantum simulations of materials. *J. Phys.: Cond. Mat.*, 21(39):395502, 2009.

[42] D. R. Hamann, M. Schlüter, and C. Chiang. Norm-conserving pseudopotentials. *Phys. Rev. Lett.*, 43:1494, 1979.

[43] N. Troullier and J. L. Martins. Efficient pseudopotentials for plane-wave calculations. *Phys. Rev. B*, 43:1993, 1991.

[44] S. G. Louie, S. Froyen, and M. L. Cohen. Nonlinear ionic pseudopotentials in spin-density-functional calculations. *Phys. Rev. B*, 26:1738, 1982.

[45] L. Kleinman and D. M. Bylander. Efficatious form for model pseudopotentials. *Phys. Rev. Lett.*, 48:1425, 1982.

[46] W. E. Pickett. Pseudopotential methods in condensed matter applications. *Comp. Phys. Rep.*, 9:115 – 198, 1989.

[47] J. Behler. Comparison of different methods and codes: (L)APW, LMTO, PAW, pseudo potentials, Gaussians, etc. Talk given at the workshop: "Density-Functional Theory Calculations for Modeling Materials and Bio-Molecular Properties and Functions - A Hands-On Computer Course" of the institute of Pure and Applied Mathematics (IPAM), University of California (UCLA), USA, November 2005.

[48] H. J. Monkhorst and J. D. Pack. Special points for Brillouin-zone integrations. *Phys. Rev. B*, 13(12):5188–5192, Jun 1976.

[49] M. Methfessel and A. T. Paxton. High-precision sampling for Brillouin-zone integration in metals. *Phys. Rev. B*, 40:3616 – 3621, 1989.

[50] J. C. Tully. Molecular dynamics with electronic transitions. *J. Chem. Phys.*, 93:1061, 1990.

[51] Matthew Stefan Mizielinski. *A Theory of Electron-Hole Pair Excitation in the Adsorption of Simple Atoms on Metal Surfaces*. PhD thesis, University of Bath, 2007.

[52] M. Head-Gordon and J. Tully. Molecular dynamics with electronic friction. *J. Chem. Phys.*, 103(23):10137 – 10145, 1995.

[53] J. Lindhard and M. Scharff. Energy dissipation by ions in the keV region. *Phys. Rev.*, 124(1):128 – 130, Oct 1961.

[54] H. Nienhaus, H. S. Bergh, B. Gergen, A. Majumdar, W. H. Weinberg, and E. W. McFarland. Direct detection of electron-hole pairs generated by chemical reactions on metal surfaces. *Surf. Sci.*, 445:335–342, 2000.

[55] H. Nienhaus, B. Gergen, W. H. Weinberg, and E. W. McFarland. Detection of chemically induced hot charge carriers with ultrathin metal film Schottky contacts. *Surf. Sci.*, 514:172–181, 2002.

[56] E. Müller-Hartmann, T. V. Ramakrishnan, and G. Toulouse. Localized dynamic perturbations in metals. *Phys. Rev. B*, 3(4):1102–1119, 1971.

[57] B. Hellsing and M. Persson. Electronic damping of atomic and molecular vibrations at metal surfaces. *Phys. Scr.*, 29:360, 1984.

[58] K. Schönhammer and O. Gunnarsson. Localized dynamic perturbations in metals. *Z. Phys. B*, 38:127–131, 1980.

[59] K. Schönhammer and O. Gunnarsson. Sticking probability on metal surfaces: Contribution from electron-hole pair excitations. *Phys. Rev. B*, 22(4):1629–1637, August 1980.

[60] K. Schönhammer and O. Gunnarsson. Sticking probability on metal surfaces: Temperature dependence of the electron-hole pair mechanism. *Phys. Rev. B*, 24(12):7084–7092, December 1981.

[61] O. Gunnarsson and K. Schönhammer. Boson approximation for localized dynamic perturbation in metals. *Phys. Rev. B*, 25:2503–2513, 1982.

[62] E. Runge and E. K. U. Gross. Density-functional theory for time-dependent systems. *Phys. Rev. Lett.*, 52(12):997, Mar 1984.

[63] M. Lindenblatt and E. Pehlke. Time-dependent density-functional molecular-dynamics study of the isotope effect in chemicurrents. *Surf. Sci.*, 600(23):5068–5073, 2006.

[64] M. Timmer and P. Kratzer. Electron-hole spectra created by adsorption on metals from density-functional theory. *Phys. Rev. B*, 79:165407, 2009.

[65] U. Hagemann, D. Krix, and H. Nienhaus. Electronic excitations generated by the deposition of Mg on Mg films. *Phys. Rev. Lett.*, 104:028301, 2010.

[66] U. Hagemann. Chemostrom-Messungen an Mg/*p*-Si(001) Schottky-Dioden bei Mg-Deposition und Oxidation und Charakterisierung epitaktischer Oxid-Schichten auf Si. Master's thesis, Universität Duisburg-Essen, January 2009.

[67] P. H. Dederichs, S. Blügel, R. Zeller, and H. Akai. Ground states of constrained systems: Applications to Cerium impurities. *Phys. Rev. Lett.*, 53(26):2512 – 2515, 1984.

[68] Q. Wu and T. Van Voorhis. Constrained density functional theory and its application in long-range electron transfer. *J. Chem. Theory Comput.*, 2:765 – 774, 2006.

[69] J. Behler, B. Delley, K. Reuter, and M. Scheffler. Nonadiabatic potential-energy surfaces by constrained density-functional theory. *Phys. Rev. B*, 75:115409, 2007.

[70] G. L. Hofacker. Quantentheorie chemischer Reaktionen. *Z. Naturforsch. A*, 18a:607, 1963.

[71] R. A. Marcus. On the analytical mechanics of chemical reactions. Classical mechanics of linear collisions. *J. Chem. Phys.*, 45:4500, 1966.

[72] D. Krix, R. Nünthel, and H. Nienhaus. Chemical interaction of H and D atoms with Ag/H:*p*-Si(111) thin film diodes. *J. Vac. Sci. Technol. A*, 25(4):1156–1160, July/August 2007.

[73] P. W. M. Jacobs, Yu. F. Zhukovskii, Yu. Mastrikov, and Yu. N. Shunin. Bulk and surface properties of metallic aluminium: DFT simulations. *Sol. Stat. Phys.*, 6(1):7–28, 2002.

[74] H. Nienhaus, D. Krix, and S. Glass. Varying the Schottky barrier of thin film Mg/H:*p*-Si(111) contacts: Properties and applications. *J. Vac. Sci. Technol. A*, 25(4):950–954, July 2007.

[75] J. Wan, Y. L. Fan, D. W. Gong, S. G. Shen, and X. Q. Fan. Surface relaxation and stress of fcc metals: Cu, Ag, Au, Ni, Pd, Pt, Al and Pb. *Modelling Simul. Mater. Sci. Eng.*, 7:189 – 206, 1999.

[76] H. Nienhaus, H. S. Bergh, B. Gergen, A. Majumdar, W. H. Weinberg, and E. W. McFarland. Electron-hole pair creation at Ag and Cu surfaces by adsorption of atomic hydrogen and deuterium. *Phys. Rev. Lett.*, 82(2):446–449, January 1999.

[77] A. M. Rappe, K. M. Rabe, E. Kaxiras, and J. D. Joannopoulos. Optimized pseudopotentials. *Phys. Rev. B*, 41(2):1227–1230, Jan 1990.

[78] A. Faust, C. Merkel, and H. Bross. Energy band structure and Fermi surface of potassium. *phys. stat. sol. (b)*, 77:591 – 600, 1976.

[79] H. Landolt [founder]. *Landolt-Bornstein Numerical Data and Functional Relationships in Science and Technology*, volume III/18. Springer, Berlin, 1984.

[80] K. Huba, D. Krix, C. Meier, and H. Nienhaus. Ultrathin K/*p*-Si(001) Schottky diodes as detectors of chemically generated hot charge carriers. *J. Vac. Sci. Technol. A*, 27(4), Jul/Aug 2009.

[81] A. Kiejna. Adhesive energies at potassium alloys interfaces. *Physica Scripta*, 35:738 – 741, 1987.

[82] L. A. Hellberg, J. Campbell, and B. Kasemo. Surface chemiluminescence of $Cl_2$ on potassium. *Surf. Sci.*, 502 – 503:399 – 404, 2002.

[83] D. Krix, K. Huba, and H. Nienhaus. Chemicurrent measurements using alkali metal covered Pd/p-Si(001) Schottky diodes. *J. Vac. Sci. Technol. A*, 27:918, 2009.

[84] John P. Perdew, J. A. Chevary, S. H. Vosko, Koblar A. Jackson, Mark R. Pederson, D. J. Singh, and Carlos Fiolhais. Atoms, molecules, solids, and surfaces: Applications of the generalized gradient approximation for exchange and correlation. *Phys. Rev. B*, 46(11):6671 – 6687, 1992.

[85] J. Meyer and M. Timmer. private communication. unpublished, 2009.

[86] M. Pozzo and D. Alfè. Structural properties and enthalpy of formation of magnesium hydride from quantum monte carlo calculations. *Phys. Rev. B*, 77:104103, 2008.

[87] H. J. Gotsis, D. A. Papaconstantopoulos, and M. J. Mehl. Tight-binding calculations of the band structure and total energies of the various phases of magnesium. *Phys. Rev. B*, 65:134101, 2002.

[88] P. T. Sprunger, K. Pohl, H. L. Davis, and E. W. Plummer. Multilayer relaxation of the Mg(0001) surface. *Surf. Sci.*, 297(1):L48 – L54, 1993.

[89] A. F. Wright, P. J. Feibelman, and S. R. Atlas. First-principles calculation of the Mg(0001) surface relaxation. *Surf. Sci.*, 302(1–2):215 – 222, 1994.

[90] S. Prakash and S. K. Joshi. Phonon frequencies of the hexagonal metals Be, Mg, and Zn. *Phys. Rev. B*, 1(4):1468–1478, Feb 1970.

[91] W. Kossel. Zur Theorie des Kristallwachstums. *Nachr. Ges. Wiss. Götting., Math.-Phys. Kl.*, pages 135 – 143, 1927.

[92] I. N. Stranski. Zur Theorie des Kristallwachstums. *Z. Phys. Chem.*, 136:259 – 278, 1928.

[93] U. O. Karlsson, G. V. Hansson, P. E. S. Persson, and S. A. Flodström. Surface electronic structure of Mg(0001). *Phys. Rev. B*, 26(4):1852 – 1858, 1982.

[94] M. Lindenblatt, J. van Heys, and E. Pehlke. Molecular dynamics of non-adiabatic processes at surfaces: Chemisorption of H/Al(111). *Surf. Sci.*, 600(18):3624–3628, 2006.

[95] J. Strömquist, L. Hellberg, B. Kasemo, and B. I. Lundqvist. Ballistic motion and abstraction in dimer dissociation at surfaces $Cl_2$ on K. *Surf. Sci.*, 352:435–441, 1996.

[96] L. Hellberg, J. Strömquist, B. Kasemo, and B. I. Lundqvist. Electron-transfer pathways in dynamic processes – $Cl_2$ on K. *Phys. Rev. Lett.*, 74:4742, 1995.

[97] D. Andersson, B. Kasemo, and L. Walldén. Surface chemiluminescence in the $K^{solid}$ + $Cl_2^{gas}$ reaction. *Surf. Sci.*, 152/153:576 – 586, 1985.

[98] J. K. Nørskov, D. M. Newns, and B. I. Lundqvist. Molecular-orbital description of surface chemoluminescence. *Surf. Sci.*, 80:179–188, 1979.

[99] B. Kasemo, E. Törnqvist, J. K. Nørskov, and B. I. Lundqvist. Photon and electron emission as indicators of intermediate states in surface reactions. *Surf. Sci.*, 89:554 – 565, 1979.

[100] B. Kasemo and L. Walldén. Photon and electron emission during halogen adsorption on sodium. *Surf. Sci.*, pages 393 – 407, 1975.

[101] A. Hellman, B. Razaznejad, and B. I. Lundqvist. Potential-energy surfaces for excited states in extended systems. *J. Chem. Phys.*, 120:4593, 2004.

[102] K. Hermann, K. Freihube, T. Greber, A. Böttcher, R. Grobecker, D. Fick, and G. Ertl. Dynamics of the interaction of $O_2$, with Li surfaces. *Surf. Sci. Letters*, 313:L806 – L810, 1994.

[103] T. Greber, K. Freihube, R. Grobecker, A. Böttcher, K. Hermann, G. Ertl, and D. Fick. Nonadiabatic processed during the oxidation of Li layers. *Phys. Rev. B*, 50(12):8755, 1994.

[104] E. Moore, editor. *Molecular Modelling and Bonding (Molecular World)*. Royal Society of Chemistry, 2002.

[105] S. Berman, J. Callaway, and R. D. Woods. Cohesive energy of potassium. *Phys. Rev.*, 101(5):1467–1468, Mar 1956.

[106] R. J. Whitefield and J. J. Brady. New value for work function of sodium and the observation of surface-plasmon effects. *Phys. Rev. Lett.*, 26(7):380–383, Feb 1971.

[107] M. Prencipe, A. Zupan, R. Dovesi, E. Aprà, and V. R. Saunders. *Ab initio* study of the structural properties of LiF, NaF, KF, LiCl, NaCl, and KCl. *Phys. Rev. B*, 51(6):3391 – 3396, 1995.

[108] G. Kresse and J. Furthmüller. Efficient iterative schemes for ab initio total-energy calculations using a plane-wave basis set. *Phys. Rev. B*, 54:11169, 1996.

[109] S. Sakong. Binding energy of $Cl_2$ with VASP. private communication, 2009.

[110] C. Carbogno. *Non-adiabatic effects in the dissociative adsorption of $O_2$ on aluminum (111) surfaces*. PhD thesis, Universität Ulm, 2009.